High Temperature Deformation Behaviour of an Al-Mg-Si-Cu Alloy and Its Relation to the Microstructural Characteristics

By

Roger Nicol Carrick

A thesis
presented to the University of Waterloo
in fulfillment of the
thesis requirement for the degree of
Master of Applied Science
in
Mechanical Engineering

Waterloo, Ontario, Canada, 2009

AUTHOR'S DECLARATION

I hereby declare that I am the sole author of this thesis. This is a true copy of the thesis, including any required final revisions, as accepted by my examiners.

I understand that my thesis may be made electronically available to the public.

Abstract

The microstructural evolution and mechanical properties at elevated temperatures of a recently fabricated fine-grained AA6xxx aluminium sheet were evaluated and compared to the commercially fabricated sheet of the same alloy in the T4P condition. The behaviour of the fine-grained and T4P sheets was compared at elevated temperatures between 350°C and 550°C, as well as room temperature. The materials were tested at various strain-rates in the range of $5.0x10^{-4}s^{-1}$ to $6.7x10^{-1}s^{-1}$. Static ageing at elevated temperatures was conducted to examine the precipitate evolution when no deformation was involved, and tensile tests were conducted at elevated temperatures to study both the deformation behaviour and the microstructural evolution during testing. The grain structure was examined before and after deformation with optical microscopy. The level of damage due to cavitation was measured and the fracture surfaces of the samples were examined after deformation using optical and scanning electron microscopy. Static exposure to elevated temperatures revealed that the precipitate structure of the fine-grained material did not change extensively. The T4P material, however, underwent extensive growth of precipitates, including a large amount of grain boundary precipitation. At room temperature, the T4P material deformed at much higher stresses than the FG material. The FG material, however, achieved greater elongations to failure than the T4P material. The greater elongation to failure of the FG material at room temperature was related to the lower stresses which delayed the onset of void formation and changed the mechanism of failure. Deformation at elevated temperatures revealed that the fine-grained material achieved significantly larger elongations to failure than the T4P material in the temperature range of 350°C-450°C. Both materials behaved similarly at 500°C and 550°C. At temperatures below 500°C, deformation resulted in elongation of the grains. Above 500°C, the grain size was greatly reduced in the T4P material, and only a slightly increased in the fine-grained material. The final grain size after deformation in both materials was found to be smaller at high strain-rates than at low strain-rates. At temperatures above 450°C, the elongation to failure in both materials generally increased with increasing strain-rate. Cavitation played a large role in the failure of both materials, particularly at the highest temperatures and lowest strain-rates.

The poor performance of the T4P material at these temperatures was attributed to the precipitate characteristics of the sheet, which lead to elevated stresses and increased cavitation. The deformation mechanism of both materials was found to be controlled by dislocation climb, accommodated by the self diffusion of aluminium at 500°C and 550°C. The deformation mechanism in the fine-grained material transitioned to power law breakdown at lower temperatures. At 350°C to 450°C, the T4P material behaved similarly to a particle hardened material with an internal stress created by the precipitates. The reduction in grain size of the T4P material after deformation at 500°C and 550°C was suggested to be caused by dynamic recovery/recrystallization. The grain size evolution of the fine-grained material may have been caused by the same mechanism and/or grain boundary sliding effects, however, no clear conclusion could be drawn. The role of a finer grain-size in the deformation behaviour at elevated temperatures was mainly related to enhanced diffusion through grain boundaries, while grain boundary sliding in the FG material at the highest deformation temperatures and the lowest strain-rates was considered as a possibility. The differences in the behaviour of the two materials were mainly attributed to the difference in the precipitation characteristics of the materials; when precipitates were present, they behaved differently, and when precipitates dissolved at high temperatures, the materials with similar reduced grain-sizes behaved similarly.

Acknowledgements

I would like to thank my academic supervisor Shahrzad Esameili for her support, understanding and guidance throughout this project. Without her guidance, this thesis would not have been completed.

I am grateful for the financial support NSERC, Novelis Global Technology Center and the University of Waterloo provided for this work.

Special thanks goes to Andy Barber for all the help that he gave in setting up experiments, and fixing equipment that inevitably malfunctioned. I would also like to thank Norval Wilhelm for all of his support in material preparation. A very big thank you to Sooky Winkler for all the help she gave me with experiments; without her help, I would still be conducting tests. I would also like to thank Dr. Haiou Jin and all the staff at Novelis for their help throughout this project.

My friends at Waterloo made this a great experience over the last two years. I would like to thank Panthea Sepehrband and Brian Langelier for their help and conversations. I would also like to thank Jon Mui for keeping me well fed these last two years with his excellent culinary skills. Special thanks to Charling Li and Alyssa Mohino for distracting me and making sure I didn't get too stressed out.

Finally, I would like to thank my family for their support throughout this project. You were the rock that helped keep my head above water.

Table of Contents

List of Tables

List of Figures

Chapter 1 Introduction

The automotive industry is under ever increasing pressure to produce more fuel-efficient vehicles in light of global warming caused by greenhouse gas emissions. One solution to this problem has been to reduce the weight of vehicles through the use of lighter materials such as aluminium. While aluminium has seen significant increases in its use in the automotive industry, it still lags far behind steel in chassis and body panel applications. Reasons for the slow adoption of aluminium alloys include higher material costs than steel as well as increased forming process costs [1].

AA6xxx aluminium alloys are used in the automotive industry for outer body panels and bumpers because of their weldability, good age-hardenability, formability, corrosion resistance, good surface finish and low cost. In a traditional auto body panel production operation, the sheet is formed at room temperature while in the T4 (naturally aged) or T4P (commercially pre-aged) condition and then age hardened during the paint bake cycle [2,3].

While the formability of aluminium is low at room temperature, the ductility of aluminium has been shown to improve at elevated temperatures [4-11]. Previous investigations have focused on either warm (200-350°C) [4,8] or hot deformation (>350°C) [5,11]. In general, elevated temperatures have been shown to significantly increase ductility, although most research has been conducted at significantly lower strain-rates than seen in industrial forming operations (~$1s^{-1}$) [12]. Investigation of material properties at higher strain-rates is very important as part production times affect the cost significantly. Additionally, higher ductility allows the production of more complex parts which can lead to a reduction in the number of fasteners or welding operations required [13]. Refinement of the grain size has also been shown to significantly increase the ductility of aluminium under certain conditions [10,13-15]. It is of interest to investigate and characterize the effect of grain refinement and elevated temperatures on ductility.

Chapter 2 Literature Review

2.1 Introduction

This study examines the deformation of fine-grained and coarse-grained AA6xxx alloys and how the microstructure affects and is influenced by deformation. In this chapter, an introduction to low temperature deformation factors, as well as high temperature deformation mechanisms are given. Then the influence of high temperature and deformation on the microstructure is reviewed. Next, the mechanisms of failure at elevated temperature are examined. Finally, AA6xxx alloys are introduced, and some related research is presented.

2.2 Low Temperature Deformation Factors

Crystalline materials deform at room temperature as a result of dislocation processes as well as twinning. Aluminium has a FCC crystal structure and therefore mainly deforms through dislocation movement. Plastic flow is a kinetic process which is affected by factors such as strain, strain-rate and temperature. The ideal shear strength is defined as the stress at which the deformation of a perfect crystal is no longer elastic; above this stress, the crystal structure becomes unstable. This strength can be calculated with knowledge of the crystal structure and inter-atomic forces [16,17]. In real situations, however, deformation occurs at stresses below the ideal shear strength by the movement of dislocations. Deformation is therefore limited by the rate of nucleation of dislocations and the rate at which these dislocations glide through a crystal. The motion of these dislocations is almost always obstacle-limited. These obstacles can include: other dislocations, solute atoms, precipitates, grain boundaries, or even the friction of the crystal lattice itself [18]. At low temperatures, below ~0.3-0.4 T_m, where T_m is the absolute melting temperature, recovery mechanisms do not play a significant role in affecting the material's microstructure [18,19]. As such, increasing the amount of strain in the material increases the number of dislocations present in the crystal structure. This increased dislocation density causes an increase in the flow stress required to facilitate the motion of the dislocations through and around each other; this is known as strain hardening [20]. At low temperatures, the effect of strain-rate is generally small compared

to the strain hardening effect, and is therefore often ignored when describing the yield strength of materials. The flow stress can therefore be related to the strain using the Hollomon equation, Equation 2.1.

$$\sigma \propto \varepsilon^{n} \quad \textbf{[21]} \qquad \textbf{Equation 2.1}$$

Where σ is the stress, ε is the strain, and n is the strain hardening coefficient. Similar to strain hardening, particles within the crystal structure can limit the movement of dislocations. When a dislocation meets a significantly hard particle, it must pass it by some means to allow deformation to continue. At low temperatures, the two main methods of passing a discrete obstacle such as a precipitate are by shearing the particle or looping it via the Orowan mechanism [18,20,22]. Each of these processes is illustrated below in Figure 2.1.

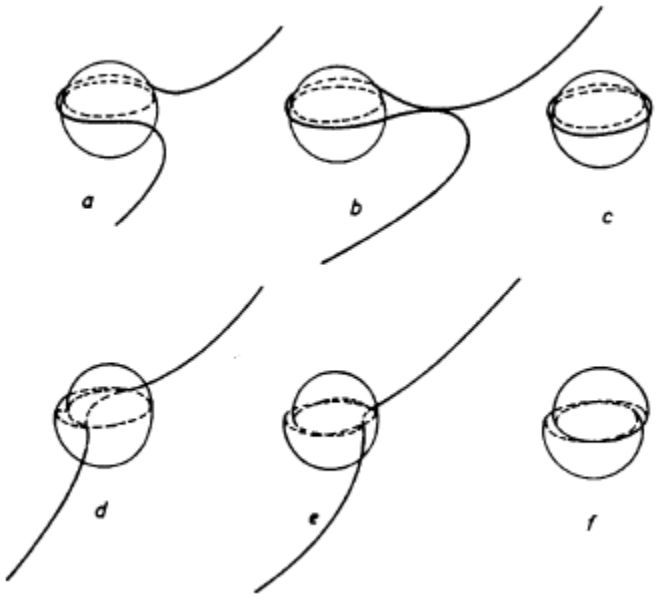

Figure 2.1: Dislocation passing of a particle by the Orowan mechanism (a-c) and by particle shearing (d-f) [23]

Dislocations will pass particles with the shearing mechanism when the particle is small (Figure 2.1 d-f). Beyond a critical particle size, r_c, the dislocation will pass through Orowan looping (Figure 2.1 a-c). The relative shear stresses required for each of these processes is illustrated in Figure 2.2.

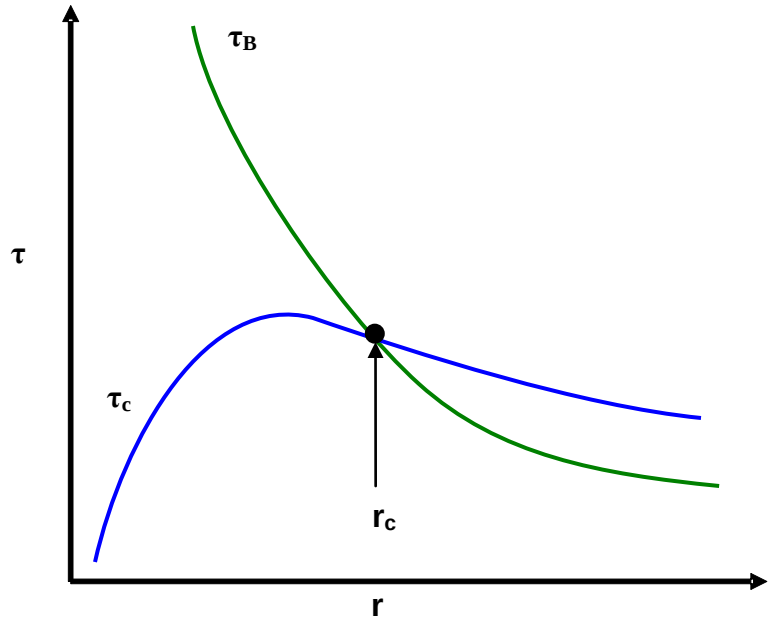

Figure 2.2: Schematic example of the shear strength vs. particle size for particle passing mechanisms, shearing, τ_c and looping, τ_B (reproduced from [24]).

In the example shown, the maximum shear strength required, and therefore the maximum strengthening, occurs before the r_c particle size. Depending on the particles and alloy system, the maximum strengthening can also occur at the r_c particle size. Further increasing the size of the particles will lower the energy required to bypass the particle due to the increased particle spacing resulting from coarsening. For this reason, the best strengthening is provided by a fine dispersion of small, hard particles [24]. Another method of strengthening in a polycrystalline material is through the use of grain boundaries. Grain boundaries are high energy defects in the crystal structure and dislocations can not easily pass through them. By decreasing the average grain size, the area fraction of grain boundaries is increased, and therefore the material is strengthened. This effect is usually illustrated by the Hall-Petch relationship.

$$\sigma_y = \sigma_0 + \frac{k_y}{\sqrt{d}} \quad \textbf{[24]} \qquad \textbf{Equation 2.2}$$

Where σ_y is the yield stress, σ_0 is the stress required to move a dislocation through the lattice, k_y is the Hall-Petch strengthening coefficient, and d is the average grain

diameter. This shows that as the grain size decreases, the yield strength will increase. This relationship holds for most materials, however if the grain size is reduced to a very small size (~<100nm), further reductions in grain size either may not affect the strength, or softening may occur. This is known as the inverse Hall-Petch relationship [25]. This is an area of ongoing research.

2.3 Elevated Temperature Effects

At elevated temperatures (>0.4T_m), thermally activated processes are the primary factor affecting mechanical deformation [19]. The deformation becomes highly dependent on the strain-rate and temperature. Strain hardening has a much reduced effect because of the increased effect of recovery processes [18,19,26]. This means that instead of describing a material based on its hardening potential, it can be characterized by its creep resistance [19,26]. Creep is defined as the time-dependent plasticity under a constant stress at an elevated temperature [26]. At low temperatures, strain hardening severely limits the amount of strain that will be produced at a constant stress, however, at elevated temperatures, recovery mechanisms allow strain to continue, even at low stresses. The general plasticity of materials in these conditions is summarized in Figure 2.3.

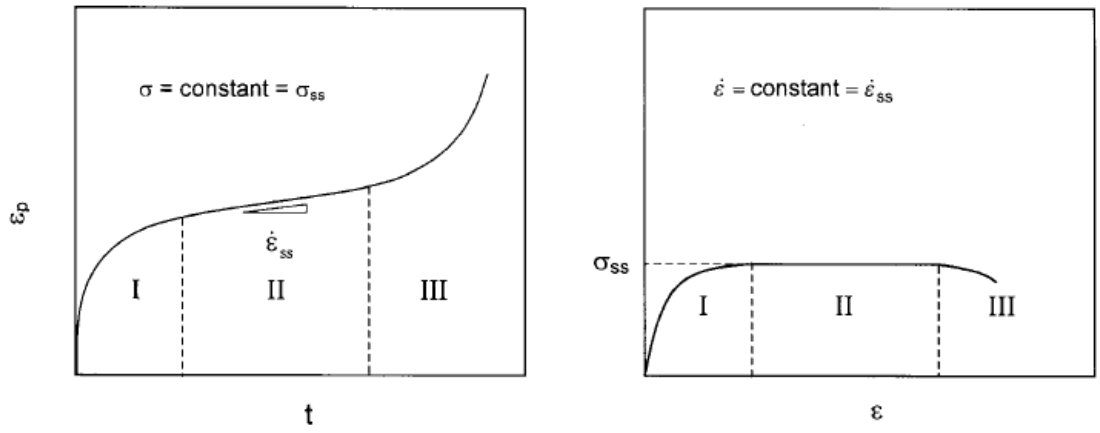

Figure 2.3: Constant stress and constant strain-rate high temperature plasticity curves [26].

The three regions shown in Figure 2.3 represent stage I, II and III creep. During stage I, or primary creep, the strain-rate, or creep rate, is decreasing with increasing strain. This is analogous to strain hardening, as in this region the dislocation density is

increasing. Stage II creep is characterized by a constant creep rate (i.e. steady-state creep). In this region, there is little change in the dislocation density; the rate of dislocation generation equals the rate of dislocation annihilation (recovery). Finally, stage III creep occurs when failure takes place within the material [26]. Stage II creep is the most important regime for the study of deformation as the largest portion of strain occurs in this region. Considering constant strain-rate experiments, if the testing strain-rate is increased, the steady-state stress will also increase [26]. The measure of this change is known as strain-rate sensitivity, *m*. The strain-rate sensitivity is defined in Equation 2.3.

$$m = \left[\frac{\delta \ln \sigma}{\delta \ln \dot{\varepsilon}}\right]_{T,s} \quad \textbf{[18,26]} \qquad \textbf{Equation 2.3}$$

T and *s* signify the strain-rate sensitivity only applies to a single temperature and structural state [18,19,26,27]. Most commonly, the strain-rate sensitivity is determined using strain-rate change tests. These tests involve straining a sample until a constant stress is achieved, then increasing the strain-rate and repeating the process. This technique is illustrated in Figure 2.4.

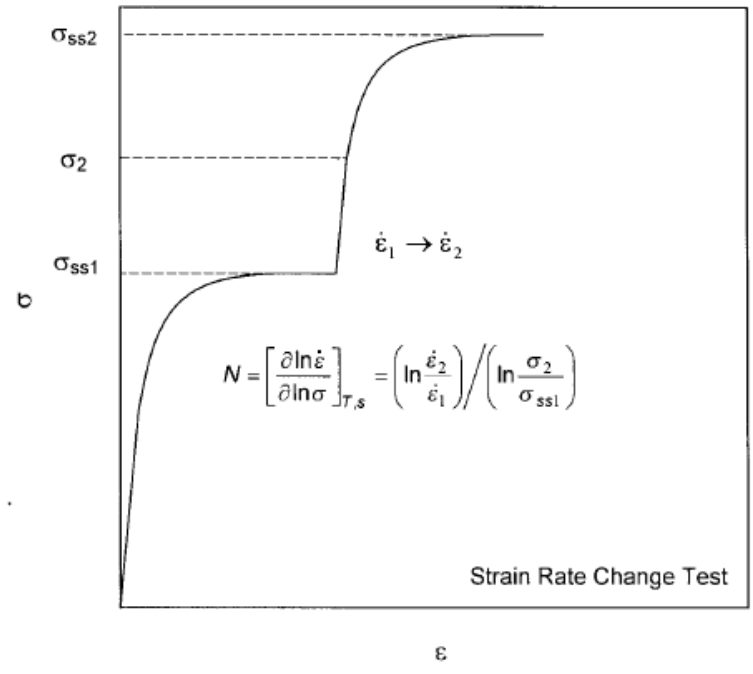

Figure 2.4: Graphical representation of the constant structure strain-rate change test (modified from [26]).

Using the strain-rate sensitivity, we can show the general relationship between stress and steady-state strain at high temperatures as:

$$\sigma \propto \dot{\varepsilon}^{m} \qquad \dot{\varepsilon} \propto \sigma^{N} \quad \textbf{[18,26]} \qquad \textbf{Equation 2.4}$$

Where N is the stress sensitivity, and $N=1/m$. At elevated temperatures, N is typically between 3 and 10, and hence the phenomenon is called "power law creep" [18]. To take into account the thermally activated processes involved in deformation at elevated temperatures, the activation energy of the deformation mechanism, Q, is added in the form of an Arrhenius type equation, as seen in Equation 2.5.

$$\dot{\varepsilon} \propto \exp\left(\frac{-Q}{RT}\right)\sigma^{N} \quad \textbf{[18,26]} \qquad \textbf{Equation 2.5}$$

Where R is the ideal gas constant. In general, Q describes the energy required to overcome an obstacle. This type equation will be further discussed in sections that follow.

Another property that temperature affects is the elastic modulus. Since the elastic modulus is related to the strength of the interatomic bonds in the crystal structure, the elastic modulus decreases with increasing temperature as the atoms spread further apart. Several studies on the elastic modulus of aluminium and its alloys have shown that the elastic modulus decreases almost linearly with increasing temperature [18,28-30]. The temperature adjusted elastic modulus is important because it is often used to normalize data tested at different temperatures. This normalization is used to maintain the constant structure requirement when determining the activation energy [26]. Applying the normalization to Equation 2.5, the relationship becomes:

$$\dot{\varepsilon} \propto \exp\left(\frac{-Q}{RT}\right)\left(\frac{\sigma}{E}\right)^{N} \quad \textbf{[18,26]} \qquad \textbf{Equation 2.6}$$

Where E is the elastic modulus at the temperature T.

Additionally, some forms of creep, such as grain boundary sliding and Harper-Dorn creep are affected by the grain size of the material. An additional term is often added to the creep equation to account for the effect of grain size, leading to Equation 2.7.

$$\dot{\varepsilon} \propto \exp\left(\frac{-Q}{RT}\right)\left(\frac{\sigma}{E}\right)^{N}\left(\frac{b}{d}\right)^{p} \quad \textbf{[31,32]} \qquad \textbf{Equation 2.7}$$

Where b is the Berger's vector, d is the grain size and p is the grain size exponent.

As stated earlier, decreasing the grain size, leads to strengthening of the material at low temperatures. There is evidence however, that this effect is suppressed at elevated temperatures. In high purity aluminium, it has been shown in [33] that the Hall-Petch constant, k_y, decreases rapidly with increasing temperature as shown in Figure 2.5. This decrease in was attributed to rapid recovery effects which are prevalent at elevated temperatures [33].

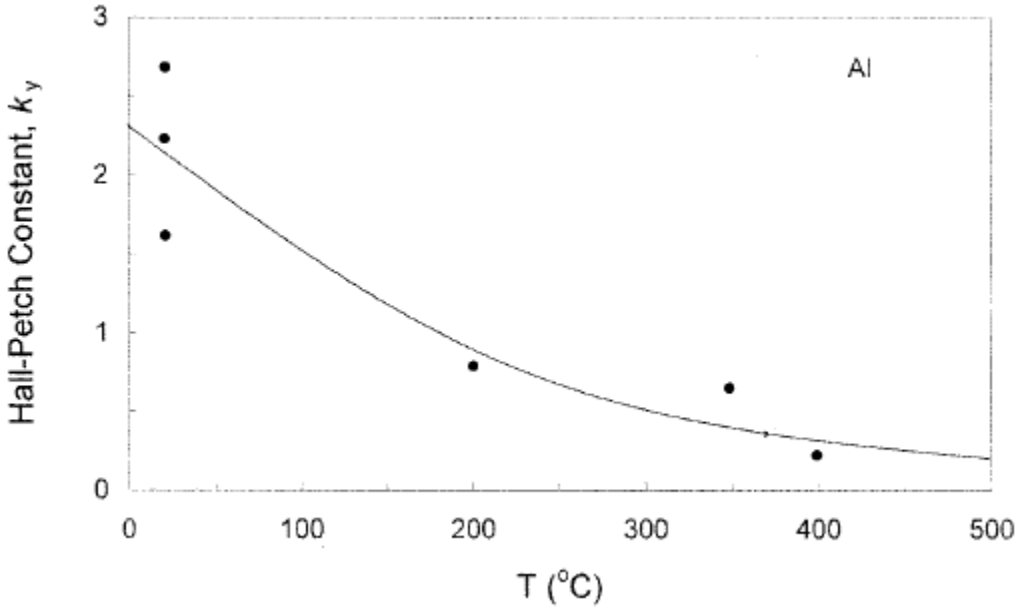

Figure 2.5: Variation of the Hall-Petch constant with temperature in pure aluminium [33].

2.3.1 Power Law Creep

At elevated temperatures, dislocations can not only glide through a crystal, they can also climb. These two mechanisms are often competing and can occur simultaneously. The slower of these two mechanisms becomes the rate controlling mechanism for deformation [18,19,26].

In solid solution strengthened alloys such as AA5xxx Al-Mg alloys, it has been shown that the rate controlling mechanism is dislocation glide [34]. The resistance to dislocation movement is caused by the way dislocations interact with the solute atoms. It has been reported that this type of creep occurs most readily in alloys where there is a large disparity between the sizes of the solute and matrix atoms, as well as high concentrations of the solute atoms [35,36]. The drag force on the dislocations is caused by the stress field in the crystal lattice around the solute atom, and the rate of dislocation movement is controlled by diffusion of solute atoms out of the path of the dislocation [37-40]. Therefore, the activation energy for creep limited by the diffusion of solute atoms is equal to the activation energy of diffusion of the solute atoms within the matrix. The stress exponent for this type of deformation is $N=3$. This type of creep is sometimes called three-power law creep or viscous-glide creep [26]. The creep curve for Al-Mg showing three-power law creep is shown in Figure 2.6

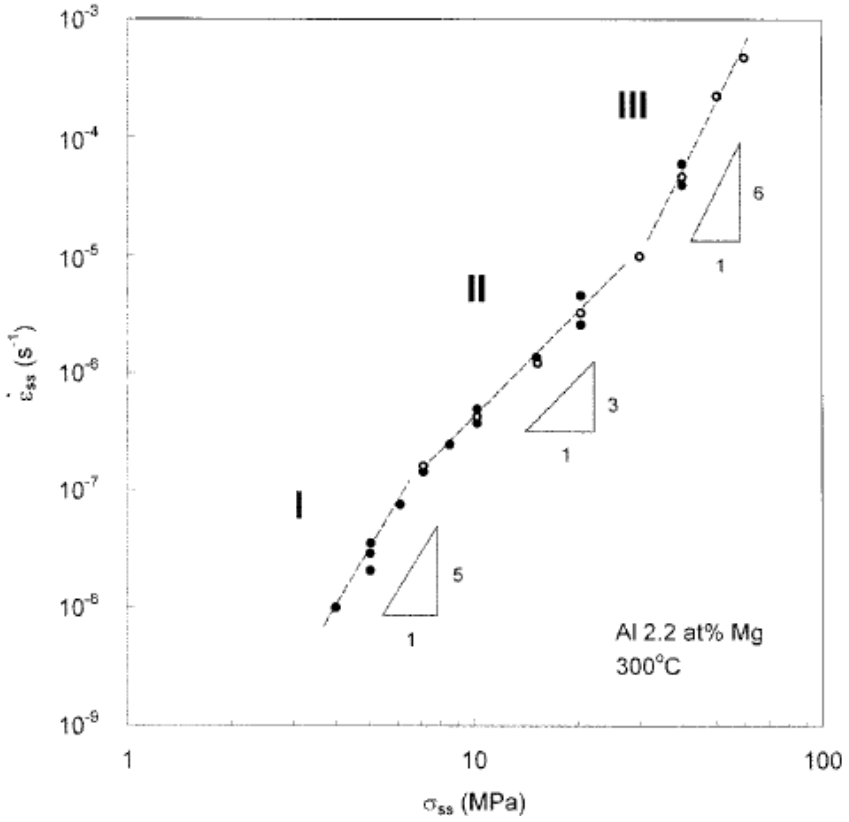

Figure 2.6: Creep curve of Al-2.2%Mg at 300C [26].

In pure metals, some alloy systems and solid solution strengthened alloys at higher stresses, the rate controlling mechanism is dislocation climb [18,19,26,41,42]. Dislocation climb is the process by which dislocations move perpendicular to their slip plane by the diffusion of atoms/vacancies to the dislocation line [20]. Due to this diffusion mechanism, the activation energy for creep is almost exactly the same as the activation energy for self diffusion [18,19,26]. The stress exponent for this type of creep varies from 4 to 7, although it is most commonly about 5. For this reason, this deformation mode is often called five-power law creep [26]. Creep by climb and viscous-drag have been found to have grain size exponents of p=0, suggesting that they are not affected by grain size [31]. The creep curve for pure aluminium is shown below. Note that the data has been normalized with the temperature adjusted shear modulus, G, and the self diffusion coefficient, D_{sd}, so that multiple temperatures may be shown on the same curve.

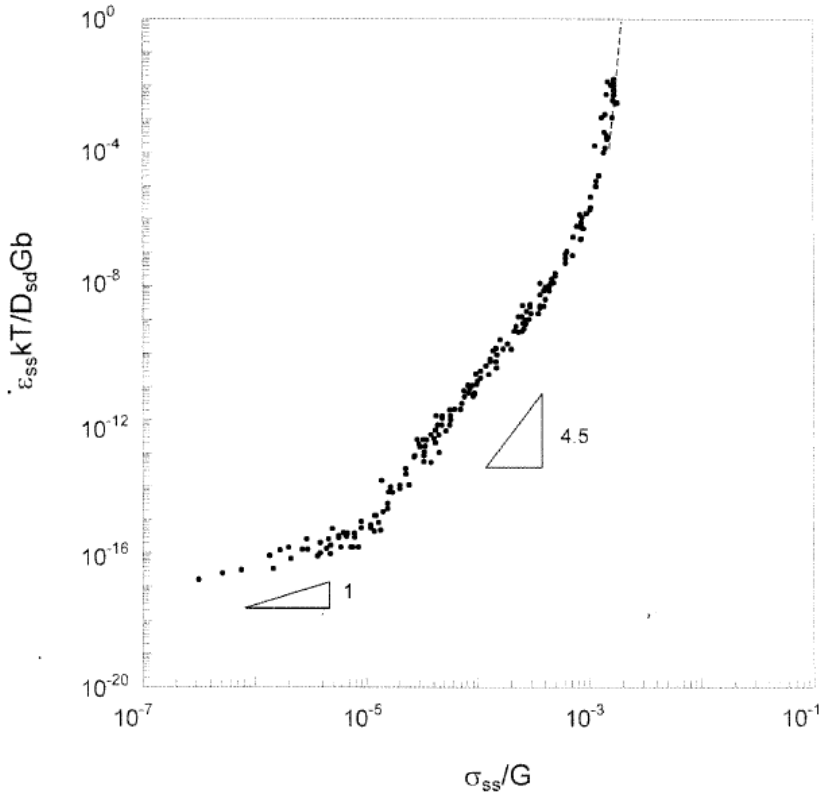

Figure 2.7: Creep curve for 99.999% pure Al [26].

Whenever dislocation climb is discussed, so too must stacking fault energy. A stacking fault is an error in the stacking sequence of atoms in close-packed planes [20]. Stacking fault energy determines the extent to which dislocations dissociate into partial dislocations through a stacking fault. When the stacking fault energy of a material is low, large separations occur between partial dislocations, which can hinder climb because the dislocation must become whole before climb can occur [19]. High stacking fault energies, such as those in FCC materials, make climb and slip easier. For this reason, climb controlled creep occurs more readily in materials with high stacking fault energies [19]. As a by-product of dislocation climb, a heterogeneous dislocation structure is formed within the grain [19,26,43]. This heterogeneous structure takes the form of cells, or subgrains. The walls of these subgrains consist of a relatively high density of dislocations. The misorientation angle between these subgrains is low (~1-3 degrees) [26,43]. This substructure is formed during primary creep and remains relatively unchanged during secondary creep. The size of the subgrains is a function of material parameters such as stacking fault energy, and of the applied stress; higher stress means

smaller subgrains [26]. The strength of materials during five-power law creep has been theorized to be related to subgrains, the internal stresses they create and the effect of polarized dislocations, and attempts to model this effect have been made [44-47]. Figure 2.8 shows a schematic of cellular formations within grains as well as possible diffusions paths for atoms and vacancies to accommodate climb.

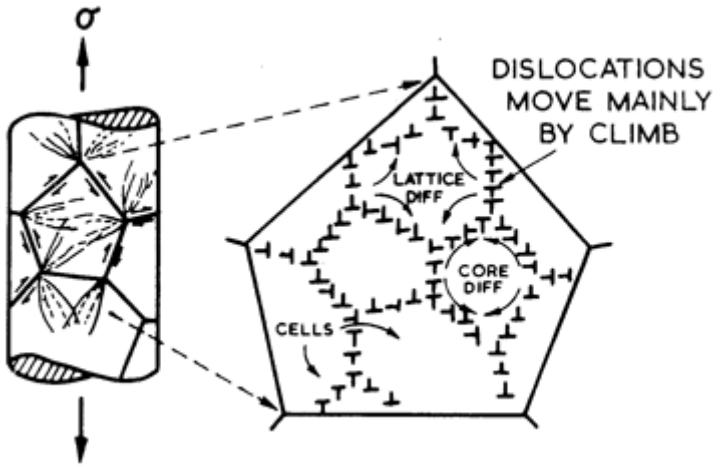

Figure 2.8: Schematic of cell formation and diffusional paths during climb controlled creep [18].

2.3.2 Power Law Breakdown and Dispersion-Hardened Alloys

At high stresses, the normal five-power law relationship breaks down, and *N* will increase in value (see Figure 2.7). Although this region of creep is not well understood [26], there are several theories as to why the increase in the creep rate is seen. Early theories suggest that the increased strain-rate are caused by a shift from climb-controlled creep to dislocation glide [18], however the presence of a well defined subgrain structure at these conditions gives evidence that dislocation climb is still the rate controlling mechanism [26]. Later theories suggest that dislocation climb is enhanced by an excess of vacancies produced in the material at these stresses [19]. More recently, the enhanced creep rates have been related to "core diffusion" of vacancies. Core diffusion involves diffusion of vacancies along dislocation structures such as subgrain walls. The activation energy for this type of diffusion is lower than that of self diffusion, and matches well with the activation energies seen during power law breakdown [26].

While most creep work has been done on single phase alloys, some work has gone into understanding creep of materials with a second hardening phase, such as metal matrix composites. Very little work has been done towards the understanding of creep in precipitation hardened materials, likely due to the time dependent nature of the structure at the temperatures where creep is found. A hardening phase is considered to be a small, closely spaced, hard particle that is coherent or semi-coherent with the matrix [48]. It has been found that these materials behave differently than their pure counterparts. First, *N* has been found to be higher than would normally be expected for power-law creep (>5) [48-52]. Additionally, the activation energy for deformation is found to be much higher than that for self diffusion [48,52,53]. It has been theorized that dislocations still bypass these obstacles by dislocation climb [53], however it has been shown that the particles prevent the creation of the subgrain structures [51]. This means that core-diffusion of vacancies cannot be responsible for the increased strain-rates seen, as core diffusion relies upon the subgrain boundaries for increased diffusion rates, nor would it account for the elevated activation energy [50,52,53]. As a result, it has been theorized that the existence of a 'threshold' or 'backpressure' causes the increased activation energies seen [50,52,53]. This leads to a modification of the normal creep relationship, as shown in Equation 2.8.

$$\dot{\varepsilon} \propto \left(\frac{\sigma - \sigma_p}{E} \right)^N \quad \textbf{[50,52,53]} \qquad \textbf{Equation 2.8}$$

Where σ_p is the opposing stress induced by the particle. The creep curves for Al, showing pure (N=4.5), solid solution strengthened (N=3), and particle hardened (N>4.5) variations are shown in Figure 2.9. Note the particle hardened material creeps at a much higher stress than the pure material. In Figure 2.9, the strain-rate is normalized using the Zener-Holloman parameter, Z_D, which is another method of presenting the data.

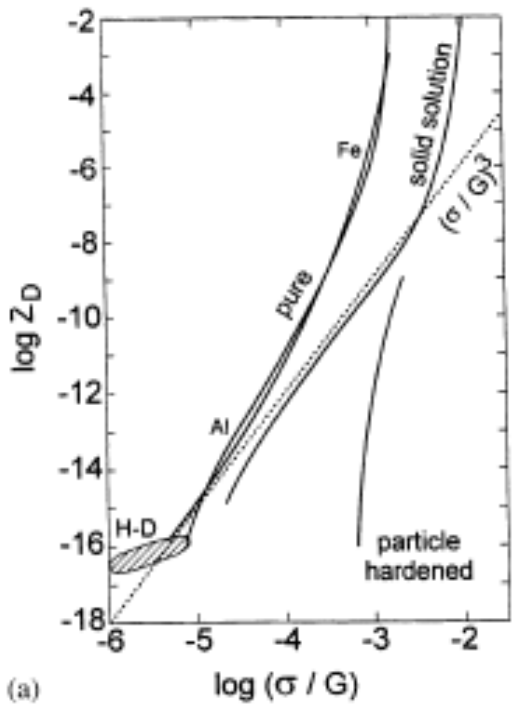

Figure 2.9: Various forms of creep in aluminium [52]

2.3.3 Low Stress Creep

At very low stresses, some unique forms of creep are seen. In the first, called diffusional creep, deformation occurs entirely by diffusion rather than by dislocation motion. This phenomenon was first described by Nabarro [54] and Herring [55]. Nabarro-Herring creep involves the diffusion of vacancies through the grain from grain boundaries normal to the tensile direction to those parallel to the tensile direction (see Figure 2.10 a). Later, Coble described a similar form of deformation, however at relatively higher creep rates [56]. The increased creep rate was found to be caused by grain boundary diffusion rather than diffusion through the grain (see Figure 2.10 b). As both of these creep mechanisms involve diffusion from one grain boundary to another, they occur more readily in materials with small grain sizes. Nabarro-Herring creep was found to have a grain size exponent of p=2, and for Coble creep, p=3 [31].

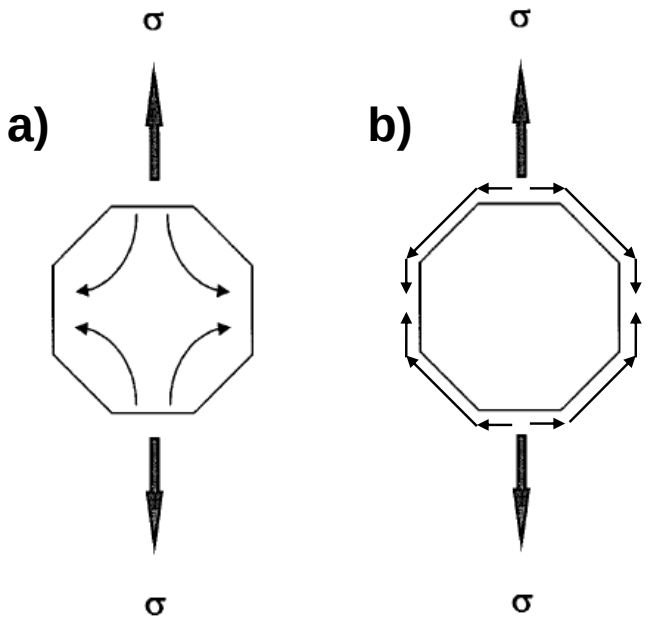

Figure 2.10: Diffusional creep by a) Nabarro-Herring creep and b) Coble creep (modified from [26]).

Another form of low stress creep was first described by Harper and Dorn [57]. This form of creep was found to be different than Nabarro-Herring or Coble creep because the creep rates seen were almost 1400 times larger than theoretically predicted by those models [26]. Also, the creep appeared to only occur above a critical grain size, below which, Nabarro-Herring creep was seen [26]. The stress exponent, *N*, was found to be 1 and the activation energy to be equal to that of self diffusion. The exact mechanism of deformation is heavily debated even now, 50 years later. Some believe that the activation energy suggests an edge dislocation climb mechanism [58], while others suggest internal stress models [59], or network dislocation models [60]. Some others believe that this deformation mechanism is simply a myth caused by inaccurate measurements and interpretation [61].

2.3.4 Superplasticity and Grain Boundary Sliding

Superplasticity is the ability of a polycrystalline material to exhibit very large tensile elongations before failure without the occurrence of necking [26]. It is generally accepted that there are two forms of superplasticity: structural superplasticity and internal stress superplasticity. While not generally considered a form of superplasticity, materials

that deform by viscous glide of dislocations (m=0.33) have been shown to exhibit large elongations before failure as well [4].

Structural superplasticity refers to superplasticity seen in materials with a fine grain structure (<10μm), usually at elevated temperatures (>0.5T_m) [62]. In non-superplastic materials, localized necking occurs during tensile tests, resulting in an increased local stress caused by the reduced cross-sectional area. This leads to failure quickly at the neck. In superplastic materials however, necking is not a localized phenomenon. When a neck starts to form, the localized strain-rate increases, but superplastic materials' flow stress is strongly strain-rate dependent (high m value). This increase in flow stress counteracts the increase in stress due to the decreased cross section and leads to a more diffuse or extended necking region [63]. Generally, the strain-rate sensitivity of a superplastic material is m>0.5 (N<2) [26]. This high strain-rate sensitivity is associated with grain boundary sliding (GBS) [26,64-67]. With grain boundary sliding, the bulk of the mechanical deformation occurs from grains moving relative to each other, rather than elongation of the grains. As the grains slide relative to each other, high stresses can be created at points where sliding of the grains becomes difficult, such as grain triple points. Therefore, GBS must be accommodated by another mechanism to allow the grains to change shape and reduce these stresses, lest cavities form [68]. These accommodation mechanisms can include grain-boundary migration, recrystallization, diffusion flow and dislocation slip [26]. The accommodation mechanism is thought to be the rate controlling mechanism [26]. From a geometric point of view, the smaller the grains, the smaller the amount of accommodation required to allow the grains to slide across one another [69].

Internal stress superplasticity is caused by high internal stresses in the material. Sources of this stress can include prior plastic deformation and coefficient of thermal expansion (CTE) mismatch in multiphase materials, or polycrystalline materials with crystal structures that have anisotropic expansion properties, such as HCP [19,26]. This form of superplasticity is of particular interest to metal matrix composites as it allows high ductility in a normally very brittle material [66]. Normally, the stresses generated

by the CTE differences generate microcracks along the boarders between the different phases, however, if the internal stress is immediately accommodated by an applied external stress, the material behaves superplastically. Extended deformation can be achieved through continuous thermal cycling of the material [70]. Using this method of producing superplastic behaviour, stress exponent values of N=1 have been achieved, allowing Newtonian-viscous behaviour [66,70].

Recently, a model for structural superplasticity was proposed that uses internal variables, rather than external variables such as the strain-rate sensitivity [67]. Dislocation kinematics are considered to reveal "internal stress" and "internal spin" tensors. These tensors are then related to observable deformation variables [67]. In this model, superplastic deformation is split into two components: grain boundary sliding, and accommodation by dislocation glide, i.e. grain matrix deformation (GMD). Superplastic deformation occurs via the superposition of these two mechanisms. The model relies upon the inelastic strain-rates taken over a broad range. A simple way to do this is using load relaxation tests, where the generated load relaxation curves can provide inelastic strain-rates over a broad range without appreciable changes to the internal structure of the material [71]. In their simplest forms, the equations for deformation are as follows:

GMD $$\left(\frac{\sigma^*}{\sigma^I}\right) = \exp\left(\frac{\dot{\alpha}^*}{\dot{\alpha}}\right)^{p^*}$$ **[67]** **Equation 2.9**

GBS $$\left(\frac{\dot{g}}{\dot{g}_0}\right) = \left[\frac{\left(\sigma - \sum_g\right)}{\sum_g}\right]^{\frac{1}{M_g}}$$ **[67]** **Equation 2.10**

Total $$\dot{\varepsilon} = \dot{\alpha} + \dot{g}$$ **[67]** **Equation 2.11**

Where σ^I is the internal stress, σ^* is an internal resistance parameter, $\dot{\alpha}$ is the inelastic strain-rate associated with GMD, $\dot{\alpha}^*$ is the reference rate of dislocation movement through a barrier and p^* is the dislocation permeability through barriers. The variable $\dot{g}$ is the strain-rate associated with GBS, $\dot{g}_0$ is the reference strain-rate, $\sum_g$ is the static

friction stress for interface sliding and M_g is a material parameter analogous to the stress exponent, N [67]. These equations are fit to stress vs. inelastic strain-rate curves generated from load relaxation tests using non-linear regression. Using this approach, it is possible to determine the strain-rates over which mechanism is dominant (GMD or GBS+GMD). An example of this can be seen in Figure 2.11.

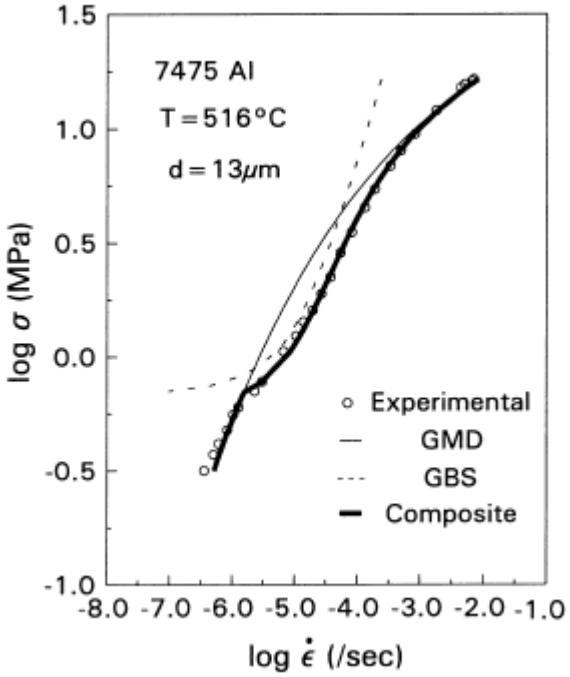

Figure 2.11: Application of internal variable approach to deformation modeling [67].

2.4 Deformation-Mechanism Maps

Each of the above described creep modeling equations describes the behaviour of a material for a range of temperatures, stresses, and strain-rates. Changing any of these parameters can alter the dominant mechanism. In order to conveniently show the range of parameters over which each mechanism is prevailing, Deformation-Mechanism Maps were created [18]. The maps are created by inserting the material parameters into the rate controlling equations, and setting the borders where two equations are equivalent. An example showing the deformation mechanisms for pure aluminium is shown in Figure 2.12.

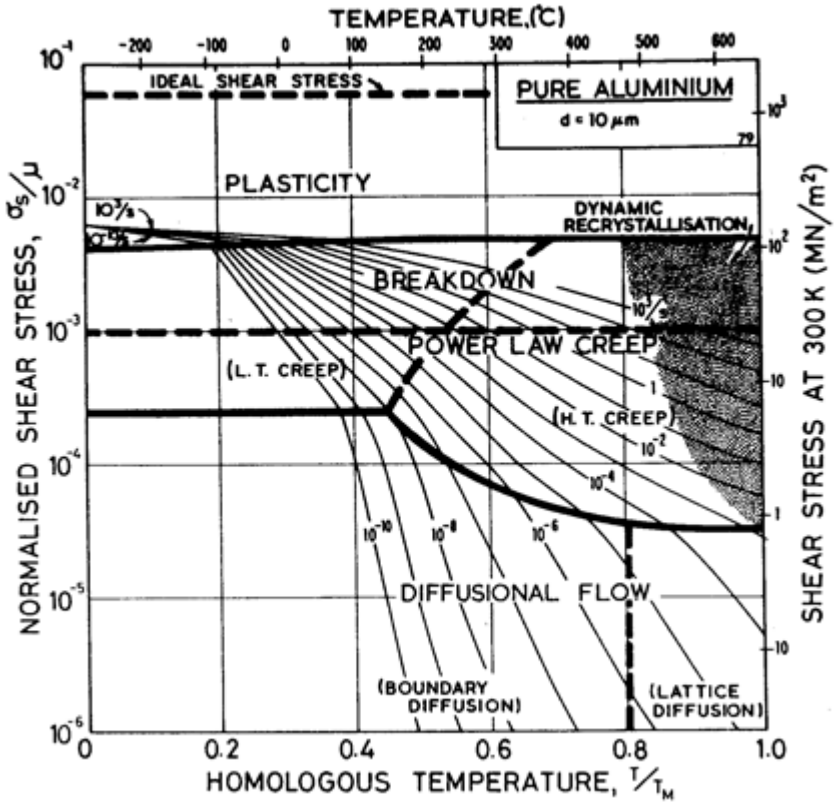

Figure 2.12: Deformation-mechanism map for pure Al with 10μm grain size [18].

Regions such as those for dynamic recrystallization or Harper-Dorn creep are added by hand for regions that have been experimentally shown to display these effects [18]. Deformation-mechanism maps were extended by Mohamed and Langdon to include the effects of changing the grain size [31]. In these maps the grain size and stress are varied, and the temperature is held as the constant variable in order to facilitate the use of a two-dimensional map. A Deformation-Mechanism map with varied grain size for pure aluminium at 250°C is shown below in Figure 2.13. Deformation-Mechanism maps have not been plotted for precipitation hardened aluminium alloys.

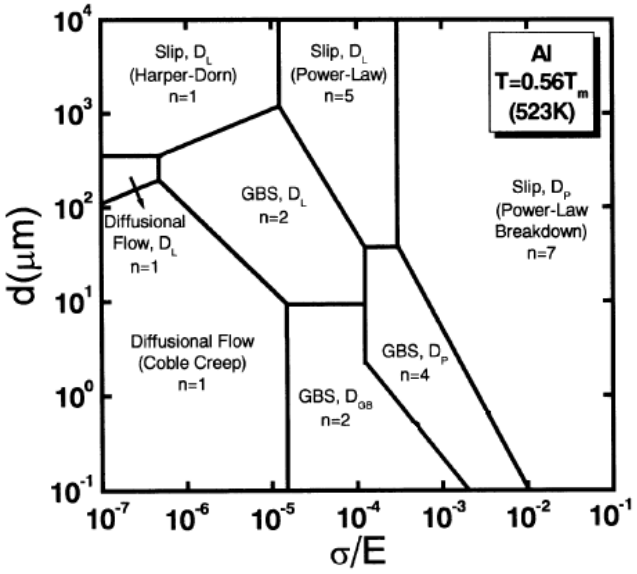

Figure 2.13: Effect of grain size on deformation mechanisms of pure aluminium at 250°C (modified from [72]).

2.5 High Temperature Microstructural Phenomena

2.5.1 Grain structure evolution

2.5.1.1 Static Grain Growth

Static grain growth, i.e. grain growth occurring while not undergoing deformation, occurs through the migration of grain boundaries so as to reduce the internal energy of the material [22]. Migration of a boundary involves the transfer of atoms from one grain to another. The transfer of atoms through the grain boundary requires activation energy to move through the disordered region of the grain boundary, usually supplied by thermal energy. The direction of flow of the atoms, i.e. flux, is dictated by the internal energy of each grain. Deformed grains have higher energy than dislocation-free grains [22]. Additionally, small grains have higher energy than large grains [22]. Therefore, atoms will flow from deformed and/or small grains into undeformed and/or large grains, causing the undeformed or larger grain to grow. When the differential energy between the grains is too small to overcome the activation energy for migration, grain growth will stop [22].

2.5.1.2 Zener Pinning

Since a fine grain size is often desired, either for strength (Hall-Petch) or for improved ductility through grain boundary diffusion/creep and grain boundary sliding mechanisms, reducing grain growth at elevated temperatures is of great interest. One method of limiting grain growth is through tailoring the structure to contain a fine dispersion of small, hard particles throughout the material. When a boundary encounters one of these particles, a pinning pressure is exerted on the boundary in opposition to the driving force for boundary migration [43]. This phenomenon is referred to as Zener Pinning [43]. The pinned boundary then requires an extra input of energy to overcome this pressure, thus reducing or halting grain growth. Zener pinning has a very large effect on the recrystalization behaviour in age hardenable aluminium alloys, and is one of the most important factors in determining the recrystallized grain size [73]. An example of where Zener pinning has been used is in AA6xxx aluminium alloys to improve the grain size stability at elevated temperatures of a fine-grained superplastic material through the addition of zirconium. Zirconium produced small precipitates which did not dissolve at high temperatures and helped to prevent grain growth [14].

2.5.1.3 Dynamic Recrystallization and Grain Growth

Recrystallization is the process by which a deformed grain structure is transformed into a low dislocation density structure. Recrystallization removes most of the strengthening effects of strain hardening, thereby reducing the stress required to deform the material. Dynamic recrystallization (DRX) is a general term describing recrystallization that occurs during deformation of a material. There are three variations of dynamic recrystallization: continuous, discontinuous and geometric dynamic recrystallization [43].

Continuous recrystallization occurs via the evolution of small angle boundaries (subgrain boundaries) into high angle boundaries and then the migration of those boundaries (grain growth) [43]. Subgrains themselves do not necessarily lead to recrystallization because low angle boundaries have a much lower mobility than higher angle boundaries [43]. In continuous dynamic recrystallization, increasing strains lead to more and more dislocations nucleating and dissociating via climb to subgrain boundaries.

This causes the misorientation angle of the boundary to increase. Eventually, the misorientation is high enough that the subgrain can be considered a new grain (~15°). This process occurs in a fairly uniform manner throughout the material [43].

Discontinuous dynamic recrystallization occurs when there are large particles (>1μm) present in the material. When a crystal with large particles present is deformed, high stresses build up around the particle due to mismatches between their elastic moduli and yield strengths. These higher stresses lead to increased dislocation nucleation rates and therefore higher dislocation densities around the particle. This can lead to the subgrains in the vicinity of the particle to increase in misorientation quicker than in the rest of the material. Subgrains will then grow and consume the surrounding subgrains. This is known as particle stimulated nucleation (PSN) [43].

Geometric dynamic recrystallization is a special version of continuous dynamic recrystallization seen at high stresses and strains in some materials, particularly aluminium [43]. At high strains, the grains of the material become flattened and elongated in the direction of the force. Also, the grain boundaries become serrated due to surface tension effects generated by the subgrains within the grains. Eventually, the two sides of a grain will touch and annihilate each other, effectively pinching the grain in two [43]. This process is schematically shown in Figure 2.14.

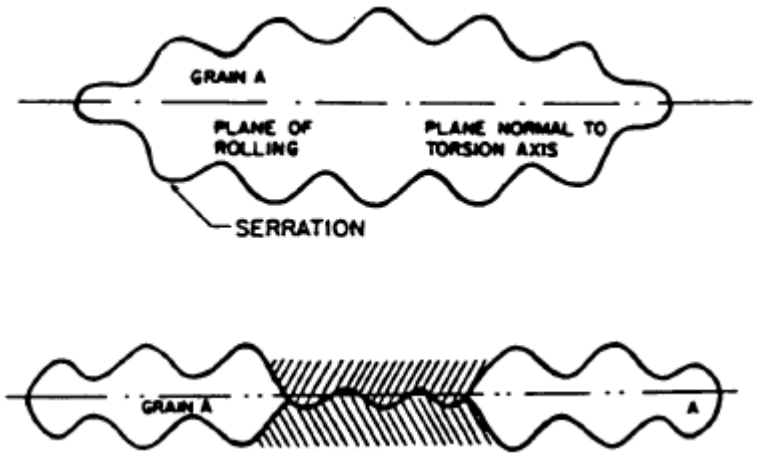

Figure 2.14: Schematic of geometric dynamic recrystallization [43].

In superplastic materials, it has been shown that during deformation, grain growth occurs more rapidly than would normally be expected during static annealing [74]. The grain growth rate has been shown to be proportional to the strain in these types of materials. It is theorized that the grain growth rates are increased to help with accommodation of grain boundary sliding at grain triple points [74].

2.5.2 High Temperature Precipitation and Precipitate Coarsening

Precipitation in metals can occur either homogeneously or heterogeneously. In a solution treated alloy, large undercooling levels due to quenching to lower temperatures can lead to near homogeneous nucleation of fine precipitates distributed evenly throughout the material due to the high driving force for nucleation. The driving force for nucleation is high at large undercooling levels due to a large free energy difference between the unstable single phase and the stable phases at the low temperatures. Homogeneous precipitation is seen in materials that are quenched and naturally aged or materials that have been aged at low temperatures. If the driving force for nucleation is low, such as is the case with low levels of undercooling, nucleation will only occur on the highest energy sites within the material. These high energy sites include dislocations, grain boundaries and pre-existing particles that were not solutionized. This is known as heterogeneous nucleation [22]. Grain boundaries are particularly effective at nucleating incoherent precipitates, due to the inherent disordered nature of grain boundaries [22]. Nucleation and growth of precipitates on grain boundaries is known as grain boundary precipitation (GBP).

Coarsening refers to the growth of some precipitates at the expense of others, leading to structure containing larger, more widely spaced precipitates. The driving force for coarsening is to decrease energy; by having a small number of large precipitates rather than many small precipitates, the total surface energy of the precipitates is decreased. This is known as the Gibbs-Thomsom Effect. Diffusion helps coarsening to proceed. The kinetics of coarsening are dependent on the diffusion-rate (i.e. temperature) [22]. Growth will occur preferentially at defects or interfaces which will lead to the

largest decrease in free energy of the system. Usually, this means preferential growth of precipitates on high angle grain boundaries.

In general, grain boundary precipitates do not form as sheets along grain boundaries, but as isolated particles. In an idealized situation where the precipitate was allowed to grow without outside influence, it would have the shape of two abated circles on each side of the boundary (Figure 2.15).

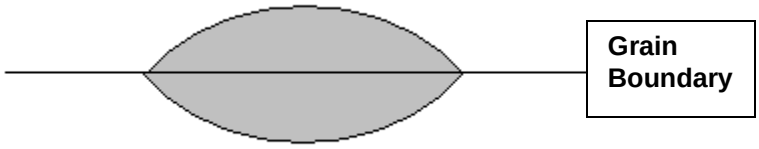

Figure 2.15: Idealized grain boundary precipitate (modified from [22])

The growth of a grain boundary precipitate occurs more rapidly than an isolated precipitate in the matrix. This is because the boundary acts as a sink for solute atoms, which are then funnelled easily along the boundary (due to its disordered nature) to the precipitate. The solute atoms can also travel easily along the precipitate's boundary with the matrix, allowing the precipitate to thicken instead of just growing along the boundary [22].

The precipitate in Figure 2.15 is an idealized shape, in which the precipitate is incoherent with both grains with which it interfaces. It is also possible that the precipitate could have a coherent or semi-coherent interface with one or both of the grains. Coherency or semi-coherency with both interfacing grains is very unlikely as it would require both grains to be aligned with a favourable orientation with the precipitate. If the precipitate has coherency with one of the grains, it will grow into that grain along a single direction. A coherent precipitate has a lower interfacial energy, but misfit can lead to coherency strain as the precipitate grows. An incoherent precipitate has a high interfacial energy, but has no misfit strain. This means that in the case of a precipitate with one coherent/semi-coherent interface and one incoherent interface, the coherent/semi-

coherent portion may grow preferentially at some times, and vice versa [22]. Even precipitates which are incoherent with both bounding grains can still grow preferentially into one of the grains if a lower energy state is achieved when one of the facets of the precipitate grows along a specific crystallographic direction in the matrix [75].

2.6 High Temperature Cavitation and Failure Mechanisms in Metals and Alloys

2.6.1 Background

It is generally accepted that at elevated temperatures, most ductile materials fail by cavitation [5,68,76-87]. Failure by cavitation is a three step process involving: nucleation, growth and coalescence of voids [76-78]. Nucleation entails the formation of a void, usually on a pre-existing defect. Growth of voids can occur through the diffusion of vacancies into pre-existing micro-cavities (diffusion growth) or by deformation of the surrounding crystalline lattice (plasticity-controlled growth). Below a critical void size, growth is primarily diffusion controlled, while larger voids are primarily plastically-controlled [79]. Finally, coalescence is the linking of adjacent voids to form an even larger void. Coalescence eventually causes failure in the material.

2.6.2 Cavitation in Single Phase Metals

In single phase alloys, cavitation occurs primarily on grain boundaries transverse to the tensile load direction [80]. The tensile load on these boundaries increases the free energy of the boundary, making it a more favourable sink for vacancies. The vacancy density will increase as vacancies are drawn to the area, and eventually micro-cavities will form. This process is known as vacancy condensation [80]. Vacancies travel easiest along grain boundaries due to 'short-circuit' diffusion [26,80]. Any effect that further increases the energy at a boundary can increase the rate of cavity formation. One such process is caused by dislocation pile-up at the boundary, e.g. the end of a slip band [81,82]. Dislocation pile-up creates a stress concentration at the boundary which can increase the vacancy condensation rate [80-82]. Another form of increased stress at boundaries is seen during grain boundary sliding. Very high stresses can be created at grain triple points, particularly if the GBS accommodation mechanism is slow. This can lead to increased cavitation rates at these triple points [68,80]. The small grain size of

materials exacerbates cavitation problems associated with GBS when not accommodated adequately because the increased area fraction of grain boundaries allows easy diffusion of vacancies [79]. These cavity formation processes are illustrated in Figure 2.16.

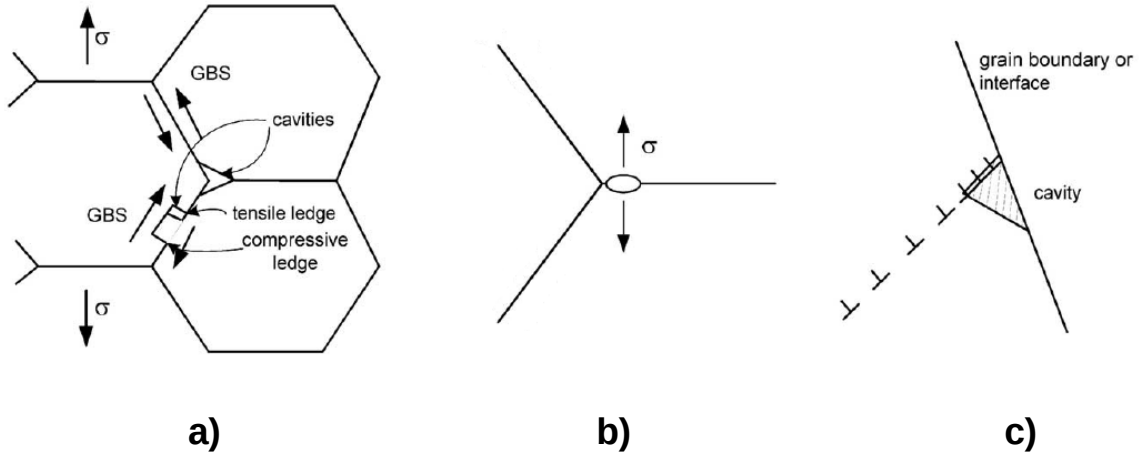

Figure 2.16: Cavitation at boundaries caused by a) grain boundary sliding, b) vacancy condensation and c) dislocation pile-up [80].

2.6.3 Cavitation in Particle-Containing Alloys

Second phase particles in a material are also a significant source of stress concentrations, which can lead to the formation of cavities. If the particles are found at grain boundaries, the stress concentrations they cause can increase the rate of vacancy condensation [80]. Additionally, particles on grain boundaries can act as initiation points for slip, which can concentrate cavities that form from dislocation pile-up at these particles, further increasing cavitation rates [83-85]. Particles in the grain matrix can also nucleate voids either by dislocation pile-up, or by vacancy condensation, however, vacancy condensation occurs at a much slower rate without the aid of short-circuit diffusion of vacancies along grain boundaries [80]. Large particles can also fracture or lose cohesion with the matrix due to strain mismatch between the particle and matrix, creating a void, although this process is stress controlled process, rather than a diffusion controlled process [86].

Precipitation hardened alloys add an additional layer of complexity to cavitation formation, particularly when inhomogeneous nucleation of precipitates, such as grain boundary precipitation, is involved. When grain boundary precipitation occurs, the precipitates grow at the expense of matrix precipitates. This leads to an area extending from the grain boundary that is relatively free of precipitates, called the precipitate free zone (PFZ). The size of this zone is dependent on many factors, such as temperature, time, and solute diffusivity [83-85,87,88]. The PFZ is important because the main strengthening effect of precipitation-hardenable alloys has been removed from this region, leaving it weaker than the grain matrix [83,84]. Under stress, this can lead to the localization of strain within the PFZ due to the lower yield point. This can strongly increase the cavitation rate at the grain boundary precipitates [83]. A schematic of the formation of cavities at grain boundary precipitates in a precipitation hardened alloy is shown in Figure 2.17.

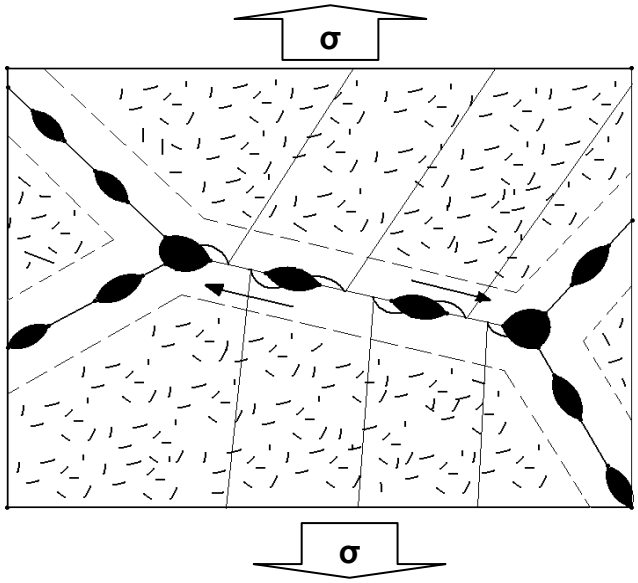

Figure 2.17: Schematic of cavity formation on grain boundary precipitates (reproduced from [83]).

2.7 AA6xxx Aluminium Alloys

2.7.1 Background

AA6xxx aluminium alloys are a group of heat treatable aluminium alloys containing magnesium and silicon, as well as copper in a number of commercial alloys. AA6xxx aluminium alloys are used in the automotive industry for outer body panels and

bumpers because of their weldability, good age-hardenability, formability, corrosion resistance, good surface finish and low cost [89]. Some alloys that are used in the automotive industry include AA6009, A6010, AA6016 and AA6111 [90]. AA6xxx alloys, such as AA6013, AA6061 and AA6113, also see limited use in the aerospace industry [90].

2.7.2 Thermomechanical Processing Methods

2.7.2.1 Commercial Sheet Manufacturing Methods

An aluminium sheet begins as a cast ingot, or a casting from a direct continuous casting operation. The ingot is usually then allowed to cool to room temperature. Following this, the ingot is reheated to approximately 500°C, and then passed through a hot rolling mill several times, reducing the thickness to approximately 4-6mm. Following this, the sheets are cold rolled to the desired thickness, then solutionized to remove any work hardening effects as well as dissolve constituents in heat treatable alloys [91]. Prior to delivery to a manufacturer, sheet material often undergoes extensive periods of natural aging. This is commonly referred to as the T4 condition [2]. T4P is used to describe the commercially pre-aged temper used by Novelis in the fabrication of sheet material [92]. The pre-aging process follows a proprietary continuous process involving solution heat treatment, followed by water quenching and pre-aging stages [2]. A schematic of this heat treatment process is shown in Figure 2.18.

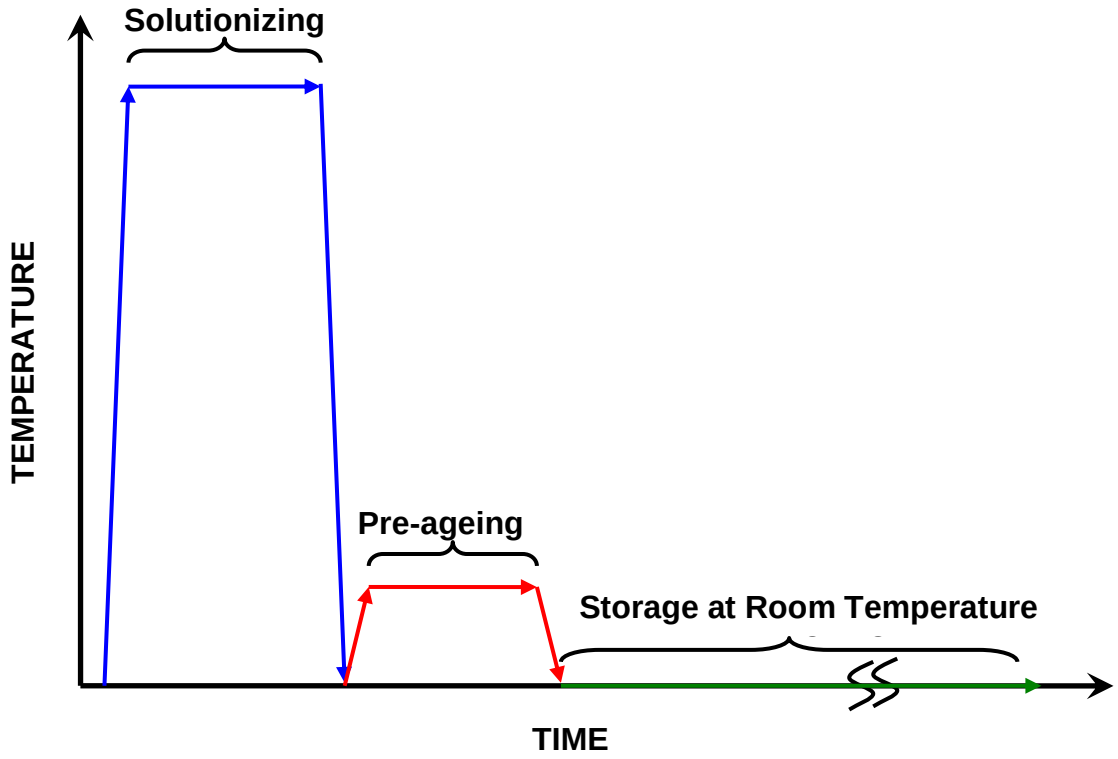

Figure 2.18: Schematic of the thermal processing history for the T4P material.

2.7.2.2 Laboratory Scale Methods for Grain Refinement

As stated earlier, a refined grain structure is advantageous because it increases the strength of the material, and it can improve the ductility of the material by allowing high diffusion rates and deformation by GBS. The improvement in ductility is of particular interest for AA6xxx aluminium alloys. It has been shown that obtaining a grain size of approximately 10μm or less can produce a superplastic behaviour [10,79,93]. The two most prominent processes used to produce fine grain structures in AA6xxx aluminium alloys, rolling followed by heat treatment and severe plastic deformation, are described below.

The first procedure involving rolling and subsequent heat treatment, pioneered in the 1970's [94,95], and more recently applied and expanded upon by Kovacs-Csetenyi *et al.* [96], Chung *et al.* [97] ,Troeger and Starke [10] and Kaibyshev *et al.* [14], makes use

of recrystallization facilitated by particle stimulated nucleation (PSN) of dislocations. The general procedure behind each of these methods is as follows. First, a homogeneous dispersion of overaged precipitates is produced. Next, the material is deformed heavily deformed to nucleate recrystallized grains at the precipitates. Finally, the material is statically recrystallized to grow the nucleated grains and produce a fully recrystallized structure [10]. See Figure 2.19 for a schematic of the procedure used by Troeger and Starke [10].

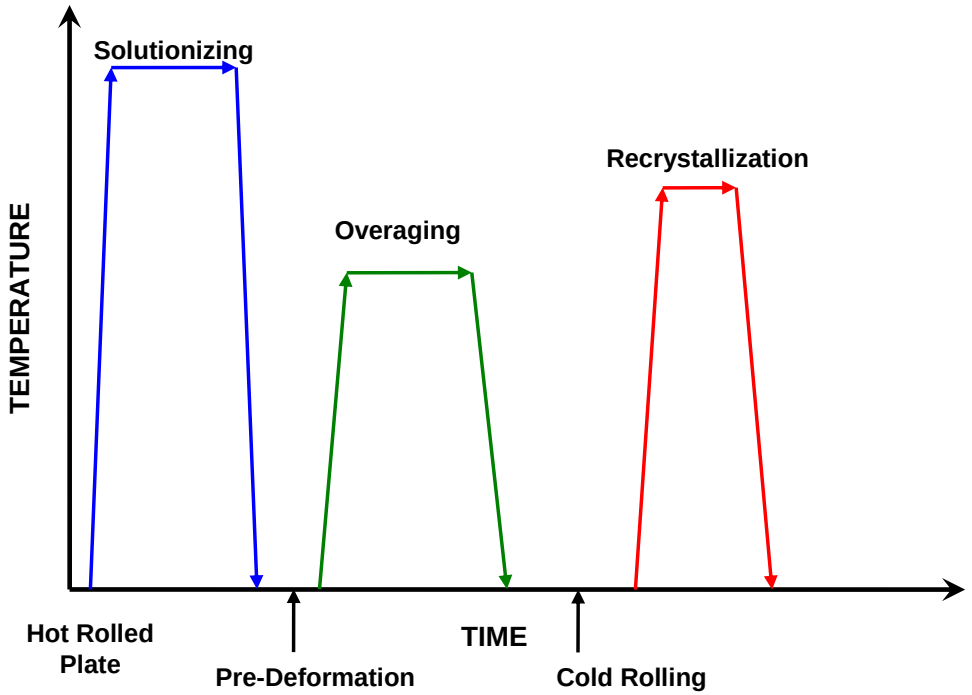

Figure 2.19: Schematic of particle stimulated nucleation applied to grain refinement applied by Troeger and Starke [10].

The main difference in these methods lies in how the uniform distribution of precipitates is achieved. Kovacs-Csetenyi *et al.* [96] produced their overaged precipitates by simply statically ageing after a solutionizing heat treatment. Chung *et al.* [10] attempted to produce a more uniform distribution of precipitates by first cold rolling the material 10%, then statically ageing, in order to promote precipitation on dislocations. However, it was found that 10% CW was not sufficient to promote precipitation on dislocations rather than other high energy sources such as grain boundaries [10]. Troeger and Starke had better success by nucleating precipitates on deformation bands produced through 60% CW [10]. Kaibyshev *et al.* [14] had similar success by warm rolling to 70%

reduction followed by overaging. The amount of CW after the overaged precipitate structure was produced varied between 60 and 80%. The grain size produced by these procedures was approximately 10μm [13,14,96]. Shown below in Figure 2.20 are the precipitate structure before deformation and grain structures after deformation and recrystallization for the materials produced by Troeger and Starke [10], and Kaibyshev [14].

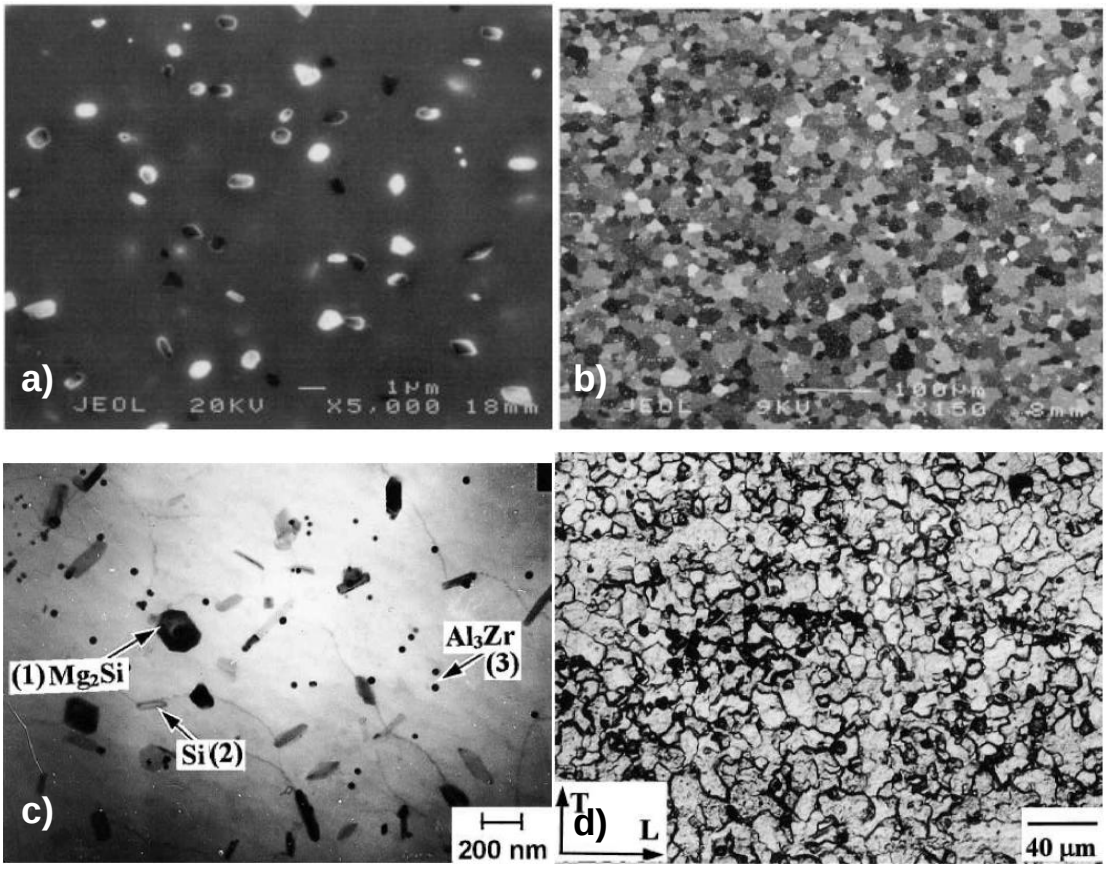

Figure 2.20: Precipitate structure after heat treatment and grain structure after deformation and recrystallization of heat-treated structure for fine-grained materials as produced by Troeger and Starke, a) and b) [10] and by Kaibyshev, c) and d) [14].

The second method of grain refinement which has been applied to AA6xxx aluminium alloys is severe plastic deformation (SPD). SPD is a general term for a number of processes that impart very large strains to a material. These processes include: equal channel angular pressing (ECAP)[98-100], high pressure torsion (HPT) [101], asymmetric rolling (AR) [102,103] and accumulative roll bonding (ARB) [104]. To the best of the author's knowledge, only ECAP, ARB and AR have been reported to be

applied to AA6xxx aluminium alloys. ARB involves the repeated rolling, dividing and stacking of a sheet material. This allows basically unlimited strains to be applied to the material. ECAP, by far the most popular form of SPD, involves the pressing of a billet, or plate through an angular channel. This imparts very high shear strains upon the material. One of the reasons for this procedure's popularity is that the part retains its dimensions after pressing, making subsequent pressings easy. All of these SPD methods of grain refinement rely either upon geometric dynamic recrystallization to produce a fine grain structure, or the introduction of a highly deformed structure followed by recrystallization. Lee *et al.* [104] were able to produce an average grain size of ~0.5μm using ARB after 6 rolling and stacking cycles; more cycles did not further reduce the grain size. Kim *et al.* [72] used ECAP to on solution treated AA6061 followed by ageing to produce a grain size of 1.4μm. Xu *et al.* [100] reported grain sizes of ~1.3μm produced using ECAP after as few as only 4 passes, similar to results found for pure aluminium [105,106]. Morris *et al.* [107] were able to produce a submicron grain structure using ECAP in an Al-Mg-Si alloy.

2.7.3 Precipitation Behaviour and Sequence

Precipitation involves the evolution of small particles, from their most unstable form to most stable, through a series of metastable phases. The alloy chemistry and processing history dictate which phases will be present. The precipitation sequence in AA6xxx aluminium alloys has been extensively studied [108-120]. One of the primary factors that affects precipitation in these alloys is whether or not the material contains copper; the precipitation sequence and strengthening precipitate is different if copper is present. Small variations in the composition of the alloys, such as silicon concentration, can also lead to variations in the precipitation sequence and the precipitates themselves [112]. The most common precipitation sequence will be described below for copper-free and copper-containing alloys.

In ternary 6000 series aluminium alloys (Al-Mg-Si), the basic precipitation sequence has been described as follows: from supersaturated solid solution (SSS), clusters of solute atoms form, followed by the formation of Guinier–Preston (GP) zones. Next, precursors

of the equilibrium β phase (Mg_2Si), β" and β', form. Finally, equilibrium is reached with the formation of the β phase. This process is illustrated in Figure 2.21

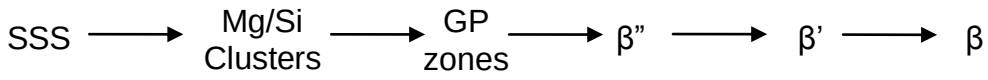

Figure 2.21: Precipitation sequence in Al-Mg-Si alloys [108].

The primary strengthening phase in this material is the β" phase. β" is needle shaped, and the lengths are aligned along the $<100>_{Al}$ directions. In the peak aged condition, the β" precipitates in AA6111 are a few nanometres in size [115]. The exact size can very greatly depending on the exact alloy composition and previous ageing history. The equilibrium β phase is plate shaped, and can grow to be several μm large [120,121].

In quaternary alloys (Al-Mg-Si-Cu), such as 6111, the addition of copper produces a new equilibrium phase is produced. This phase is the quaternary Q phase. In high-copper alloys such as 6111, the precipitation sequence has been reported as:

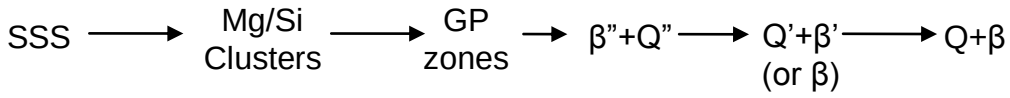

Figure 2.22: Precipitation sequence in Al-Mg-Si-Cu alloys [120].

Here, the primary strengthening precipitates are the β" and Q" phases. The Q" phase has a lath morphology. The length of the lath-shaped precipitate lies along the $<100>_{Al}$ direction, while the habit plane normal to the $\{100\}_{Al}$ plane [120]. The average equivalent radius of Q" in AA6111 has been reported as ~2nm and the length as ~30nm in the peak aged condition immediately following solutionizing [115]. Again, small changes to the composition and thermal processing history can greatly affect these values. The equilibrium Q phase can grow to similarly large sizes as the β phase [115,120,122,75].

2.7.4 Coarsening and Grain Boundary Precipitation

With extended exposure to elevated temperatures, the precipitation composition of AA6xxx aluminium alloys has been shown to evolve from the peak aged condition containing β" and Q", to a structure containing the equilibrium phases β and Q [120]. The formation of these precipitates has been shown to occur concurrently with an increase in size, and decrease in number of each of these precipitates [120,122]. The thermodynamic stability of each of the equilibrium phases can be calculated. The equilibrium phase compositions are shown for the common alloy AA6111 below in Figure 2.23.

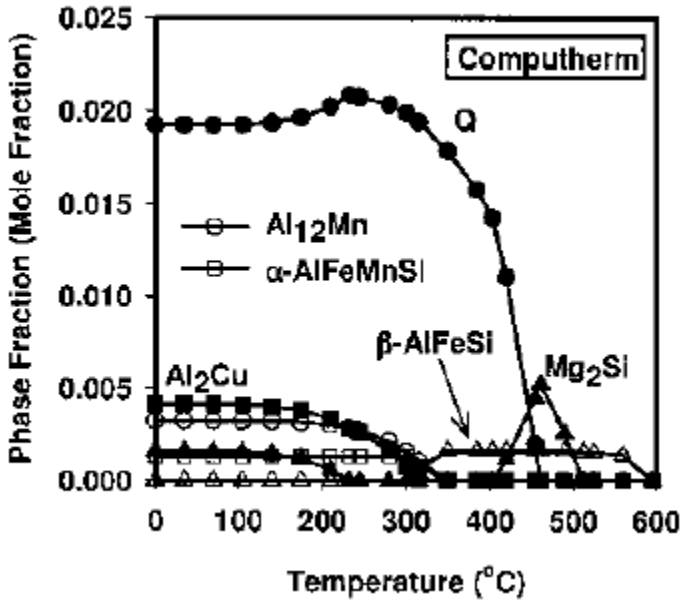

Figure 2.23: Calculated equilibrium phase compositions for AA6111 [123].

This shows that the primary phase at temperatures below ~450°C is the Q phase, while the β phase (Mg_2Si) is dominant at higher temperatures. Note that different processing routes can have a very large effect on the proportion of each phase in the material. The overaged microstructure of an AA6111 sample is shown in Figure 2.24 which highlights the morphology and orientation relationship of each of the equilibrium phases.

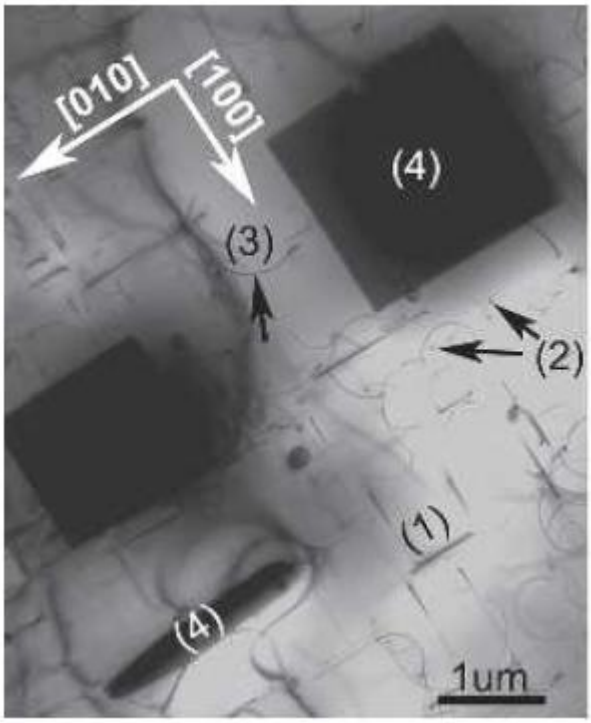

Figure 2.24: Precipitate structure of AA6111 overaged for 21 days at 300°C [120].

In this image, the large, plate shaped β precipitates can be seen (marked as (4) in the image), as well as the lath-shaped Q phase (marked as (1) in the image). The curved precipitates marked as (3) are chemically reacted Mg_2Si rods left as a by-product of the etching process. The round-ended precipitates marked as (2) are suspected to be β' precipitates [120].

Heterogeneous nucleation of precipitates on grain boundaries has been shown to occur in AA6xxx aluminium alloys during exposure to elevated temperatures [124]. Shown in Figure 2.25 is an example of grain boundary precipitation which occurred in AA6111 which had been cooled at a slow rate from the solutionized state; the sample which was quenched quickly does not show grain boundary precipitation [124].

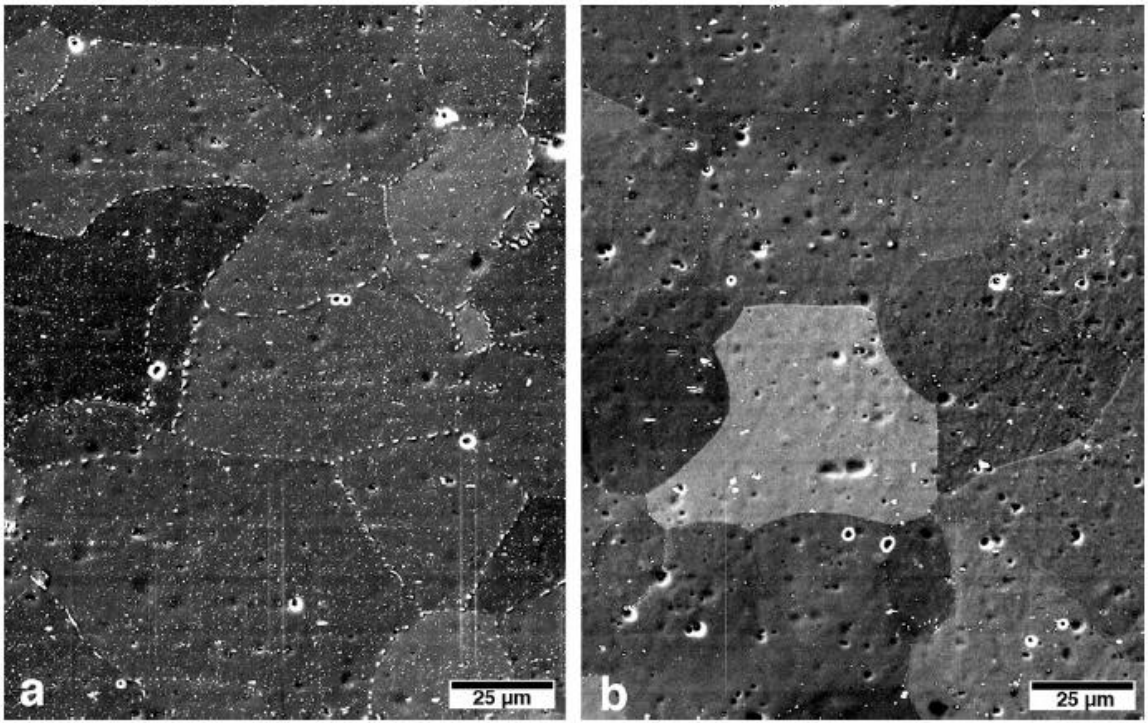

Figure 2.25: Effect of quench rate, (a) 7°C/s and (b) 140°C/s, on grain boundary precipitation in AA6111 [124].

It was shown by Weatherly *et al.* [75] that all the grain boundary precipitates in their study on overaged AA6111 were of the Q phase. It was also highlighted in that study that the Q precipitates maintained a preferred orientation relationship with one of the grains if the boundary did not contain a favourable orientation, which resulted in the precipitate growing into that grain from the grain boundary [75].

2.7.5 Mechanical Behaviour

2.7.5.1 Room Temperature Tensile Behaviour

The room temperature tensile behaviour of 6000 series aluminium alloys has been well documented (e.g. [3,125,126]). The level of precipitation in the alloy can significantly affect the strain to fracture in the material. It has been shown that the fracture strain varies linearly with the yield strength [125], while the yield strength is a function of the aging condition of the alloy. Figure 2.26 shows the variation of the fracture strain with yield strength in AA6111 aged at various temperatures [125].

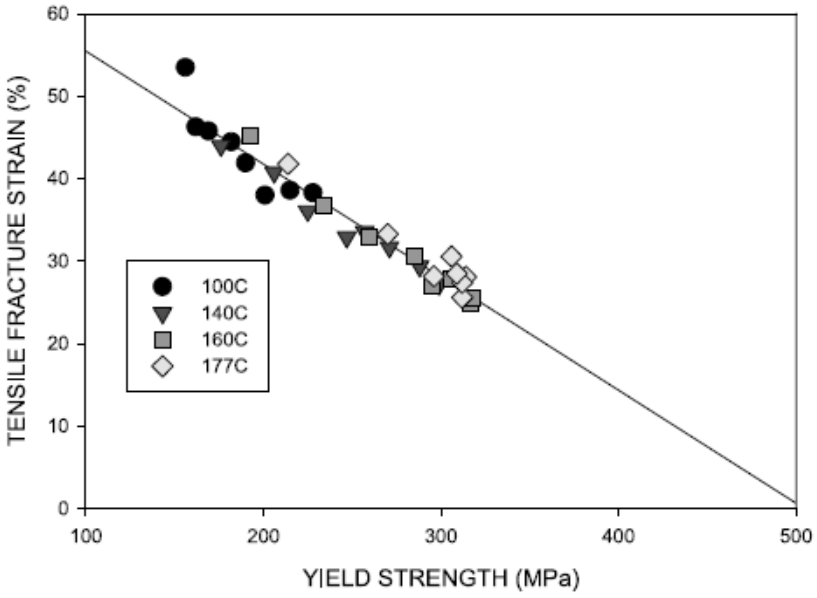

Figure 2.26: The scaling of fracture strain with yield strength in AA6111[125].

As stated before, failure in ductile materials such as aluminium is caused by nucleation, growth and coalescence of voids. In 6000 series alloys, it has been found that voids primarily nucleate on large, iron containing particles [125]. Nucleation of these voids happens rapidly at the onset of necking in the material, concentrated at a favoured shear angle (~45°) [3,125]. Figure 2.27 shows a schematic of this process.

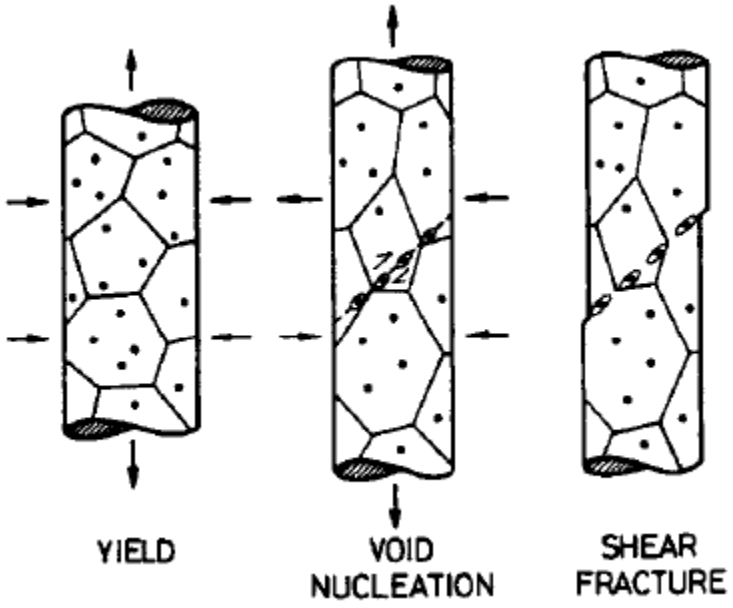

Figure 2.27: Void sheeting leading to ductile shear failure [127].

It has been shown that the strain-rate sensitivity of these alloys are very low ($m \approx 0$) [4], and as a result, there is very little resistance to strain localization, which leads to the rapid necking and failure [125].

2.7.5.2 High Temperature Tensile Behaviour

There has been very little work to study the tensile behaviour of AA6xxx aluminium alloys at high temperatures, likely due to the effect elevated temperatures have on the age-hardenability of the material. The body of work that does exist is divided into two groups: deformation of conventional alloys, and deformation of fine-grained materials.

Li and Ghosh [4,12] have reported on the tensile properties of AA6111 under warm deformation conditions (200-350°C). In these reports, AA6111 in the T4 condition was compared to several 5000 series aluminium alloys at various temperature and strain-rate conditions. It was found that testing at elevated temperatures increased the elongation to failure, however, the improvement was not nearly as much as the 5000 series alloys. Additionally, the strain to failure was found to decrease with increasing strain-rate. Figure 2.28 shows the elongation to failure as a function of temperature as found by Li and Ghosh. Additionally, they found that the strain-rate sensitivity, *m*, did increase with temperature, but not significantly. Figure 2.28 shows the value of the strain-rate sensitivity as a function of time for the three alloys.

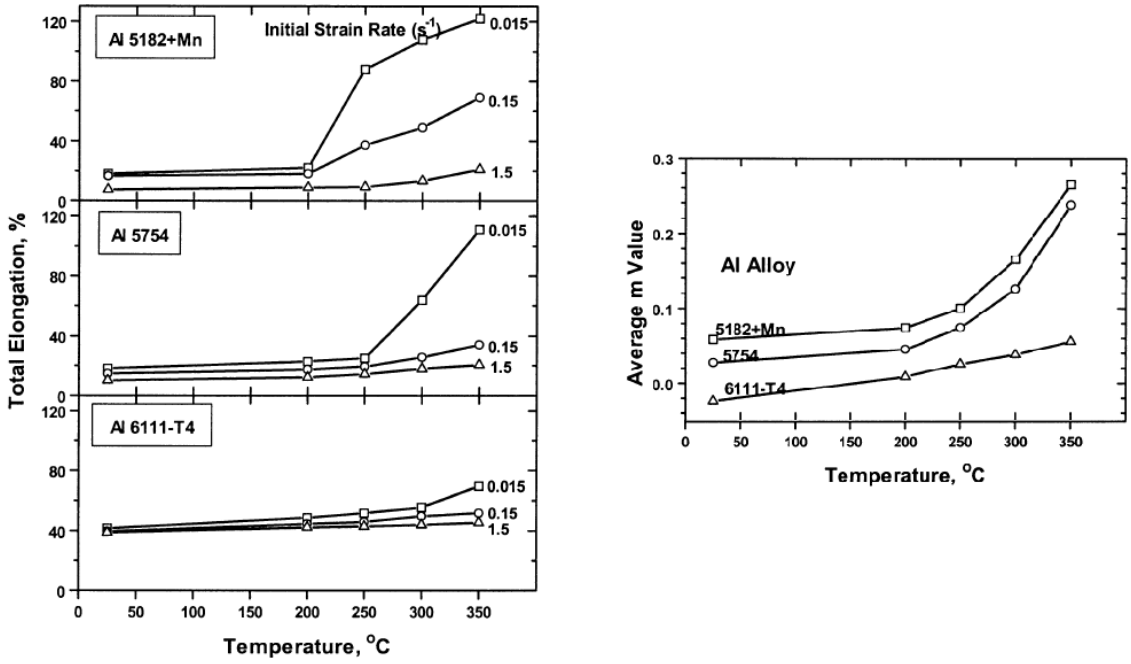

Figure 2.28: Scaling of elongation to failure and strain-rate sensitivity with temperature in several Al alloys [4].

In a study by Lassance *et al.* [11], AA6060 and AA6005A cast samples were tested at temperatures between 450°C and 600°C [11]. They found similar moderate increases in the elongation to failure (from 28% at room temperature to 50% at 590°C) with elevated temperatures. The strain-rate sensitivity was found to be very high, almost 0.5 at the highest temperature, despite the low elongations. Failure was determined to be due to void formation. Interestingly, they found that the volume fraction of voids decreased with increasing strain-rate. They theorized that this was due to increased local stress triaxiality around nucleating voids, leading to decreased growth rates [11]. They also found that void formation could be reduced by transforming the jagged β intermetallics into rounded α intermetallics through annealing [11].

In the fine-grained class of reported tests, Troeger and Starke [10,13,93] have reported superplastic behaviour caused by grain boundary sliding in AA6013 and AA6111 with a fine-grain structure (~10μm) produced by a combination of rolling and heat treatment processes, as shown in Figure 2.19. The reported maximum elongation was 375% at a strain-rate of $5x10^{-4}s^{-1}$ and a temperature of 540°C [93,10,13]. Failure was

caused by cavitation. Higher strain-rates led to increased cavitation rates. Figure 2.29 shows the elongation to failure and strain-rate sensitivity of the material studied by Troeger and Starke [13].

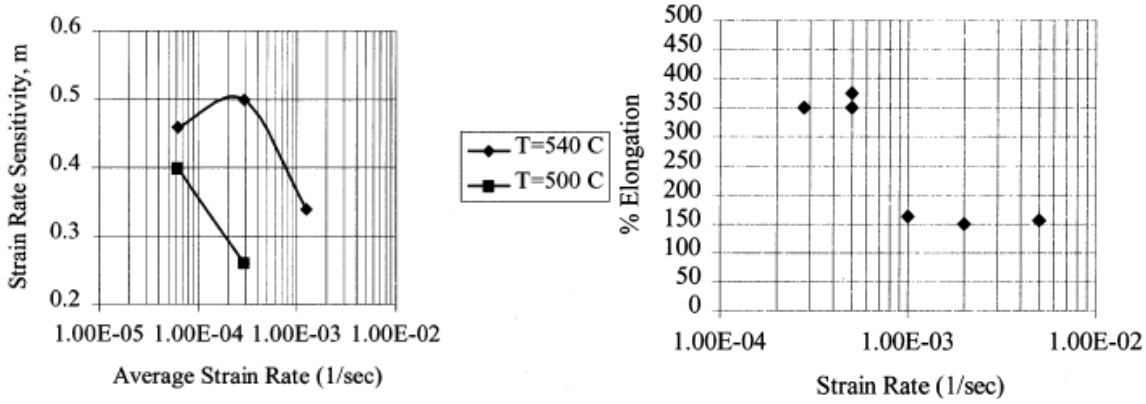

Figure 2.29: Strain-rate sensitivity and elongation to failure of a fine-grained 6xxx aluminium alloy as found by Troeger and Starke [13].

Park *et al.* [15] tested an AA6013 alloy that had been produced through warm rolling and annealing, and achieved superplastic elongations of 370% at a strain-rate of $1x10^{-4}s^{-1}$ and a temperature of 560°C [15]. In each of these reports, superplastic behaviour was only found in a very narrow range of strain-rates and temperatures. Kaibyshev *et al.* [14] produced a fine grain structure in AA6061 modified with Zr through PSN, and achieved elongations of 580% at a strain-rate of $2.8x10^{-4}s^{-1}$ and a temperature of 570°C [14]. Kaibyshev *et al.* [128] went on to test the same material at even higher temperatures, where incipient melting occurs, i.e. at 590°C, and produced an elongation of 1300%. Melting was though to aid accommodation of GBS and repair any cavities that were generated [128]. Figure 2.30 shows the elongation to failure and strain-rate sensitivity found by Kaibyshev *et al.* [128] for their modified AA6061 alloy.

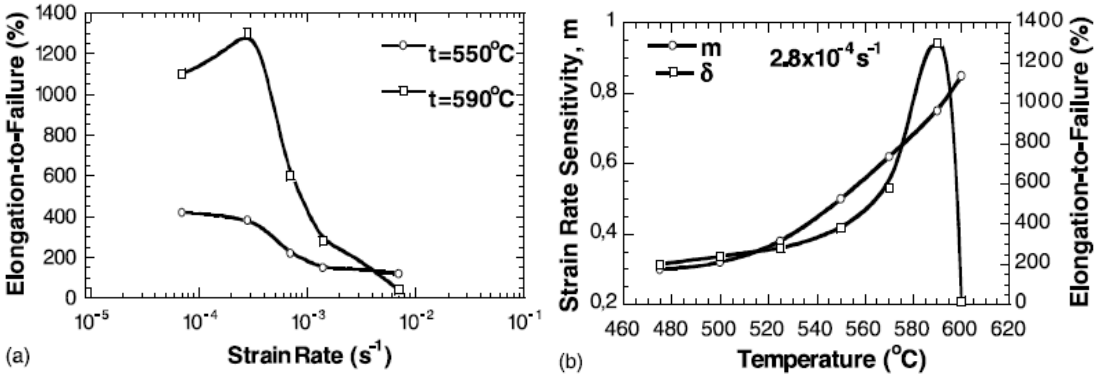

Figure 2.30: Elongation to failure and strain-rate sensitivity found by Kaibyshev *et al.* for a modified fine-grained AA6061 alloy [128].

Kim *et al.* [72] produced a fine grain structure in AA6061 through ECAP, and managed to achieve elongations of 280% at a strain-rate of $3x10^{-4}s^{-1}$ and a temperature of 540°C. Figure 2.31 shows the stress-strain curves for this testing condition. Once again, the strain-rate sensitivity was found to be m=0.5, consistent with grain boundary sliding mechanism for high temperature deformation of Al alloys [72].

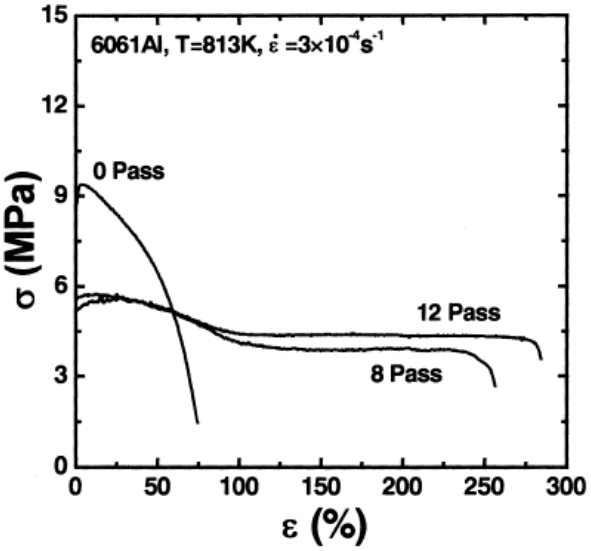

Figure 2.31: Stress-strain curves for AA6061 processed by ECAP for 8 and 12 passes and the unprocessed material, tensile tested at 540°C [72].

Chapter 3 Scope and Objectives

The present work aims to examine the properties of a recently developed fine-grained AA6451 aluminium sheet under room and elevated temperature deformation and relate these properties to microstructural changes within the material. The behaviour will be compared to that of the commercially-processed AA6451 aluminium alloy to assess improvement in the properties.

To achieve the goals of this project, several experiments are conducted. Each material's grain structure and precipitate structure are examined after various stages of high temperature exposure to determine the effect of temperature on the material. Samples are deformed at various elevated temperatures and strain-rates to evaluate the stress-strain properties and the mechanisms of deformation. The fracture surfaces are examined to determine the mode of failure, and the microstructure of the deformed samples are re-evaluated to determine the effect of deformation on the grain structure.

The testing procedures and equipment used in the evaluation of the materials are introduced in Chapter 4. The results of the experiments are shown in Chapter 5, followed by a discussion of the results in Chapter 6. Finally, conclusions are drawn and recommendations for future work are provided. In order to provide a comprehensive report, some of the experimental results obtained by research collaborators are also included and acknowledged.

Chapter 4 Experimental Methodology

4.1 Introduction

This chapter on experimental methodology covers four topics: materials, mechanical testing procedures, sample preparation methods and microstructural examination procedures. A description of each material's composition and thermomechanical history is given. This is followed by the procedure used to prepare samples for elevated temperature uniaxial tensile tests and stress relief tests, as well as a description of the equipment used in these tests. Next, the mechanical polishing, electropolishing and chemical etching procedures are described. Finally, each of the microstructural investigation methods is described. These include: cavitation measurement, precipitate examination, grain size examination and fracture surface examination.

4.2 Materials

4.2.1 T4P AA6451 Aluminium

The AA6451 aluminium alloy was supplied by Novelis Global Technology Center. The alloy composition is given in Table 4.1.

Table 4.1: Nominal composition of AA6451 aluminium alloy (wt%)

Mg	Si	Cu	Fe	Mn	Ti	Zn	V	Ni	Cr	Zr
0.64	0.77	0.31	0.26	0.23	0.024	0.019	0.012	0.006	0.001	<0.001

The as-received sheet had a thickness of 1mm. The sheet had been fabricated from a DC-cast ingot and processed through hot-rolling, cold-rolling and solution heat treatment. The material was supplied in the T4P condition. For the purposes of this document, this material will be referred to as T4P.

4.2.2 Fine-grained AA6451 Aluminium

The fine-grained AA6451 had the same chemical composition as the T4P material, however, it was fabricated using a proprietary [129] thermomechanical

processing route. The DC-cast material was hot rolled to a thickness of 5mm or 4.5mm. Next, the material was solutionized for 15 minutes at 560°C, and then quenched in water. The material was then allowed to naturally age (NA) for 2 weeks. This was followed by 80% cold rolling to a thickness of 1mm or 0.9mm, respectively (total cold reduction=80%). Finally, the material was ramp-heated at a rate of 0.4°C/minute to 380°C and held there for 20 minutes, then furnace cooled to room temperature. The thermal processing history of the fine-grained material is given in Figure 4.1. For the purposes of this document, this material will be referred to as FG.

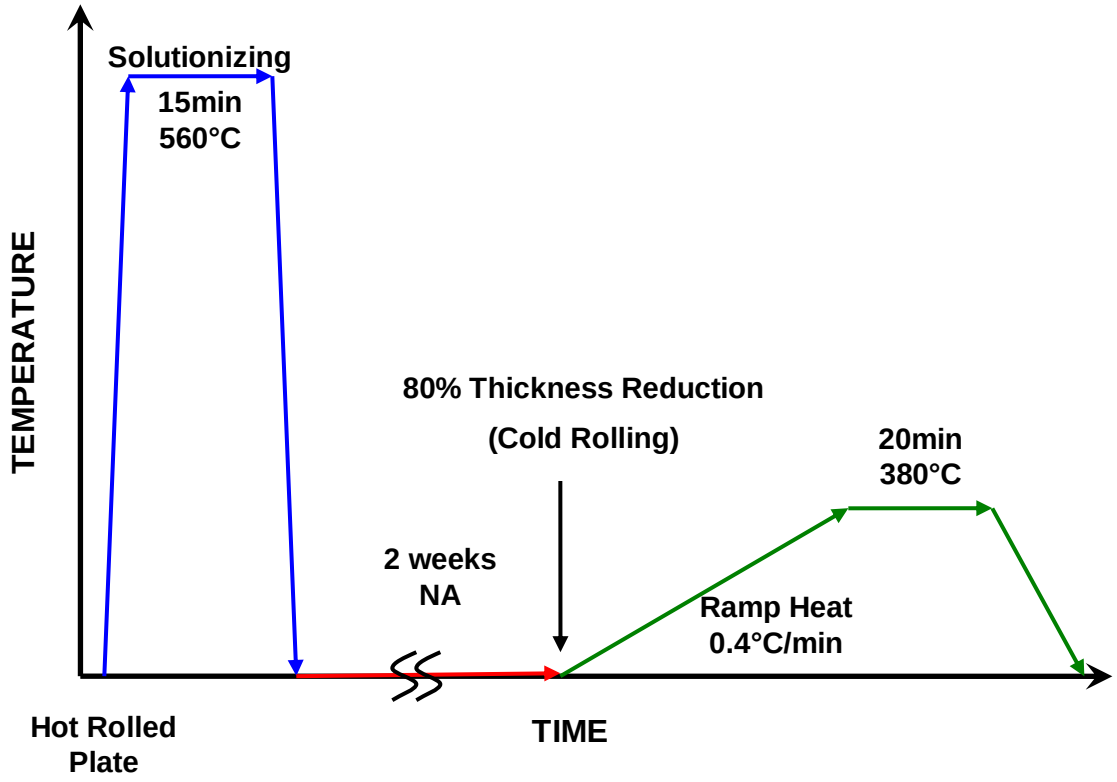

Figure 4.1: Schematic of the thermomechanical processing history for the fine-grained sheet [129].

4.3 Mechanical Testing

Mechanical testing, consisting of uniaxial tensile tests and stress relaxation tests, were conducted using Instron test frames. Early uniaxial tensile tests were conducted at the Novelis Global Research Center on a servo-driven Instron 4400 test frame fit with an environmental chamber. Temperature feedback was supplied by K-type thermocouples

attached to the grips within the chamber. Data was collected using the Bluehill software package from Instron. The strain was measured using a video extensometer. Load was measured using a 10kN load cell, and crosshead position was measured with a linear variable differential transformer (LVDT).

The bulk of the uniaxial tensile tests and the stress relaxation tests were conducted at the University of Waterloo on an Instron 1331 hydraulic test frame utilizing a FastTrack 8800 controller. Load was measured using an Instron Dynacell 25kN dynamic load cell (with a lower rated accurate range of ~1000N), while crosshead position was measured using an LVDT. The test frame was fitted with an ATS 3210 clamshell furnace with three controllable temperature zones. The temperature was controlled via an ATS 3-zone temperature controller. Feedback was supplied to the controller by a K-type thermocouple positioned 1mm from the surface of the test specimen. Tests were run, and data was collected using the Bluehill 2 software package from Instron. Figure 4.2 shows the experimental setup of the mechanical testing equipment.

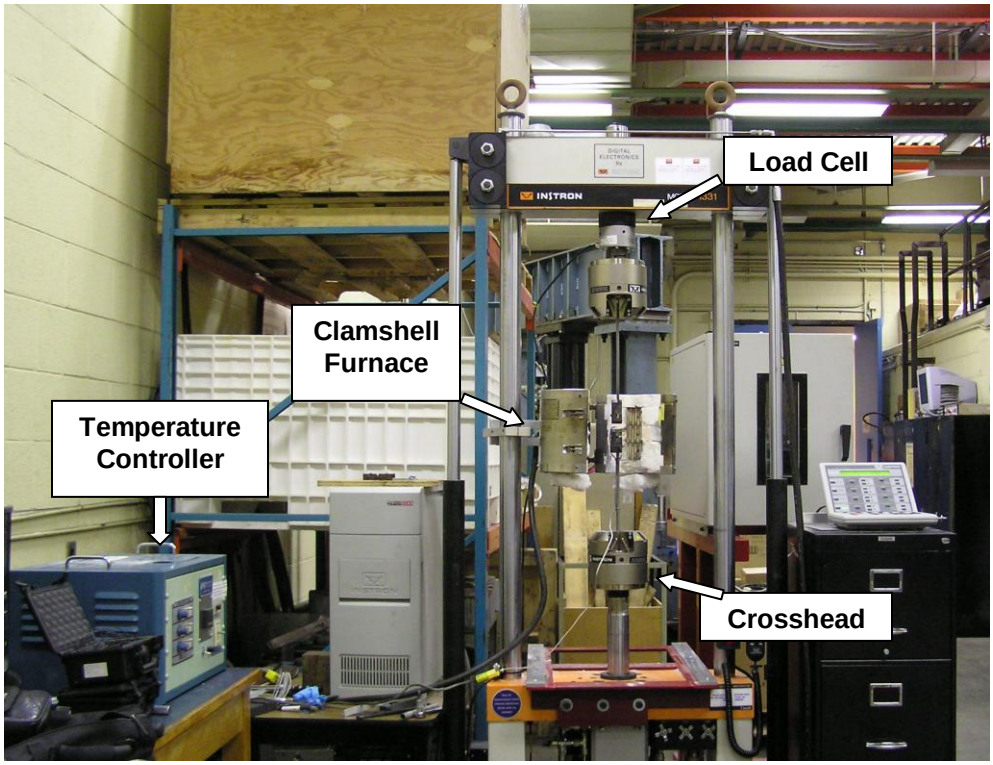

Figure 4.2: Mechanical testing rig.

4.3.1 Grip Design and Sample Dimensions

The specimen grips for the high temperature mechanical testing were originally designed by Novelis to allow rapid insertion of a sample into the grips, so as to minimize the time that the environmental chamber must remain open. The original design was modified by the author for use with the clamshell furnace, while still maintaining the same specimen geometry (so that the data from the two testing facilities may be compared). A rendering of the grips is shown in Figure 4.3.

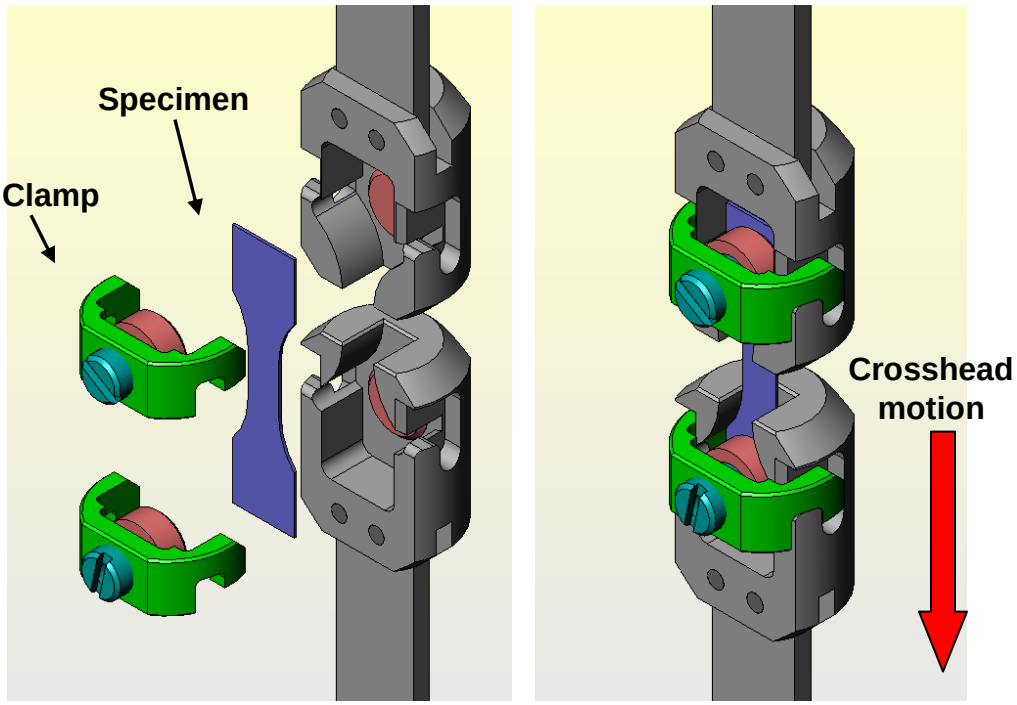

Figure 4.3: Rendering of high temperature specimen grips.

Due to the way the grips were designed, the specimen width was fixed, however the length of the specimen could be varied. For this study, the fully reduced length was selected to be 0.75 inches or 19.05mm. This length was chosen to maximize the number of sample that could be made from the limited amount of material available, as well as minimize the variation in temperature along the length due to convective effects within the furnace. The specimen geometry is shown in Figure 4.4.

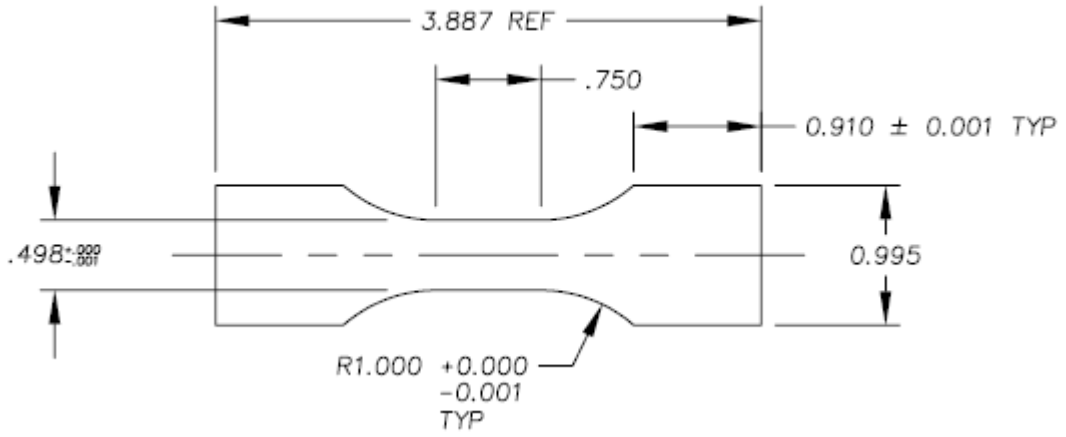

Figure 4.4: Tensile and stress relaxation specimen geometry (dimensions in inches).

The reduced length of the tensile specimen was greater than 0.5 inches to allow a transition zone, as is suggested by ASTM standards [130]. The specimen geometry does not match those laid out by ASTM, and as such, the results of the mechanical tests should not be considered directly comparable with tests done on standard ASTM tensile specimens.

Tensile specimens were cut from the sheets in the rolling directing using a CNC machine. Prior to each test, the specimen width and thickness were measured using a micrometer at three positions along the specimen reduced area and averaged. These values were input into the Bluehill software to be used in stress and strain calculations. The gauge length was taken to be exactly 19.05mm as measurement of this dimension is not possible with any accuracy.

4.3.2 Clamshell Furnace

Prior to testing, a number of trial runs were conducted to calibrate the clamshell furnace and to ensure the temperature was even over the length of the tensile specimen. This was done by raising the temperature of the furnace and grips to the desired point, then allowing the temperature to stabilize. The furnace was then opened, a sample inserted into the grips, and the furnace closed again. The specimen was allowed to soak for 2 minutes at temperature, and then a handheld thermocouple and temperature reader were used to check the temperature at various points along the specimen's length. The

furnace was calibrated such that the desired temperature was reached at the center of the gauge length. The temperature varied by ±5°C along the gauge length, with the specimen being hottest at the top and coolest at the bottom. Despite increasing the current output to the lowest zone of the furnace and decreasing the current output to the upper zone, this could not be improved. When a large sample, simulating a sample that had undergone an elongation of 400%, was tested in this manner, the variation in temperature along the length of the specimen increased to as much as ±15°C. These variations in temperature were attributed to convective currents within furnace.

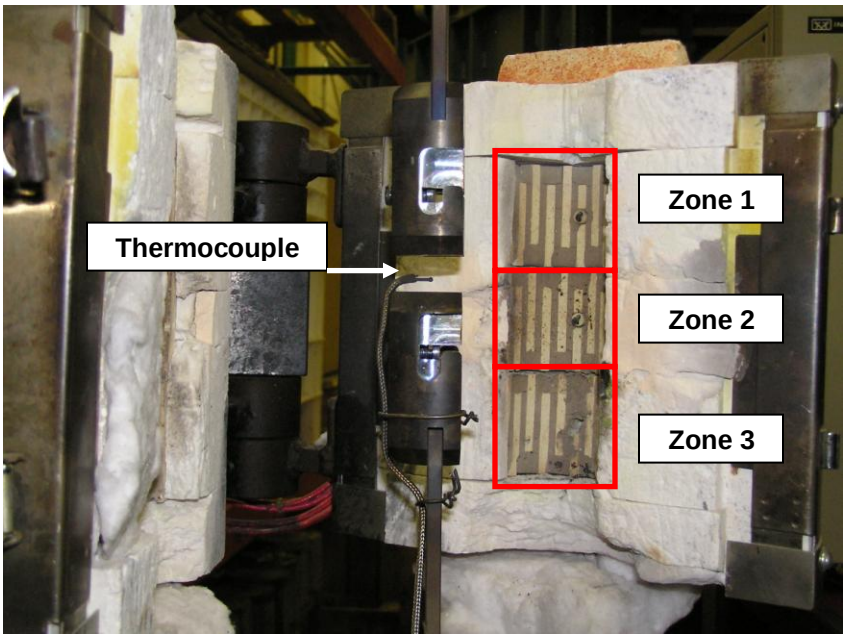

Figure 4.5: Clamshell furnace showing three temperature zones.

4.3.3 Static Ageing

Static ageing was conducted on samples by placing the samples into a preheated furnace for a predetermined amount of time. Samples were then immediately quenched in water to halt any temperature related effects during cooling. A BlueM chamber furnace was used for the experiments, and temperature was controlled using a K-type thermocouple positioned within 1cm of the samples.

4.3.4 Uniaxial Tensile Testing

As stated earlier, some tensile tests were conducted at the Novelis Global Research Center, while the majority were conducted at the University of Waterloo. The

early tests conducted at Novelis included all temperatures at strain-rates of $5.0x10^{-4}s^{-1}$ and $2.0x10^{-3}s^{-1}$, and at $2.0x10^{-2}s^{-1}$at 500 and 550°C. Most of these experiments were repeated at the University of Waterloo to ensure repeatability and accuracy. The same procedure, preheat time and insertion method, was followed for every test. The test matrix for each material is given in Table 4.2. Each test was repeated at least once, and any sample that failed outside of the sample's reduced area was discarded.

Table 4.2: Uniaxial tensile test matrix for each material.

Initial Crosshead Speed (mm/min)	0.57	2.29	22.86	76.20	760.00
Initial Strain Rate (s^{-1})	$5.0x10^{-4}$	$2.0x10^{-3}$	$2.0x10^{-2}$	$6.7x10^{-2}$	$6.7x10^{-1}$
Room Temperature	x	x	x	x	x
350°C	x	x	x	x	x
400°C	x	x	x	x	x
450°C	x	x	x	x	x
500°C	x	x	x	x	x
550°C	x	x	x	x	x

Prior to testing, the alignment of the grips was checked to insure that the specimen was not twisted, and remained vertical throughout the test. The crosshead was positioned so that the sample could be easily inserted into the grips. For high temperature tests, the furnace was closed around the grips with the clamps in place, and heated to the desired temperature. In each test, the strain is produced through moving the crosshead at a constant rate. The initial strain-rate is related to this crosshead rate of travel by Equation 4.1.

$$\dot{e} = \frac{\dot{X}}{L_0} \qquad \textbf{Equation 4.1}$$

Where $\dot{e}$ is the initial strain-rate, $\dot{X}$ is the crosshead speed and L_0 is the specimen reduced area length. The crosshead speed and the specimen dimensions were entered into the Bluehill software. When the temperature in the furnace had stabilized, the

furnace was opened and the clamps were removed. The specimen was then placed into the grips, the clamps were placed back into position and the furnace was closed. The specimen was held in the furnace for two minutes before the test was started to allow the furnace to equalize again, and allow the specimen to reach the desired temperature. The test was then started with the Bluehill software. The test was stopped manually when the specimen failed. When the test was finished, the furnace was opened and the specimen was removed. Failed specimens were allowed to air cool.

In all high temperature tests, the strain reported is calculated from the motion of the crosshead using Equation 4.2.

$$e = \frac{L - L_0}{L_0} = \frac{X}{L_0} \qquad \textbf{Equation 4.2}$$

Where e is the engineering strain, L is the current length of the specimen and X is the distance the crosshead has traveled. This method of strain measurement is not ideal as it includes any strain occurring outside of the gauge length, however it has been used often in similar tests in literature [4,99]. The tests conducted at Novelis included measurements from a video extensometer, and a comparison of this strain data with crosshead strain showed that, on average, there was a 10-20% underestimation of the % elongation when Equation 4.2 was used. An example of a stress-strain plot showing both the strain measured by the crosshead motion and the strain measured by a video extensometer is shown in Figure 4.6.

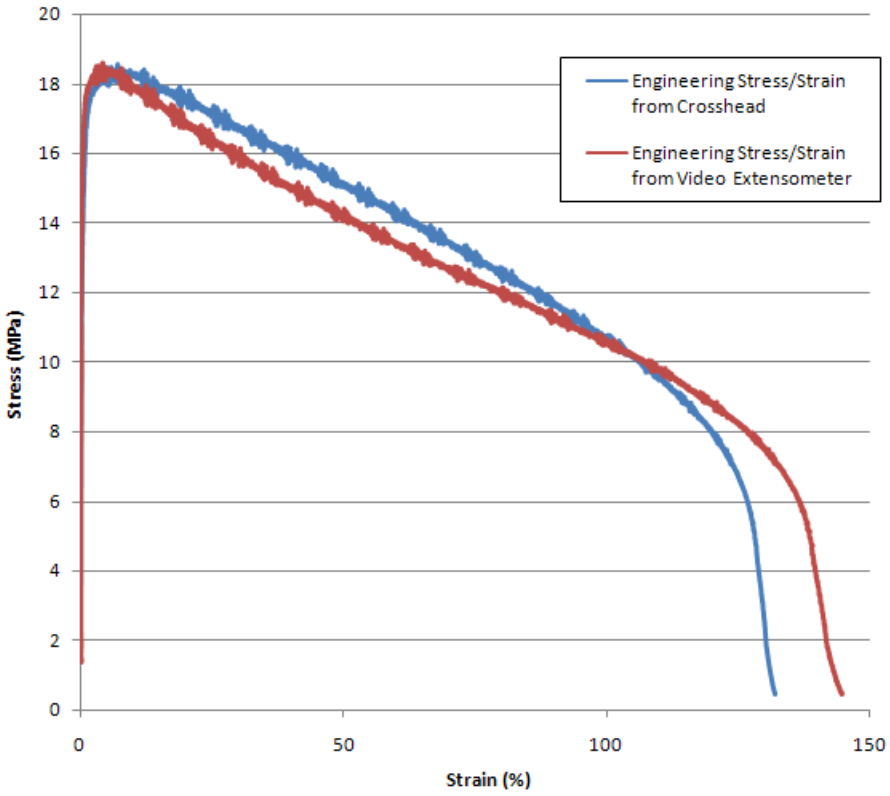

Figure 4.6: Comparison of stress and strain measured by crosshead displacement and video extensometer.

In tensile tests conducted at room temperature, the strain was measured using an Instron 2620-601 Dynamic Extensometer. The extensometer could support gauge lengths of 12.5mm, 25 mm or 50 mm, with a travel of ±5 mm. This allowed measurement of the strain, elastic modulus and yield stress. In these tests, the gauge length, 0.5 inches, was used to calculate strain. It was observed that deformation outside of the gauge was more prominent at room temperature.

The stress reported in all uniaxial tensile tests is the engineering stress, as calculated by Equation 4.3.

$$\sigma = \frac{P}{A_0} \qquad \textbf{Equation 4.3}$$

Where σ is the engineering stress, P is the applied load and A_0 is the cross-sectional area of the undeformed tensile specimen's reduced length. Calculation of the necking

corrected true stress of a rectangular specimen was not considered for this investigation due to the difficulties involved with measuring the cross-sectional area of the specimen in real-time [131,132].

There are 4 important pieces of data that can be extracted from a stress-strain curve: elastic modulus (E), yield stress (YS), peak stress or ultimate tensile stress (UTS) and the elongation or strain at failure (e_f). The elastic modulus was found by taking the slope of the stress-strain curve in the linear region. The yield stress, or the stress at which the material begins to deform plastically, was determined by finding the point where a line parallel to the linear region, offset by 0.2% strain, crosses the stress-strain curve. The estimation of the elastic modulus was only used to ensure the accuracy of the tensile tests. The UTS is the maximum stress on the stress-strain curve; this value is used to report the strength at high temperatures. The failure strain is difficult to determine when testing at high temperatures due to the highly ductile nature of the failure. In order to have a consistent method of determining the failure strain, the point of maximum negative slope at the end of the stress-strain curve was chosen. Examples of the UTS and failure strain are shown Figure 4.7.

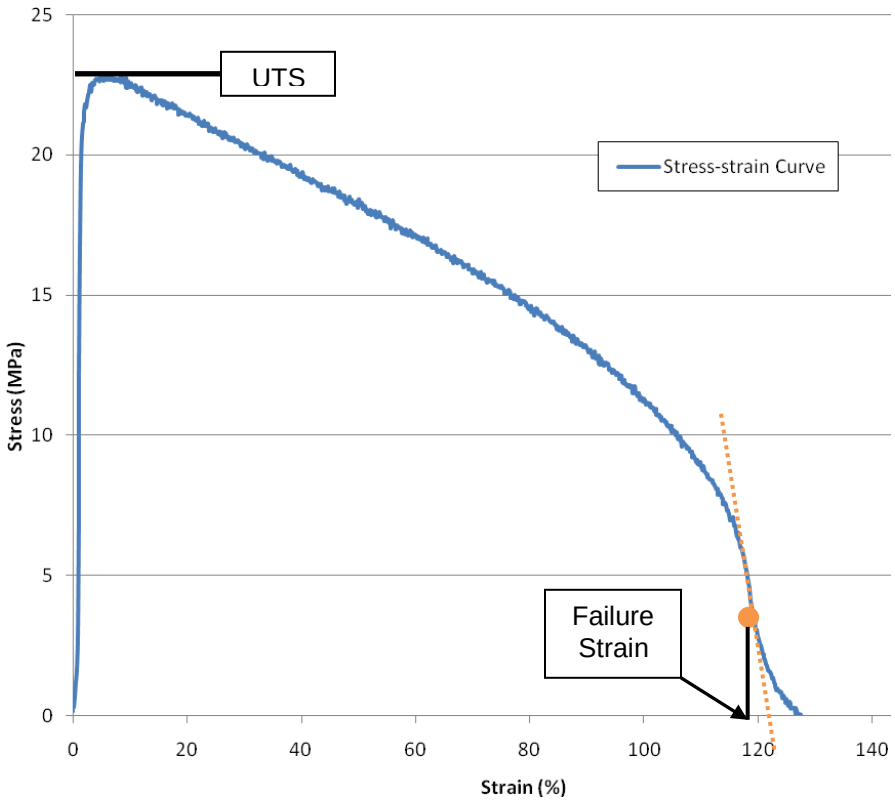

Figure 4.7: An example of a UTS and a failure strain measurement from a stress-strain curve.

To calculate the strain-rate sensitivity, *m*, the procedure described by Hedworth and Stowell [27] and applied by Li and Ghosh [4] was used. Using this method, the strain-rate sensitivity is defined as by Equation 4.4.

$$m = \frac{\ln\left(\frac{\sigma_{UTS,1}}{\sigma_{UTS,2}}\right)}{\ln\left(\frac{\dot{\varepsilon}_{I,1}}{\dot{\varepsilon}_{I,2}}\right)} \quad \textbf{[27,4]} \qquad \textbf{Equation 4.4}$$

Where $\sigma_{UTS,1}$ and $\sigma_{UTS,2}$ are the UTS of two tensile curves (same temperature), and $\dot{\varepsilon}_{I,1}$ and $\dot{\varepsilon}_{I,2}$ are the initial strain-rates of those curves. The average value of *m* for each temperature is calculated by fitting a curve to the log(σ_{UTS}) vs. log($\frac{\dot{\varepsilon}}{E}$) plots for each

temperature, and taking the slope of that line. The activation energy, Q, can also be calculated using the same data, as given by Equation 4.5.

$$Q = -R\left[\frac{\ln\left(\frac{\dot{\varepsilon}_1}{\dot{\varepsilon}_2}\right)}{\left(\frac{1}{T_1}-\frac{1}{T_2}\right)}\right]_{\sigma} \quad \textbf{[133]} \qquad \textbf{Equation 4.5}$$

Where $\dot{\varepsilon}_1$ and $\dot{\varepsilon}_2$ are strain-rates at temperatures T_1 and T_2, respectively, at a constant stress, σ, and R is the ideal gas constant. In practice, the strain-rates at various temperatures and a constant stress were not measured, therefore, the data was extrapolated from the curve fits described above. The values of Q reported were taken as the average of the activation energies calculated at the lower and upper extremes of stresses measured, and only on adjacent temperatures. The determination of Q and m are illustrated in Figure 4.8.

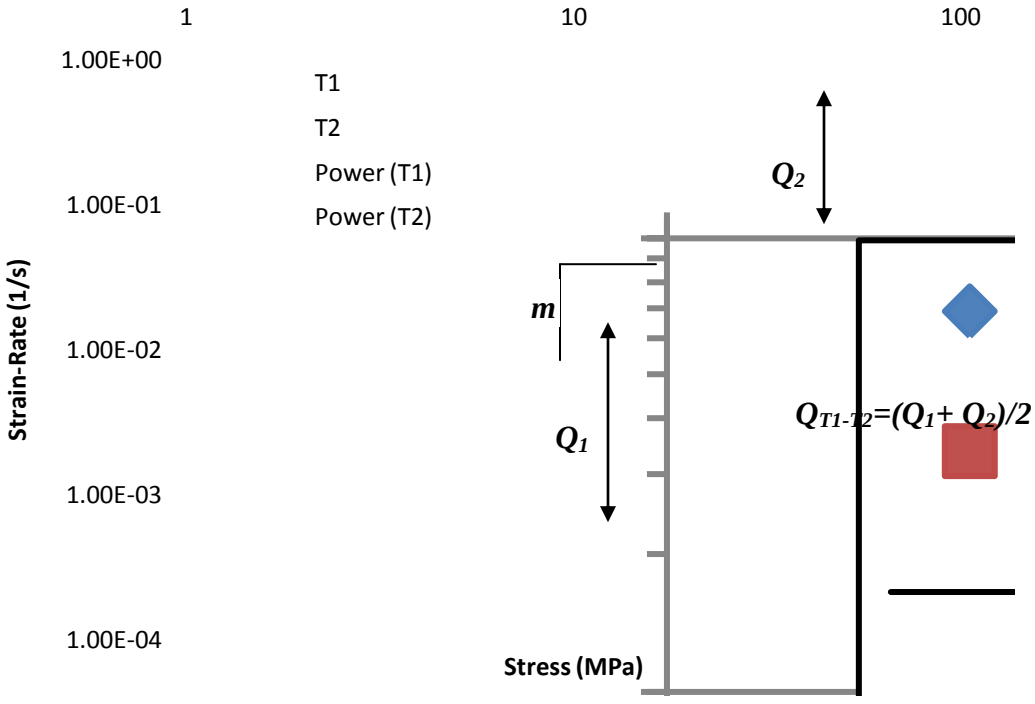

Figure 4.8: Illustration of the strain-rate sensitivity, m, and the activation energy, Q.

In Chapter 2, it was shown that log(σ) vs. log($\dot{\varepsilon}$) plots of data at different temperatures may be consolidated into a single curve by normalizing the data with the

elastic modulus, E, and the self diffusion coefficient, D_{SD} (Figure 2.7 and Figure 2.9). These parameters are calculated using Equation 4.6 and Equation 4.7, respectively. E is taken from a curve fit to empirical data from Köster for pure Al [134].

$$E = 77630 - 12.98T - 0.03084T^2 \quad \textbf{[134]} \qquad \textbf{Equation 4.6}$$

$$D_{SD} = D_0 \exp\left(\frac{-Q_{SD}}{RT}\right) \quad \textbf{[18]} \qquad \textbf{Equation 4.7}$$

Where E is in MPa, T is the temperature in K, D_0 is the lattice diffusion constant ($1.7 \times 10^{-4} m^2/s$ in Al [18]) and Q_{SD} is the self diffusion activation energy (142kJ/mol in Al [18]).

4.3.5 Stress Relaxation Testing

Stress relaxation tests were conducted using the Instron 1331 hydraulic test frame in the same configuration used for uniaxial tensile tests, and the preparation procedure followed was the same. In the stress relaxation test, rather than strain the sample to failure, the sample was strained to a low level of strain, 3%, and then the crosshead was halted. Load vs. time data was gathered for 10 minutes after the crosshead has stopped. The initial strain-rate chosen for the straining of the samples was chosen to be $4.37 \times 10^{-2} s^{-1}$, corresponding to a cross-head speed of 50mm/minute. This value was the maximum possible without causing excessive vibrations within the system when the crosshead was stopped. These vibrations caused large fluctuations in the load reading, overshadowing the relaxation data. The data capture rate was set to the maximum value possible (200 recorded samples/second) to allow capture of the rapid relaxation seen immediately after the crosshead was stopped. A sample load vs. time curve for a stress relaxation test up to a total of 50 seconds is shown in Figure 4.9.

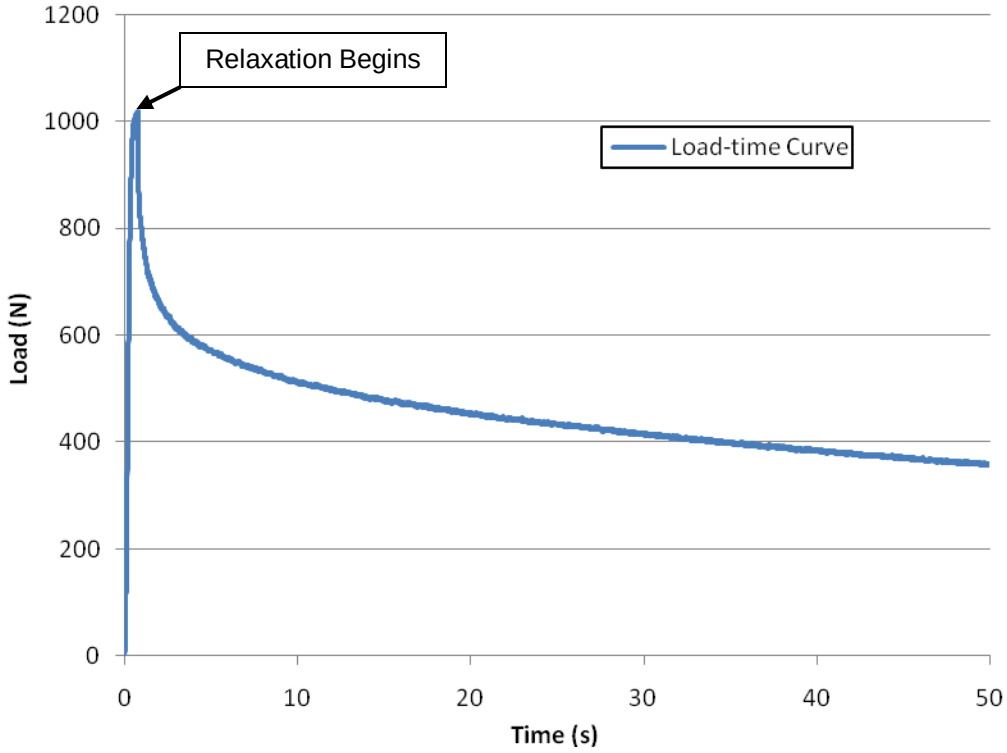

Figure 4.9: Example of load-time curve from a stress relaxation test.

The procedure for determining the flow stress and inelastic strain-rate was laid out by Lee and Hart [71]. The first step in this process was to determine the elastic constant of the system, or inverse of the system compliance, K. This value can be calculated using Equation 4.8.

$$K = \left(C_m + \frac{L}{AE} \right)^{-1} = \left(C_m + \left(\frac{L}{L_0} \right)^2 \left(\frac{L_0}{A_0 E} \right) \right)^{-1} \quad \textbf{[71]} \qquad \textbf{Equation 4.8}$$

Where C_m is the machine compliance, L is the length of gauge section less its elastic extension, A and A_0 are the current and initial cross-sectional areas of the gauge, respectively and L_0 is the initial gauge length. Accurate determination of the machine compliance was difficult, as was determination of the elastic modulus of the material at elevated temperatures. The system compliance was therefore measured for each test by taking the slope of the linear region of the loading curve. Figure 4.10 shows an example of a sample loading curve along with the system compliance.

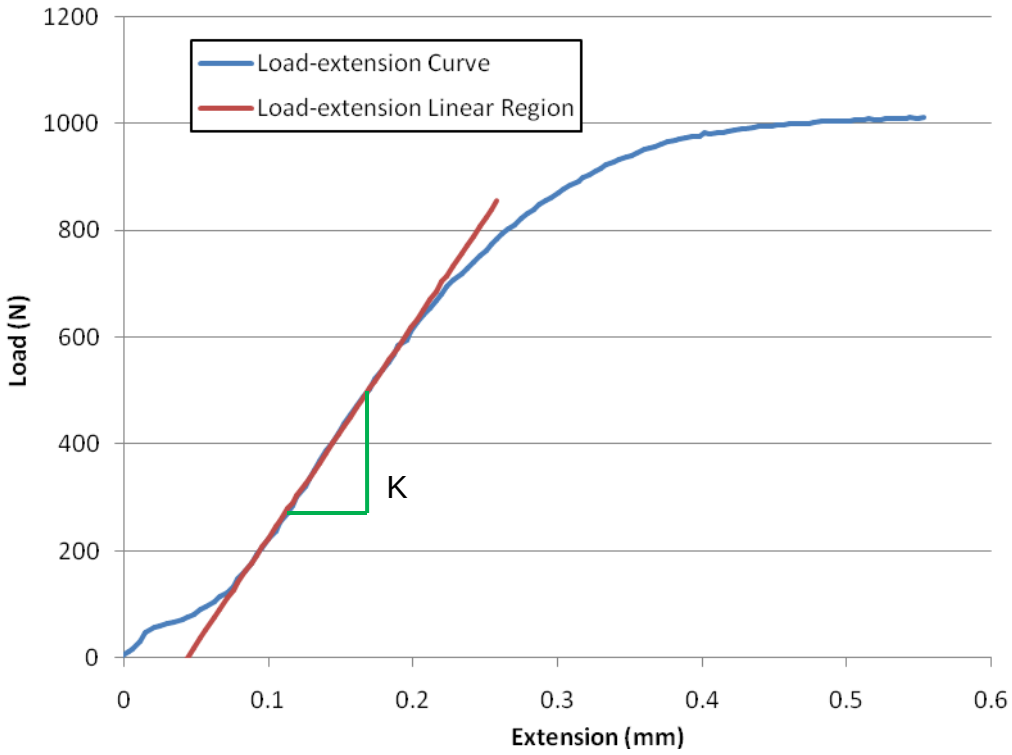

Figure 4.10: Example of extraction of system compliance from stress relaxation test.

To facilitate further processing, the resolution of the data was adjusted. A high resolution was maintained at very early times, and as the time is increased, the data resolution was decreased. At each point where the resolution was decreased, the data point was taken as the average of surrounding data points. This generated a curve with many fewer data points while maintaining the shape of the relaxation curve. An example of the recorded and reduced resolution data curves are shown in Figure 4.11.

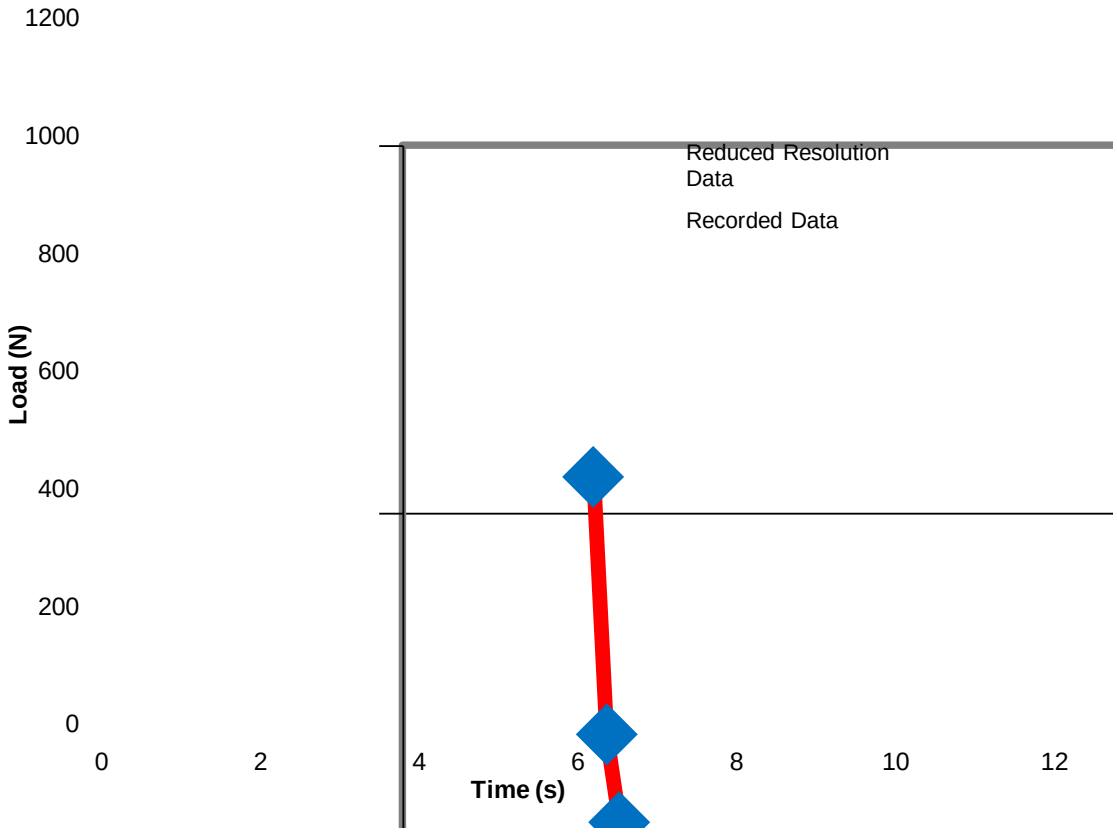

Figure 4.11: Example of data point reduction of load-time curve.

At any point in time, L is given by the relationship in Equation 4.9.

$$L = L_0 + X - \frac{P}{K} \quad [71] \qquad \textbf{Equation 4.9}$$

Additionally, from the load vs. time data, the rate of change of load with time, $\dot{P}$, is determined. Differentiating Equation 4.9, the rate of change in the inelastic length, $\dot{L}$, is determined.

$$\dot{L} = \dot{L}_1 - \frac{\dot{P}}{K} \quad [71] \qquad \textbf{Equation 4.10}$$

Where $\dot{L}_1$ is the rate of change of the length of the reduced length. During a relaxation test, however, since the crosshead does not move, this value equals to zero. Finally, the stress (σ) and inelastic strain-rate ($\dot{\varepsilon}$) is determined using Equation 4.11 and Equation 4.12, respectively. The stress vs. inelastic strain-rate is then plotted on a log-log scale.

$$\sigma = \frac{P}{A} = \frac{PL}{A_0 L_0} \quad \textbf{[71]} \qquad \textbf{Equation 4.11}$$

$$\dot{\varepsilon} = \frac{\dot{L}}{L} \quad \textbf{[71]} \qquad \textbf{Equation 4.12}$$

Once the plots are complete, the constitutive parameters (σ^* and $\dot{\varepsilon}^*$) from Equation 2.9 and Equation 2.10 are determined. This is done by applying non-linear regression to the equations, and fitting them to the data points using the SigmaPlot software suite.

4.4 Sample Preparation for Various Measurements

This section describes the procedures by which the samples are prepared for further microstructural examination. These preparation methods include: mechanical polishing, electropolishing and chemical etching.

4.4.1 Mechanical Polishing Procedure

All samples were polished prior to metallographic examination. Samples prepared for grain size and cavitation measurements were mounted in an epoxy resin prior to polishing. Samples which were to be electropolished (e.g. for precipitate examination), were not mounted. Samples were first ground to the mid-plane of the sample using SiC paper with grits ranging from 400 to 5000, followed by polishing in a 3μm and 1μm diamond suspension. Samples prepared for cavitation measurements were given a final polish in water based colloidal silica (~0.04μm) and glycerol. Samples were washed with water and alcohol between each step. Figure 4.12 shows a schematic of the polishing procedure.

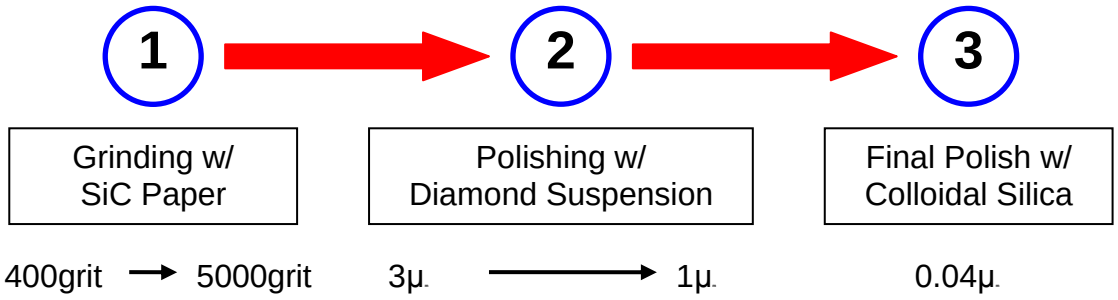

Figure 4.12: Schematic of mechanical polishing procedure.

4.4.2 Electropolishing Procedure

Electropolishing is an electro-chemical process by which material is removed from the surface of a sample. An electropolishing setup consists of four major components: anode, cathode, electrolyte and power supply. When the anode, or specimen, is placed into the electrolyte bath, immediately a layer, called the polishing layer, will be deposited on the surface of the material. This layer is more viscous than the rest of the electrolyte and has a higher electrical resistance. Bumps on the surface of the material will be closer to the surface of the layer, which means that there will be less resistance. This means that there is higher current reaching the bump, which causes it to dissolve faster [135].

The basis for the electropolishing procedure used in this project has been described by [124]. This procedure has the additional effect of oxidizing any magnesium containing particles on the surface of the sample, making them highly visible when viewed in secondary electron mode in the scanning electron microscope (SEM) In this procedure, the electrolyte used is 30% nitric acid in methanol held at -30°C. Note that mixing nitric acid with methanol is an exothermic reaction, and to reduce the risk of explosion, the methanol should be cooled to at least -20°C before the nitric acid is added. Cooling was provided by a bath of dry ice and methanol. The cathode used was commercially pure aluminium and the operating voltage was 9 volts. The electropolishing setup with each of the components is shown in Figure 4.13.

1. **BK Precision 1715A DC power supply (60V/2A)**
2. **Fisher Thermik Magnetic Stirring Hotplate 210T**
3. **Dry ice in methanol cooling bath**
4. **Stirred electrolyte solution (30% nitric acid in methanol)**
5. **Mercury thermometer**
6. **Pure aluminium cathode**
7. **Connection for sample**

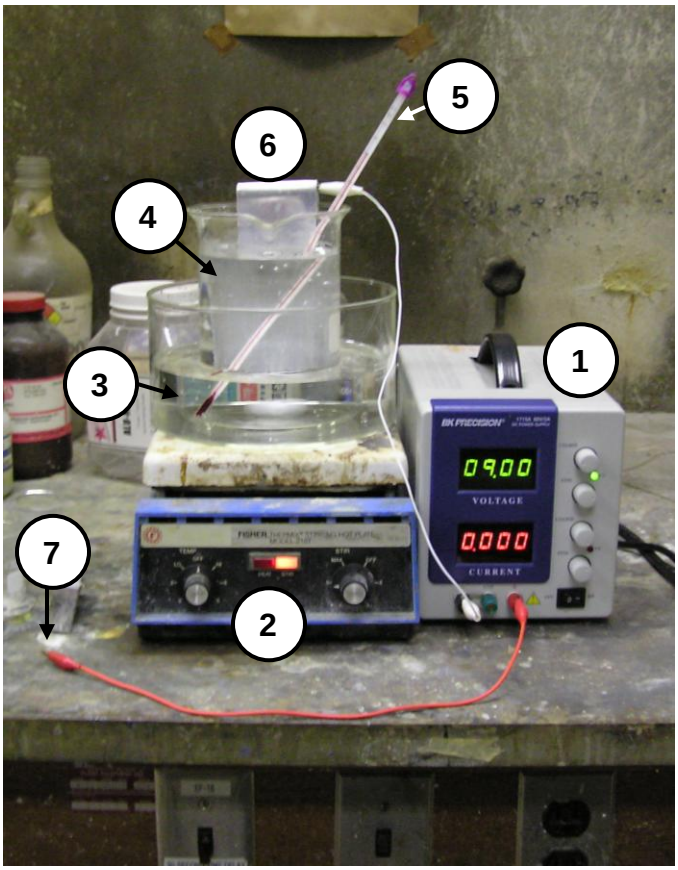

Figure 4.13: Electropolishing setup.

Prior to electropolishing, the mechanically polished sample was masked using masking tape so that only an area ~5mm^2 was exposed (see Figure 4.14).

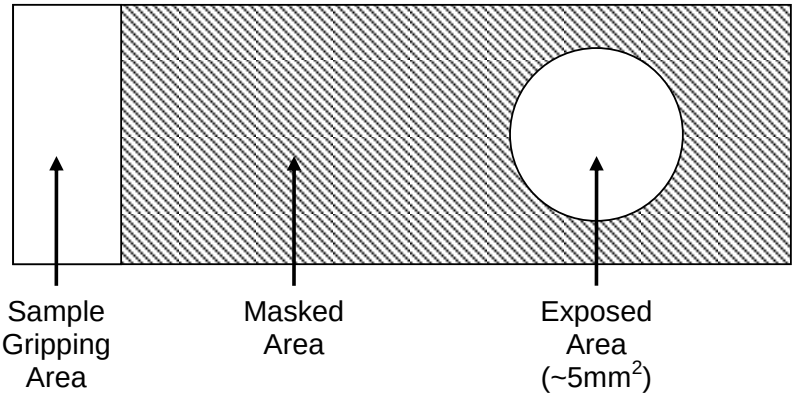

Figure 4.14: Masked electropolishing sample.

The masked sample was connected to the anode of the power supply, which had been set to keep a constant voltage of 9 volts, with an alligator clip within the gripping area. The

masked and exposed areas of the sample were submerged in the agitated electrolyte, and additional agitation was provided by gently shaking the specimen. Neither the alligator clip, nor the gripping area touched the solution in order to keep the current flow concentrated in the masked area. The sample was electropolished for 45 seconds, then immediately rinsed in methanol. The mask was then removed cautiously so that the exposed area was not touched.

4.4.3 Chemical Etching Procedure

Many potential etchants were tried; however, the etchant that gave the best results was 5mL HF in 100mL of H_2O. The etchant was applied by swabbing the sample with cotton balls for approximately 1.5 minutes.

4.5 Cavitation Measurement

Cavitation measurement was conducted using an Olympus BH60 optical microscope equipped with an ImagePro Plus 5.1 image analysis software. These measurements were conducted on the cross-section of the failed tensile specimens. Samples were mounted and polished, and a high resolution image of the entire sample was taken. The image analysis software was then used to determine the area fraction of voids present by measuring the area fraction of black areas (voids) in the image. These measurements were taken at intervals of 50-200μm. Cavitation measurements were conducted by Dr. Sooky Winkler.

4.6 Precipitate Examination

Samples were statically aged for 15 minutes and 2 hours at elevated temperatures prior to precipitate examination, however, it should be noted that only images from 2 hours are reported in this document. 2 hours was chosen to represent each material as the longer ageing time leads to coarser, more visible precipitates, allowing better differentiation between the conditions. The precipitate structure was examined using a Jeol JSM-6460 Scanning Electron Microscope (SEM). Electropolished samples were viewed under secondary electron (SE) mode at an acceleration voltage of 20kV and a working distance of 10mm. It should be noted that as a side effect of the electropolishing procedure, the precipitates grew larger than they were before electropolishing, and Mg

was largely eliminated [124]. Particle chemical composition was identified using EDS analysis.

4.7 Grain Size Examination

Samples for grain size examination were prepared for examination using the above described polishing and chemical etching procedures. Samples were then examined using an Olympus BH2-UMA optical microscope equipped with an ImagePro Plus 4.5 image analysis software. Images were taken at a magnification that showed an area of at least 30X30 grains (achieved with 100X magnification). The grain size was measured using the mean linear intercept method in both the rolling (or tensile) and transverse directions. This method employs a grid of lines placed over the image, and the grain size is found by dividing the length of the lines by the number of grain boundaries that the line crosses. At least 6 measurements were taken and averaged for each sample.

Additional grain size measurements were conducted using a FEG-SEM fit with an EBSD detector at the Novelis Global Technology Center, set at a 7.5° boundary level cutoff and a step size of 2μm. Tests were conducted by Dr. Haiou Jin. Samples were electropolished using a procedure similar to that described in 4.4.2.

4.8 Fracture Surface Examination

The fracture surfaces were examined using the SEM. Failed tensile specimens were cut and placed within the SEM so that the fracture surfaces were facing upwards. The samples were viewed under SE mode at 20kV and a working distance of 15mm to allow a large depth of field. Fracture surfaces were examined primarily on the Jeol JSM-6460 SEM, as well as some high resolution images taken by Dr. Sooky Winkler on the LEO 1530 FESEM.

Chapter 5 Experimental Results

5.1 Introduction

The results of the experiments described in Chapter 4 are described in this chapter. This section is split between describing the original materials' characteristics and their characteristics after exposure to elevated temperatures. Emphasis is placed on describing the elevated temperature properties.

5.2 Basic Characteristics

In this section, the basic or baseline characteristics of the FG and T4P materials are examined for comparison with the high temperatures properties.

5.2.1 Microstructural Characteristics of As-Received Materials

5.2.1.1 T4P Material

An optical micrograph of the initial grain structure of the T4P material is shown in Figure 5.1. The grains are not initially elongated in either the rolling or transverse directions and have an average grain diameter of ~45μm viewed in the rolling plane. The large black spots on the image are a result of the etchant reacting with large particles in the material.

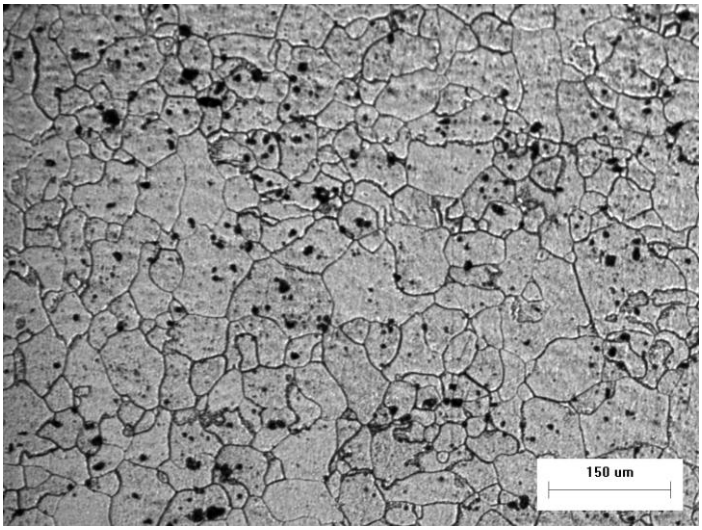

Figure 5.1: Optical micrograph of the T4P sheet revealing the as-received grain structure in the rolling plane.

An SEM micrograph of the as-received and electropolished T4P is shown in Figure 5.2. The microstructure consists of an array of small particles throughout the material, and a small number of large particles, which have been circled for clarity. The black circles around the particles are an artefact left by the electropolishing process. The smaller particles are generally round or oval in shape. Figure 5.3 shows an SEM image where the small particles were examined by EDS. The scan showed that these particles are primarily aluminium and silicon rich. Spectrum 4 in Figure 5.4 did not detect the particle. EDS analysis reveals that the large particles are iron containing particles. The large particles are arranged randomly throughout the sample, while the small particles show a small preference for grain boundaries.

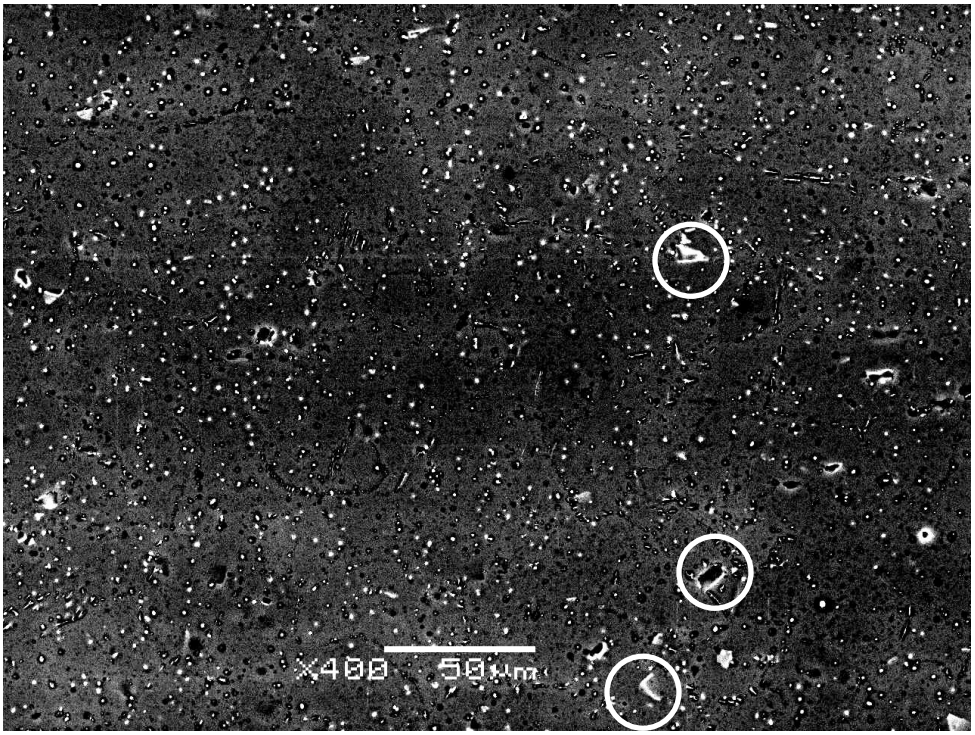

Figure 5.2: SEM micrograph of the T4P as-received particle structure (SE mode). Large particles are circled for clarity.

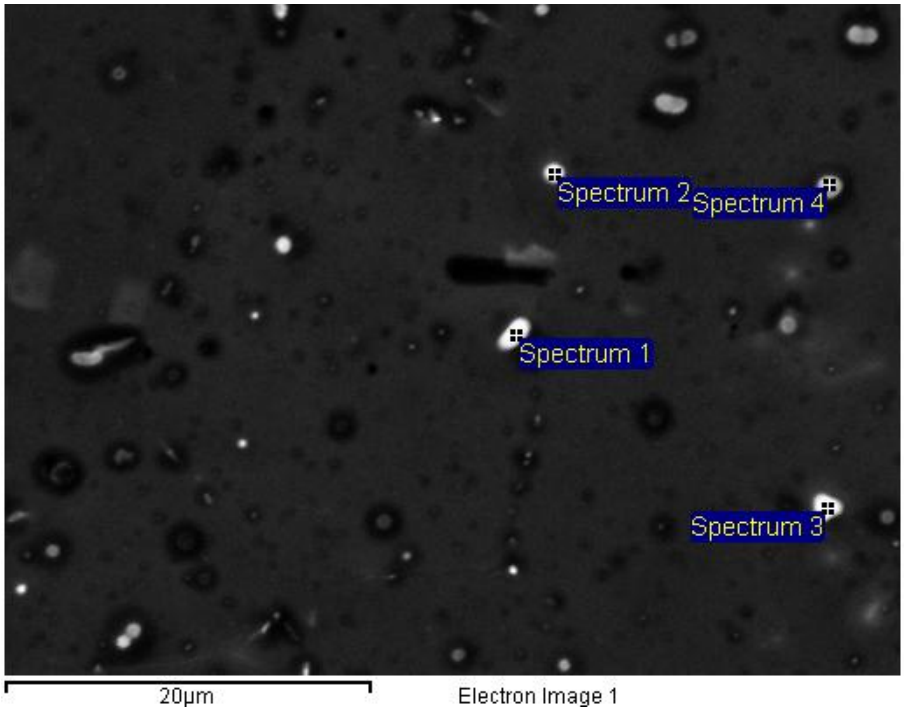

Spectrum	Average Composition (weight %)		
	Si	O	Al
1	7.4	17.7	Bal
2	6.7	14.0	Bal
3	7.1	15.7	Bal
4	0	0	Bal

Figure 5.3: EDS analysed image of T4P material examining small particles found in the as-received condition and measured composition of particles (SE mode).

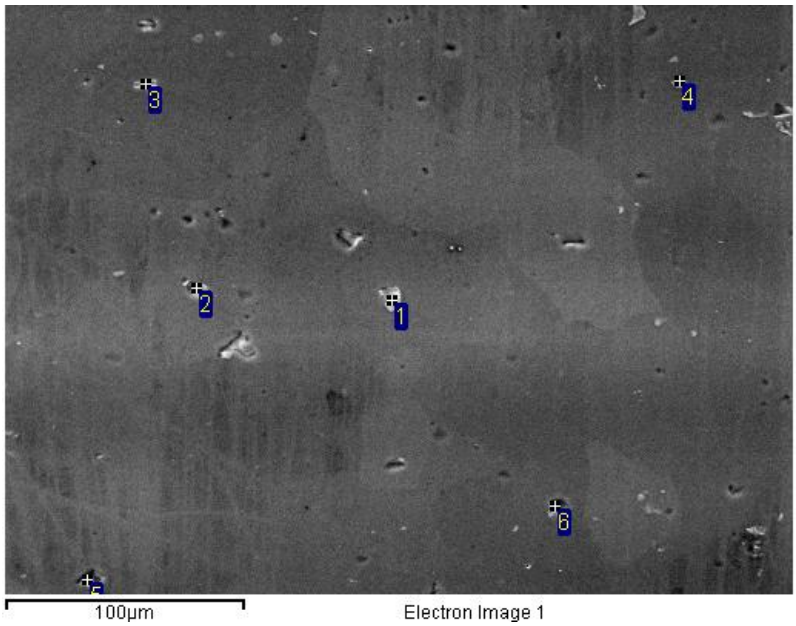

Spectrum	Average Composition (weight %)			
	Si	Fe	Mn	Al
1	6.9	14.4	3.3	Bal
2	6.7	19.2	4.4	Bal
3	6.2	24.4	4.3	Bal
4	2.7	8.0	2.4	Bal
5	6.7	17.0	3.8	Bal
6	2.0	1.7	1.2	Bal

Figure 5.4: EDS analysed image of T4P material (as seen in backscatter mode) and measured composition of large particles.

5.2.1.2 FG Material

An optical micrograph of the as-received FG sheet is not produced due to difficulties in achieving an appropriate etch to reveal the grain boundaries of the FG material. An EBSD image of the initial grain structure is shown in Figure 5.5. Again, the grains are equiaxed, however the average grain diameter is approximately ¼ the average grain size of the T4P material (i.e. ~11µm in the rolling plane).

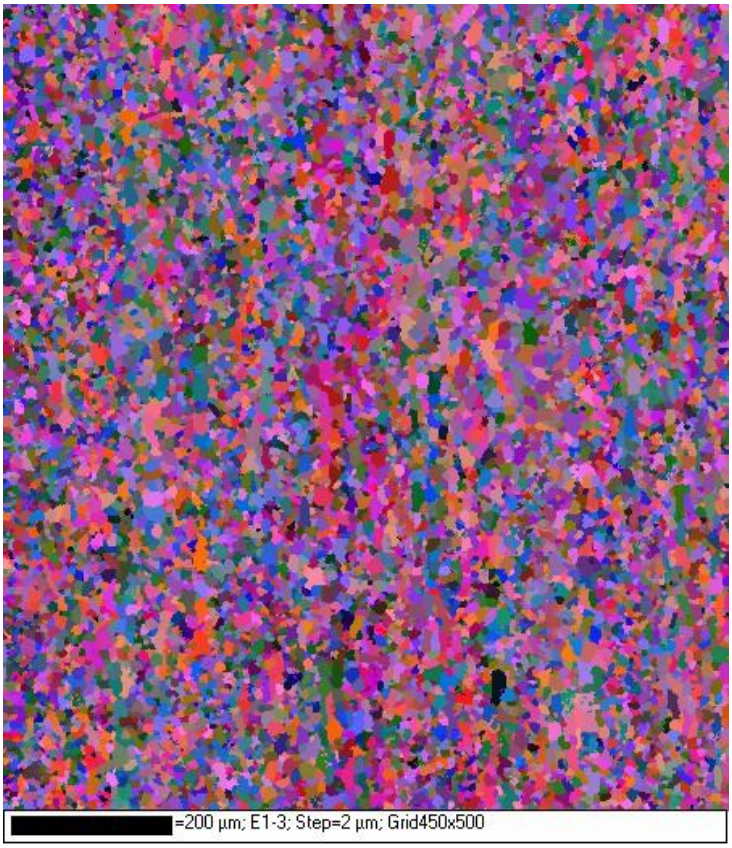

Figure 5.5: EBSD orientation map of the FG material (image by Haiou Jin).

The SEM micrograph of the precipitation structure of the as-received FG material is shown in Figure 5.6. As expected, this material contains the same large iron containing particles as the T4P material, as shown circled in white. There are also a large quantity of smaller, round particles. The dispersion of particles is also much more even compared to the T4P material; there does not appear to be a preference for grain boundary precipitation.

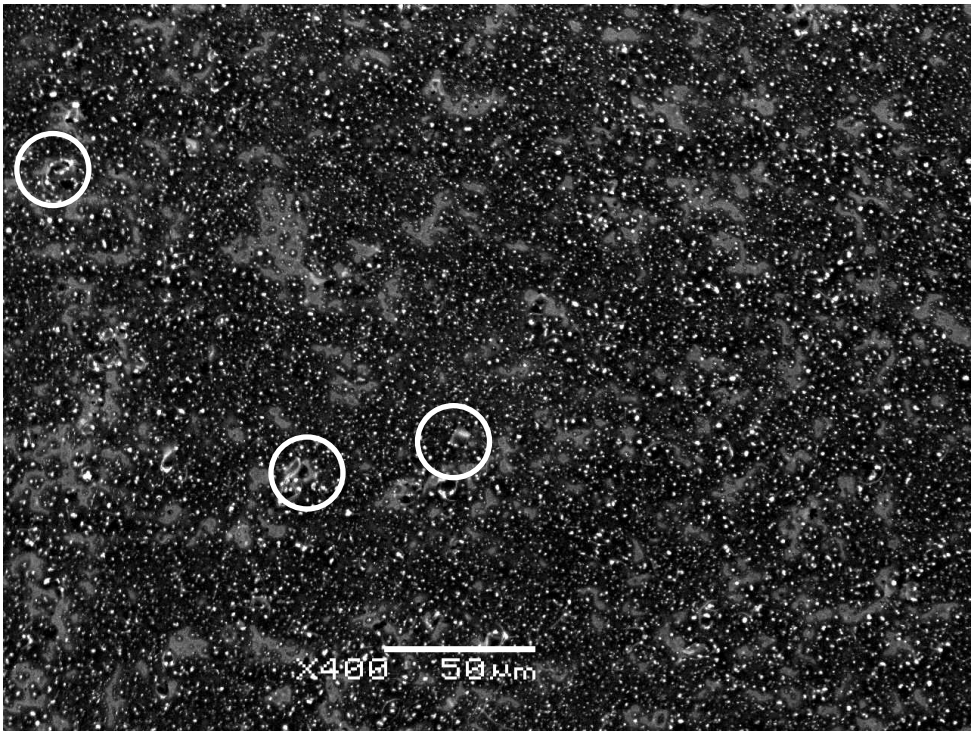

Figure 5.6: SEM micrograph of the FG material as-received precipitate structure. Large particles are circled for clarity (SE mode).

5.2.2 Mechanical Behaviour at Room Temperature

5.2.2.1 Stress-Strain Behaviour

5.2.2.1.1 T4P Material

Figure 5.7 shows the stress-strain curves for the T4P material at the lowest and highest strain-rates. As can be seen, there is very little variation in the total elongation, yield stress, or UTS, even with large changes in the strain-rate. There is a minor increase in the yield and flow stress with increasing strain-rate. The small fluctuations seen in the low strain-rate curve are attributed to feedback created by the hydraulic pumps and crosshead position control system. The combined results of the tensile tests are shown in Table 5.1. The elongation to failure did not show any trend relating to strain-rate, and fluctuations of this value were attributed to errors caused by sample variability.

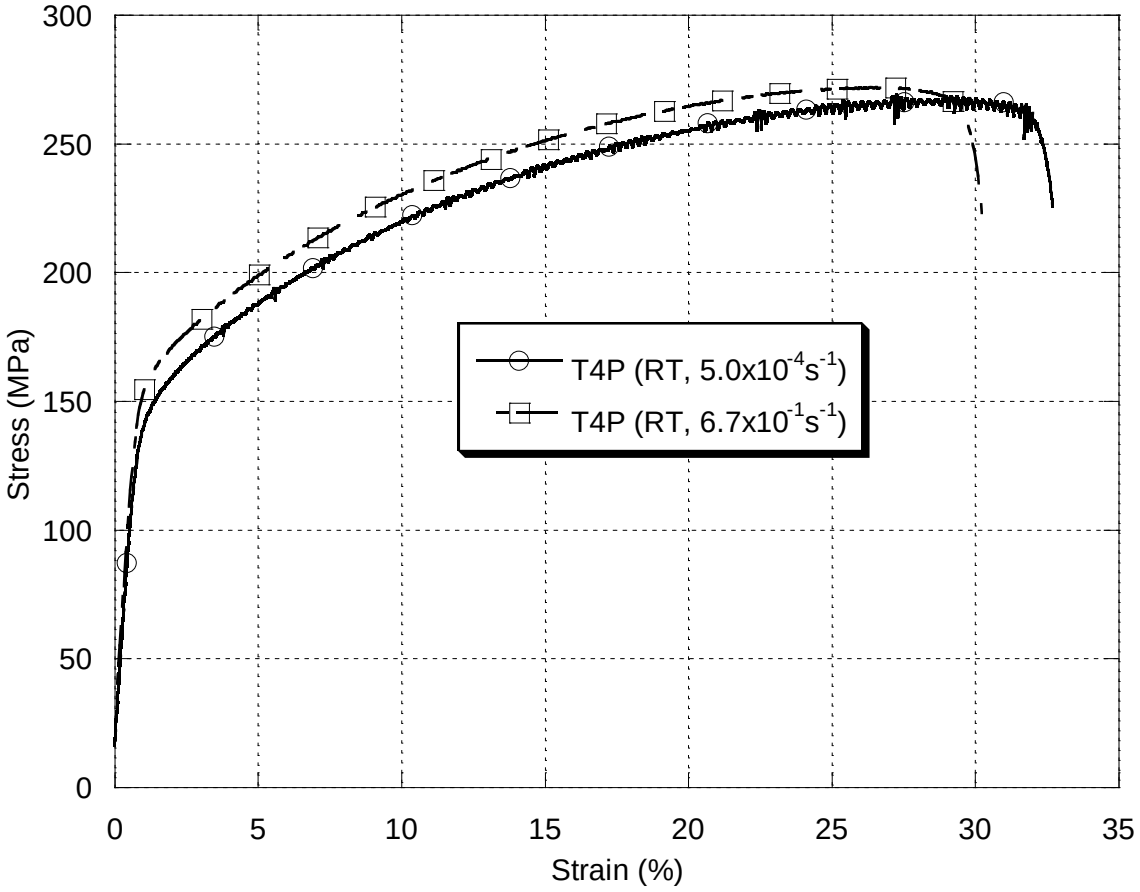

Figure 5.7: Stress-strain curves of T4P sheet tensile tested at room temperature at $5.0x10^{-4}s^{-1}$ and $6.7x10^{-1}s^{-1}$.

Table 5.1: Room temperature tensile properties of the T4P material.

Strain-Rate (s^{-1})	Elongation to Failure (%)	Yield Stress (MPa)	Ultimate Tensile Stress (MPa)
$5.0x10^{-4}$	32.7	140.3	268.9
$2.0x10^{-3}$	30.6	147.6	267.8
$2.0x10^{-2}$	30.1	148.9	269.9
$6.7x10^{-2}$	29.2	151.72	268.4
$6.7x10^{-1}$	30.2	154.7	272.0

5.2.2.1.2 FG Material

Figure 5.8 shows typical stress-strain curves for the FG material at the lowest and highest strain-rates. Fluctuations in the stress are seen in the low strain-rate curve, and are attributed to the same mechanism as the T4P material (i.e. hydraulic pump feedback). The tensile properties are summarized in Table 5.2. The FG material again shows that there is little change in the material characteristics at room temperature with changes in strain-rate. The values are, however, quite different than the T4P material. The average elongation to failure increases by approximately 10%, and the yield stress and UTS are significantly reduced. As with the T4P material, the flow stress increases slightly with the higher strain-rates.

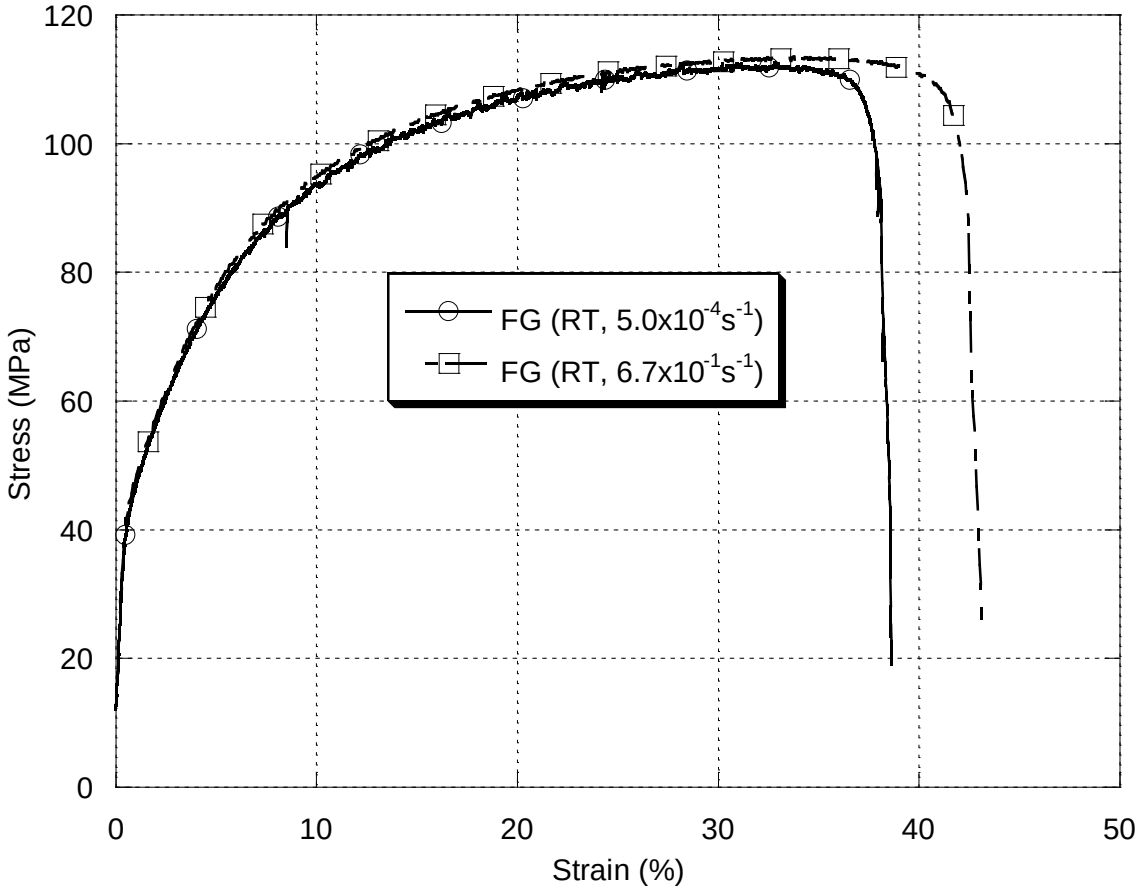

Figure 5.8: Stress-strain curves of FG sheet tensile tested at room temperature at $5.0x10^{-4}s^{-1}$ and $6.7x10^{-1}s^{-1}$.

Table 5.2: Room temperature tensile properties of the FG material.

Strain-Rate (s^{-1})	Elongation to Failure (%)	Yield Stress (MPa)	Ultimate Tensile Stress (MPa)
$5.0x10^{-4}$	38.7	41.5	112.6
$2.0x10^{-3}$	40.9	39.6	110.9
$2.0x10^{-2}$	39.9	41.9	112.1
$6.7x10^{-2}$	41.4	39.6	110.2
$6.7x10^{-1}$	42.9	42.7	113.5

5.2.2.2 Damage and Fracture Behaviour

5.2.2.2.1 T4P Material

In the through-thickness view of a T4P sample tested to failure at $2.0x10^{-3}s^{-1}$, Figure 5.9, the fracture surface is inclined at ~45°. There is minimal necking seen in the sample, even up to the fracture surface. There is a very small amount of void formation seen close to the fracture surface of the sample. As can be seen in the enlarged area of Figure 5.9, the voids (black areas) seem to initiate from fractured large particles (grey areas) and particle decohesion as indicated by the arrows. Figure 5.10 shows the fracture surface of a T4P sample tested to failure at $2.0x10^{-3}s^{-1}$. The fracture surface is dimpled and also shows evidence of shear. Some areas show heavy dimpling, with the dimples spaced closely together, while others areas have few dimples, and the dimples are widely spaced.

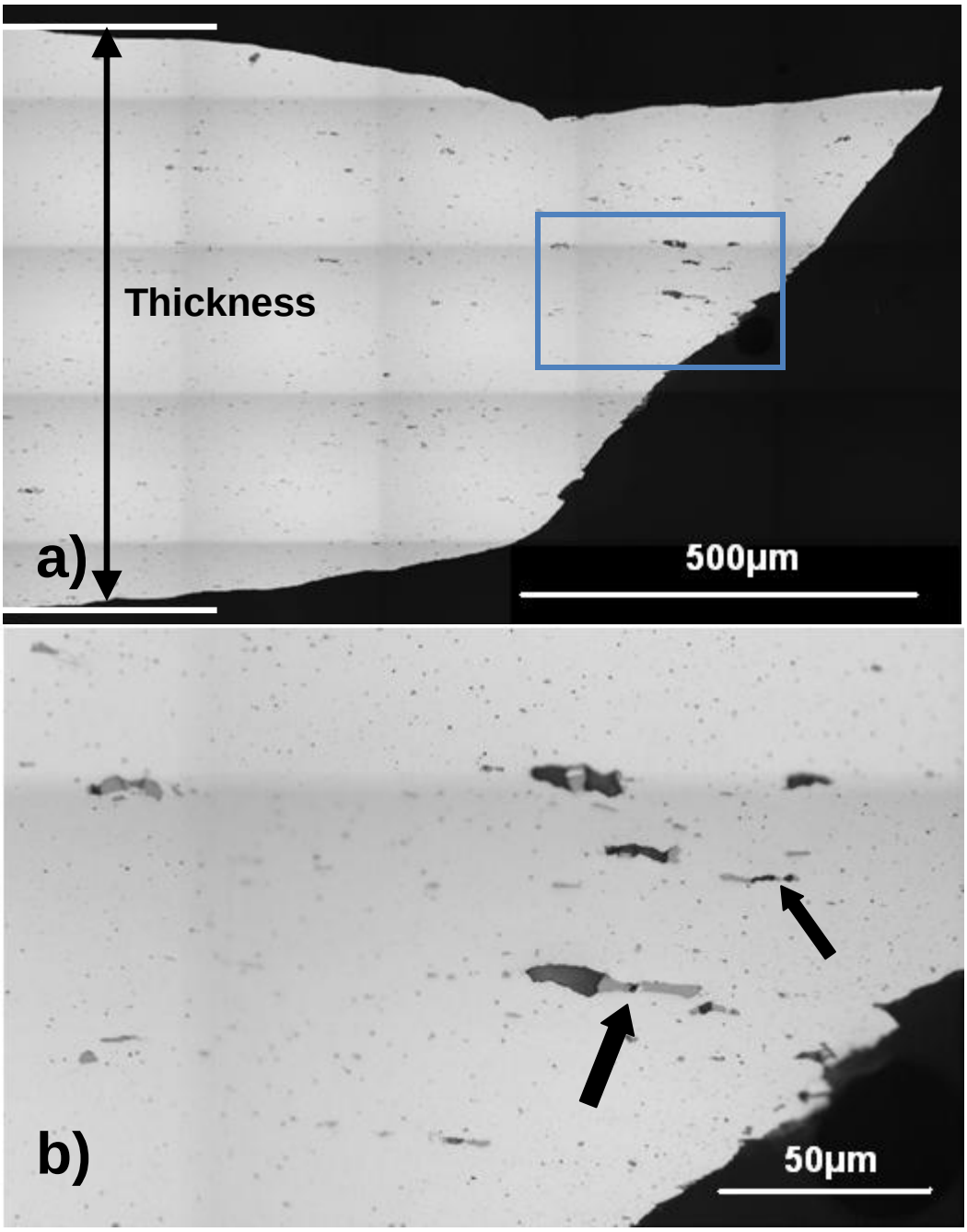

Figure 5.9: Through-thickness view of T4P sheet tensile tested at room temperature at $2.0x10^{-3}s^{-1}$ a) overall image and b) insert view (images by Sooky Winkler).

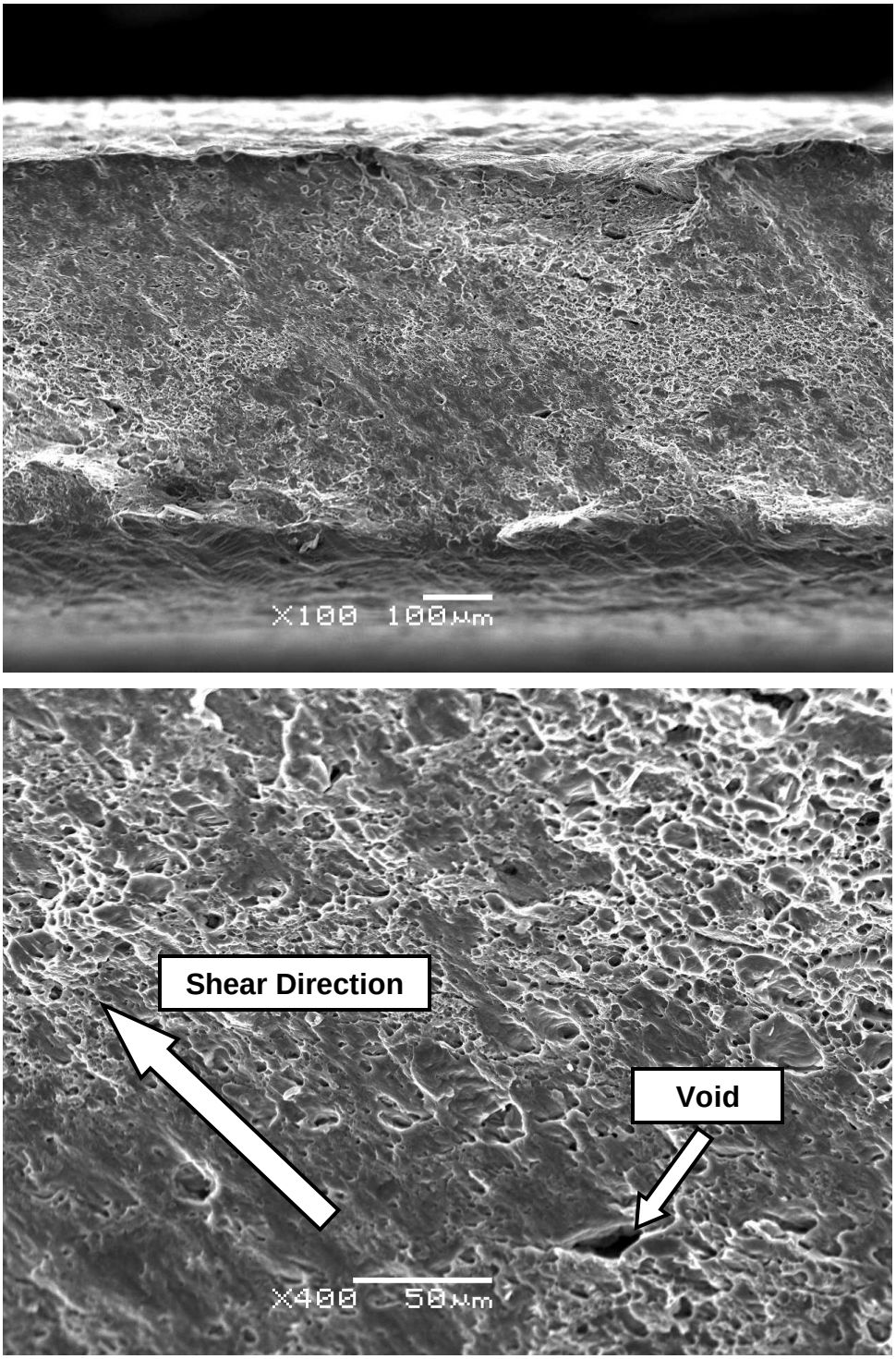

Figure 5.10: Fracture surface of T4P sheet tensile tested at room temperature at $2.0x10^{-3}s^{-1}$(SE mode).

5.2.2.2.2 FG Material

Figure 5.11 and Figure 5.12 show the through-thickness view and fracture surface of the fracture area, respectively, of a FG sample tested at $2.0x10^{-3}s^{-1}$. The through-thickness view shows that there is minimal void formation in the material. If the sample is examined closely, the beginnings of voids can be seen, as indicated by the arrows. As with the T4P material, the initiation appears to be caused by the fracture of large particles as well as decohesion. From the fracture surface, it can be seen that the sample has thinned to smaller area prior to fracture than the T4P material. Additionally, using the same magnification as in the case of the T4P material, the dimples appear closely spaced over the entire fracture surface.

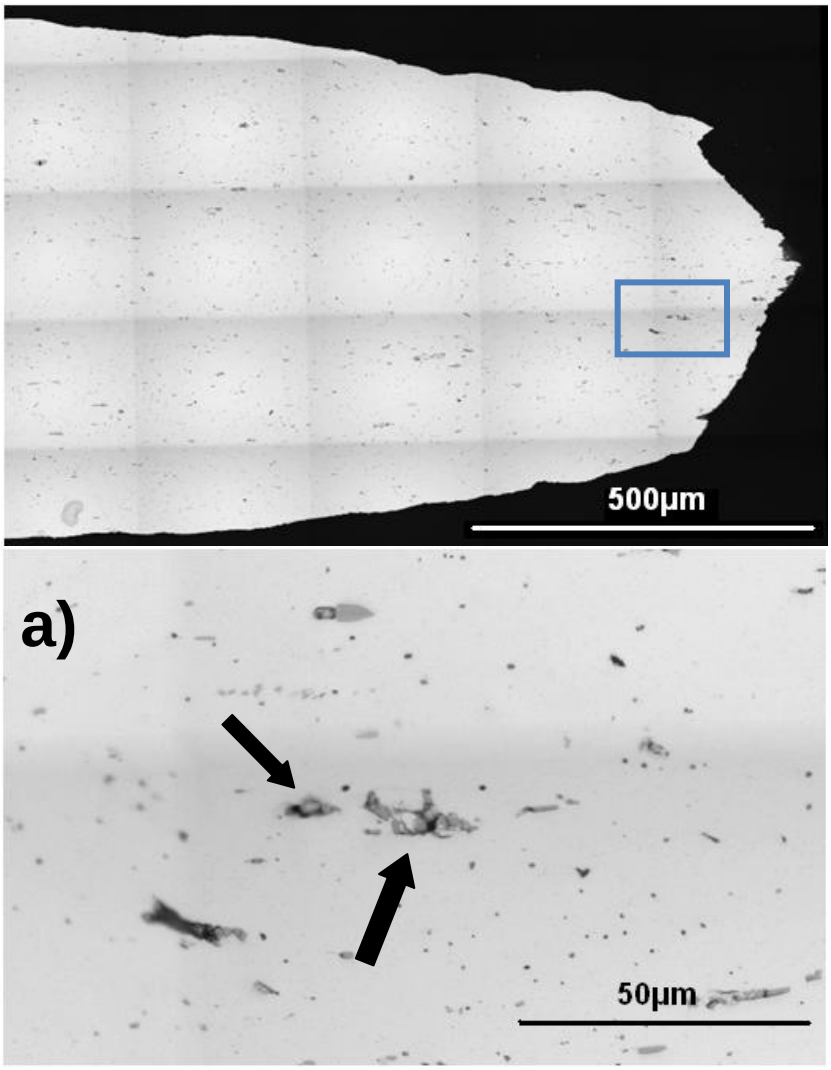

Figure 5.11: Through-thickness view of FG sheet tensile tested at room temperature at $5.0x10^{-4}s^{-1}$ a) overall image and b) insert view (images by Sooky Winkler).

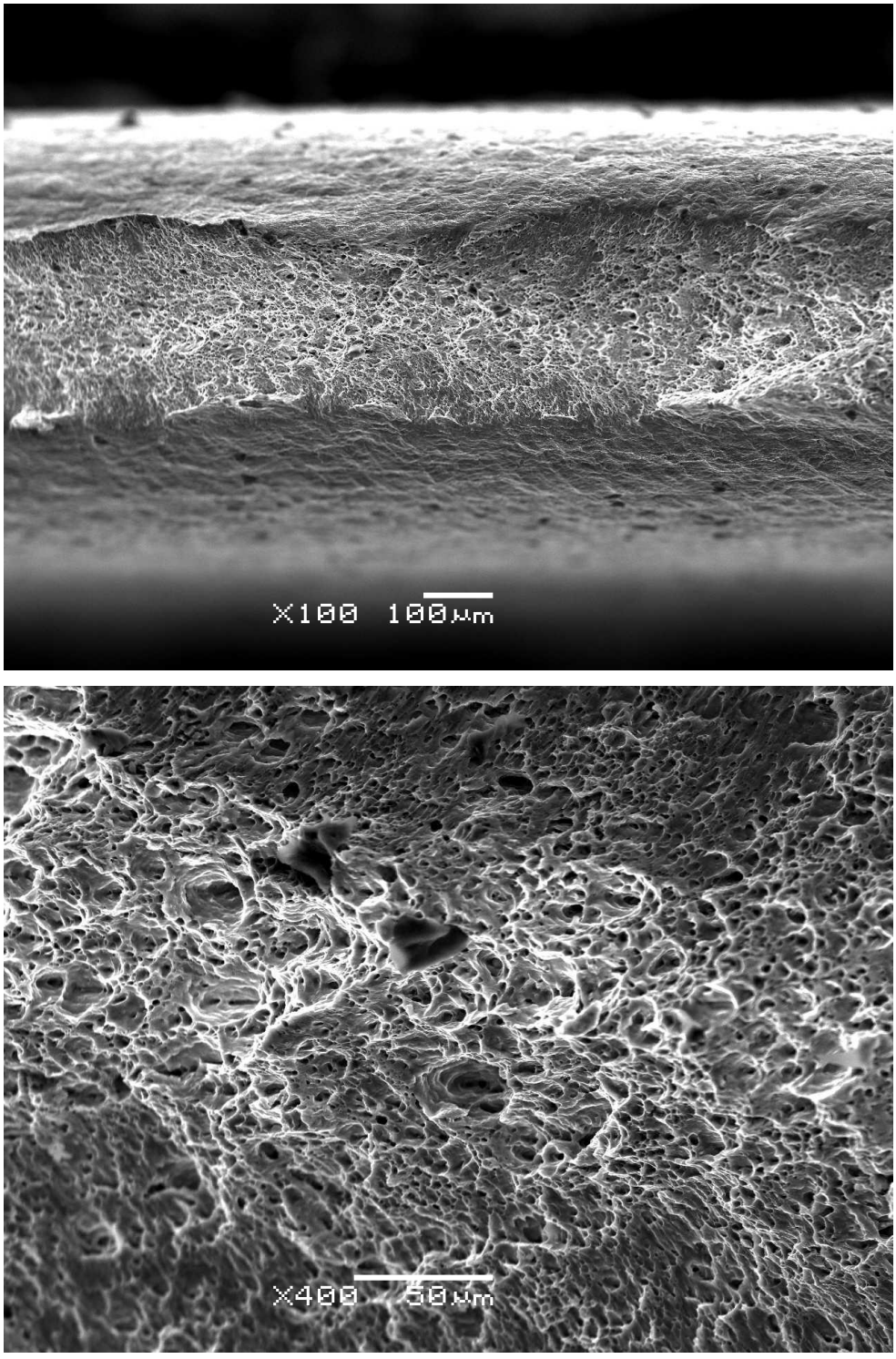

Figure 5.12: Fracture surface of FG sheet tensile tested at room temperature at $2.0x10^{-3}s^{-1}$(SE mode).

5.3 High Temperature Behaviour

In this section, the high temperature behaviour of the material is examined. First, the effect of high temperature on the microstructure is examined under static conditions. This is to determine the effect of temperature alone on the evolution of the microstructure, so that it may be taken into consideration when examining the properties under high temperature deformation. Finally, full investigations of the tensile properties, as well as the microstructural evolution during high temperature deformation are studied using tensile tests, stress relaxation tests and failure mechanism examination.

5.3.1 Static Microstructural Evolution

5.3.1.1 Average Grain Size

5.3.1.1.1 T4P Material

The average grain size of the statically-aged samples are summarized in Table 5.3. These results show no significant change in the grain diameter of the material due to exposure to high temperature.

Table 5.3: T4P average grain diameter after statically heating for 15 minutes.

Ageing Temperature (°C)	Grain Diameter (μm) Initial = 45.45μm
350	46.19
400	46.75
450	47.14
500	44.40
550	43.44

5.3.1.1.2 FG Material

The results of the EBSD measurements on a similarly processed FG samples aged at T≥400°C are shown in Figure 5.13.

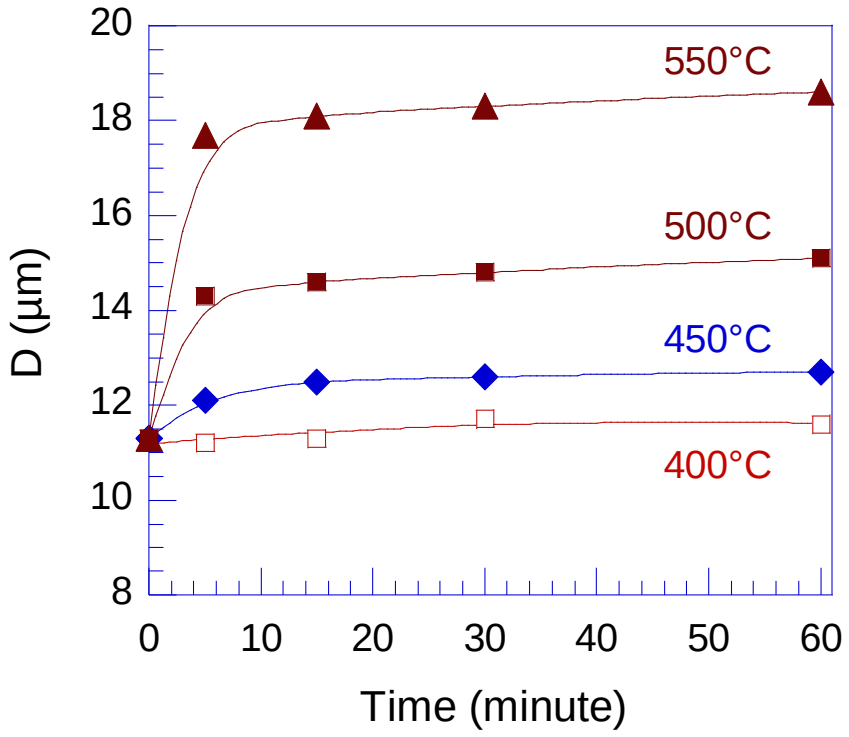

Figure 5.13: Grain size evolution of FG sheet after isothermal heating at various temperatures, measured using EBSD on planar surface cross-sections (measurements by Haiou Jin).

These results indicate that the grain sizes are stable during aging for one hour at 400°C. The grain size slightly increases during the first 5 minutes of ageing at 450°C and then remains stable up to 60 minutes. The increase in average grain size becomes more significant by increasing the temperature to 500°C and 550°C. At these temperatures, the grain size appears to grow rapidly in the first ~10 minutes, beyond which the grains grow at a much slower rate. The grain diameter reaches ~14µm and ~18µm when heat treatments at 500°C and 550°C, respectively, continue for 1 hour.

5.3.1.2 Precipitation state

5.3.1.2.1 T4P Material

Figure 5.14 shows the precipitate state of the T4P material after statically ageing for 2 hours at each temperature.

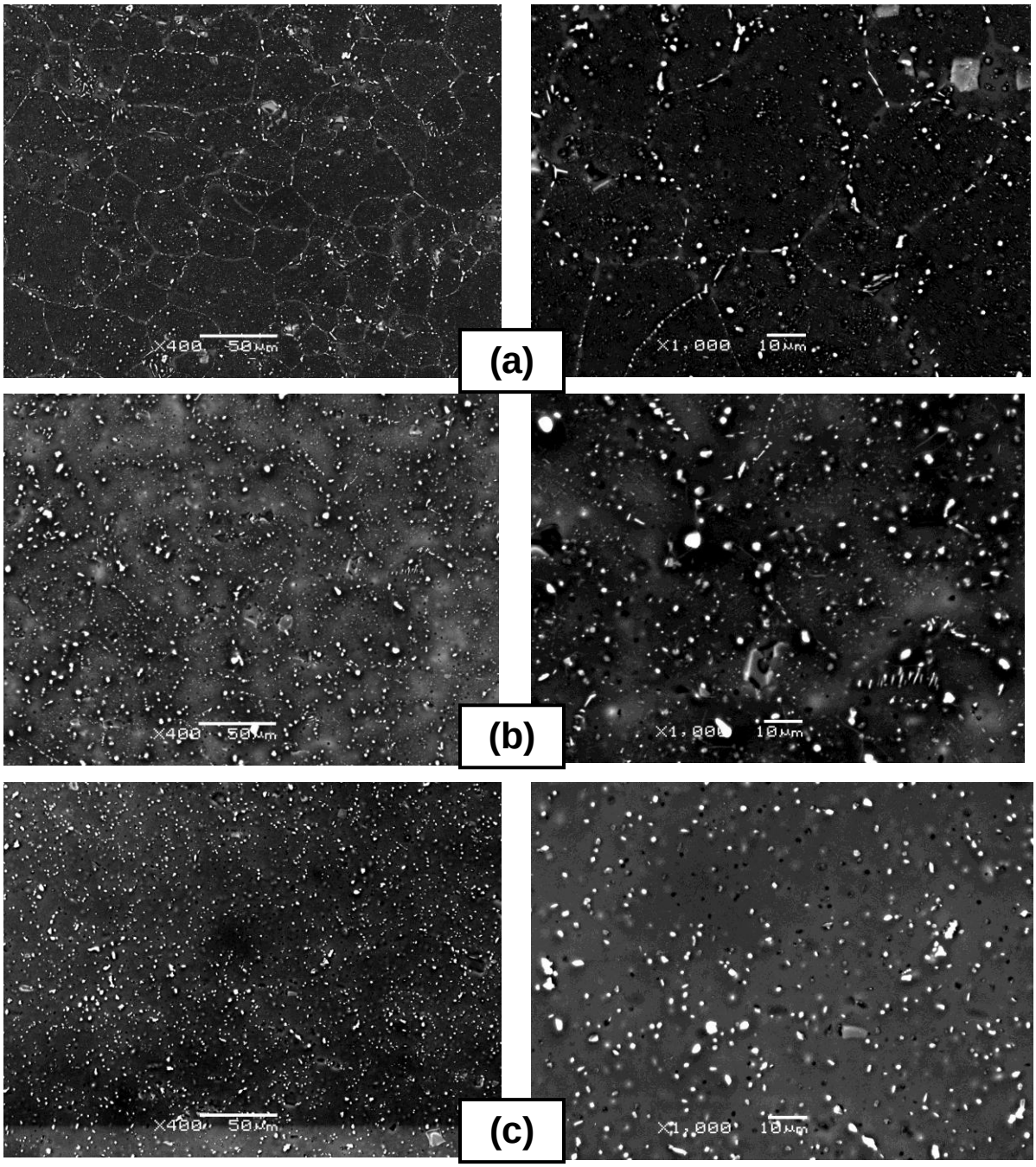
×400 50μm
×1,000 10μm
(a)
×400 50μm
×1,000 10μm
(b)
×400 50μm
×1,000 10μm
(c)

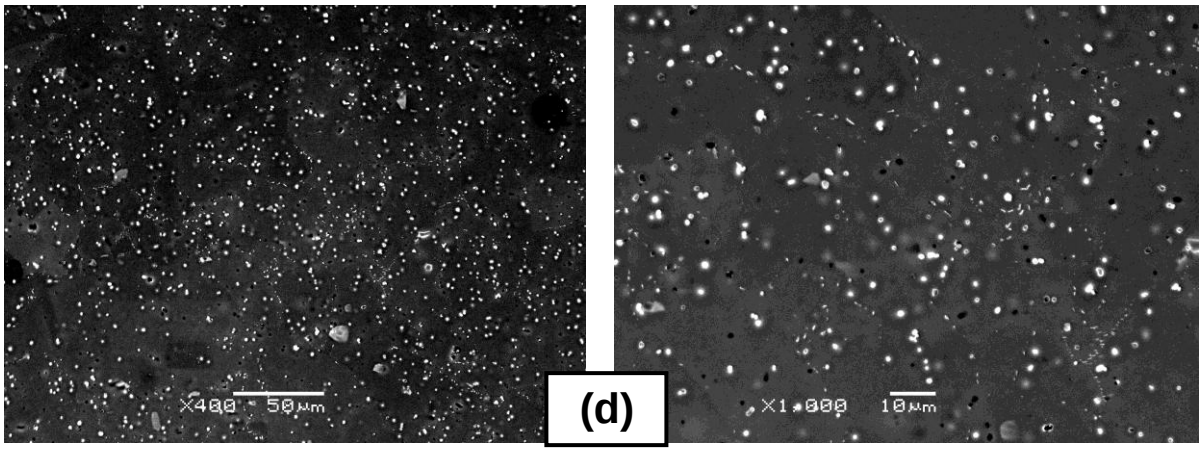

Figure 5.14: Precipitate structure of T4P sheet after ageing for 2h at (a) 350°C, (b) 400°C, (c) 450°C, (d) 500°C (SE mode).

After ageing for 2h at 350°C, large, blocky and elongated precipitates grow on the grain boundaries, which were not seen in the as-received material (Figure 5.2). The interior of the grains can be seen to contain smaller, more homogeneously distributed thin elongated precipitates (see Figure 5.15). The precipitates at grain boundaries and in grain interiors grow preferentially in certain directions (see Figure 5.16), however this relationship is not as clearly seen at lower temperatures, as the grain boundary precipiates appear more oblong shape. The EDS spectrums in Figure 5.15 show that the large blocky particles within the grains contain silicon and oxygen, while the large particles on the grain boundaries contain silicon, copper and oxygen. The oxygen content is due to the electropolishing procedure, and the removal of the magnesium. Areas immediately around the grain boundaries and grain boundary precipitates have fewer of the smaller precipitates (see Figure 5.15). As the ageing temperature increases to 400°C, the precipitates become coarser, especially the ones on the grain boundaries. The precipitates in the grain interiors also become larger and coarser, and the spacing between them increases. At 450°C, the elongated precipitates are not as prominent on the grain boundaries and in the grain interiors. At the same time, blocky and round shaped precipitates begin to dominate the microstructure. These new precipitates do not appear to preferentially grow on grain boundaries. At 500°C the grain boundary precipitates have significantly reduced, however, the blocky, and round precipitates in the material seem to have grown in size and number.

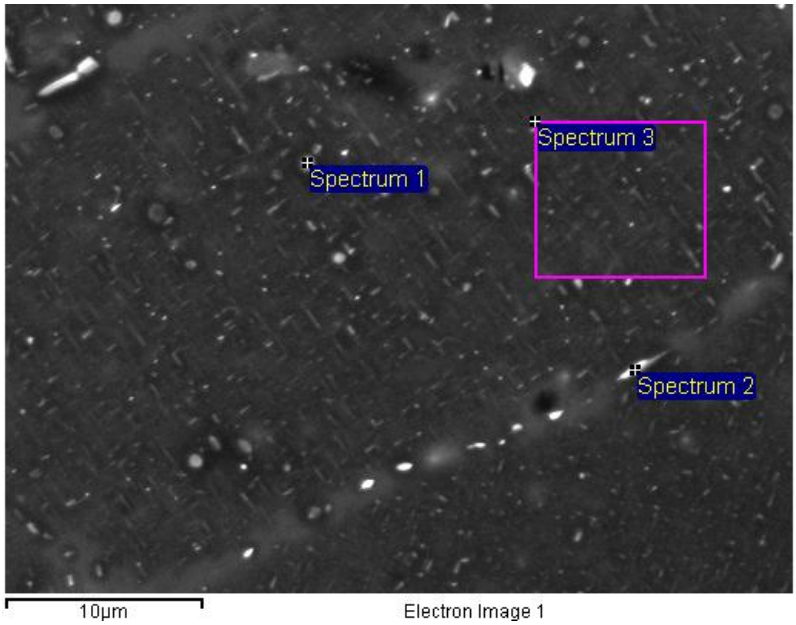

Average Composition (weight %)	Si	Cu	O	Al
Spectrum 1 (Blocky Particle)	3.19	0	9.99	Bal
Spectrum 2 (Particle on grain boundary)	2.71	7.19	7.03	Bal
Spectrum 3	0	0	0	100%

Figure 5.15: EDS analysed image of the T4P material precipitation state after ageing for 2 hours at 350°C (SE mode).

A high magnification of a T4P sample that had been aged for 2 hours at 450°C is shown in Figure 5.16. This figure highlights the various phases present in the material. The large particle could be a particle located below the surface of the sample or an artefact left by the electropolishing procedure.

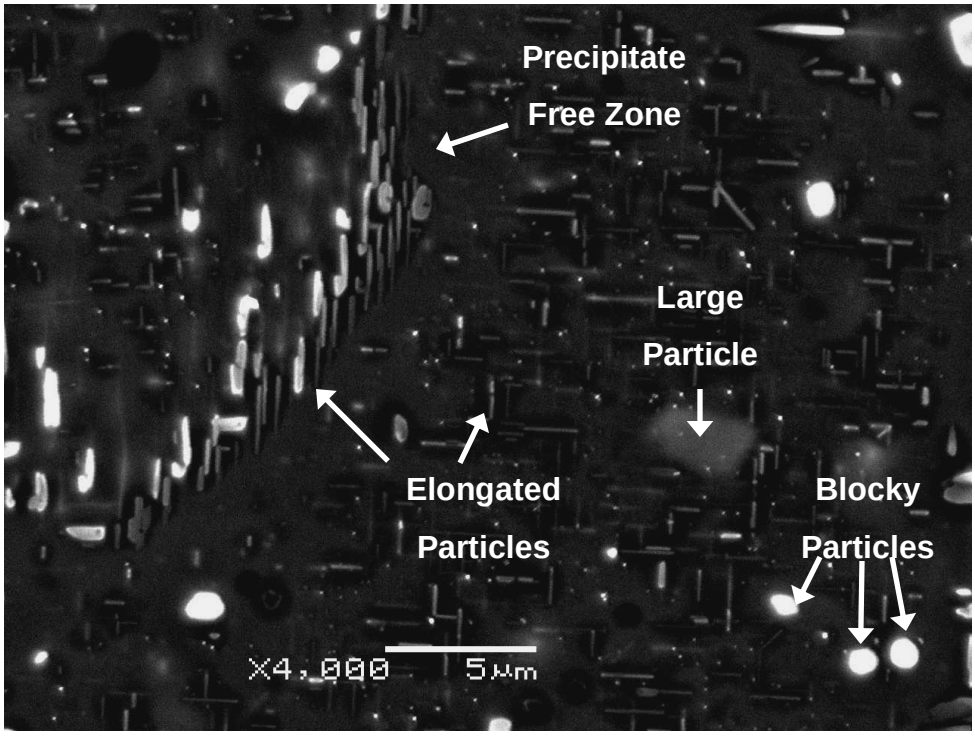

Figure 5.16: High magnification view of the T4P material after isothermal heating at 450°C for 2 hours.

5.3.1.2.2 FG Material

Figure 5.17 shows the precipitate structure of the FG material after ageing for 2 hours at each temperature.

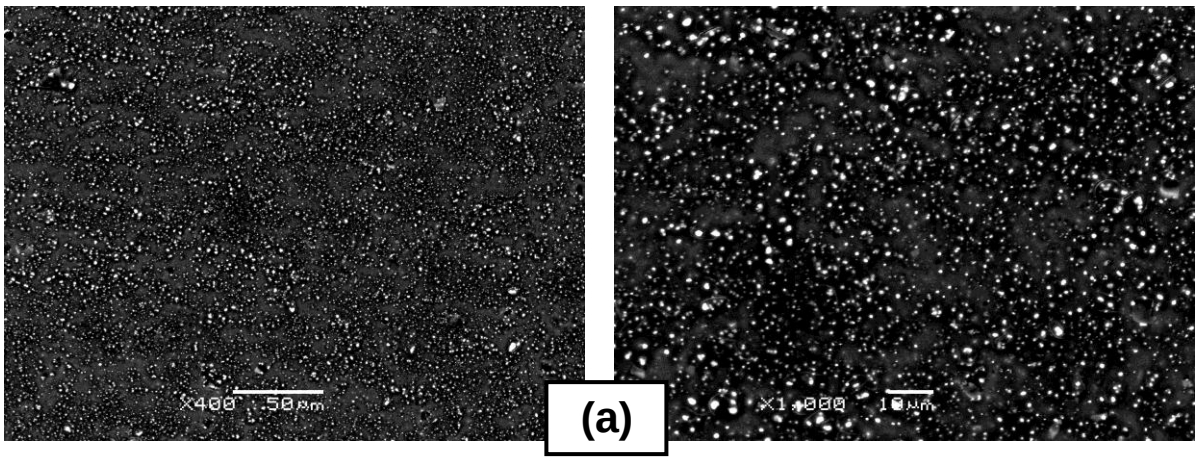

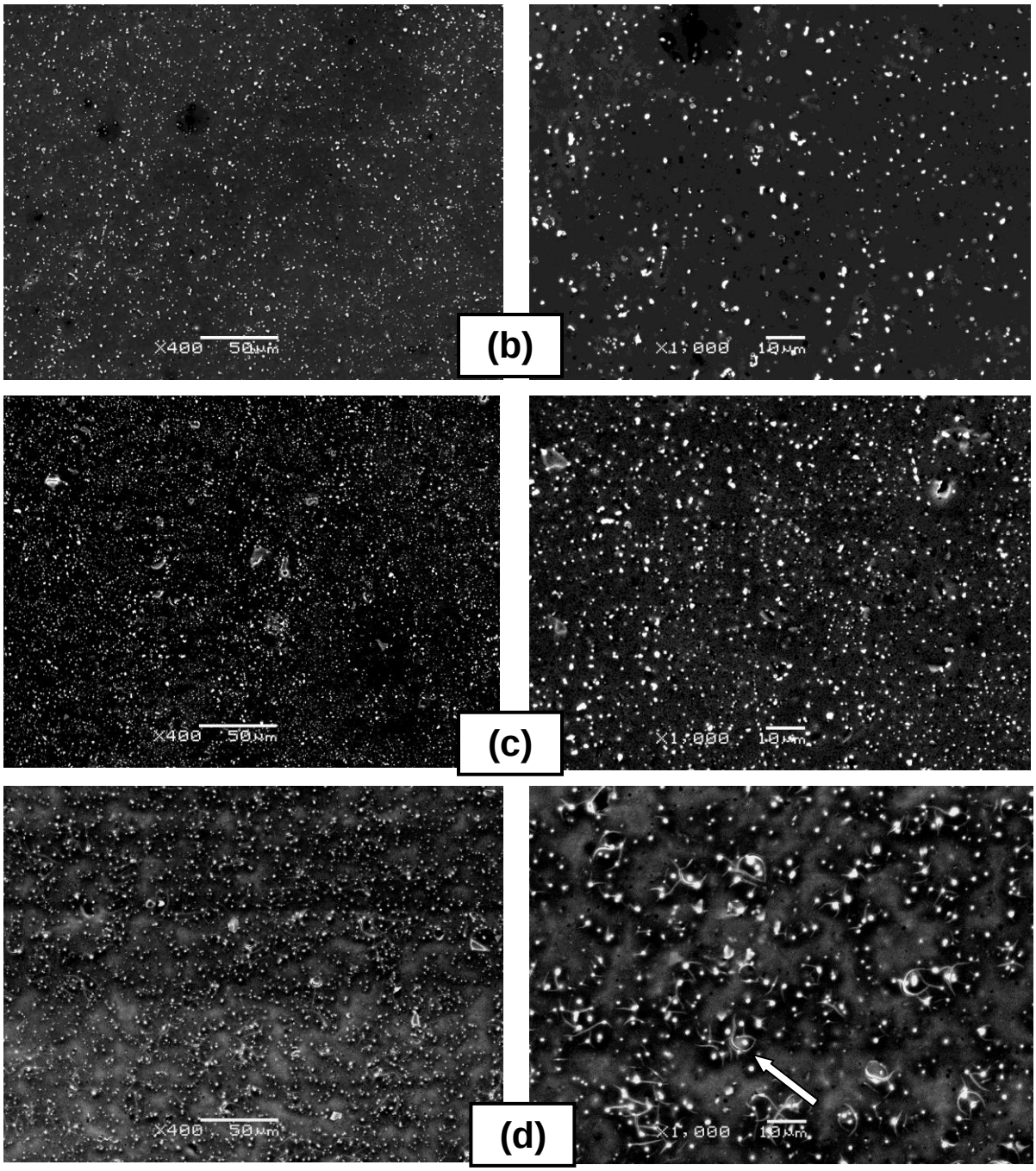

Figure 5.17: Precipitate structure of FG after ageing for 2h at (a) 350°C, (b) 400°C, (c) 450°C, (d) 500°C (SE mode).

At 350°C, the structure is very similar to the as-received material, i.e. a random distribution of round shaped precipitates. When the temperature is increased to 400°C, there is a sudden drop in the volume fraction of precipitates in the material. As the temperature is increased to 450°C, the precipitate population increases. Finally, at

500°C, the precipitate structure coarsens, leaving a distribution of larger precipitates. The fine white lines seen in the 500°C sample (highlighted by the arrow) may be chemically reacted β precipitates as reported by Wang et al. [120] in overaged AA6111 or other artefacts produced by the electropolishing process, and not part of the microstructure. A high magnification of a FG sample that had been aged for 2 hours at 450°C is shown in Figure 5.18. This figure highlights the various phases present in the material.

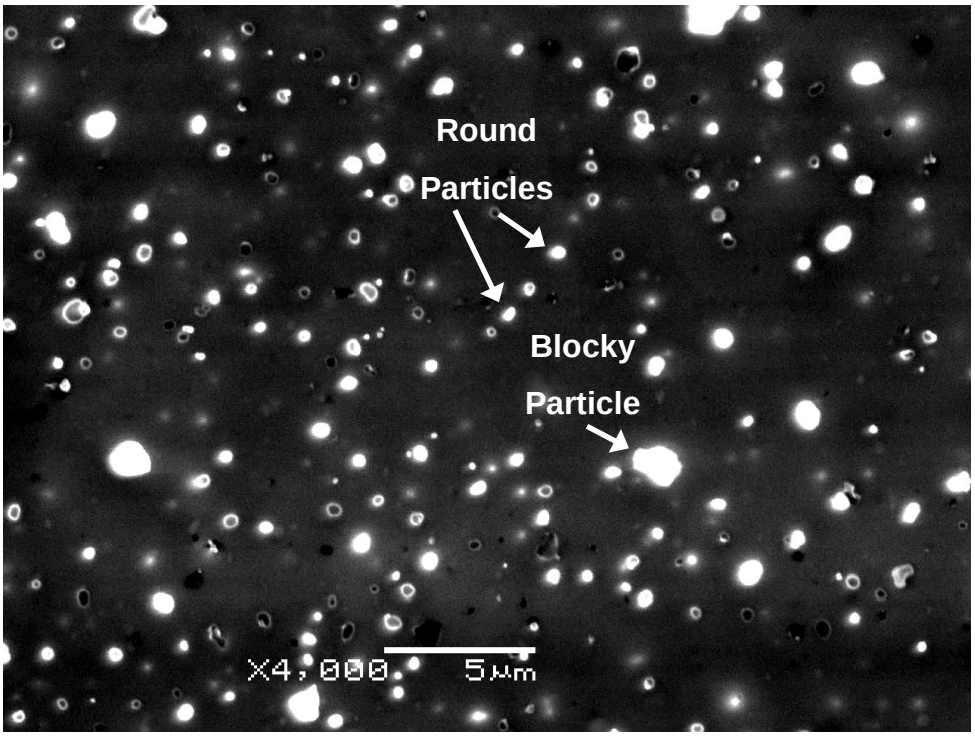

Figure 5.18: High magnification view of the FG material after isothermal heating at 450°C for 2 hours.

5.3.2 Mechanical Behaviour

Selected stress-strain curves are shown to highlight how these curves change with temperature and strain-rate. The stress-strain curves shown are typical of the other repetitions. The conditions selected to highlight are: 350°C-all strain-rates, 450°C-all strain-rates, 550°C-all strain-rates, $5.0 \times 10^{-4} s^{-1}$-all temperatures, $2.0 \times 10^{-2} s^{-1}$-all temperatures and $6.7 \times 10^{-1} s^{-1}$-all temperatures. Tensile test data from every test can be found in tabular form in the Appendix.

5.3.2.1 T4P Material

5.3.2.1.1 Strain-Rate Dependence

The stress-strain curves of samples tested at 350°C are summarized in Figure 5.19. This graph shows that the shape of the curves are very similar; a peak is reached followed by a steady decrease in flow stress in each case. The figure shows a steady increase in the peak stress of the sample by increasing the strain-rate. In each case, the peak stress is seen in less than 10% strain (a trend seen in all of the elevated temperature tests), and this strain decreases with increasing strain-rate.

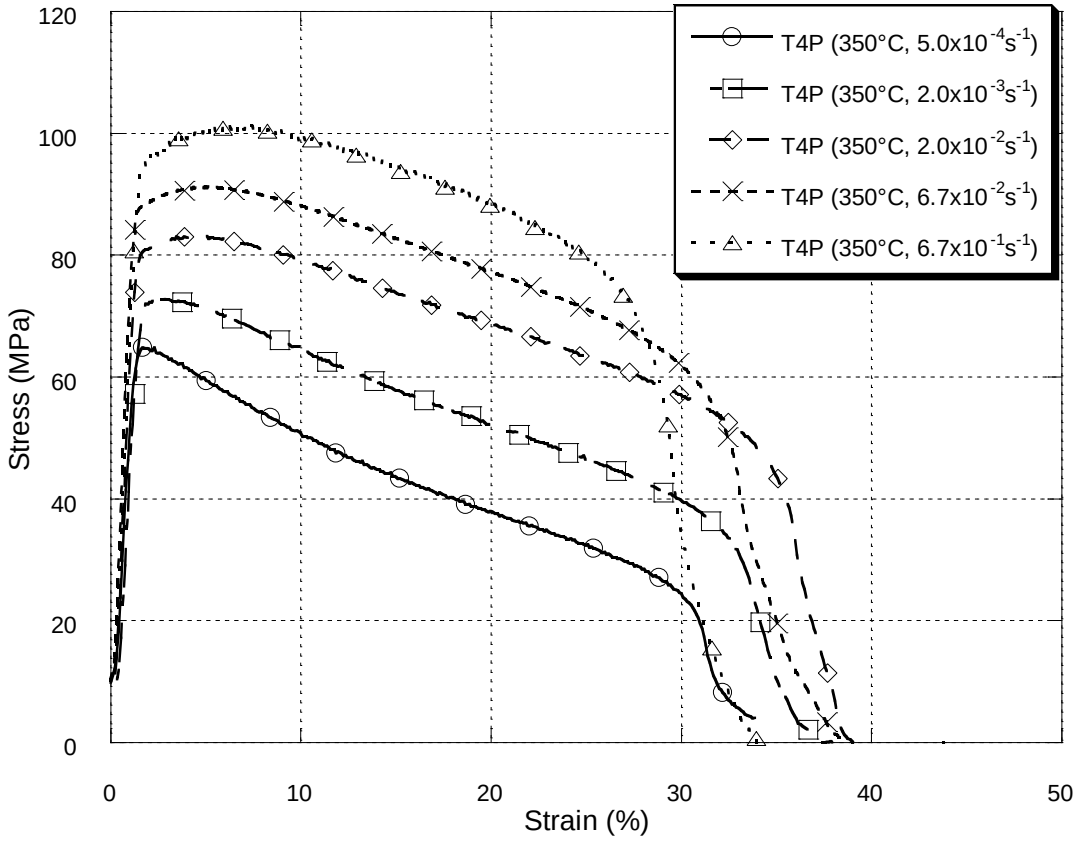

Figure 5.19: Stress-strain curves of T4P sheet tensile tested at 350°C.

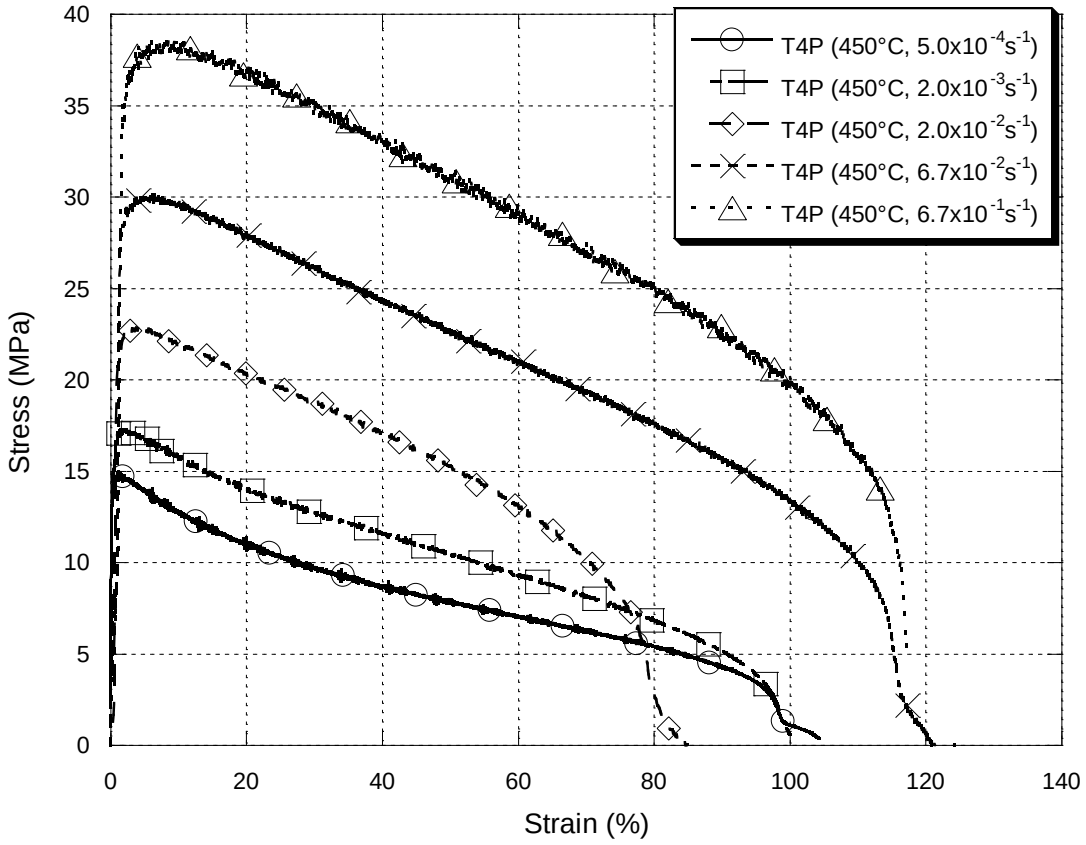

Figure 5.20: Stress-strain curves of T4P sheet tensile tested at 450°C.

At higher temperatures, as seen in Figure 5.20, increasing strain-rates show larger increases in the peak stress than is seen at 350°C . At even higher temperatures, such as those seen in Figure 5.21, the rate of decrease of the flow stress changes with varying strain-rates. At the lowest strain-rates, the drop in flow stress with increasing strain is not as pronounced as the higher strain-rates. This is particularly prevalent at 550°C and $5.0x10^{-4}s^{-1}$ beyond 100% strain where the flow stress does not decrease significantly until failure.

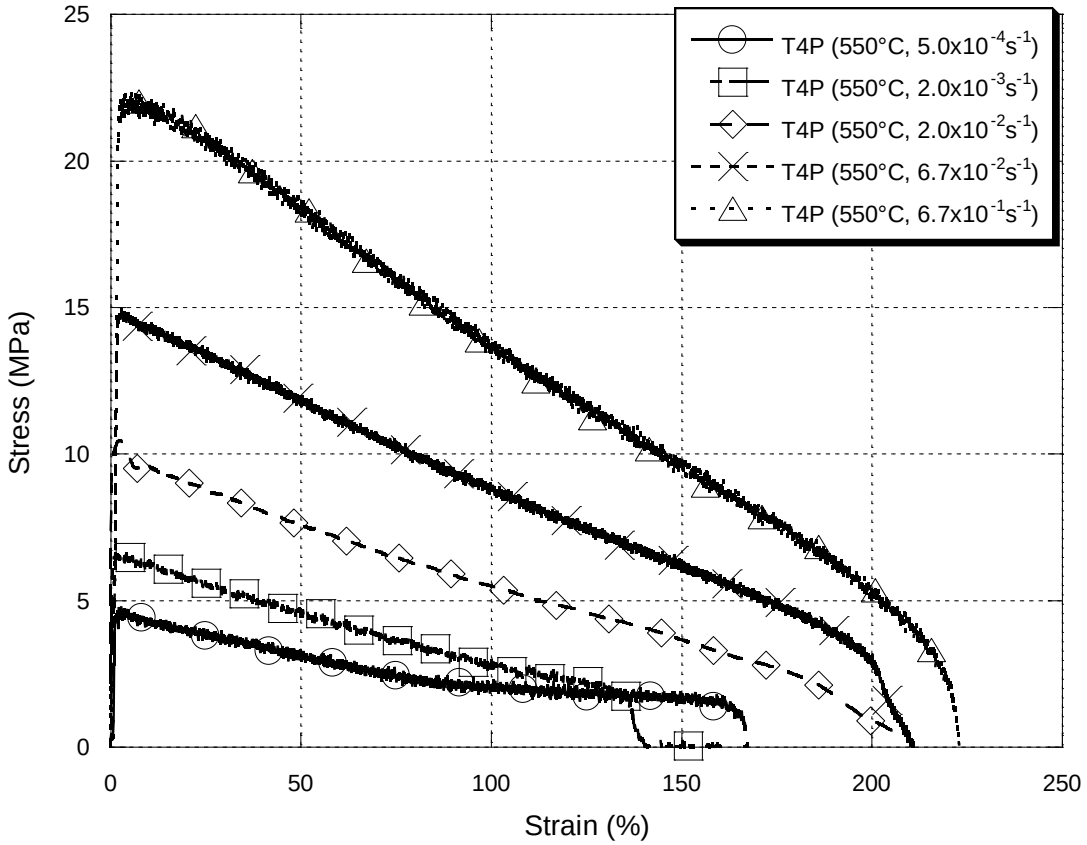

Figure 5.21: Stress-strain curves of T4P sheet tensile tested at 550°C.

5.3.2.1.2 Temperature Dependence

Figure 5.22, Figure 5.23 and Figure 5.24 show the variation of the stress-strain curves with temperature at strain-rates of $5.0x10^{-4}s^{-1}$, $2.0x10^{-2}s^{-1}$ and $6.7x10^{-1}s^{-1}$, respectively. These curves highlight how the rate of decrease of flow stress of the stress-strain curves change with varying temperature. At the lower temperatures, a high peak stress is reached, followed by a significant decrease in the stress, and then failure. At high temperatures, the peak stress is much lower, and the flow stress does not decrease as appreciably. Of interest to note is the relative values of the peak stress at the lower temperatures to those at the higher temperatures. At the lowest strain-rate, $5.0x10^{-4}s^{-1}$, the difference in peak stress between 350°C and 400°C is similar to the difference in peak stress between 400°C and 450°C. As the strain-rate is increased however, the peak stress decrease between 350°C and 400°C becomes much smaller than the decrease between 400°C and 450°C. The relative peak stress differences between the higher temperatures remains similar across all strain-rates. These graphs show that in each case, the strain to peak stress decreases with increasing temperature.

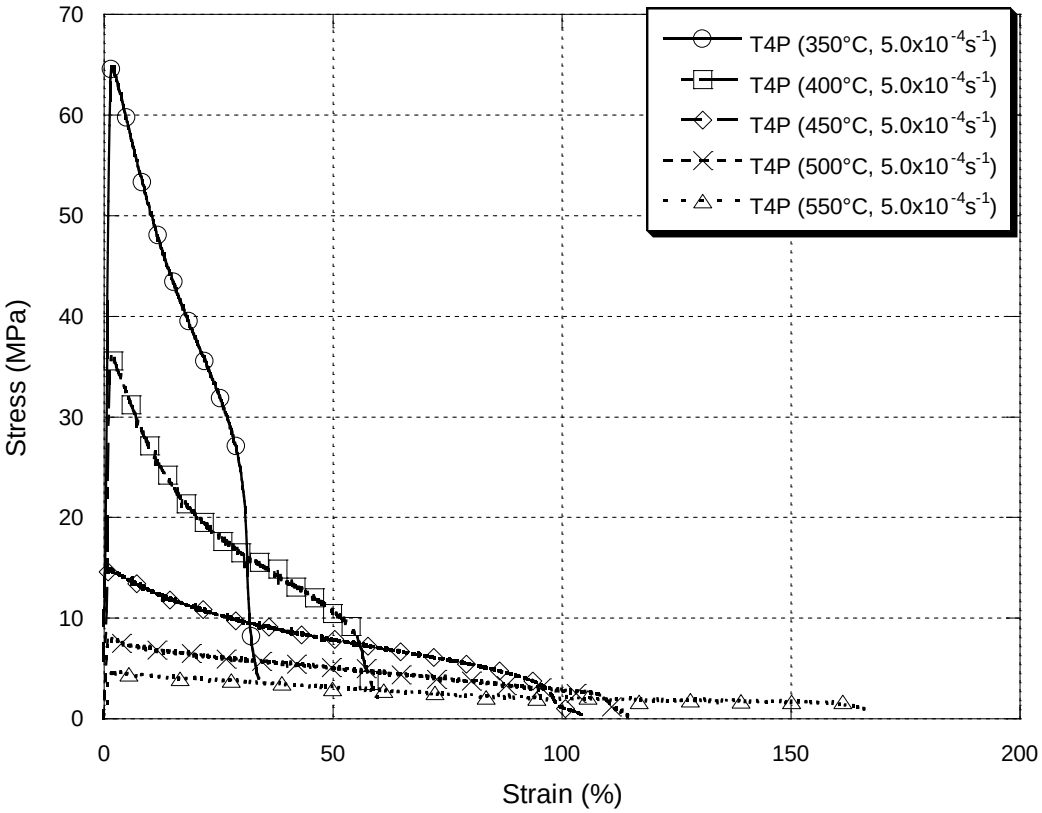

Figure 5.22: Stress-strain curves of T4P sheet tensile tested at $5.0x10^{-4}s^{-1}$.

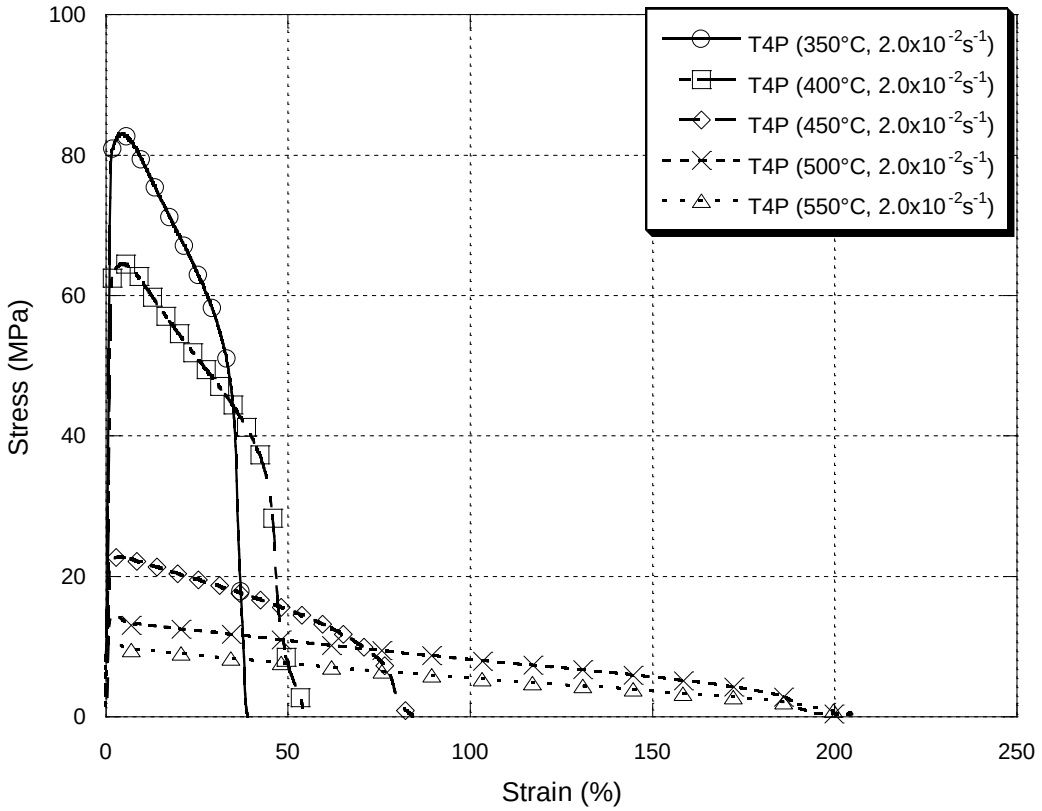

Figure 5.23: Stress-strain curves of T4P sheet tensile tested at $2.0x10^{-2}s^{-1}$.

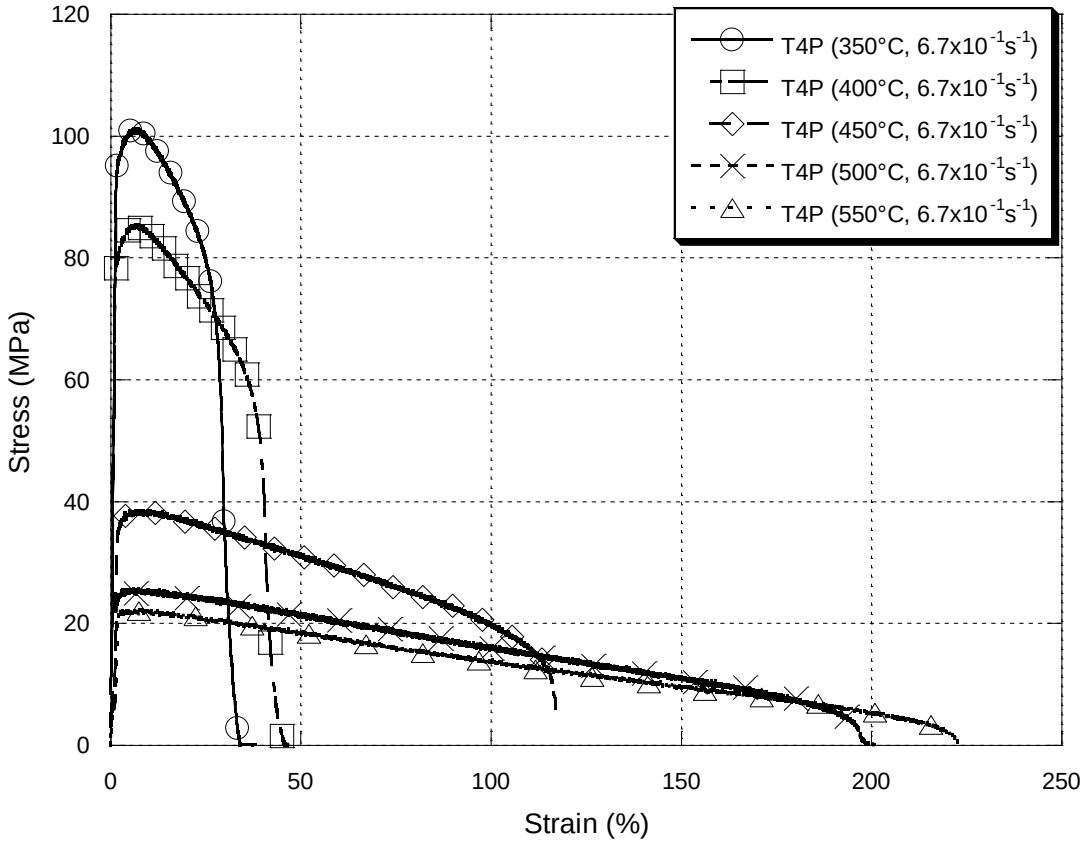

Figure 5.24: Stress-strain curves of T4P sheet tensile tested at $6.7x10^{-1}s^{-1}$.

5.3.2.1.3 Stress relaxation

The measured load vs. time plots for the T4P material at each temperature are shown in Figure 5.25. Shown in this plot are the first 10 seconds of data after beginning relaxation. Beyond this point, the load does not significantly decrease with increasing time. In each test, the load decreases rapidly after relaxation begins. The decrease in load between the lower temperature plots, e.g. 350°C to 400°C. is much larger than the difference between the high temperature plots, eg 500°C to 550°C, a trend similar to that seen in the stress-strain data.

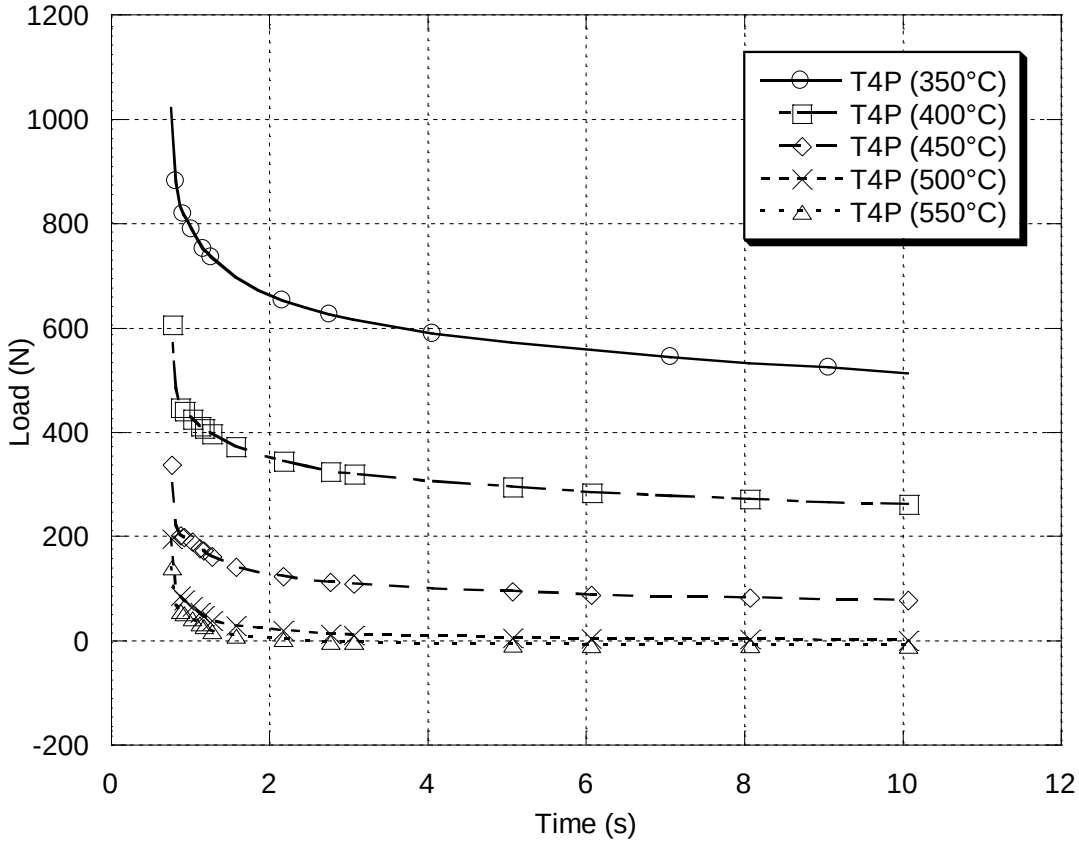

Figure 5.25: Load vs. Time plots for the T4P material at various temperatures.

5.3.2.1.4 Elongation to Failure and Peak Flow Stress

The elongation to failure of the T4P material in each condition is summarized in Figure 5.26. The results show that at lower temperatures, 350°C and 400°C, the strain-rate has little effect on the elongation to failure. Samples fail at approximately 35% and 50%, respectively, regardless of the strain-rate. At 450°C however, material begins to be affected by the strain-rate. At this temperature, the lowest strain-rate achieves an elongation of ~100%, while at the highest strain-rate, the elongation is ~125%. At the two highest temperatures, the strain-rate has an even more pronounced effect. An increase of almost 100% total elongation to failure going from the lowest to the highest strain-rate was found. The maximum average elongation to failure was seen at 550°C at a strain-rate of $6.7x10^{-1}s^{-1}$ with ~225%.

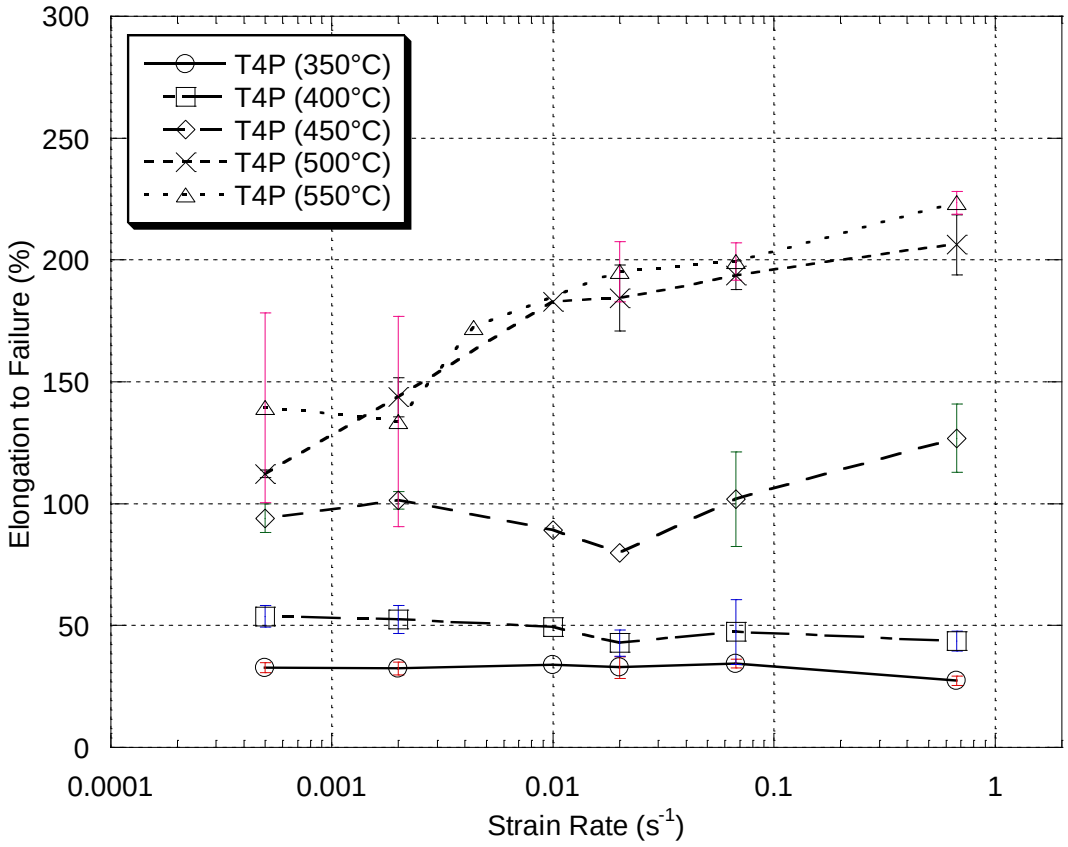

Figure 5.26: Elongation to failure of T4P sheet tensile tested at elevated temperatures.

Figure 5.27 summarizes the peak flow stress vs. strain-rate for various temperatures and shows that as the strain-rate increases, so does the peak stress. The slope of the plots for the three highest temperatures are very similar, and the peak stresses are very close to each other, with the lowest peak stress, 5.4MPa, seen at the highest temperature (550°C) and the lowest strain-rate, $5.0 \times 10^{-4} s^{-1}$. At the two lowest temperatures, the earlier reported trend of a large difference in peak stress at the lowest strain-rate, and a smaller difference in peak flow stress at higher strain-rates is clearly illustrated. The highest peak flow stress was 95.6MPa, found at 350°C and $6.7 \times 10^{-1} s^{-1}$.

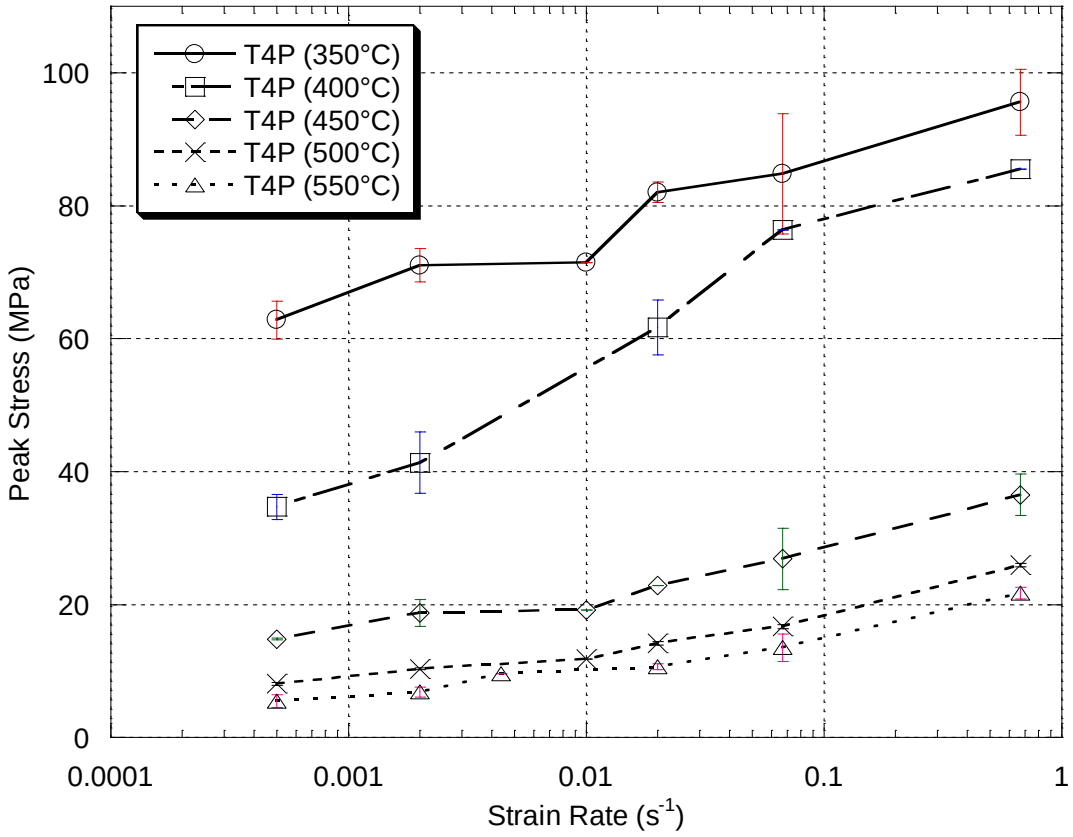

Figure 5.27: Peak flow stress of T4P sheet tensile tested at elevated temperatures.

5.3.2.2 FG Material

5.3.2.2.1 Strain-Rate Dependence

The stress-strain behaviour of the FG material at 350°C, 450°C and 550°C and various strain-rates are shown in Figure 5.28, Figure 5.29 and Figure 5.30, respectively. At each temperature, it can be seen that increasing the strain-rate leads to an increase in the flow stress. The flow stress in each case reaches a peak value early (less than 20% strain), and then steadily decreases until failure, however at the higher strain-rates, the decrease in flow stress is more rapid, as indicated by the slope of the stress-strain curve. At each temperature, the strain required to reach the peak stress increases with increasing strain-rates, however this effect is most pronounced at the highest temperature.

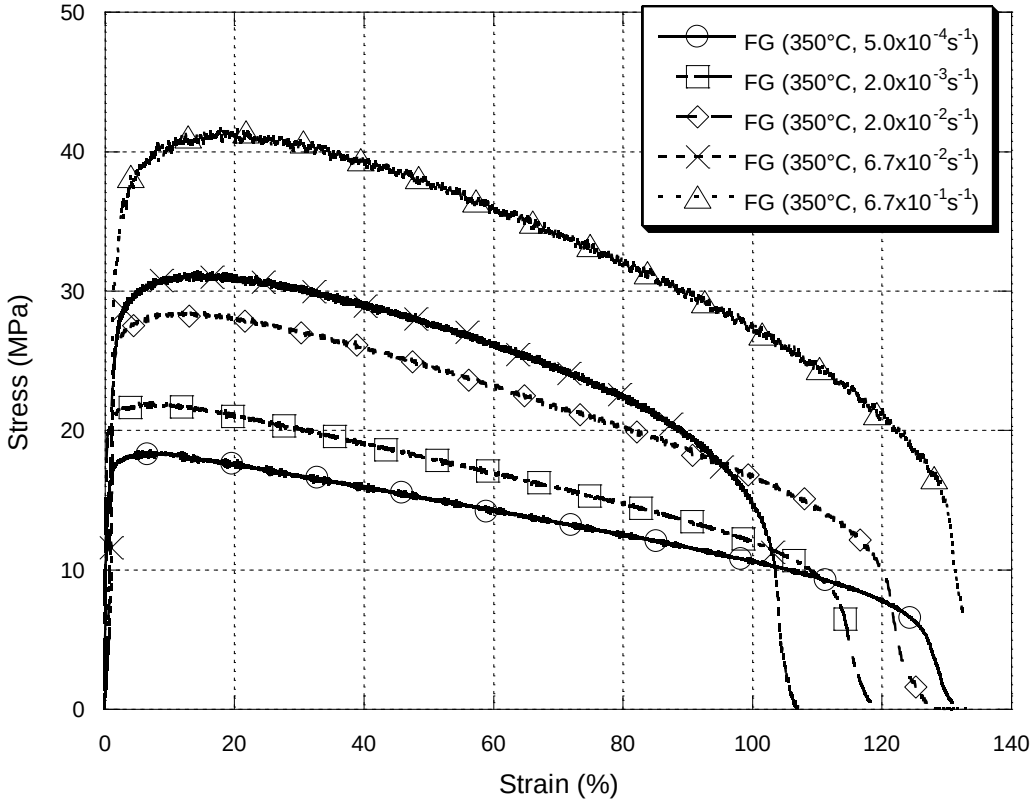

Figure 5.28: Stress-strain curves for FG sheet tensile tested at 350°C.

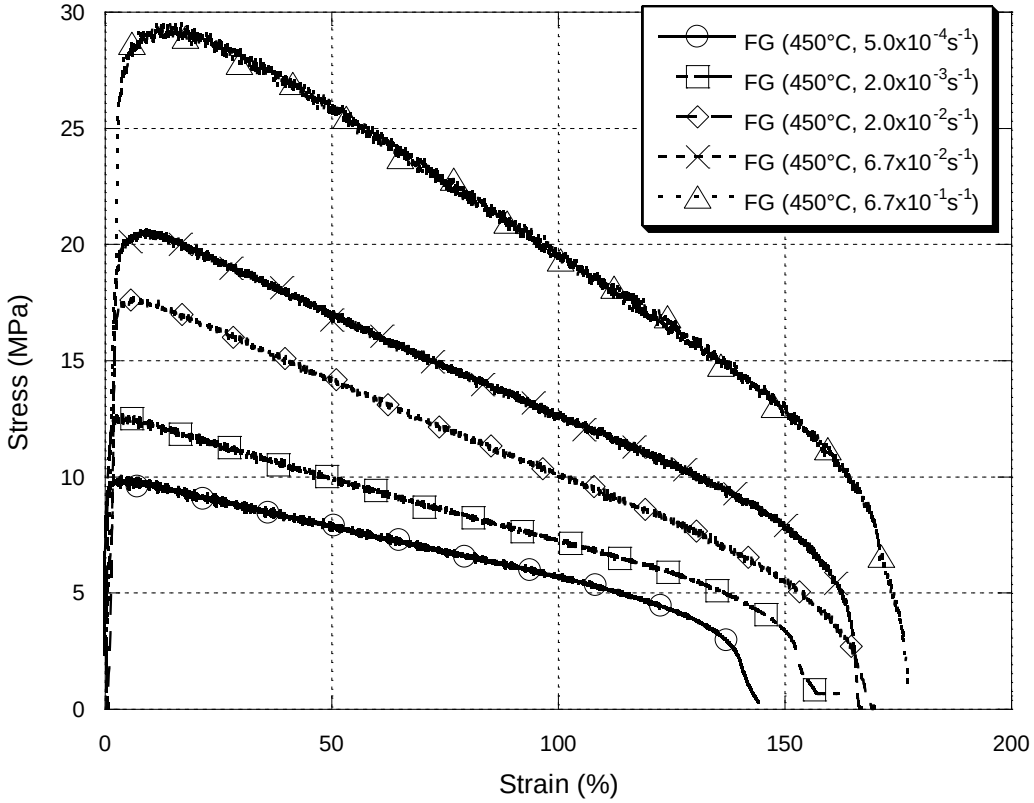

Figure 5.29: Stress-strain curves for FG sheet tensile tested at 450°C.

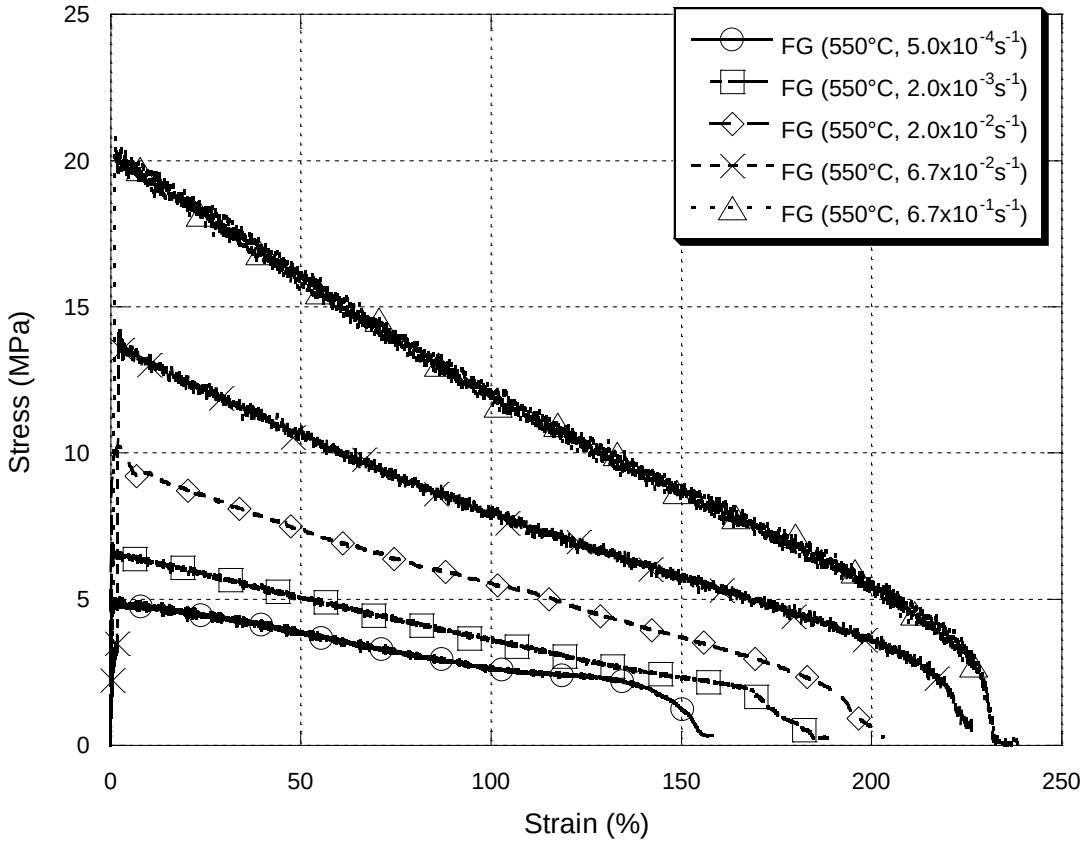

Figure 5.30: Stress-strain curves for FG sheet tensile tested at 550°C.

5.3.2.2.2 Temperature Dependence

Figure 5.31, Figure 5.32 and Figure 5.33 show the effect of temperature on the stress-strain curves at a constant strain-rate. At the lowest strain-rate, $5.0x10^{-4}s^{-1}$, the difference in peak stress is greatest at the lower temperatures, while at higher strain-rates, the difference in peak stress at each temperature jump is very similar. At the lowest strain-rate, and highest temperature, 550°C, the slope of the stress-strain changes after approximately 100% elongation; the flow stress decreases at a much lower rate, and continues in this manner until failure. The curves shows that the strain required to reach the peak stress decreases with increasing temperature. The small fluctuation seen at the start of the 500°C curve in Figure 5.32 is likely due to a small slip of the sample in the grip, causing the error in the measured value of the stress seen.

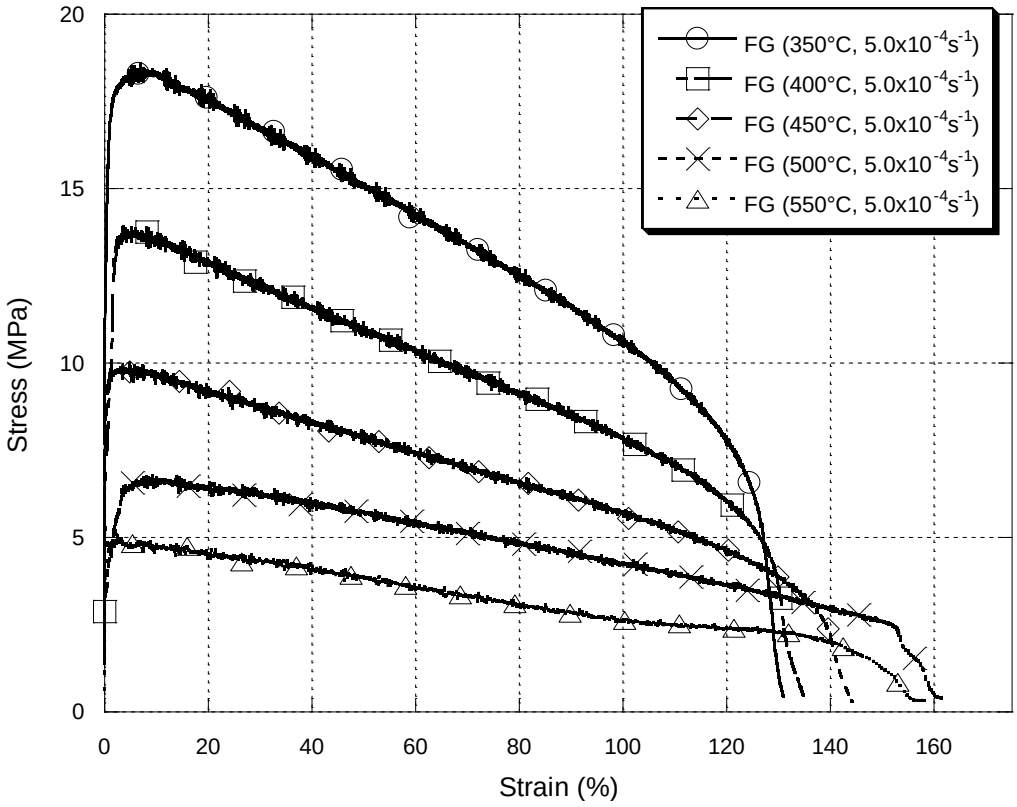

Figure 5.31: Stress-strain curves for FG sheet tensile tested at $5.0x10^{-4}s^{-1}$.

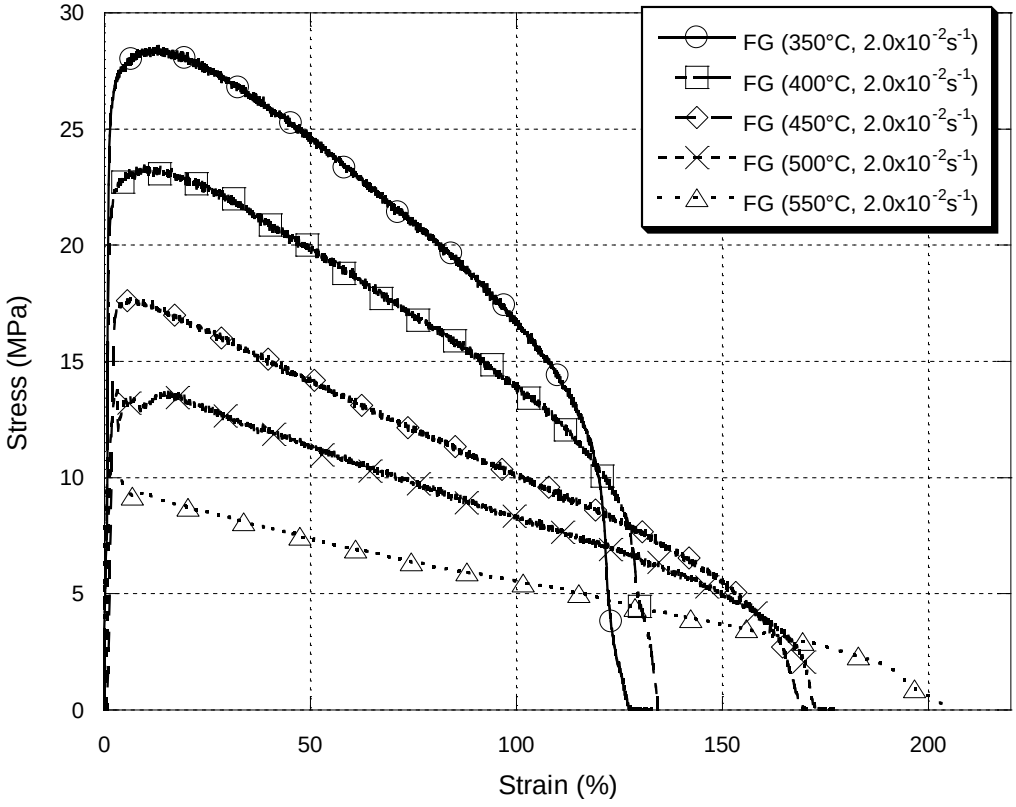

Figure 5.32: Stress-strain curves for FG sheet tensile tested at $2.0x10^{-2}s^{-1}$.

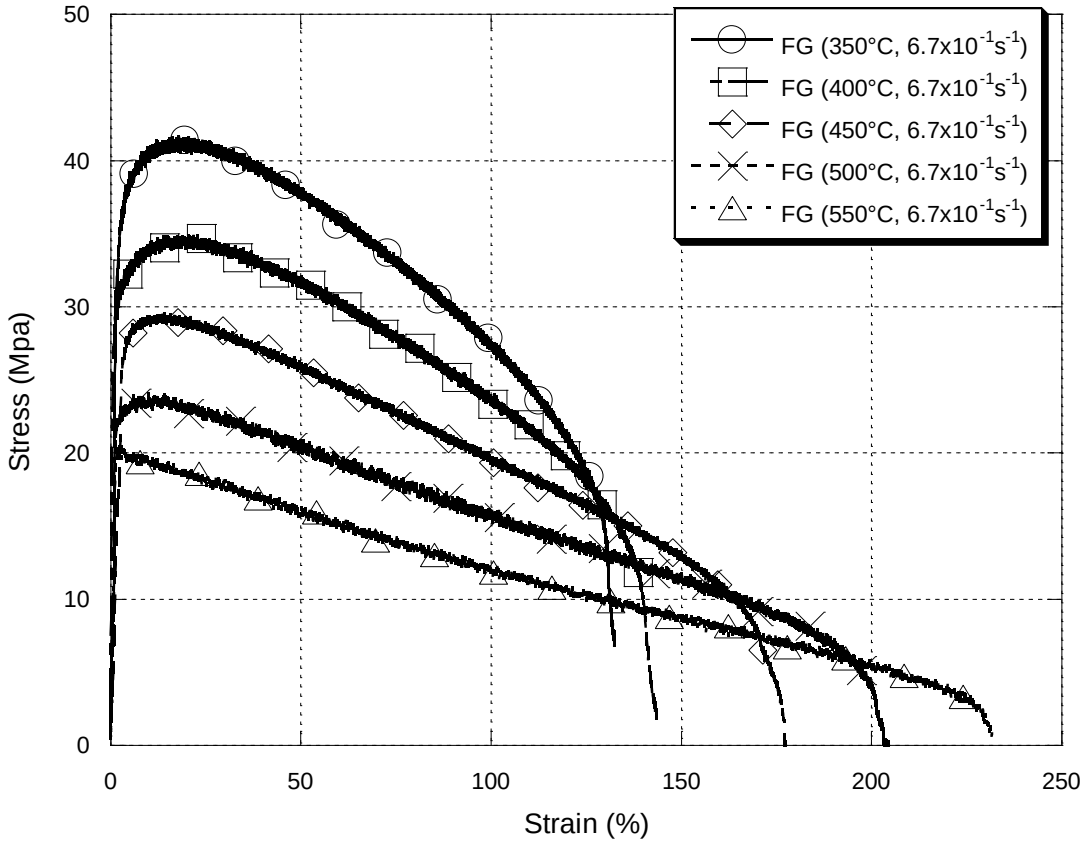

Figure 5.33: Stress-strain curves for FG sheet tensile tested at $6.7x10^{-1}s^{-1}$.

5.3.2.2.3 Stress relaxation

The load vs. time plots for the FG material are shown in Figure 5.34. There is a slight trend toward a larger difference between the load curves at lower temperatures (e.g. 350°C and 400°C) than at higher temperatures (e.g. 500°C and 550°C). In each instance, there is a rapid decrease in load within the first two seconds of relaxation. This is followed by a slower decrease in load, and eventually a point is reached where the load does not decrease appreciably. The plateau is reached by approximately 5 seconds in the test conducted at 550°C, while the plateau for the test conducted at 350°C is only reached beyond 15 seconds. The load relaxation tests mirror the results of the tensile tests well; there is a slight trend towards a larger difference in the load values at low temperatures than there are at high temperatures. The minor compressive load seen at high temperatures is likely caused by a minor expansion in machine components caused by exposure to the elevated temperatures.

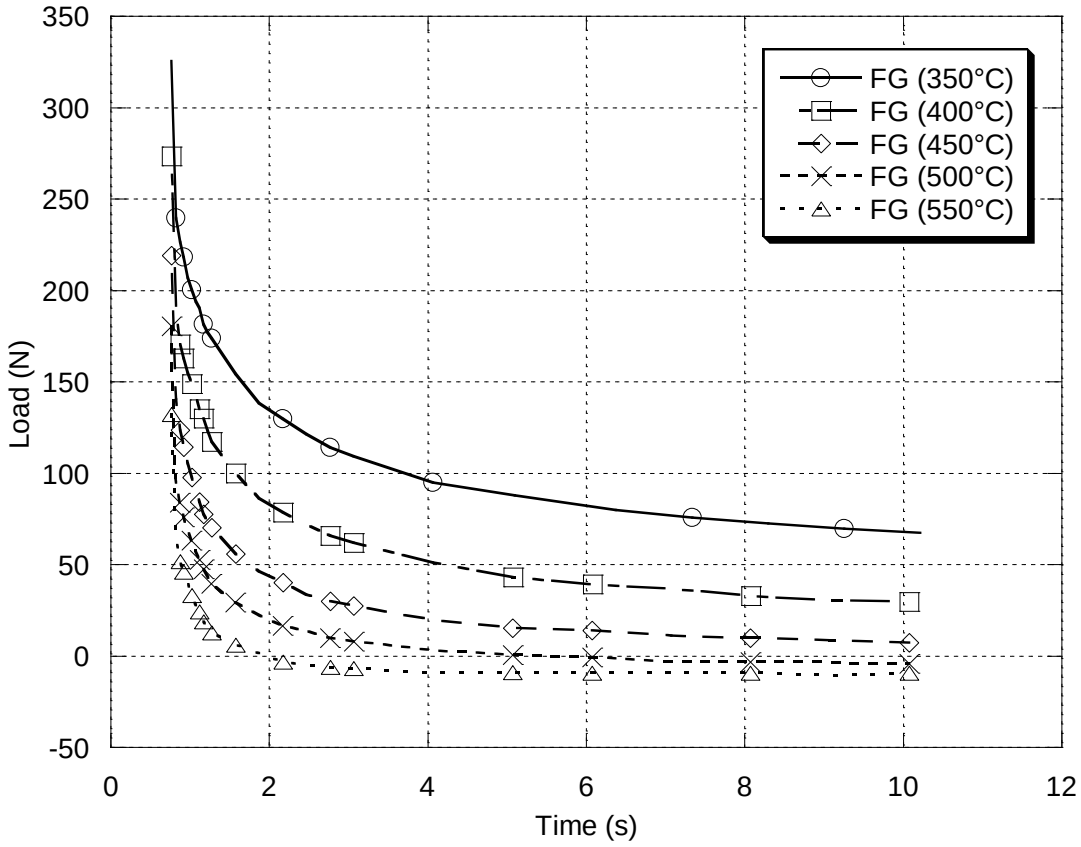

Figure 5.34: Load vs. Time curves for FG material at various temperatures.

5.3.2.2.4 Elongation to Failure and Peak Flow Stress

Figure 5.35 summarizes the total percent elongation to failure of the FG material at each temperature and strain-rate. At 350°C and 400°C, increased strain-rate does not lead to an appreciable change in the total elongation. The elongations seen at these temperatures are ~125%. At the 3 highest temperatures the FG material trends towards increasing elongation with increasing strain-rate, however, beyond a strain-rate of $2.0x10^{-2}s^{-1}$, the elongation to failure does not further increase. The maximum average elongation to failure seen in this material is ~220% at 550°C and a strain-rate of $2.0x10^{-2}s^{-1}$.

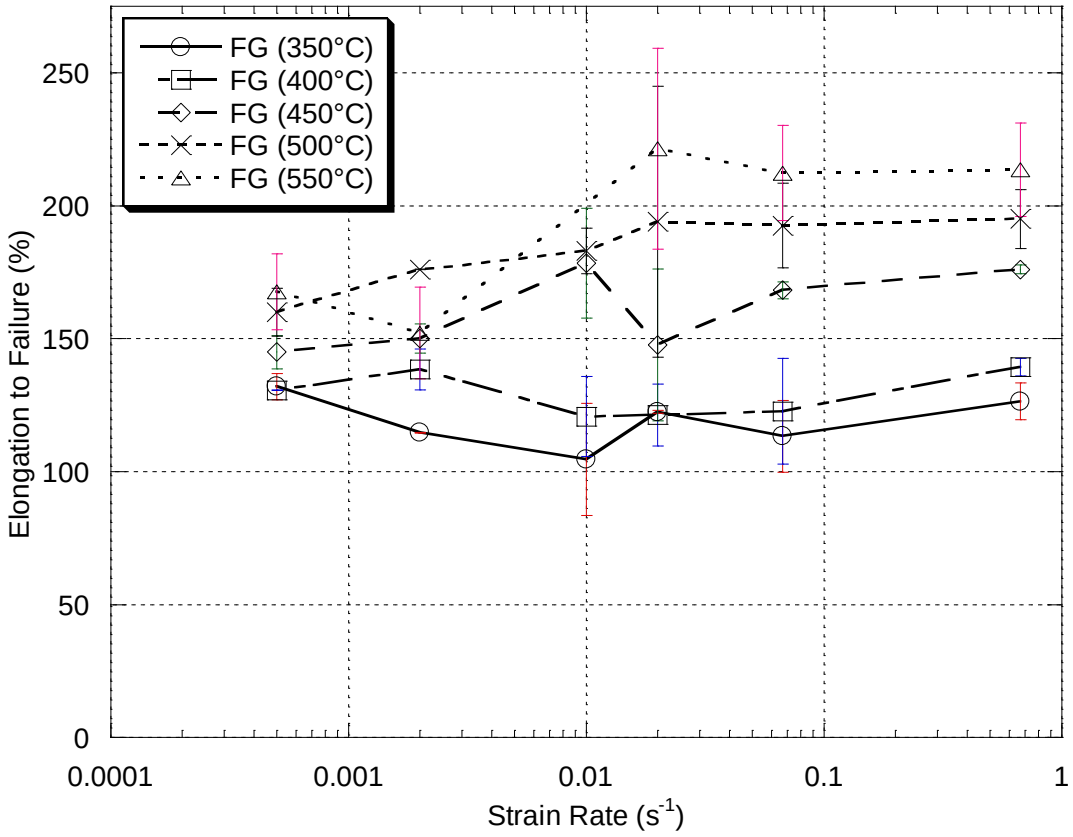

Figure 5.35: Elongation to failure of FG sheet tensile tested at elevated temperatures.

The peak flow stresses as a function of strain-rate for the tensile tested FG material are summarized in Figure 5.36. Here, the slopes of the peak stress vs. strain-rate curves at each temperature are almost identical, and there are no large increases in stress with decreasing temperature such as those seen in the T4P material. The highest peak flow stress, 41.1MPa, was seen at 350°C and a strain-rate of $6.7x10^{-1}s^{-1}$. The lowest peak flow stress was seen at 550°C, and a strain-rate of $5.0x10^{-4}s^{-1}$.

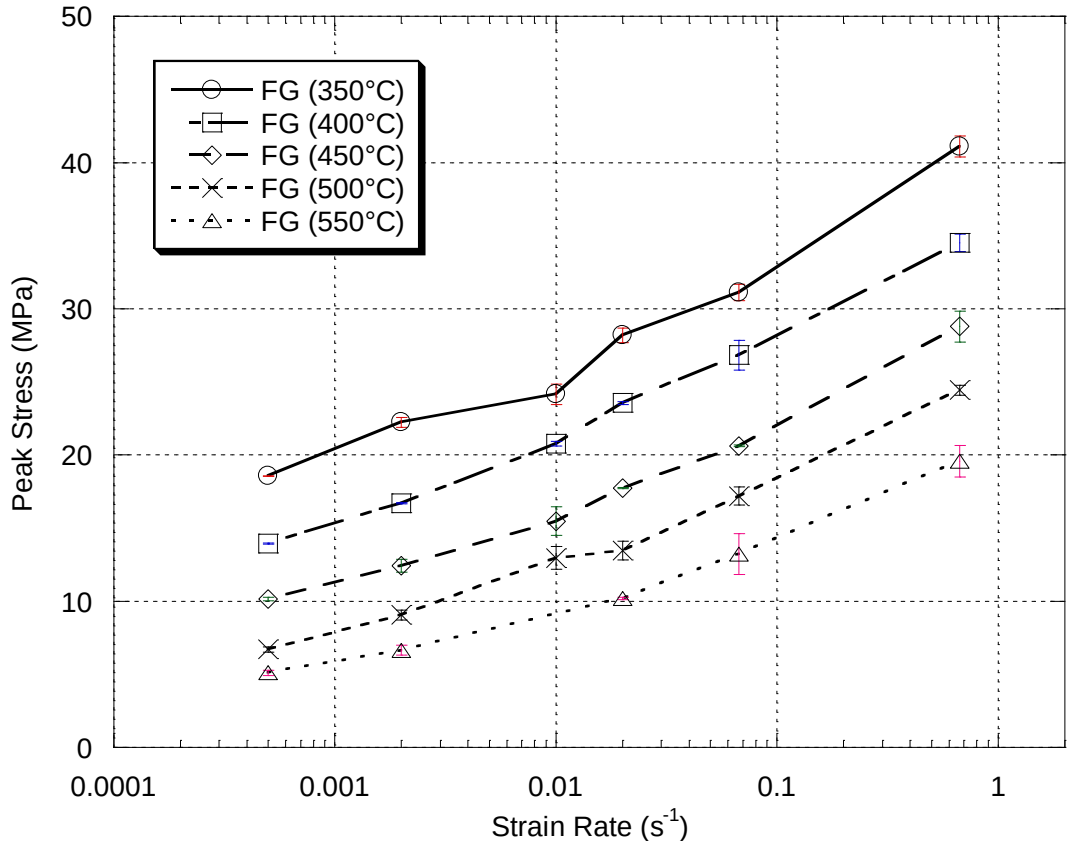

Figure 5.36: Peak flow stress of FG sheet tensile tested at elevated temperatures.

5.3.2.3 Material Comparison

The most pronounced differences in mechanical behaviour between the T4P and FG materials occur at the lower temperatures, 350°C, 400°C, and to a lesser degree at 450°C. At these temperatures, the elongation to failure of the T4P material is low, reaching only about 35% elongation at 350°C, while under the same conditions, the FG material achieves an elongation of approximately 120%. At 400°C, the elongations to failure for the T4P and FG materials were about 50% and 130%, respectively (T4P: 110% and FG:170% at 450°C). These differences can be seen in Figure 5.37. The differences in maximum elongation decrease with increasing temperature, and both materials achieve similar elongations at 500°C and strain-rates $\geq 6.7 \times 10^{-2} s^{-1}$. The FG material shows higher elongations at all strain-rates at 550°C except at the highest strain-rate. The comparison of the elongation to failure at 500°C and 550°C is shown in Figure 5.38.

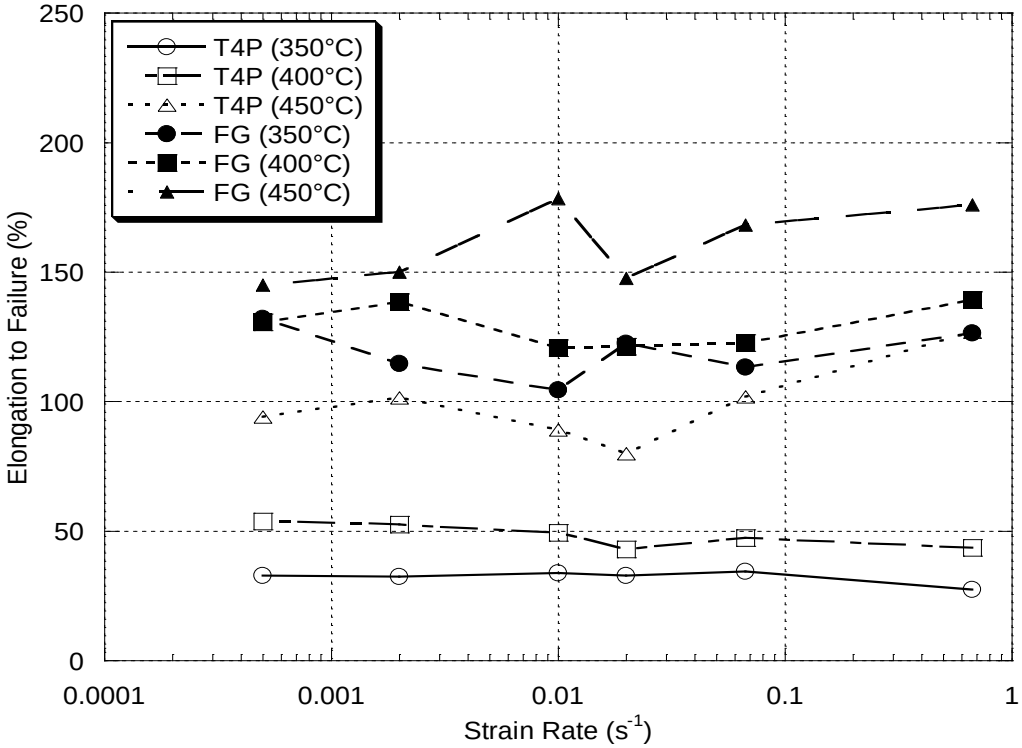

Figure 5.37: Comparison of the elongations to failure of the T4P and FG materials at lower temperatures

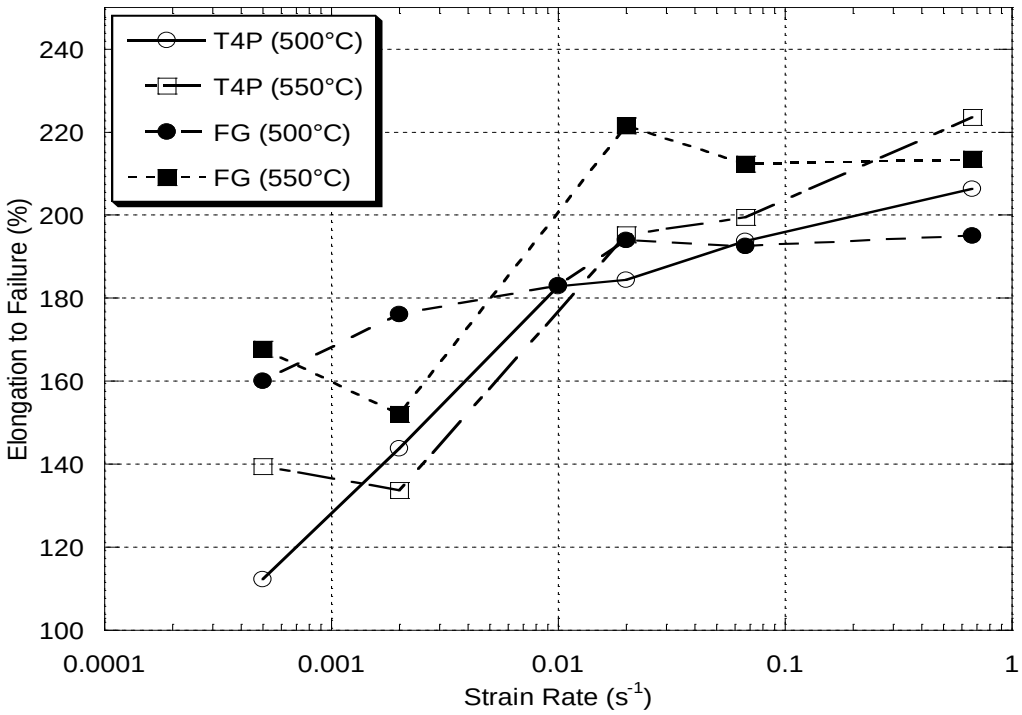

Figure 5.38: Comparison of the elongations to failure of the T4P and FG materials at higher temperatures

Similarly, the peak stress values in the T4P material are quite different at low temperatures, but less so at the higher temperatures. The T4P material exhibits much larger peak stress values than the FG material at low temperatures, 95.6MPa and 41.1MPa for the T4P and FG materials at 350°C and the highest strain-rate, respectively. Additionally, the peak stress of the T4P material at low temperatures shows a much larger dependence on strain-rate than the FG material. The peak flow stresses of the two materials are compared in Figure 5.39 and Figure 5.40. Finally, the strain required to reach the peak stress is less in the T4P material, particularly at the low temperatures.

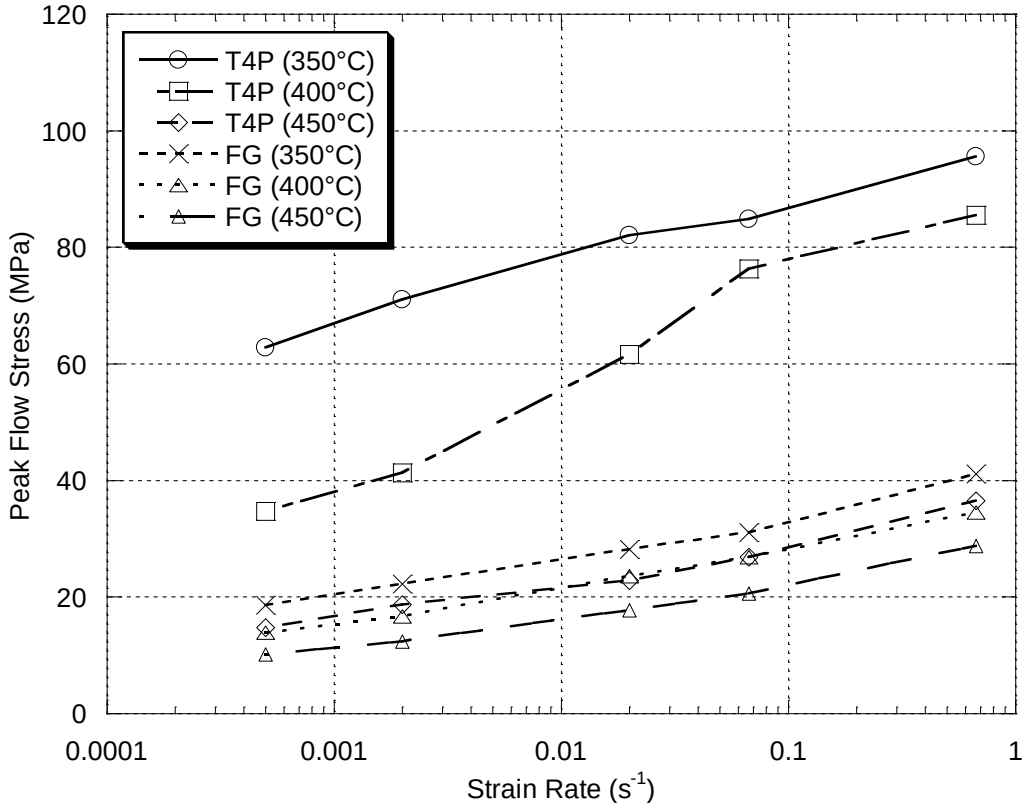

Figure 5.39: Comparison of the peak flow stresses of the T4P and FG materials at 350°C through 450°C.

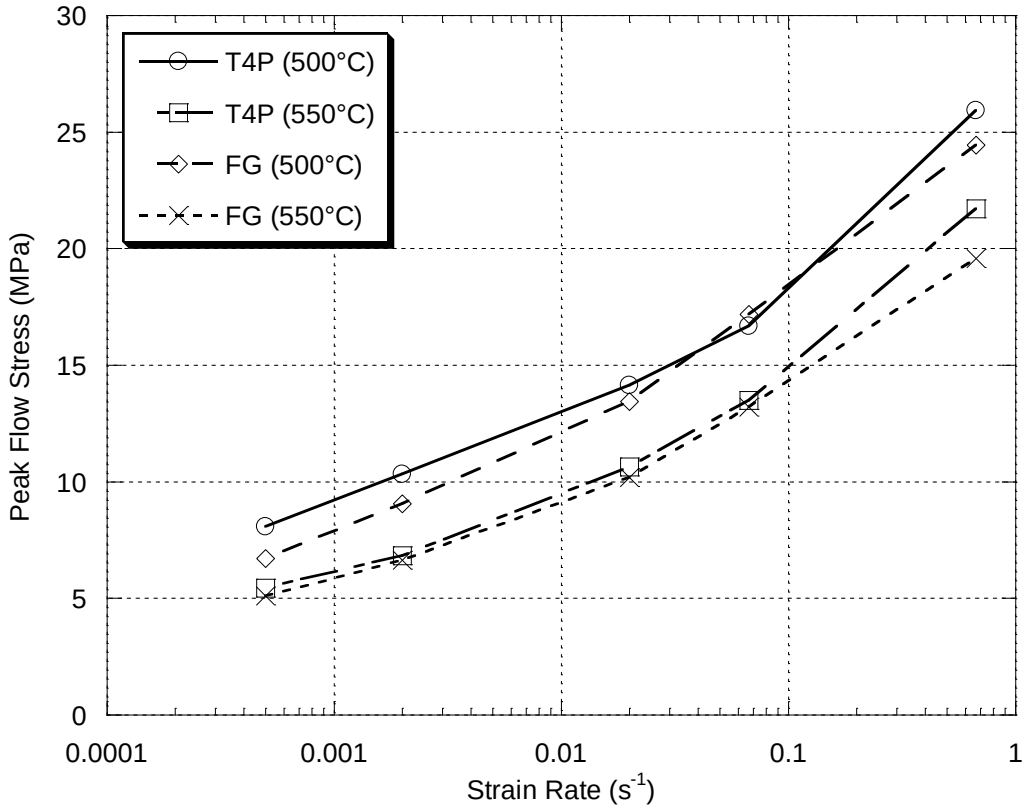

Figure 5.40: Comparison of the peak flow stresses of the T4P and FG materials at 500°C and 550°C.

5.3.2.4 Data Analysis

In this section, the data gathered from the stress-strain and load relaxation tests is used to determine material parameters such as strain-rate sensitivity and activation energy for deformation.

5.3.2.4.1 T4P Material

Figure 5.41 shows the initial strain-rate vs. UTS normalized with the elastic modulus plots for the T4P material. Using this plot, the average strain-rate sensitivity, and the stress exponent, at each temperature and the activation energies for deformation for each temperature interval were calculated. The methods and equations utilized are described in Chapter 4. These values can be found in Table 5.4 and

Table 5.5, respectively.

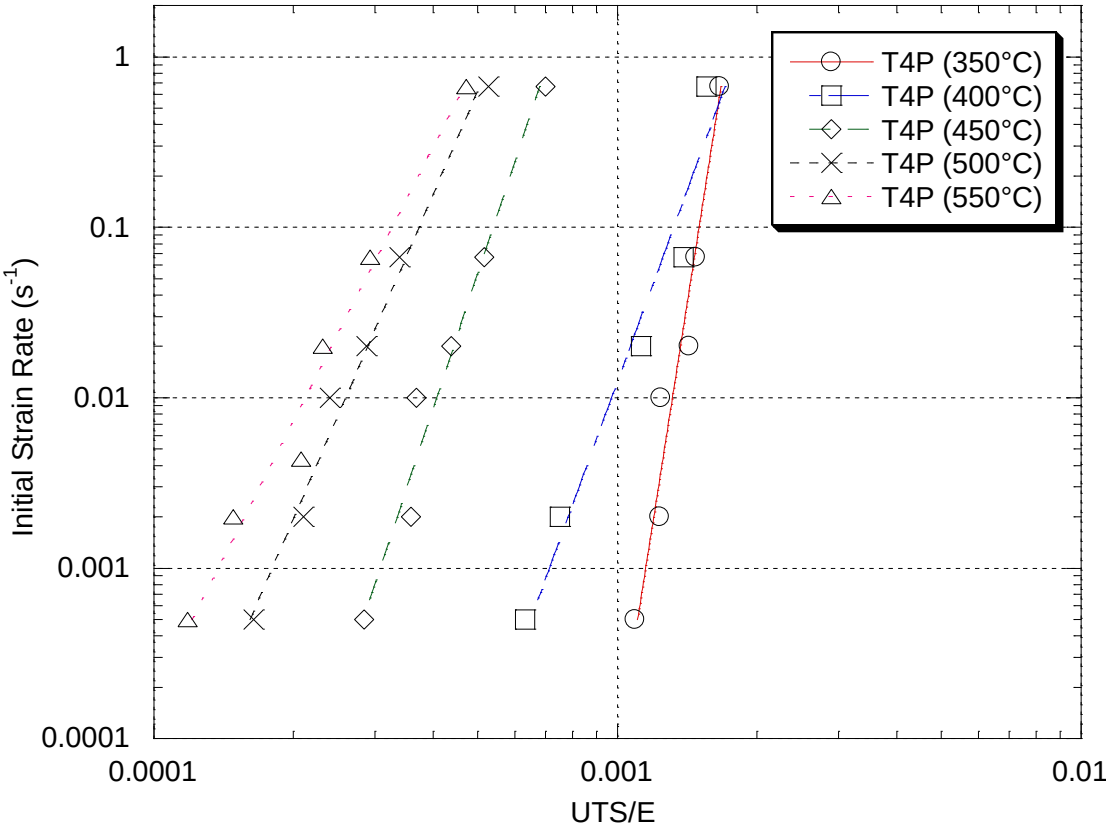

Figure 5.41: Strain-rate vs. modulus normalized stress for T4P material.

Table 5.4: Strain-rate sensitivity and stress exponent for T4P at each temperature.

Temperature (°C)	Strain-Rate Sensitivity, m	Stress Exponent, N
350	0.06	16.47
400	0.14	7.17
450	0.13	7.95
500	0.16	6.23
550	0.19	5.22

Table 5.5: Activation energy for deformation at each temperature for the T4P material.

Temperature Interval (°C)	Average Activation Energy, Q (kJ/mol)
350-400	343.2
400-450	512.6
450-500	287.9
500-550	134.0

The highest strain-rate sensitivity, 0.19, is found at a temperature of 550°C, while the lowest, 0.06, is found at 350°C. The activation energy was found to be the lowest, 134kJ/mol, in the temperature interval of 500-550°C, and the greatest, 512.6kJ/mol, between 400°C and 450°C following the procedure described in Section 4.3.3 of Chapter 4. Normalizing the strain-rate using the self-diffusion coefficient, the variation in temperature can be accounted for. This data is plotted in Figure 5.42.

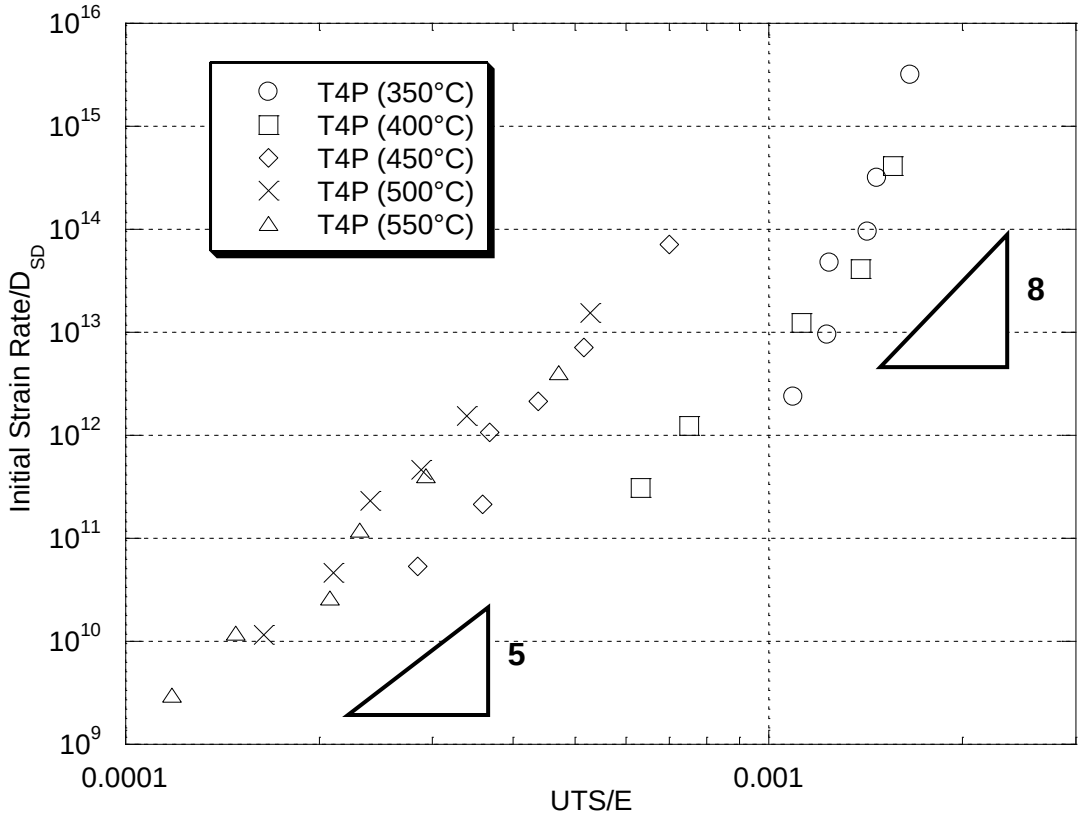

Figure 5.42: Self diffusion normalized strain-rate vs. modulus normalized stress for T4P material.

The data from the load relaxation tests was transformed into stress vs. inelastic strain-rate data according to the method described in Section 4.3.5 of Chapter 4, and plotted in Figure 5.43. Additionally, the data was fit using the internal variable equation for GMD (Equation 2.9). The constitutive parameters for these curve-fits and the accuracy of each fit (R^2) are listed in Table 5.6. No fit could be found for the grain boundary sliding (GBS) equation (Equation 2.10). The accuracy of the grain-matrix deformation (GMD) curve-fit to the data is very good for 350°C, 400°C and 450°C. At higher temperatures, the accuracy rapidly decreases. The stress parameter is the highest at 350°C, while the strain-rate parameter is the lowest. The strain-rate increases with increasing temperature.

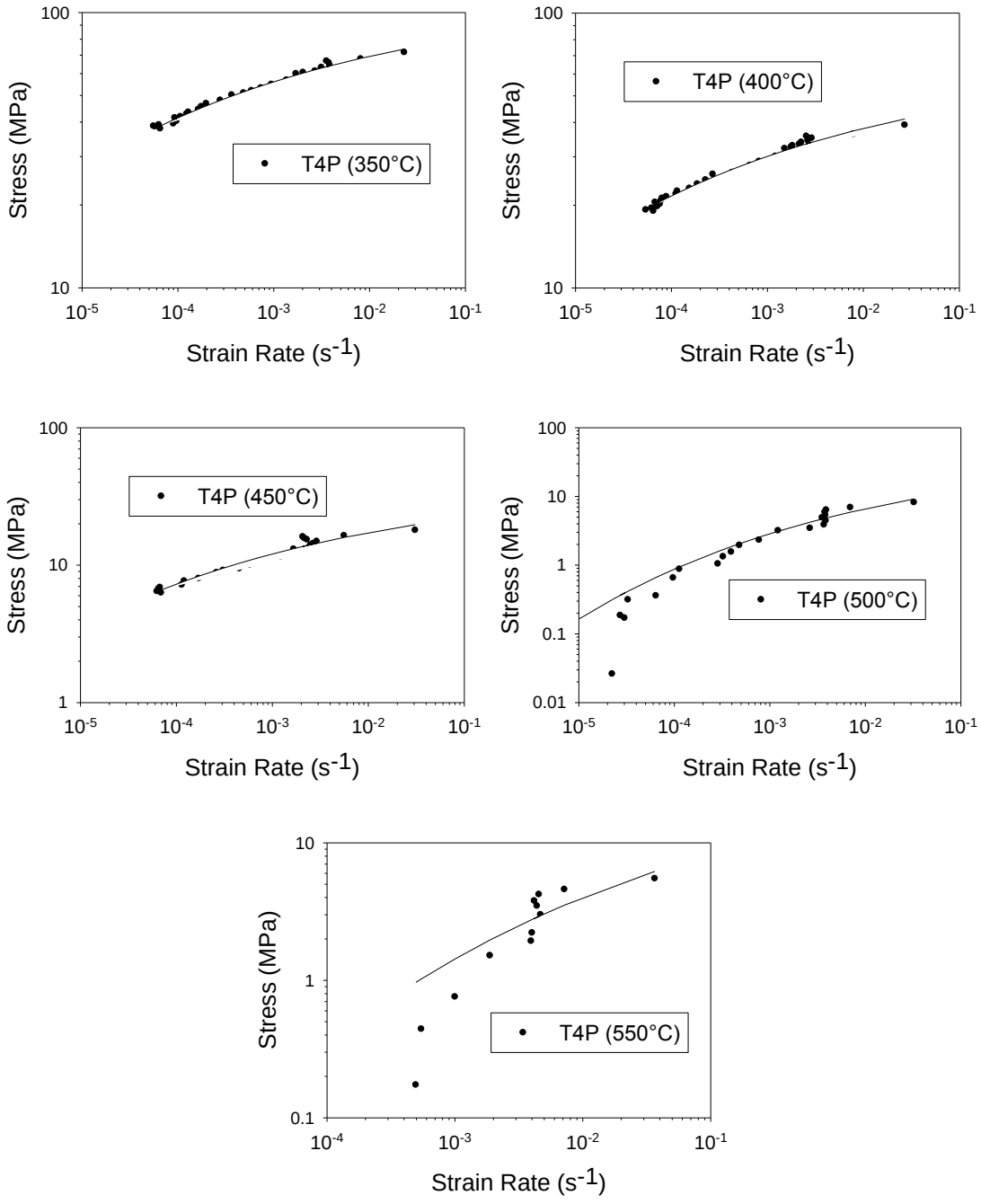

Figure 5.43: Flow stress vs. inelastic strain-rate curves for T4P sheet at each temperature. GMD calculated flow curves are also shown.

Table 5.6: Constitutive parameters for GMD calculated (Equation 2.9) from the flow curves for the T4P material.

Temperature (°C)	logσ^*	log$\dot{\varepsilon}^*$	p^*	R^2
350	2.065	-3.911	0.15	0.9772
400	1.828	-3.634	0.15	0.9685
450	1.613	-2.415	0.15	0.9769
500	1.703	0.054	0.15	0.9293
550	1.683	0.641	0.15	0.728

5.3.2.4.2 FG Material

The initial strain-rate vs. UTS normalized by the elastic modulus plots for the FG material are shown in Figure 5.44. The calculated strain-rate sensitivities and activation energies are presented in Table 5.7 and Table 5.8, respectively.

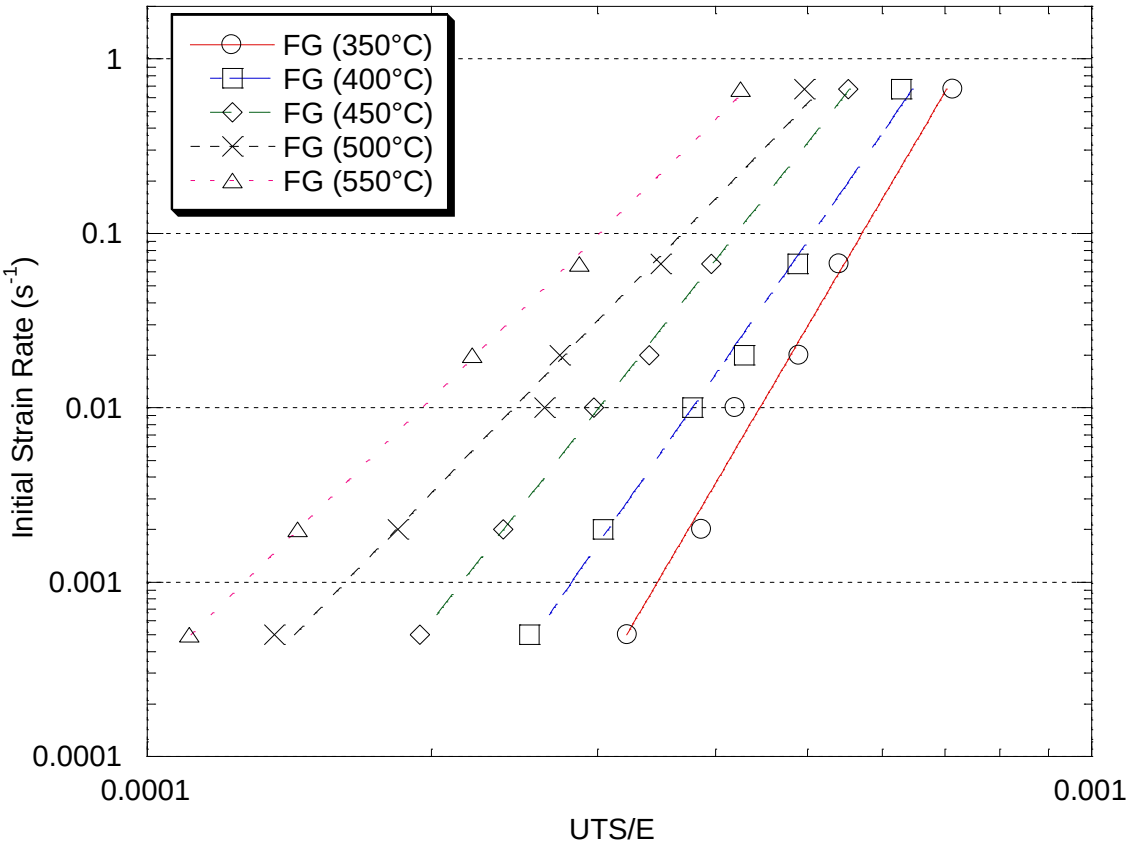

Figure 5.44: Strain-rate vs. modulus normalized stress for FG material.

Table 5.7: Strain-rate sensitivity and stress exponent for FG at each temperature.

Temperature (°C)	Strain-rate Sensitivity, m	Stress Exponent, N
350	0.11	9.10
400	0.13	7.79
450	0.15	6.88
500	0.18	5.56
550	0.19	5.31

Table 5.8: Activation energy for deformation at each temperature for the FG material.

Temperature Interval (°C)	Average Activation Energy, Q (kJ/mol)
350-400	93.5
400-450	126.2
450-500	132.0
500-550	134.2

The highest strain-rate sensitivity, 0.19, is found at a temperature of 550°C, while the lowest, 0.11, is found at 350°C. The activation energy was found to be the lowest, 93.5kJ/mol, in the temperature interval of 350-400°C, and the greatest, 134.2kJ/mol, between 500°C and 550°C. Note that the maximum activation energy is found at the highest temperature, rather than the low temperatures, as in the T4P material. The self-diffusion compensated strain-rate vs. elastic modulus compensated stress plot for the FG material is shown in Figure 5.45.

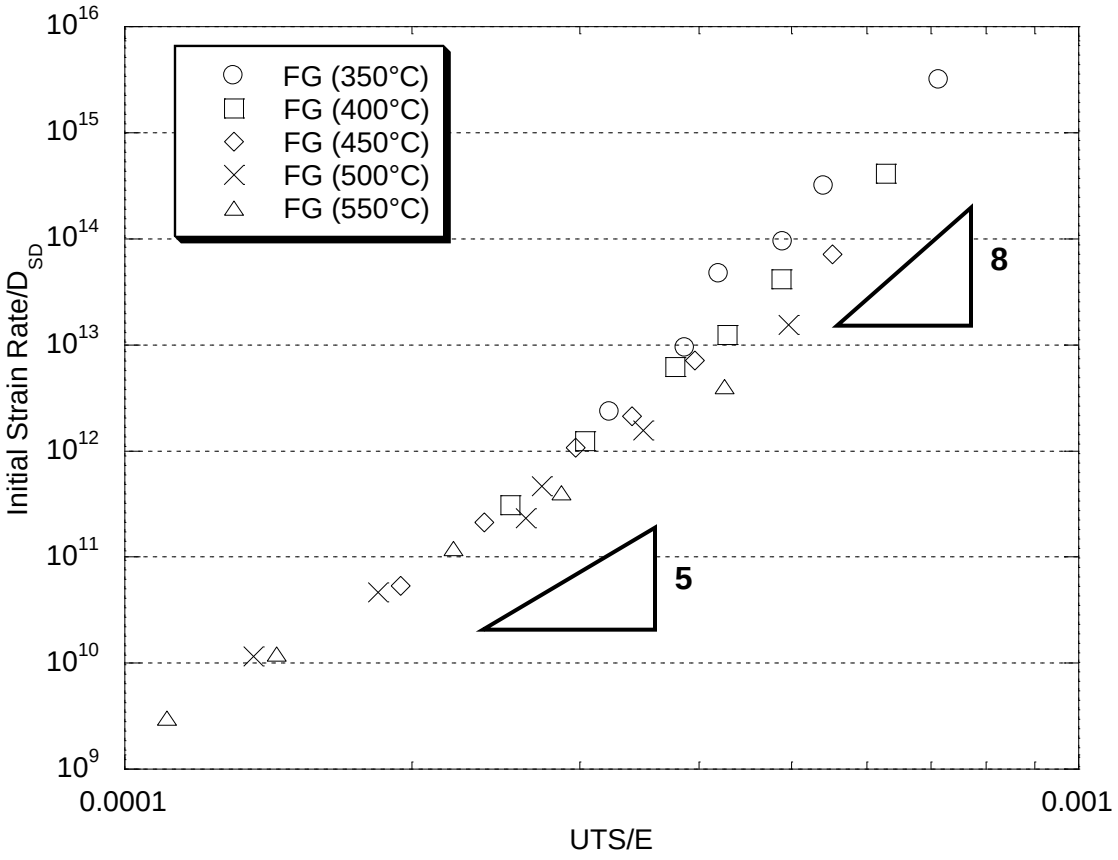

Figure 5.45: Self diffusion normalized strain-rate vs. modulus normalized stress for FG material.

The stress vs. inelastic strain-rate plots for the FG material are shown in Figure 5.46, along with the GMD curve fits. The constitutive parameters for GMD and the accuracies of the fits to experimental data is tabulated in Table 5.9. No fit could be found for the GBS equation. As with the T4P material, the GMD curve-fit is quite accurate at 350°C, 400°C and 450°C, and the accuracy rapidly decreases at 500°C and 550°C. The stress parameter of the FG material remains close to a value of 1.8 at all temperatures, and the strain-rate parameter tends to increase within increasing temperatures, just as the T4P material did.

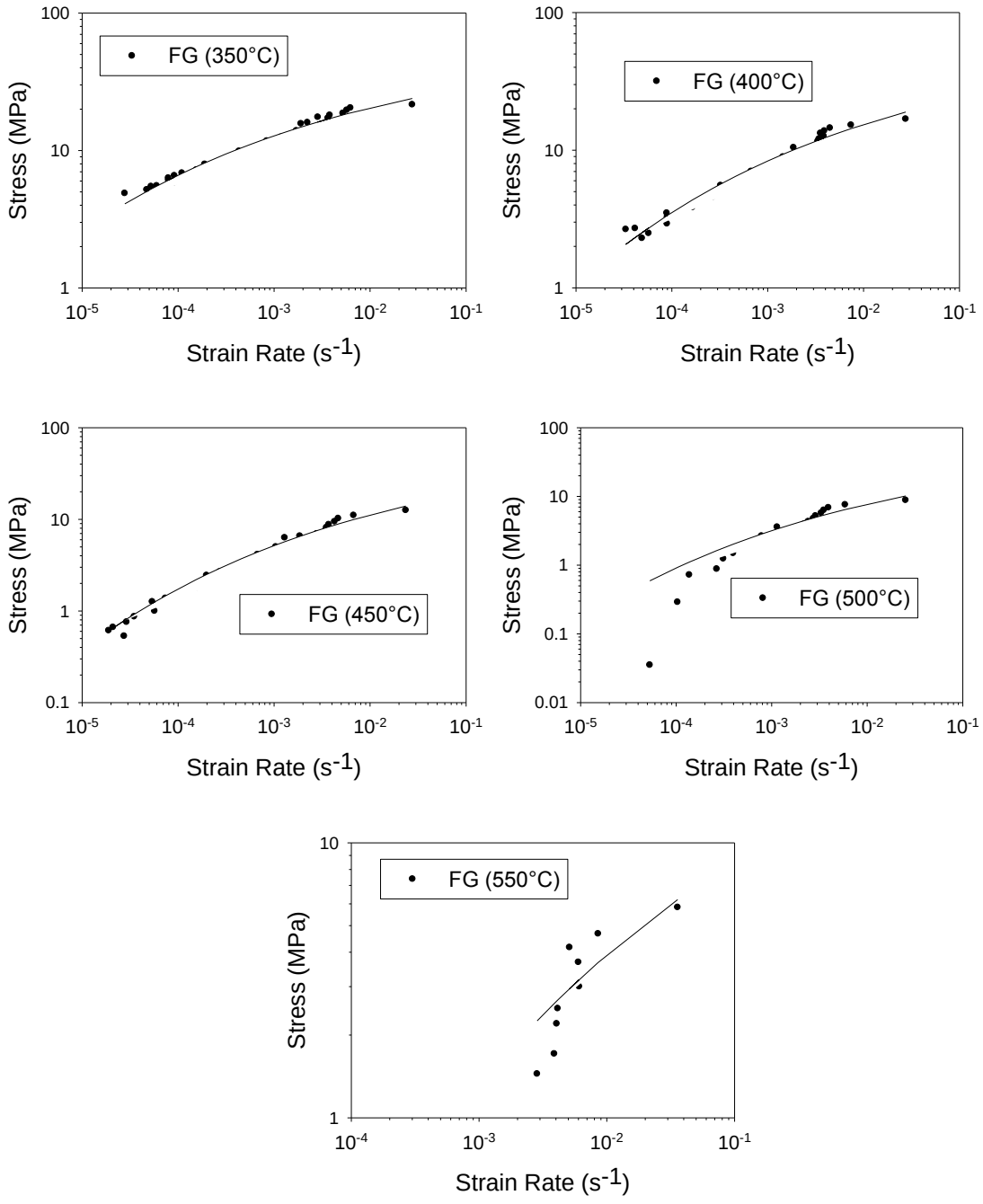

Figure 5.46: Flow stress vs. inelastic strain-rate curves for FG at each temperature. GMD calculated flow curves are also shown.

Table 5.9: Constitutive parameters for GMD calculated (Equation 2.9) from the flow curves for the FG material.

Temperature (°C)	logσ^*	log$\dot{\varepsilon}^*$	p^*	R^2
350	1.802	-1.636	0.15	0.9772
400	1.829	-0.867	0.15	0.9685
450	1.858	-0.1927	0.15	0.9769
500	1.819	0.213	0.15	0.9293
550	1.747	0.833	0.15	0.728

5.3.3 Grain Size after Tensile Testing at Temperature

This section illustrates the effect that high temperature deformation has upon the grain structure. First, the grain size and morphology is shown after tensile testing at various temperatures, followed by the effect of strain-rate upon the recrystallized grains found at 500°C and 550°C. In all images shown, the tensile direction, and the original rolling direction are in the horizontal direction.

5.3.3.1 T4P Material

Figure 5.47 and Figure 5.48 show the deformed grain structure of the T4P material after testing at 350°C and 400°C, respectively, and at the strain-rate of $6.7x10^{-1}s^{-1}$. The grain structure can be seen to be largely unchanged from the initial microstructure, except for a slight elongation of the grains in the tensile direction. The poor etch, and as a result, poorly defined grains is likely a result of the deformation structure within the material.

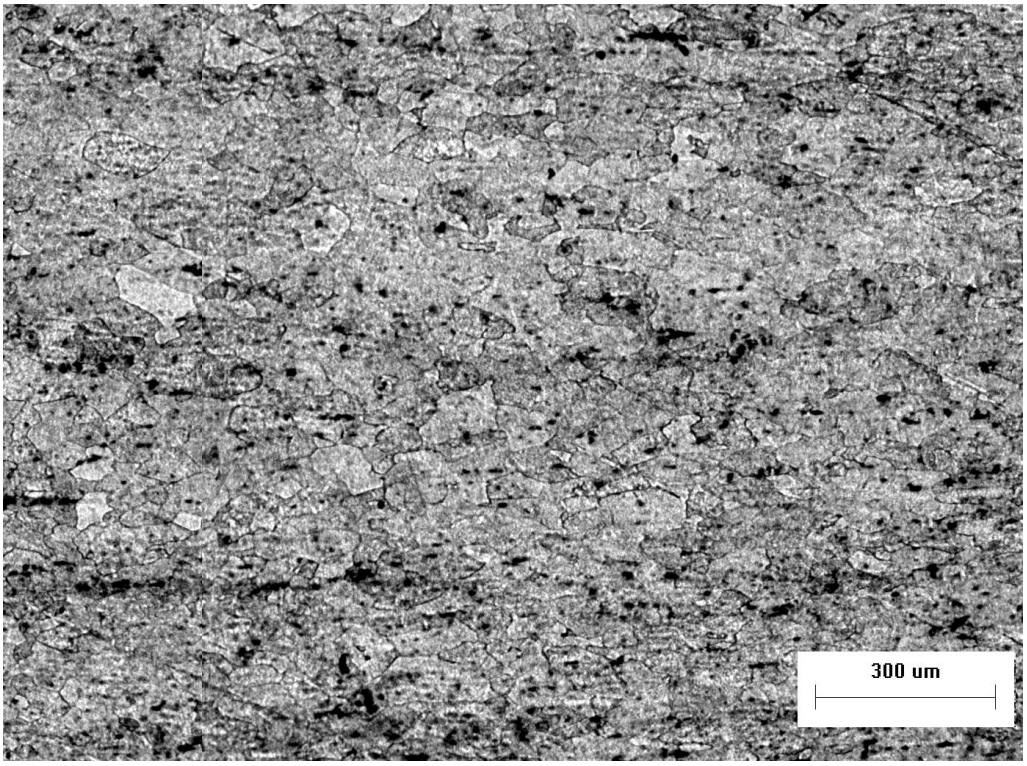

Figure 5.47: Grain structure of T4P sheet after tensile testing at 350°C and the strain-rate of $6.7x10^{-1}s^{-1}$.

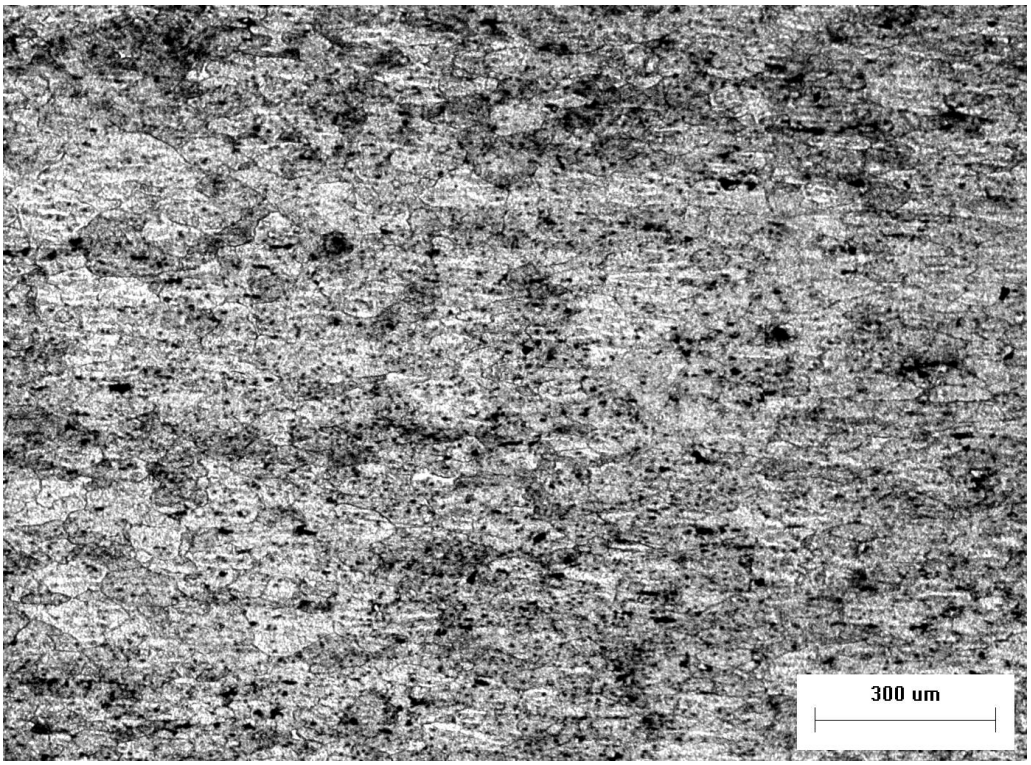

Figure 5.48: Grain structure of T4P sheet after tensile testing at 400°C and the strain-rate of $6.7x10^{-1}s^{-1}$.

At 450°C and a strain-rate of $6.7x10^{-1}s^{-1}$, where a significant jump in the elongation to failure is seen, the observed grain structure is very different. The grains are significantly thinned and elongated in the tensile direction, as seen in Figure 5.49. The grain boundaries remain somewhat indistinct at the temperature.

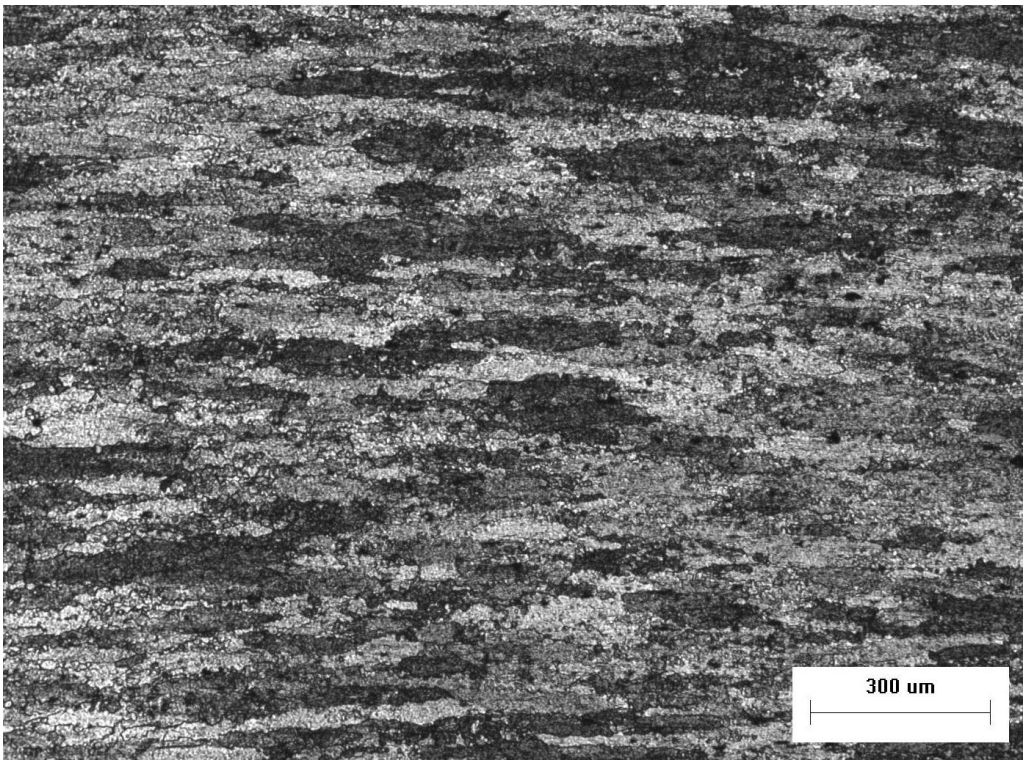

Figure 5.49: Grain structure of T4P sheet after tensile testing at 450°C and the strain-rate of $6.7x10^{-1}s^{-1}$.

Considering again a strain-rate of $6.7x10^{-1}s^{-1}$ and temperatures of 500°C and 550°C, the grain structure changes significantly as shown by Figure 5.50 and Figure 5.51, respectively. Here, despite undergoing the largest elongations, the observed grains show very little elongation in the tensile direction. The grains at 500°C are slightly smaller than those at 550°C, however, the grains are more defined at 550°C. The grains at both of these temperatures are smaller than in the original material.

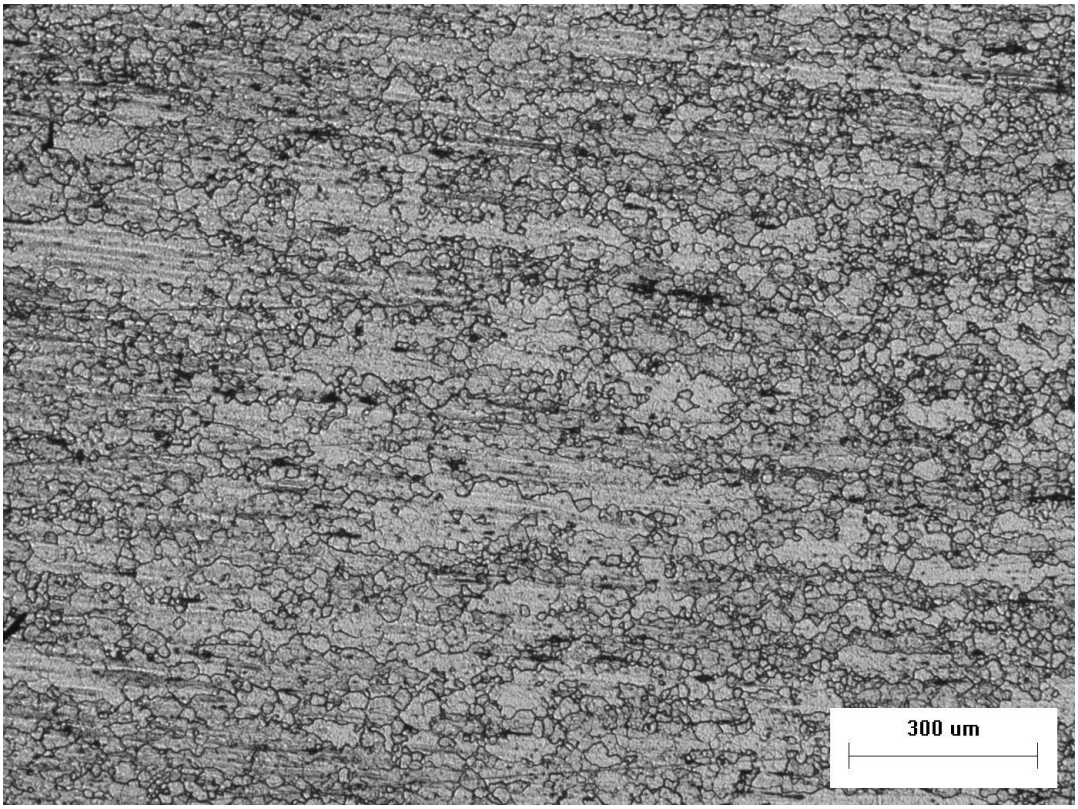

Figure 5.50: Grain structure of T4P sheet after tensile testing at 500°C and the strain-rate of $6.7x10^{-1}s^{-1}$.

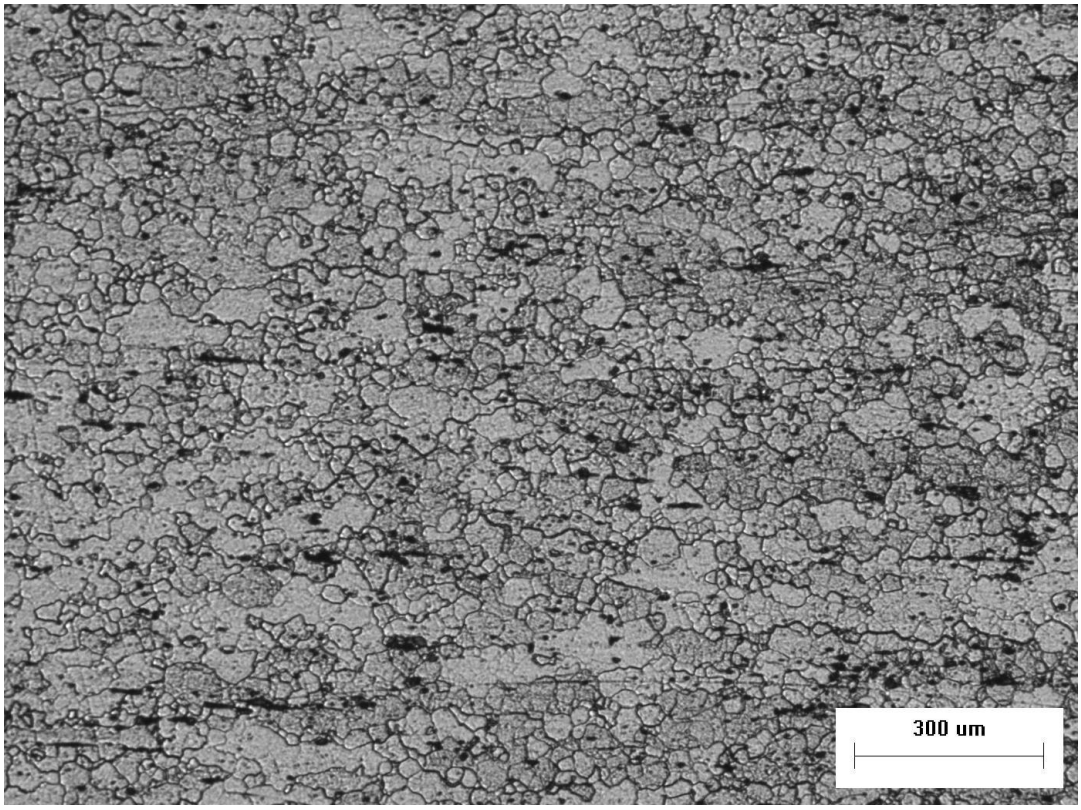

Figure 5.51: Grain structure of T4P sheet after tensile testing at 550°C and the strain-rate of $6.7x10^{-1}s^{-1}$.

5.3.3.2 FG Material

Optical microscopy images of the microstructure of the FG material after deformation at a strain-rate of $6.7x10^{-1}s^{-1}$.and various temperatures are shown in Figure 5.52 through Figure 5.56. At temperatures between 350°C and 450°C, the grain structures are similar to one another. The grain structure at these conditions consists of small elongated grains, however, at 450°C (Figure 5.54), the boundaries of these grains become somewhat serrated, as highlighted by the black arrows.

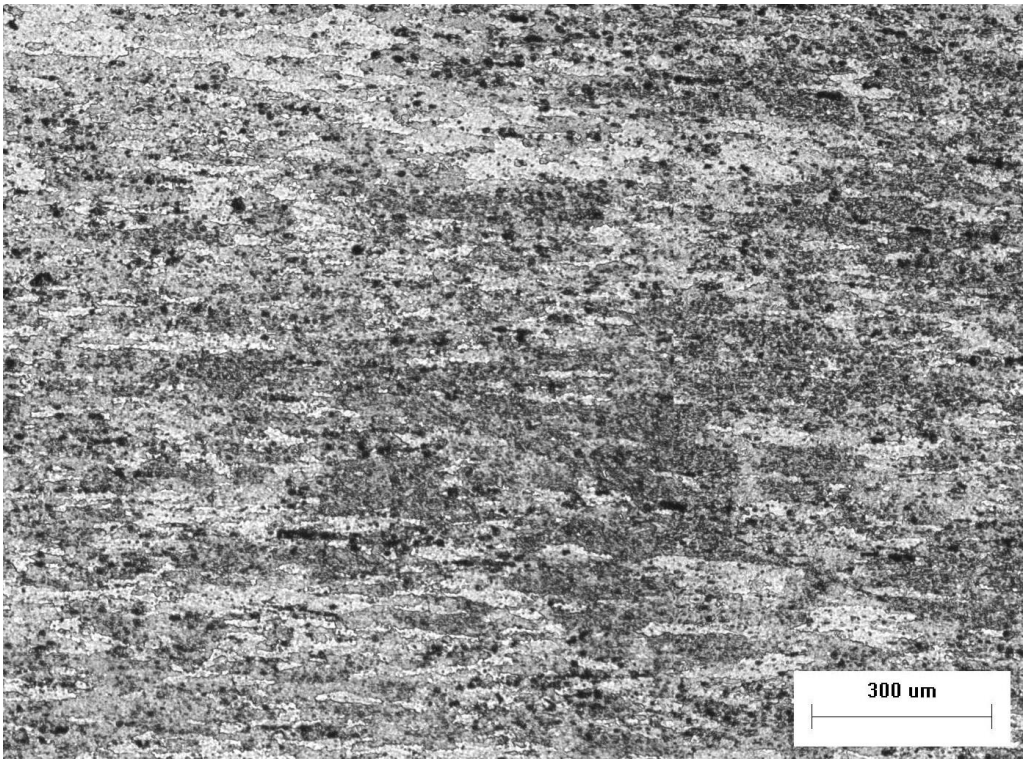

Figure 5.52: Grain structure of FG sheet after tensile testing at 350°C and the strain-rate of $6.7x10^{-1}s^{-1}$.

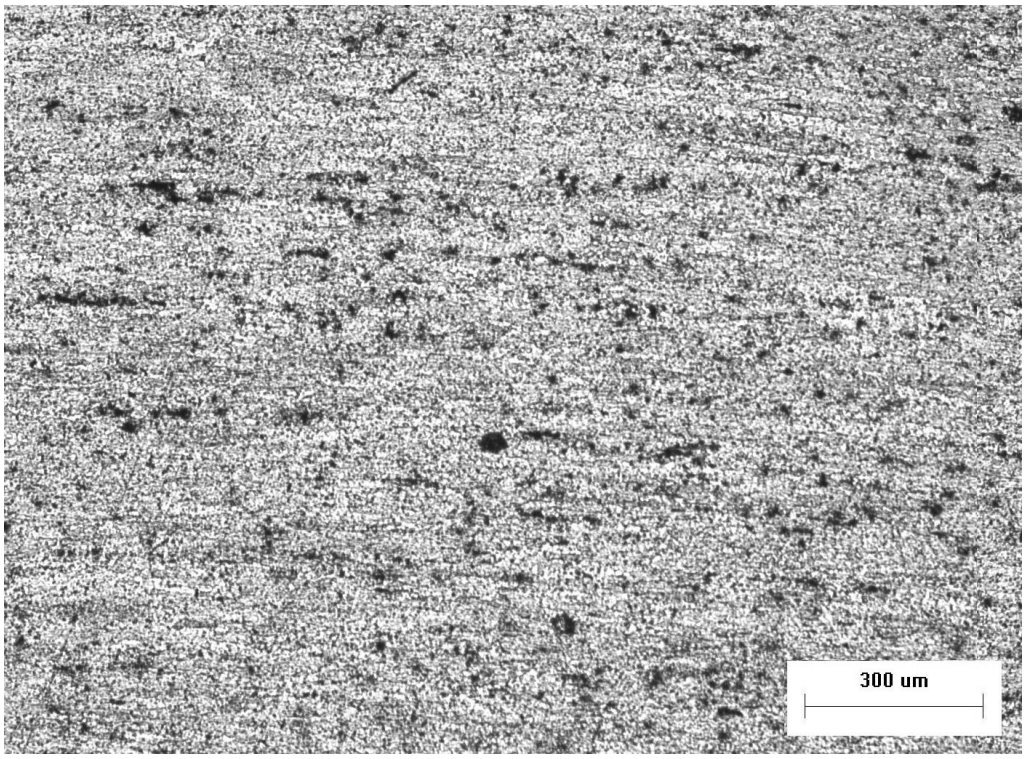

Figure 5.53: Grain structure of FG sheet after tensile testing at 400°C and the strain-rate of $6.7x10^{-1}s^{-1}$.

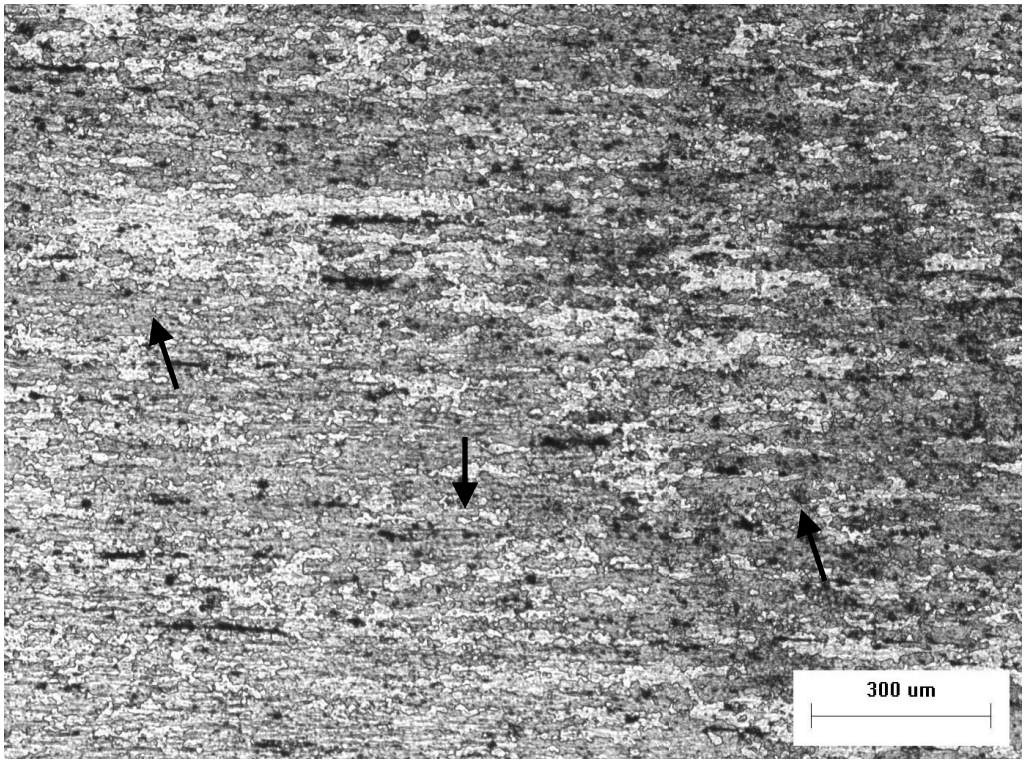

Figure 5.54: Grain structure of FG sheet after tensile testing at 450°C and the strain-rate of $6.7x10^{-1}s^{-1}$.

At 500°C, the jaggedness of the grain boundaries is reduced, leaving smoother grain boundaries, and the grains appear to be a mix of elongated grains, and smaller, equiaxed grains (Figure 5.55).

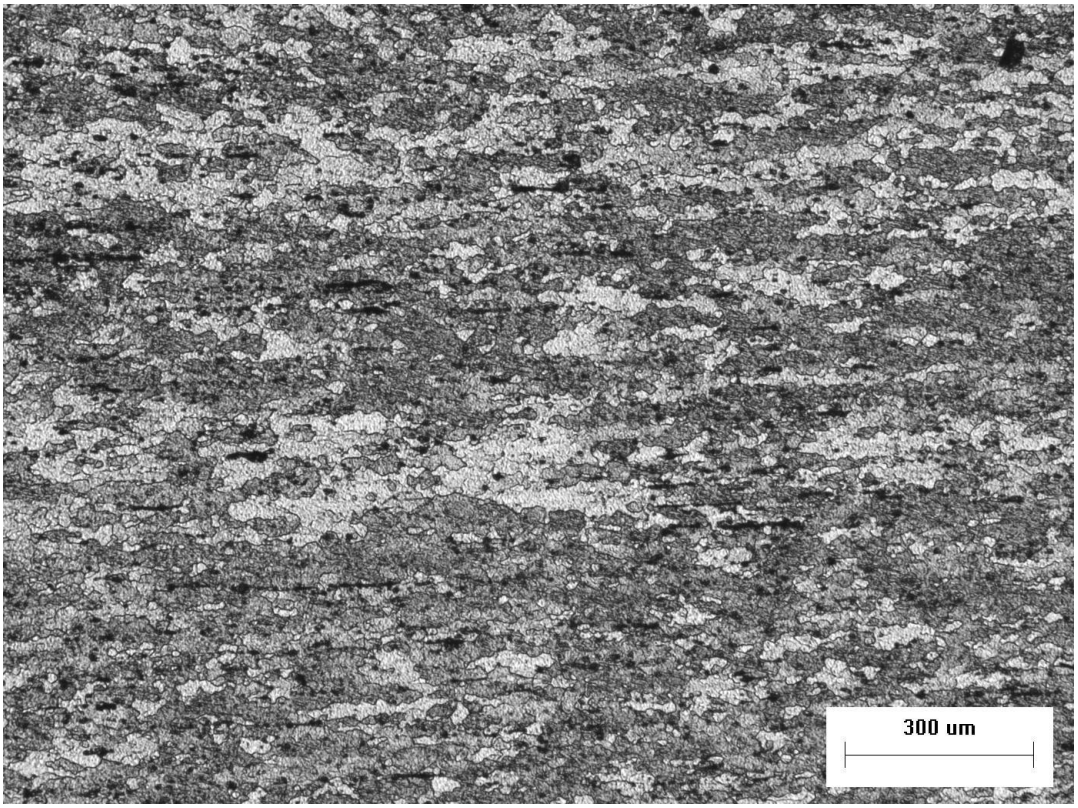

Figure 5.55: Grain structure of FG sheet after tensile testing at 500°C and the strain-rate of $6.7x10^{-1}s^{-1}$.

Figure 5.56 shows the grain structure of the FG material after testing at 550°C. The grains are equiaxed and show no significant elongation in the tensile direction.

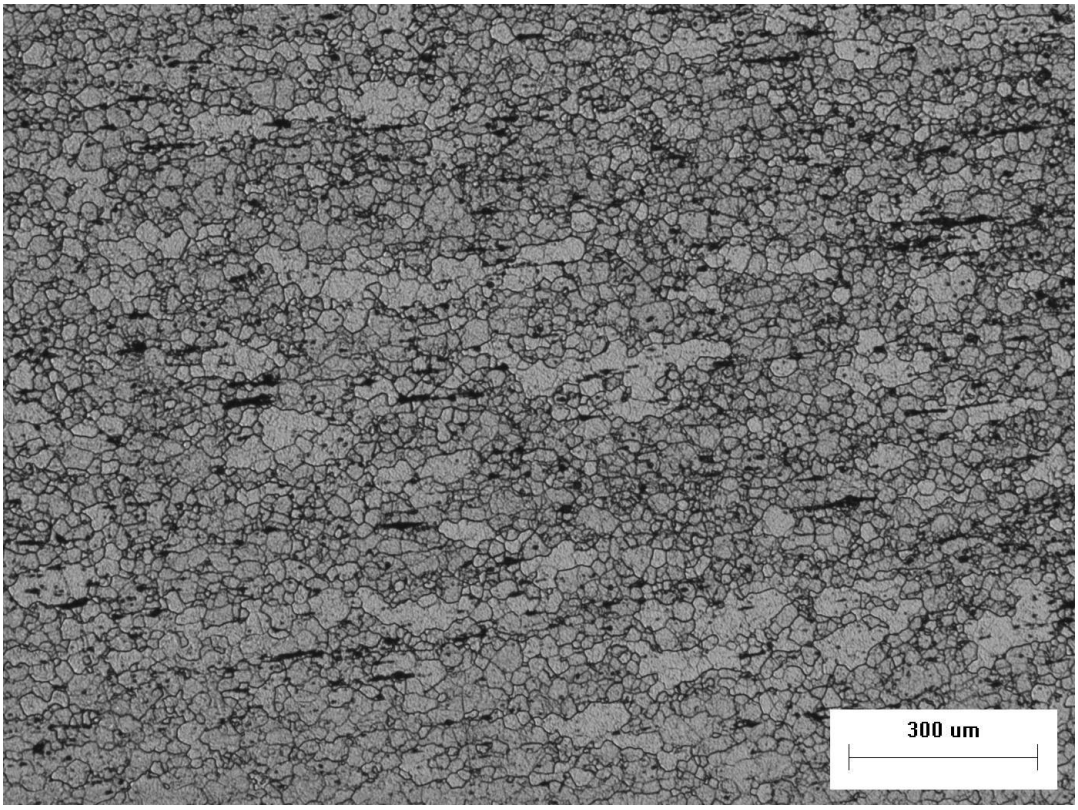

Figure 5.56: Grain structure of FG sheet after tensile testing at 550°C and the strain-rate of $6.7x10^{-1}s^{-1}$.

5.3.3.3 Comparison of Average Grain Sizes in Tensile Tested FG and T4P Sheets

At 500°C and 550°C, the grain structure was defined sufficiently to be measured in the conventional manner. Figure 5.57 shows the average grain diameter after tensile testing at the indicated strain-rates. On average, the FG material retains a smaller grain size than the T4P material; however the difference is not nearly as large as the difference in grain size in the as-received condition. The grains in both materials are slightly elongated in the tensile direction, with an average anisotropy value, of 1.45. The common trend in both materials is a decrease in grain size with increasing strain-rate. It should be noted that the final grain size of the T4P material is lower than the initial size, and the opposite is true for the FG material.

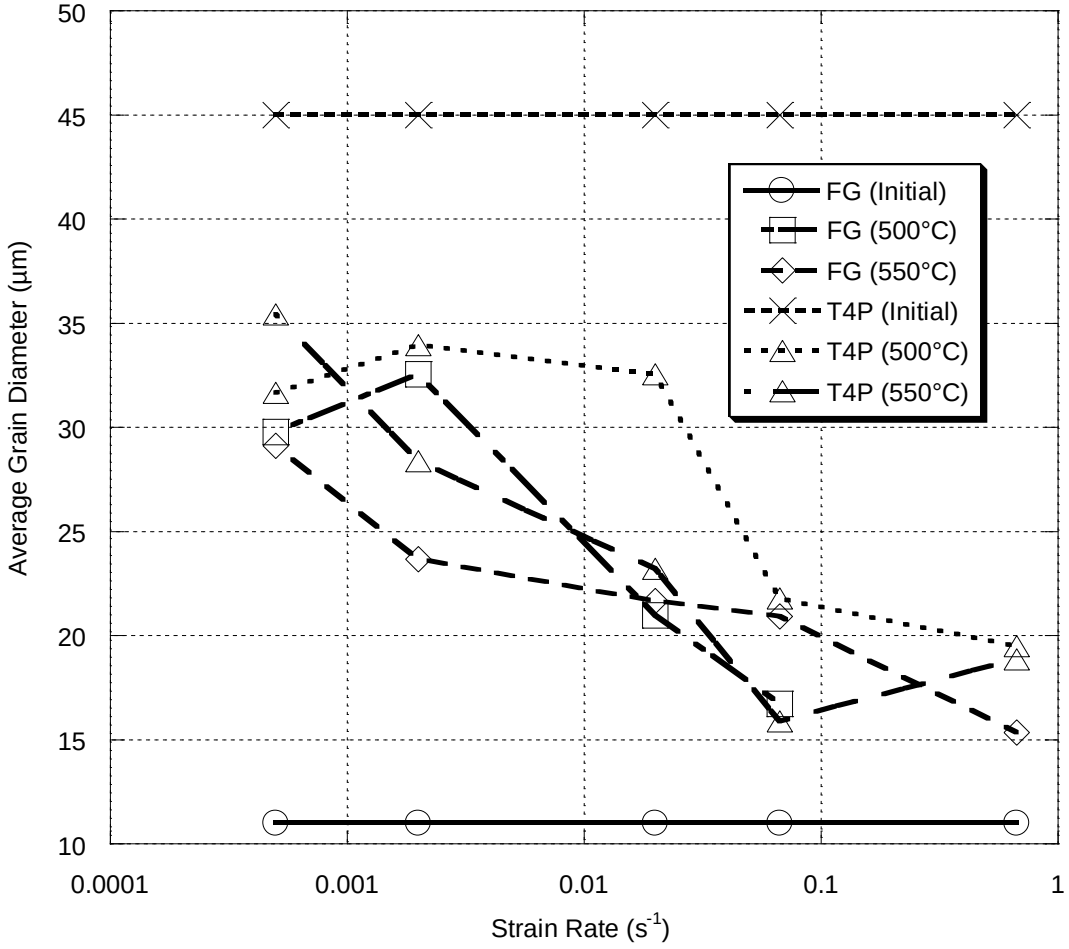

Figure 5.57: Average grain diameter of tensile tested samples taken 4mm from the fracture surface.

5.3.3.4 Abnormal Grain Growth

An interesting feature that was discovered during the examination of the grain structure was several cases of abnormal grain growth at the fracture tip of the tensile tested sample. Figure 5.58 and Figure 5.59 show two examples of this phenomenon in the T4P and fine-grained materials, respectively. These very large grains are many times larger than the grains in the rest of the material (>300µm in diameter). The conditions at which this phenomenon was observed are listed in Table 5.10. This was not observed at any other conditions.

Table 5.10: Conditions where abnormal grain growth were observed

Material	Strain-rate	Temperature
T4P	$6.7x10^{-1}s^{-1}$	450°C
T4P	$6.7x10^{-1}s^{-1}$	500°C
FG	$6.7x10^{-1}s^{-1}$	450°C
FG	$6.7x10^{-1}s^{-1}$	500°C
FG	$6.7x10^{-2}s^{-1}$	550°C
FG	$6.7x10^{-1}s^{-1}$	550°C

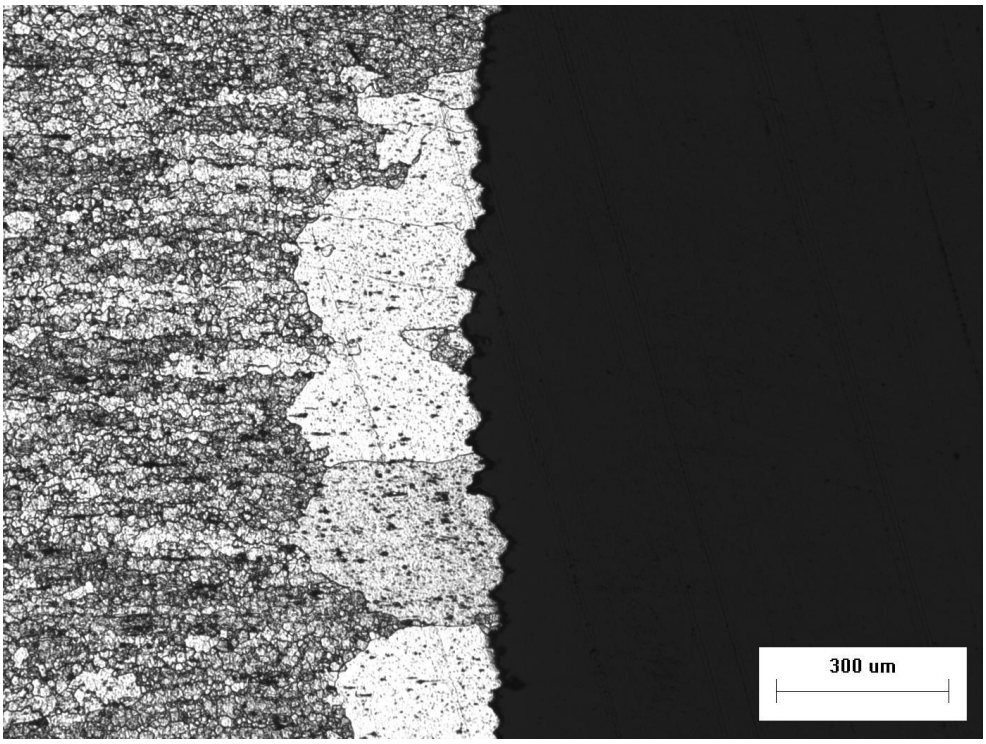

Figure 5.58: Abnormal grain growth at fracture tip of T4P sheet tensile tested at 500°C and an initial strain-rate of $6.7x10^{-1}s^{-1}$.

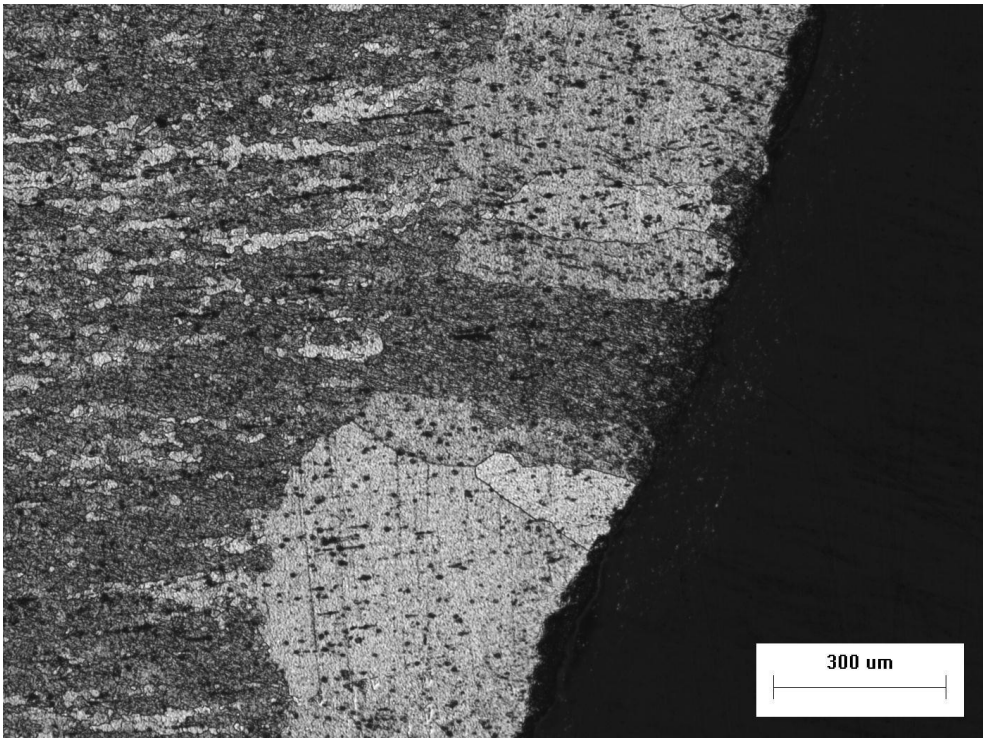

Figure 5.59: Abnormal grain growth at fracture tip of FG sheet tensile tested at 500°C and an initial strain-rate of $6.7x10^{-1}s^{-1}$.

5.3.4 Cavitation in Tensile Tested Samples

In addition to the in-plane grain examination, samples were cut in the through-thickness plane and examined for cavitation damage. Only certain conditions were examined in this manner. These conditions were: RT, 350°C, 450°C and 500°C, at strain-rates of $5.0x10^{-4}s^{-1}$, $2.0x10^{-2}s^{-1}$ and $6.7x10^{-1}s^{-1}$. These conditions were examined because they represent significant changes in the mechanical behaviour of the material. These measurements were conducted by Dr. Sooky Winkler.

5.3.4.1 T4P Material

In Figure 5.60, the results of the cavitation damage measurements on the T4P material can be seen. At most of the conditions examined, the area fraction of voids is very small (<0.5%), except for at 500°C and a strain-rate of $5.0x10^{-4}s^{-1}$; at this condition, there is a significant area fraction of voids (~7%).

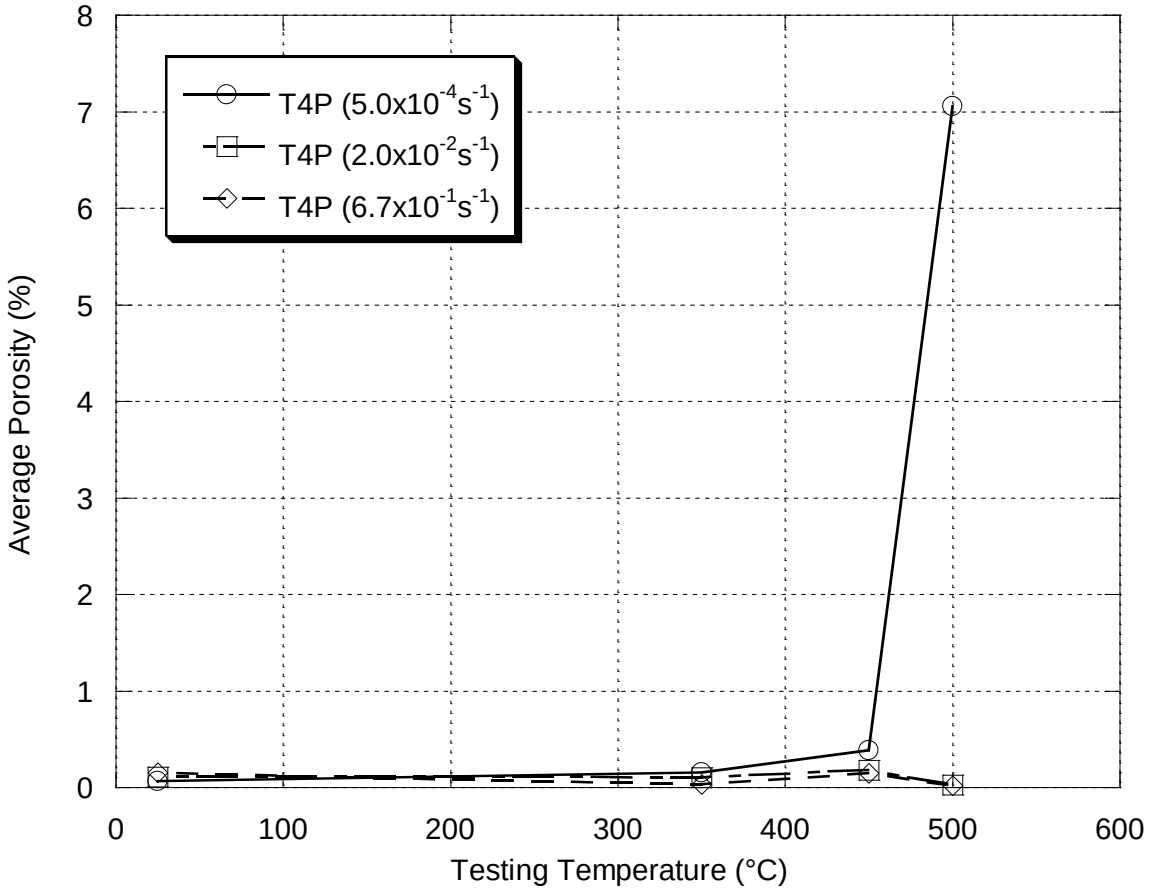

Figure 5.60: Average area fraction of voids in the through thickness plane of T4P samples tested at elevated temperatures, measured from 0-3mm from the fracture surface (data by Dr. Sooky Winkler).

Figure 5.61 shows the through-thickness view of a sample tested at 350°C and the lowest strain-rate. As can be seen, the material thins rapidly close to the fracture tip, and large voids can be seen at the fracture surface. The insert shows an enlarged view of the fracture tip. Figure 5.62 shows the fracture area of a sample tested at 350°C and the highest strain-rate. Here, it can be seen that the sample thinned down to a point, and the point has a slightly jagged edge, suggesting cavity formation. The cavities at the fracture tip are not as large as those seen at the lower strain-rate. In the insert view, it can be seen that one of the voids might have initiated from a large particle, as highlighted by the arrow.

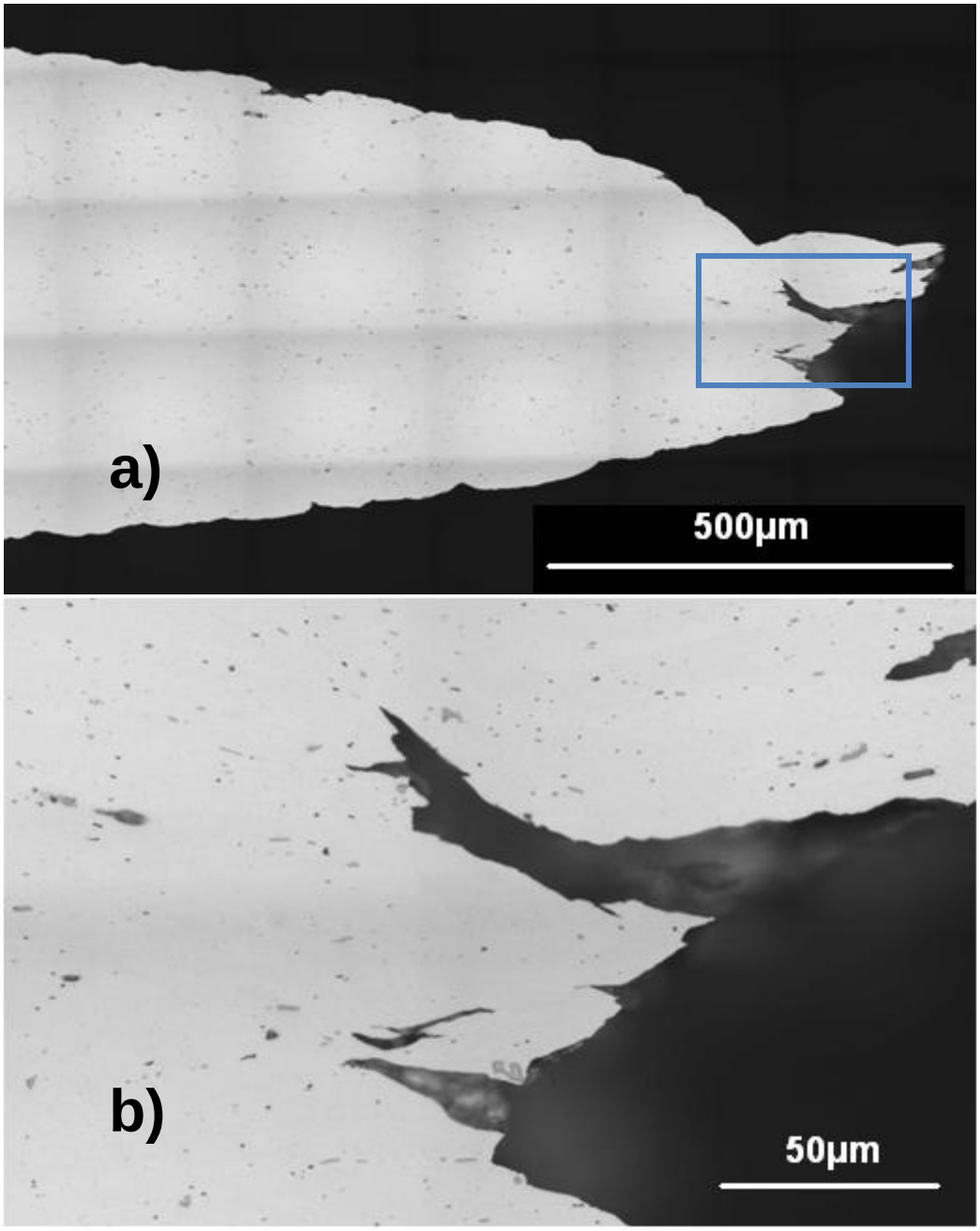

Figure 5.61: Through-thickness view of a T4P sample tested at 350°C and $5.0x10^{-4}s^{-1}$ a) overall view of fracture area and b) insert view (images by Dr. Sooky Winkler).

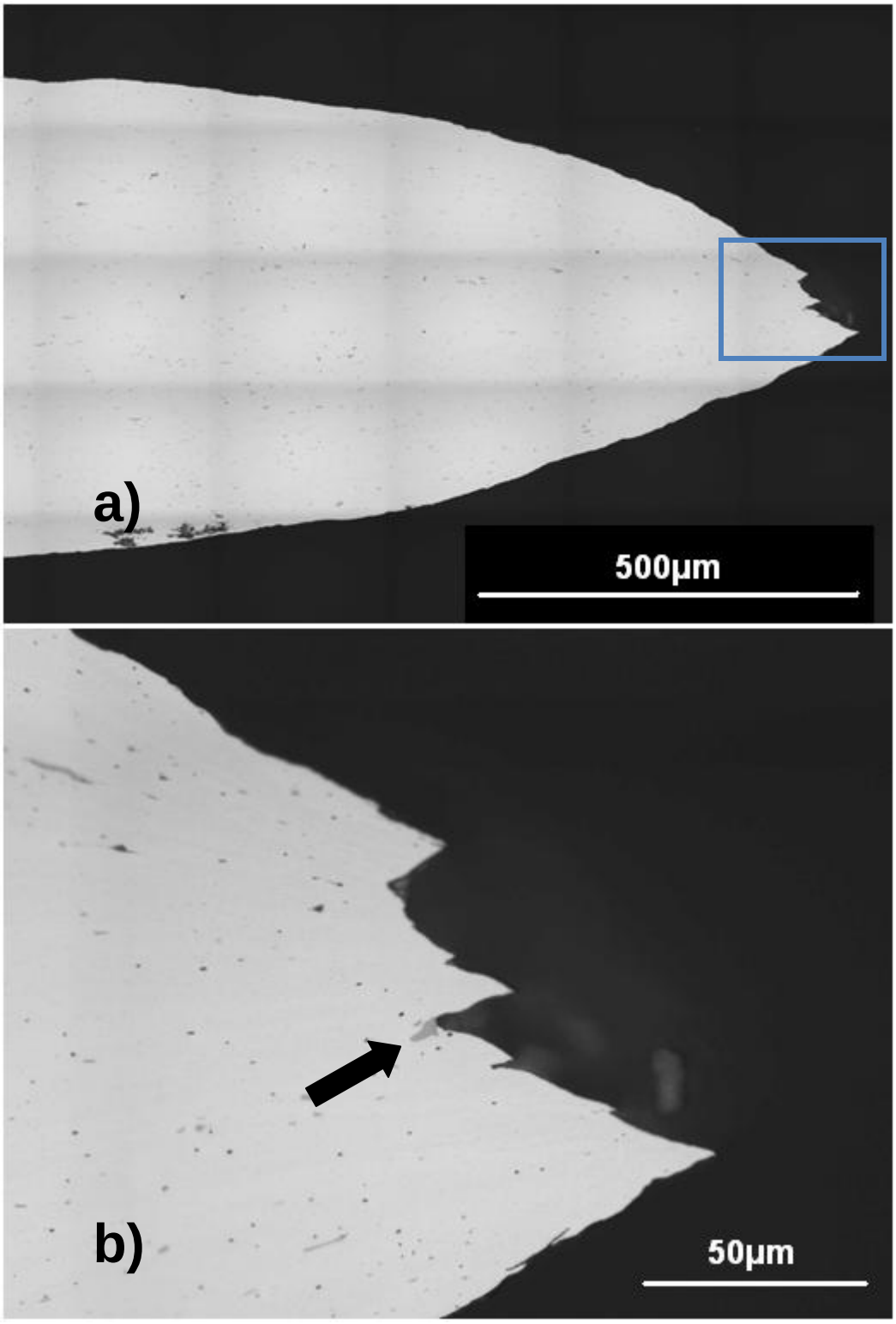

Figure 5.62: Through-thickness view of a T4P sample tested at 350°C and $6.7x10^{-1}s^{-1}$ a) overall view of fracture area and b) insert view (images by Dr. Sooky Winkler).

Figure 5.63 shows the through-thickness view of a sample tensile tested at 500°C and a strain-rate of $5.0x10^{-4}s^{-1}$, which shows a very high area fraction of voids. As can be seen, the material does not thin down to a point, but leaves a jagged edge at the fracture tip, suggesting failure by accumulation of voids. In the insert view, it can be seen that these voids appear to initiate by the decohesion of large particles from the matrix. A sample tested at the same temperature, but the highest strain-rate is shown in Figure 5.64. Here the fracture area can be seen to be significantly different than the low strain-rate counterpart. The fracture tip thins down to a point, with very little cavitation seen. In the insert view, thin strings of cavities can be seen, and one can be seen to initiate at the tip of a particle.

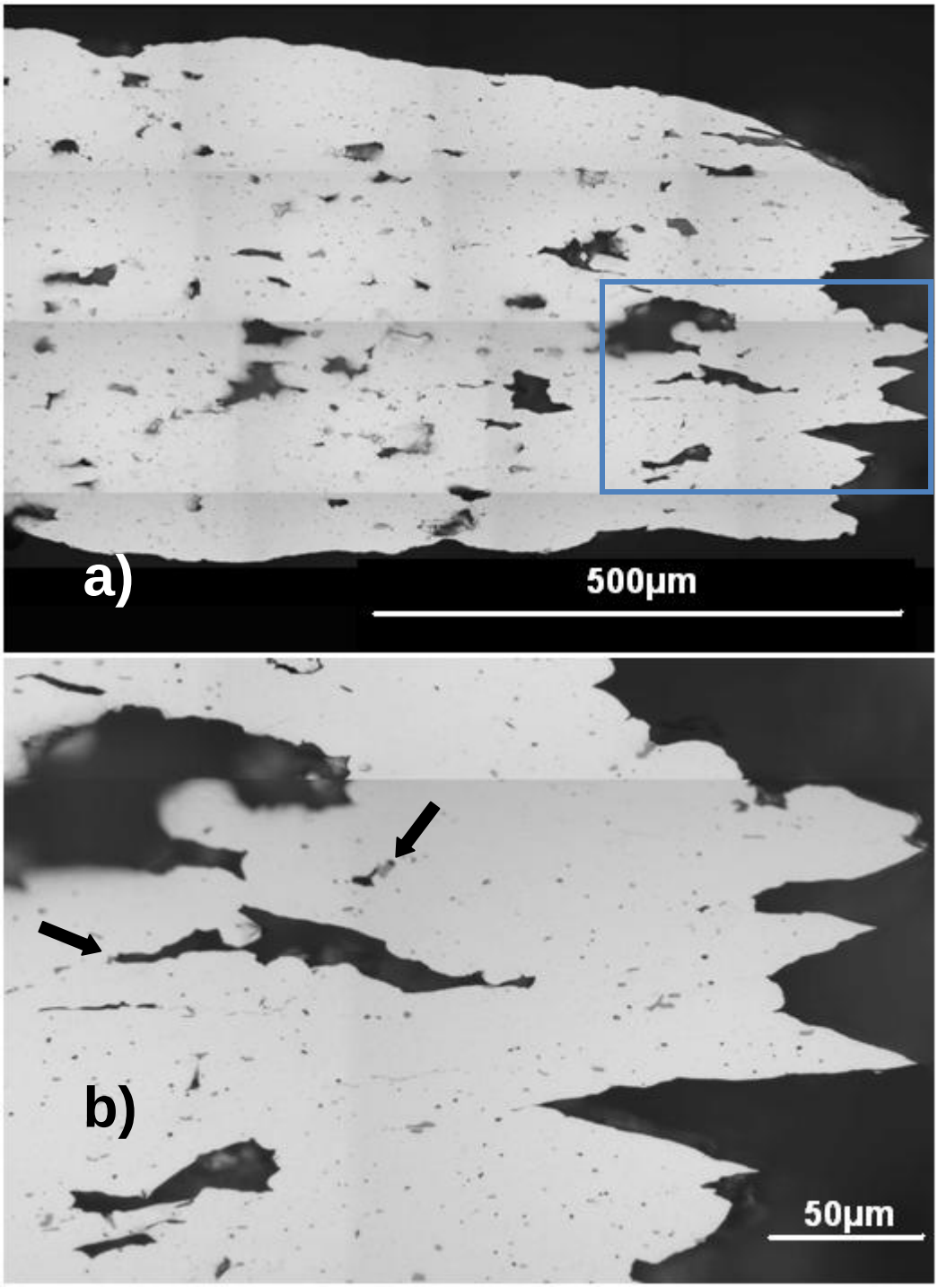

Figure 5.63: Through-thickness view of a T4P sample tested at 500°C and $5.0x10^{-4}s^{-1}$ a) overall view of fracture area and b) insert view (images by Dr. Sooky Winkler).

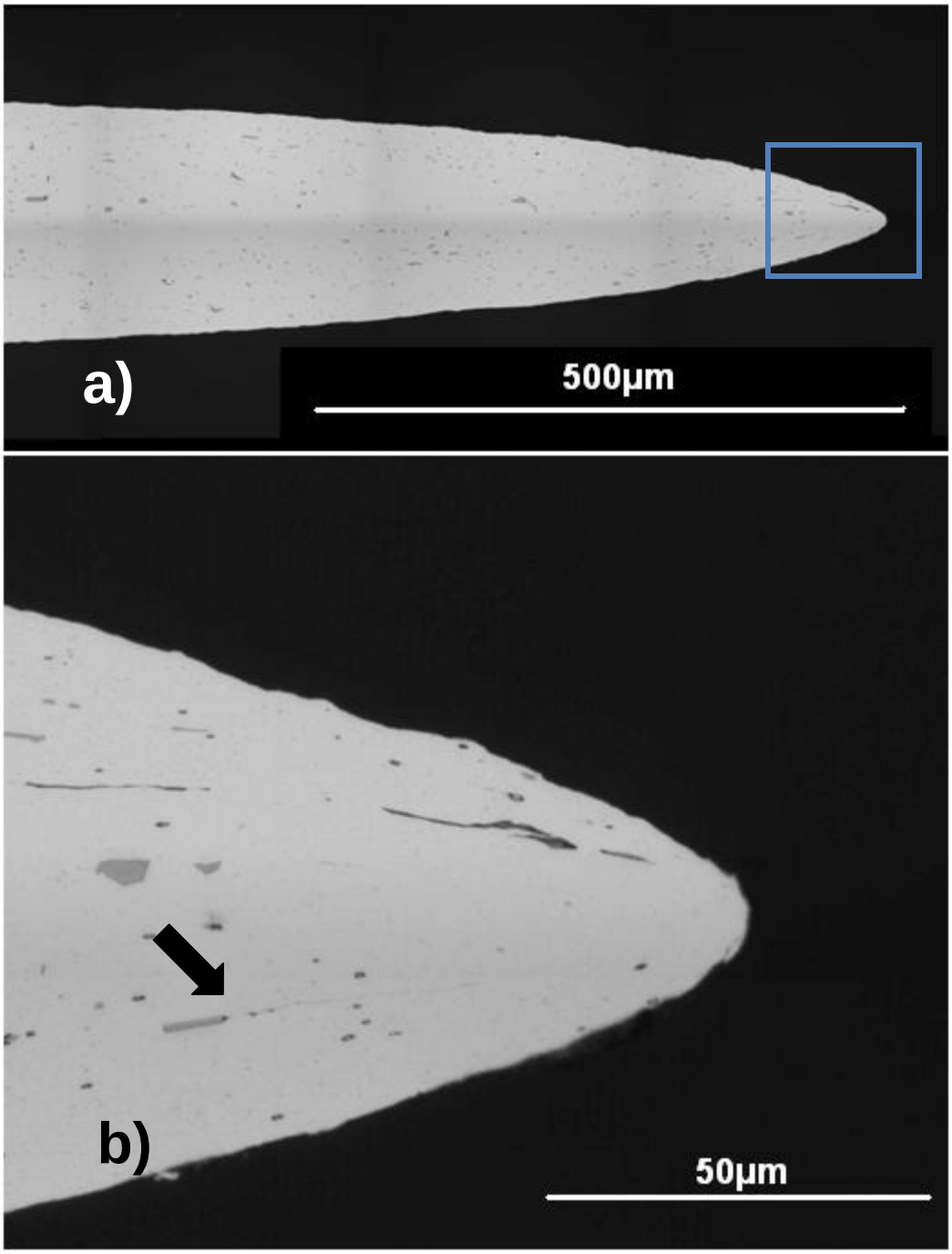

Figure 5.64: Through-thickness view of a T4P sample tested at 500°C and $6.7x10^{-1}s^{-1}$ a) overall view of fracture area and b) insert view (images by Dr. Sooky Winkler).

5.3.4.2 FG Material

The average area fraction of voids for the FG material are shown in Figure 5.65. This graph shows that under all conditions examined except at 500°C and $5.0x10^{-4}s^{-1}$, the area fraction of voids is less than 1%; at this condition, the fraction of voids is greater than 3.5%.

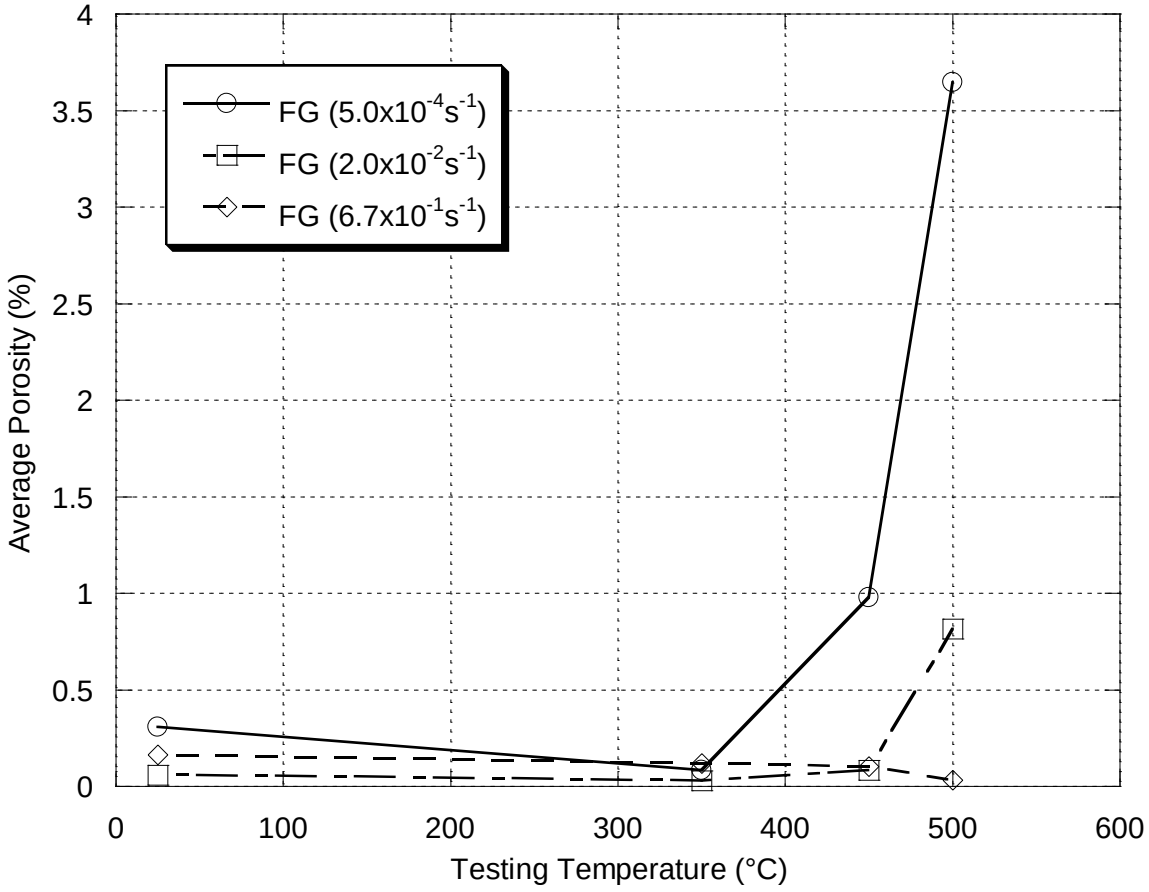

Figure 5.65: Average area fraction of voids in the through-thickness plane of FG samples tested at elevated temperature, measured from 0-3mm from the fracture surface (data by Dr. Sooky Winkler).

Figure 5.66 shows the through-thickness view of a FG sample tested at 350°C and the lowest strain-rate. Here, the sample can be seen to thin down to a point with minimal cavitation. The insert view shows a small void at the fracture tip. At the same temperature, and the highest strain-rate (Figure 5.67), the fracture surface is similar, with a slightly more jagged fracture tip, suggesting a higher concentration of voids. The insert view shows one large void stringer originating from a large particle.

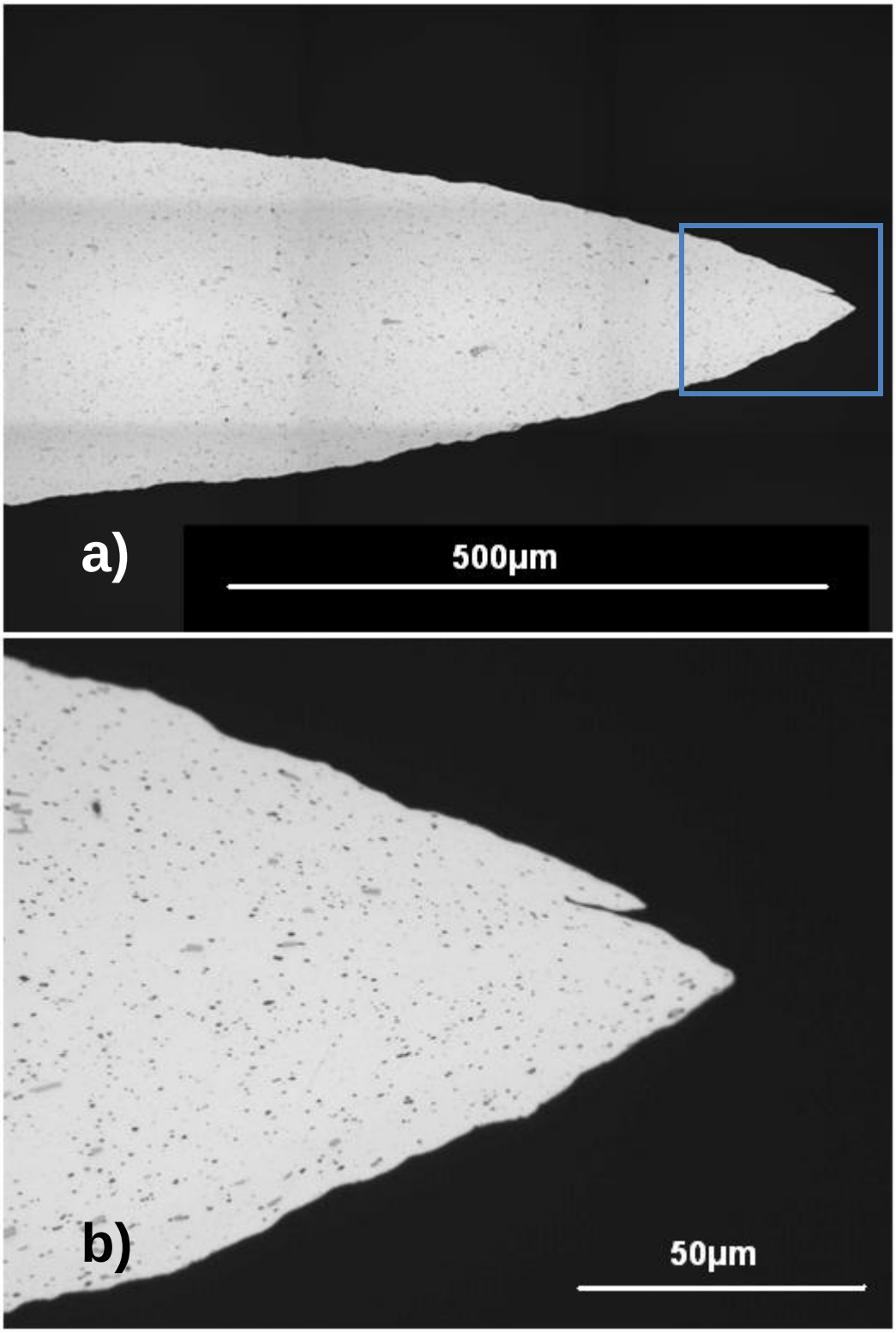

Figure 5.66: Through-thickness view of a FG sample tested at 350°C and $5.0x10^{-4}s^{-1}$ a) overall view of fracture area and b) insert view (images by Dr. Sooky Winkler).

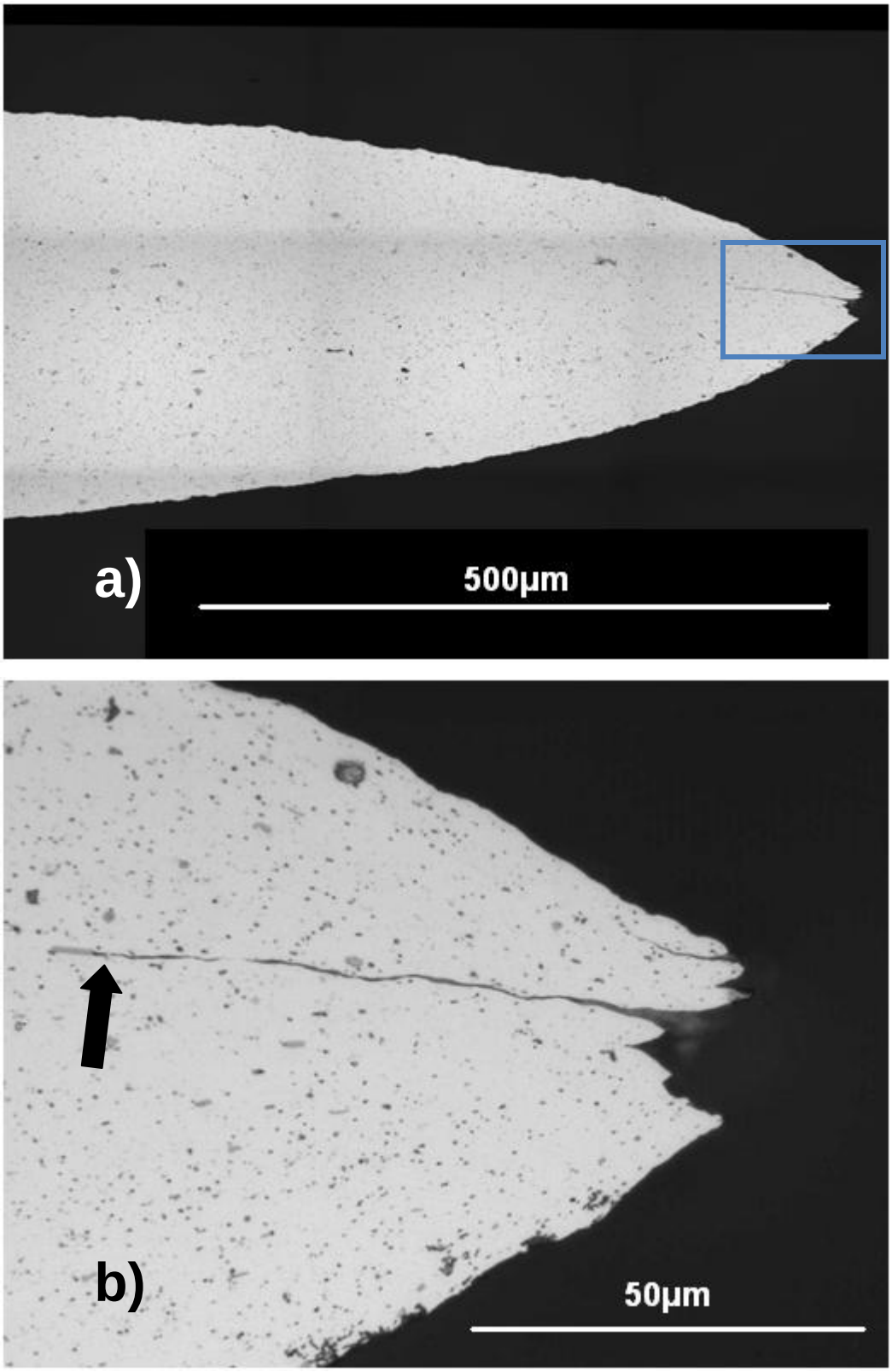

Figure 5.67: Through-thickness view of a FG sample tested at 350°C and $6.7x10^{-1}s^{-1}$ a) overall view of fracture area and b) insert view (images by Dr. Sooky Winkler).

The condition with the highest area fraction of voids, 500°C and $5.0x10^{-4}s^{-1}$, is shown in Figure 5.68. The fracture surface of the sample does not thin down to a point, and the fracture surface is very jagged. A number of large voids can be seen throughout the sample. In the insert view, it can be seen that the voids initiate (or terminate) at large particles, and these particles appear to have lost cohesion with the matrix. Contrary to the low strain-rate case, at the highest strain-rate at 500°C, seen in Figure 5.69, the area fraction of voids is significantly reduced, and the sample thins down to a point. The insert view shows a very small void that has initiated through de-cohesion of a large particle.

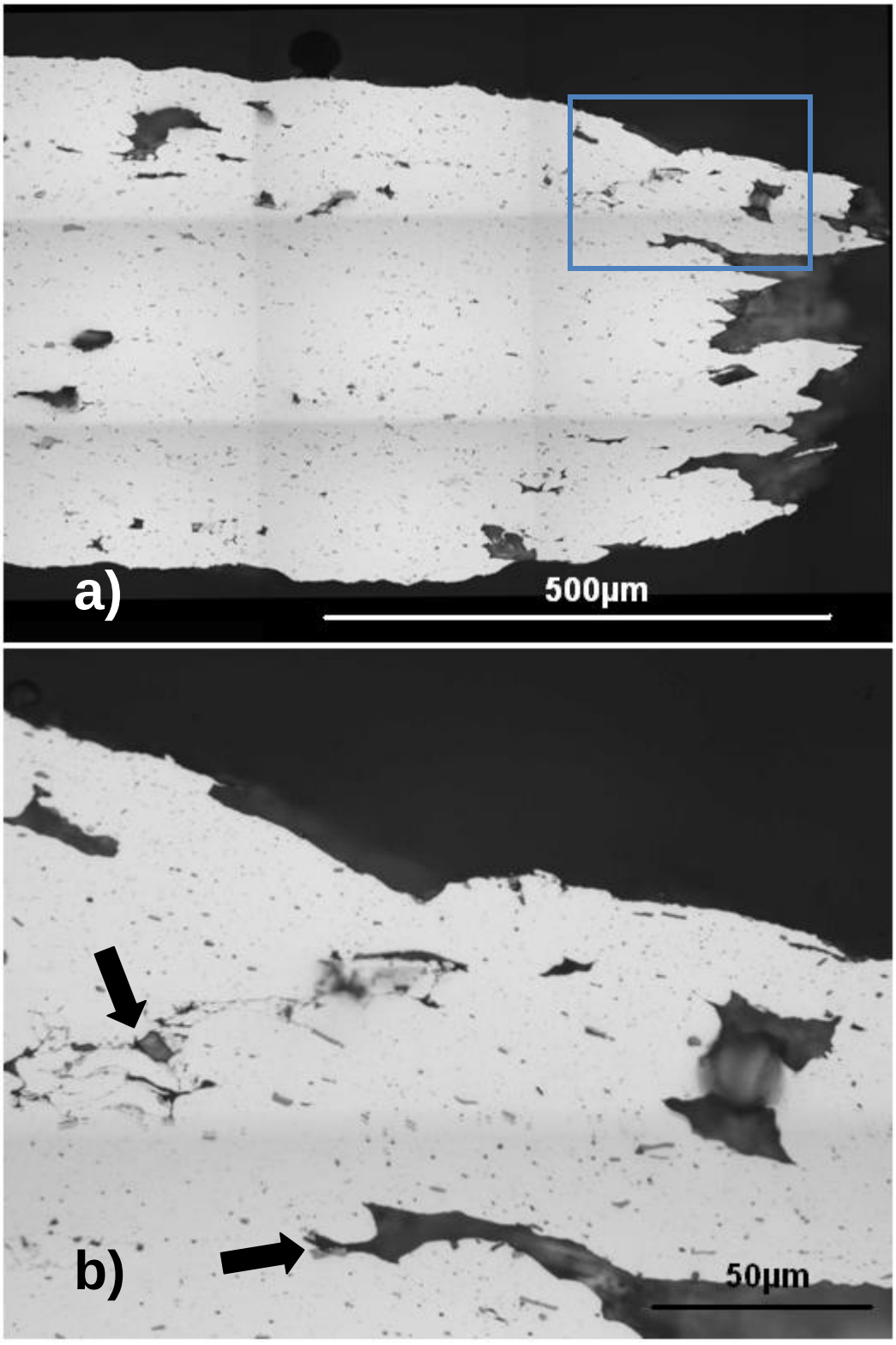

Figure 5.68: Through-thickness view of a FG sample tested at 500°C and $5.0x10^{-4}s^{-1}$ a) overall view of fracture area and b) insert view (images by Dr. Sooky Winkler).

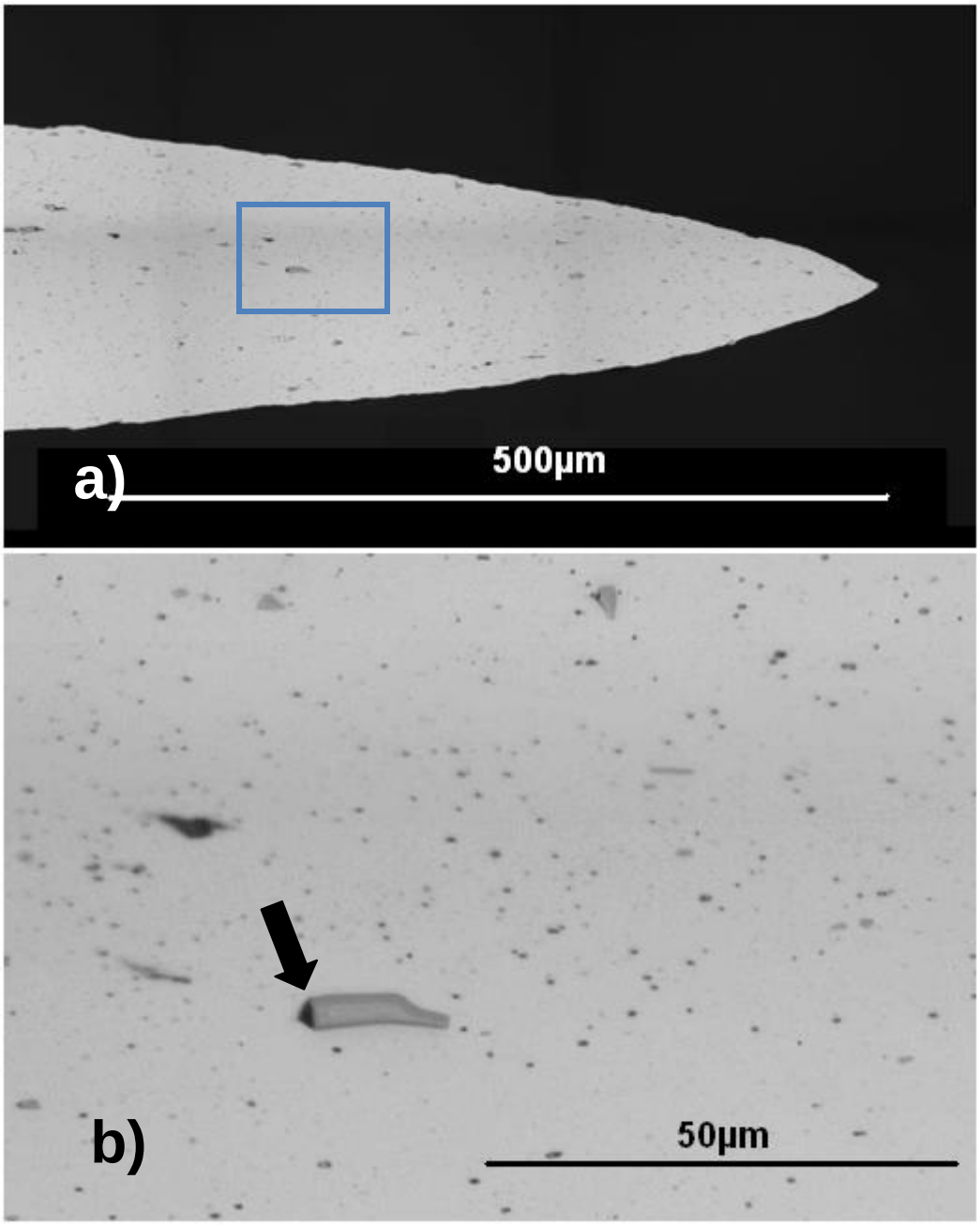

Figure 5.69: Through-thickness view of a FG sample tested at 500°C and $6.7x10^{-1}s^{-1}$ a) overall view of fracture area and b) insert view (images by Dr. Sooky Winkler).

5.3.5 Fracture Analysis

The fracture surfaces of select tensile samples are examined in this section. To help highlight the most significant changes in the mechanical behaviour, 3 temperatures, 350°C, 450°C and 550°C and 3 strain-rates, $5.0x10^{-4}s^{-1}$, $2.0x10^{-2}s^{-1}$ and $6.7x10^{-1}s^{-1}$, are shown. In each figure, an overall image of the fracture surface is shown, followed by a higher magnification image taken at the middle, or tip of the fracture area; focus may be poor to the areas on either side of the fracture tip. Magnifications were chosen that best show the structure of the surface.

5.3.5.1 T4P Material

The fracture surface images of T4P samples tensile tested at 350°C are shown in Figure 5.70. At the lowest strain-rate, the fracture surface exhibits a heavily dimpled surface, over a wide area. With increasing strain-rate, the number of dimples decreases, and the area over which dimples are seen also decreases. On average, the dimples appear to be ~10μm in diameter at $5.0x10^{-4}s^{-1}$ and decrease in size with increasing strain-rate.

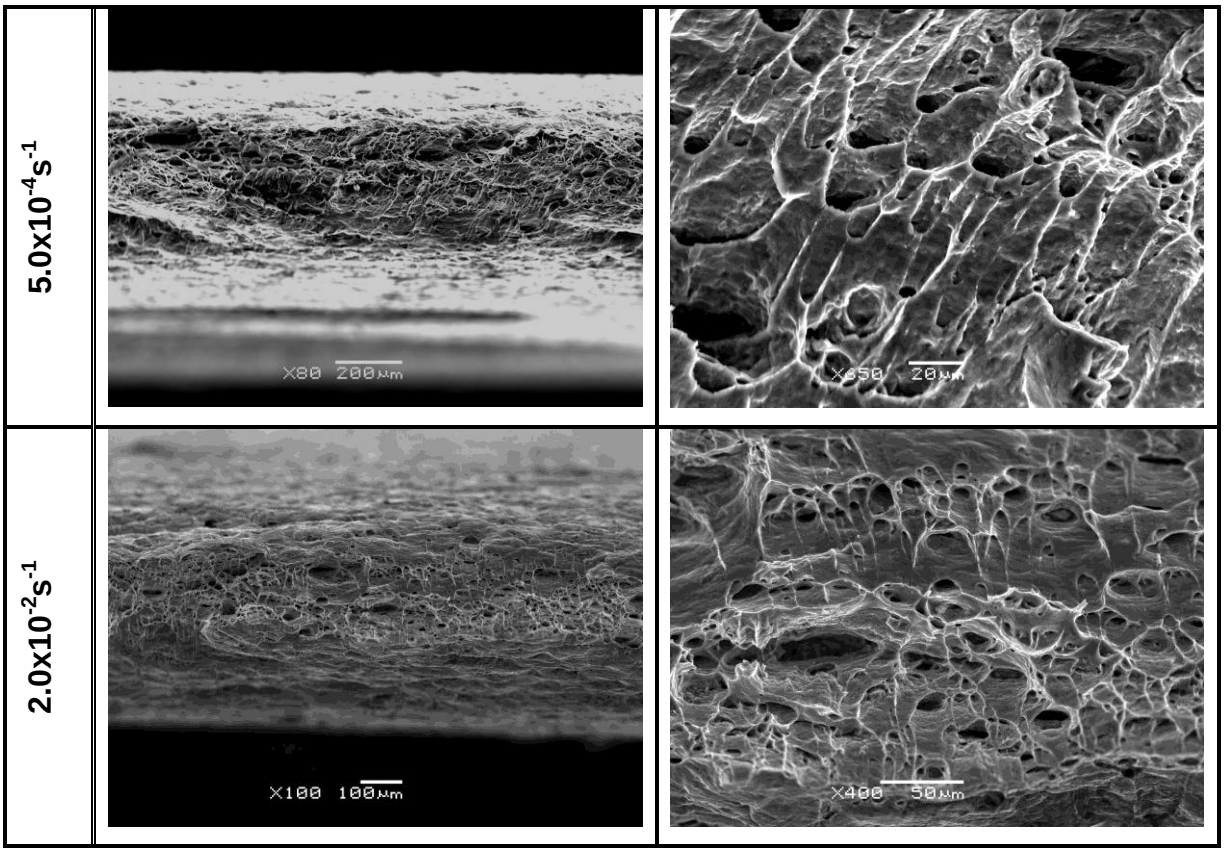

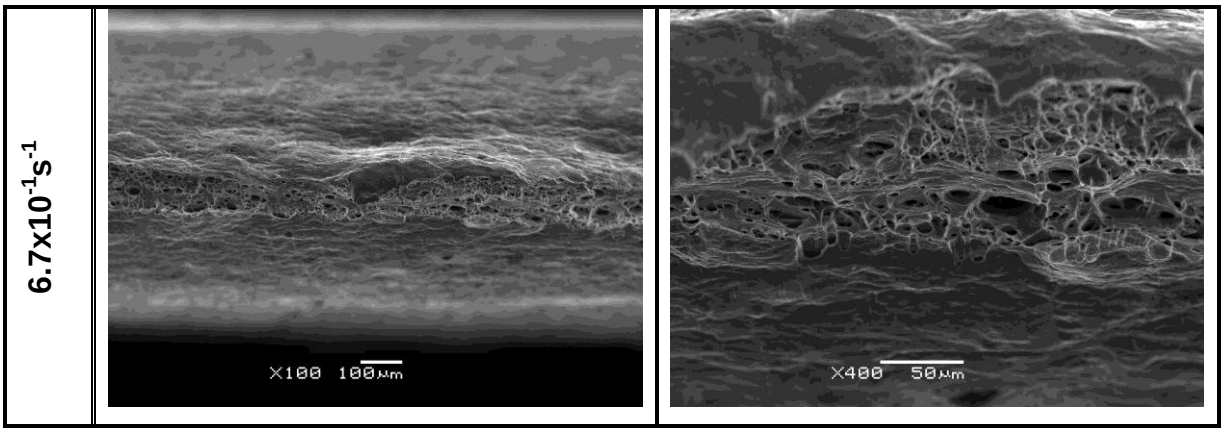

Figure 5.70: T4P sheet tensile tested at 350°C fracture surface images (SE mode).

At 450°C, Figure 5.71, very few dimples are visible at the fracture surface. The fracture surface itself, comes to a point. At the very tip of this point, a single line of voids can be seen. This is true for all strain-rates examined at this temperature.

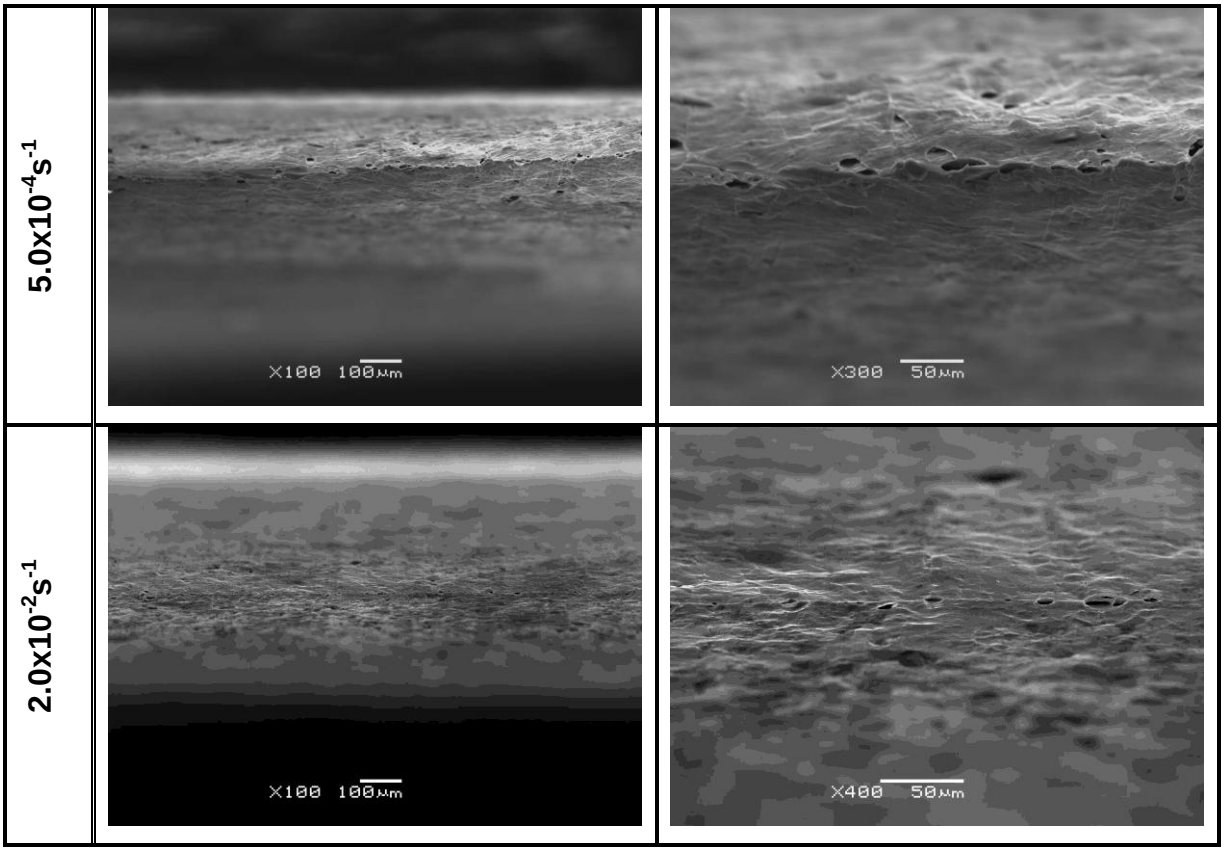

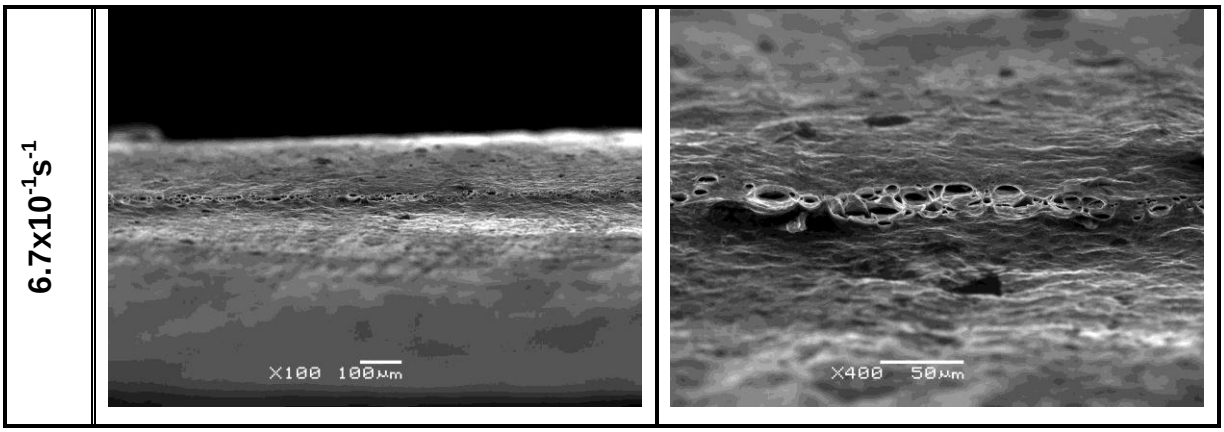

Figure 5.71: T4P sheet tensile tested at 450°C fracture surface images (SE mode).

At 550°C, Figure 5.72, the morphology of the fracture surface at the lowest strain-rate is very different than any seen at lower temperatures or higher strain-rates. Here, a very jagged fracture surface can be seen with very deep holes. The fracture surface does not thin down to a point at all. At $2.0x10^{-2}s^{-1}$, the fracture surface becomes similar to other conditions examined, thinning down to a point, with a small number of voids along the fracture tip. At $6.7x10^{-1}s^{-1}$, no voids are seen along the fracture tip.

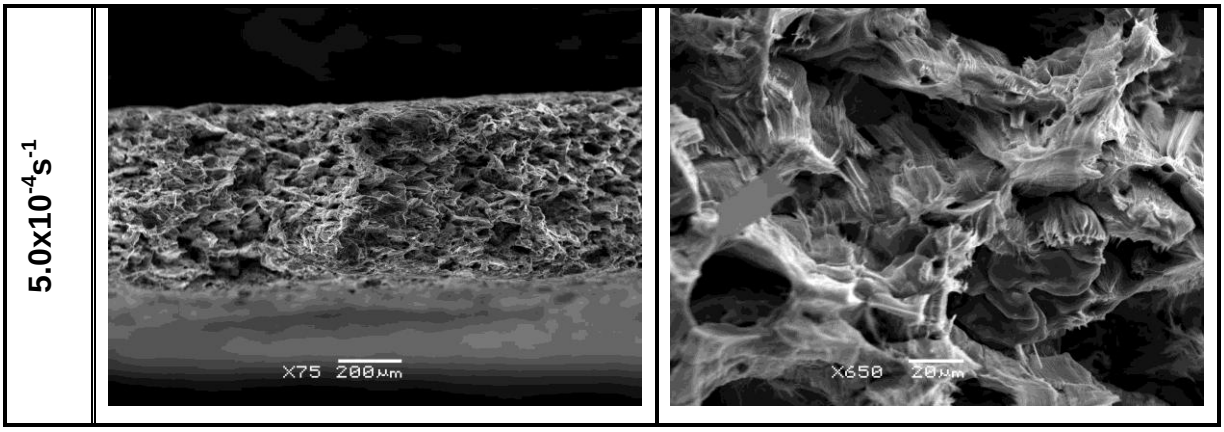

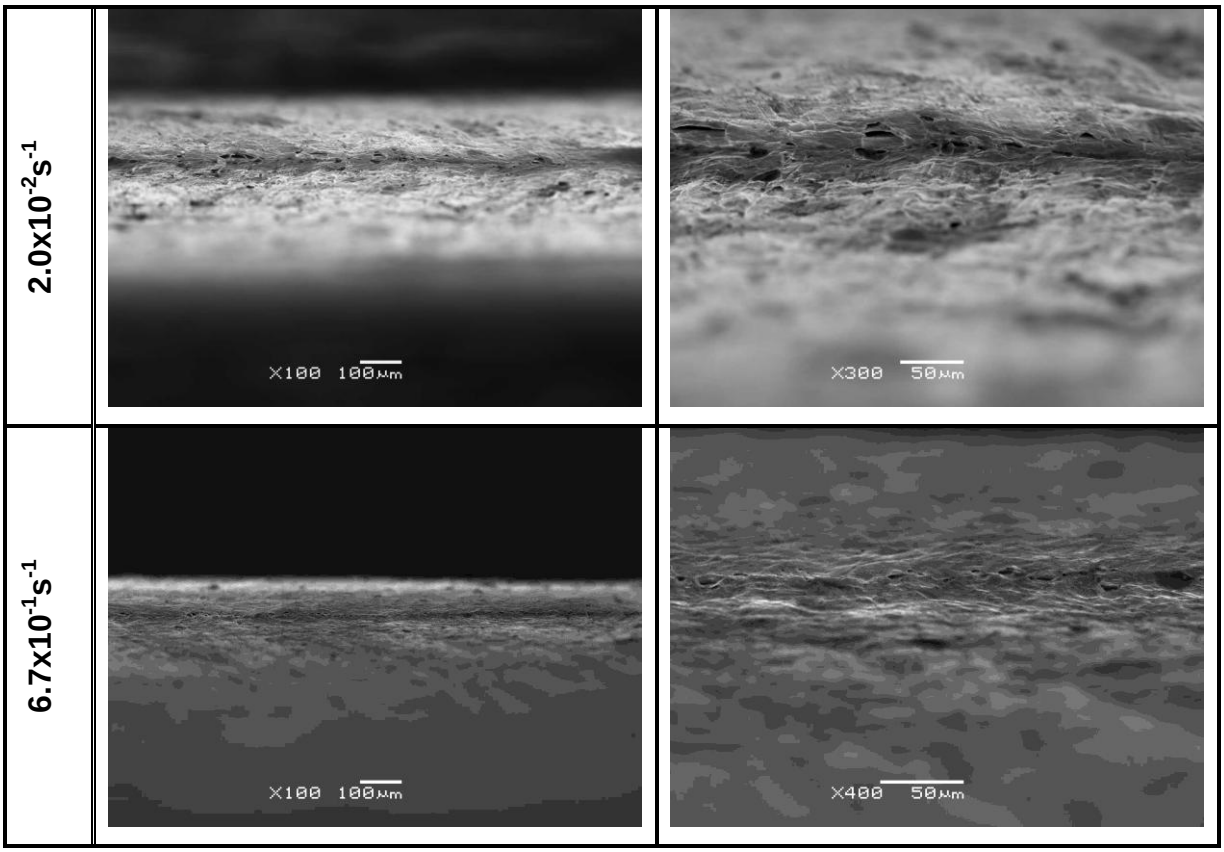

Figure 5.72: T4P sheet tensile tested at 550°C fracture surface images (SE mode).

5.3.5.2 FG Material

At 350°C, Figure 5.73, the FG material shows a very low level of voids along the fracture tip, particularly at the lowest strain-rate. The apparent number of voids increases slightly with increasing strain-rates.

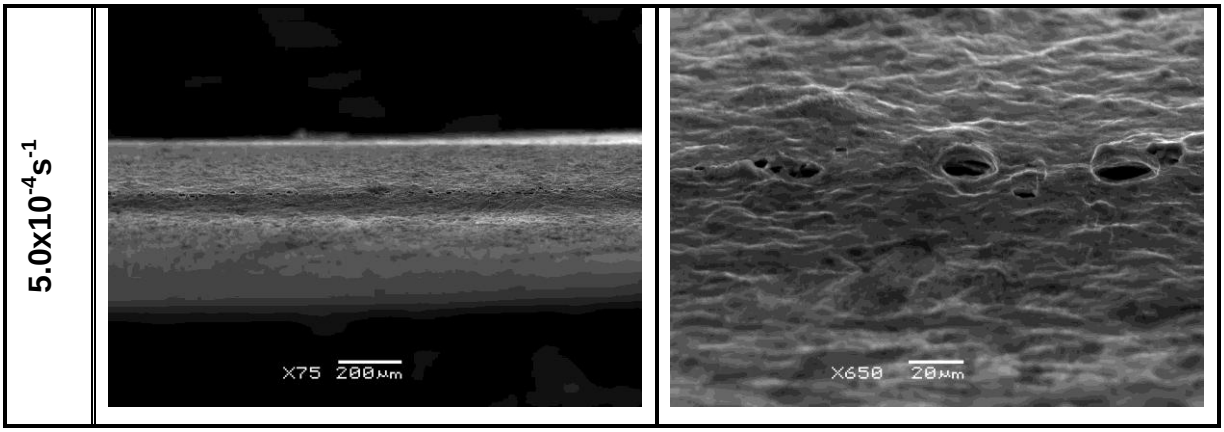

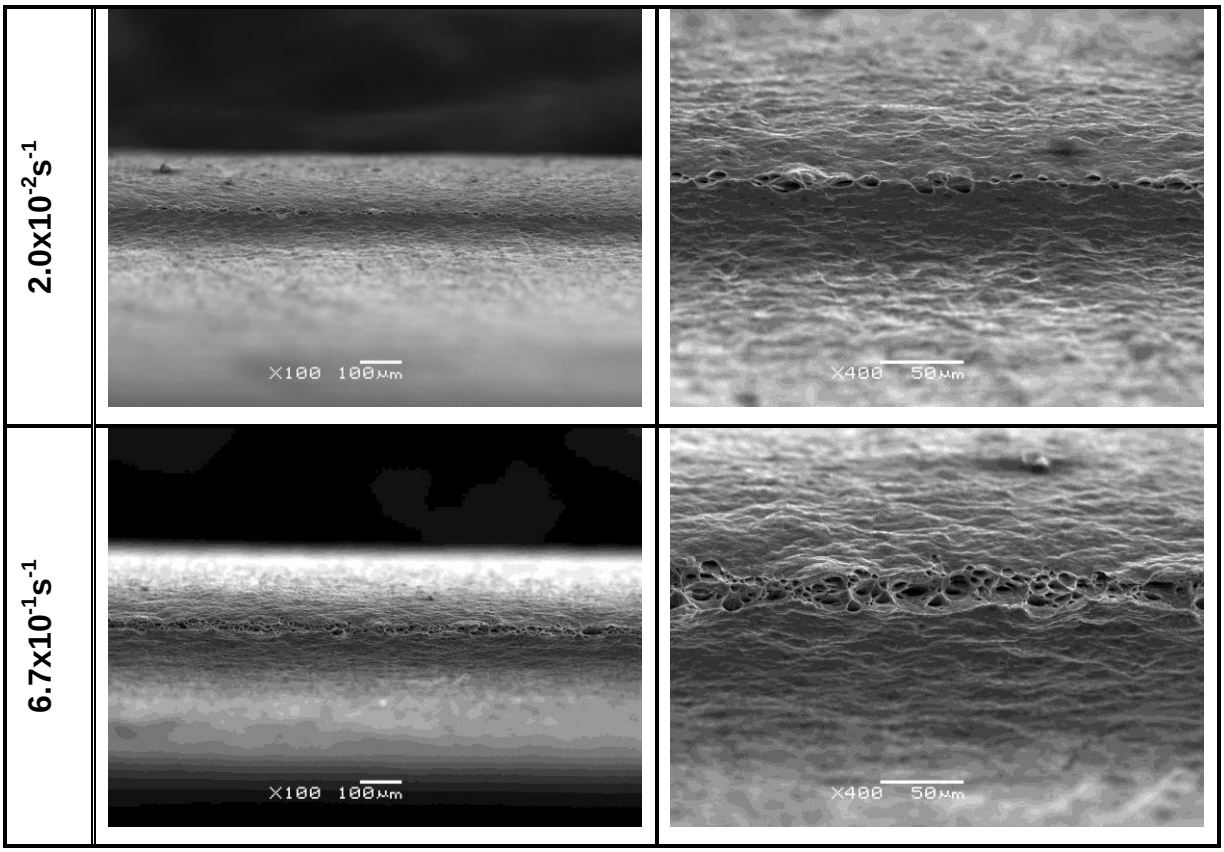

Figure 5.73: FG sheet tensile tested at 350°C fracture surface images (SE mode).

Figure 5.74 shows the fracture surface images at 450°C. A moderate number of voids are seen at the lowest strain-rate. These voids are not localized to the fracture tip, and are observed at many points along the failed surface. As the strain-rate increases, the voids become limited to just the fracture tip, and decrease in number and size.

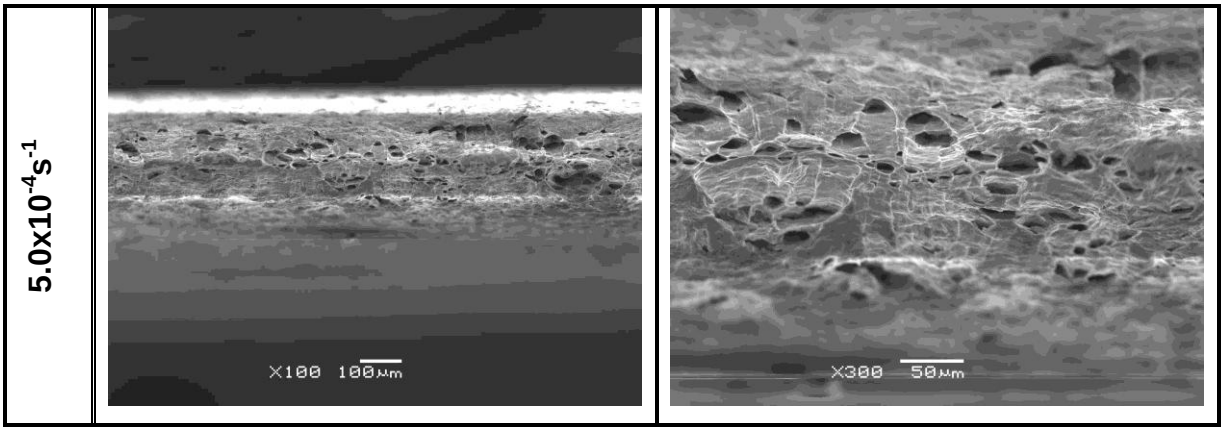

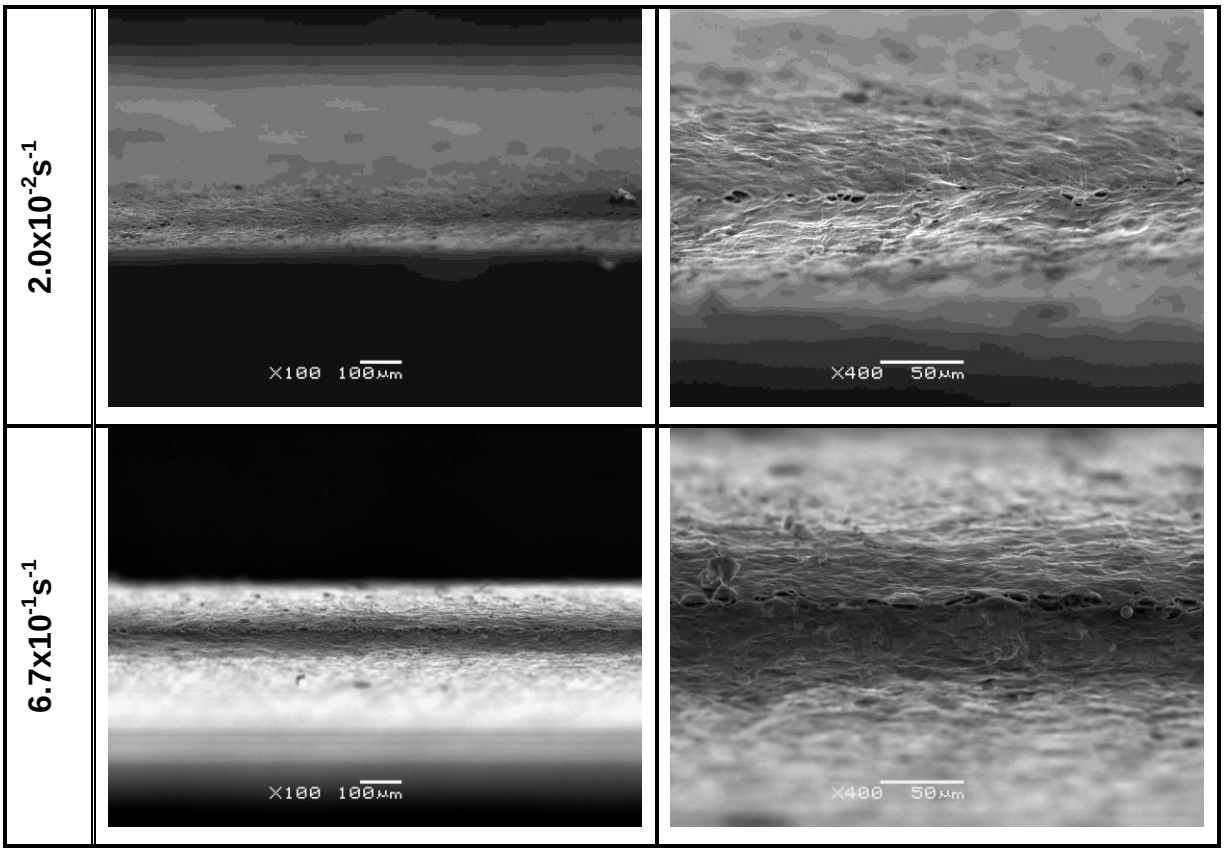

Figure 5.74: FG sheet tensile tested at 450°C fracture surface images (SE mode).

The fracture surface images at 550°C can be seen in Figure 5.75. At the lowest strain-rate, the fracture surface of the FG material is jagged, and fracture occurs over a large area. At higher strain-rates, the fracture zone thins to a point, and the number of voids decreases until there are very few voids visible at $6.7x10^{-1}s^{-1}$.

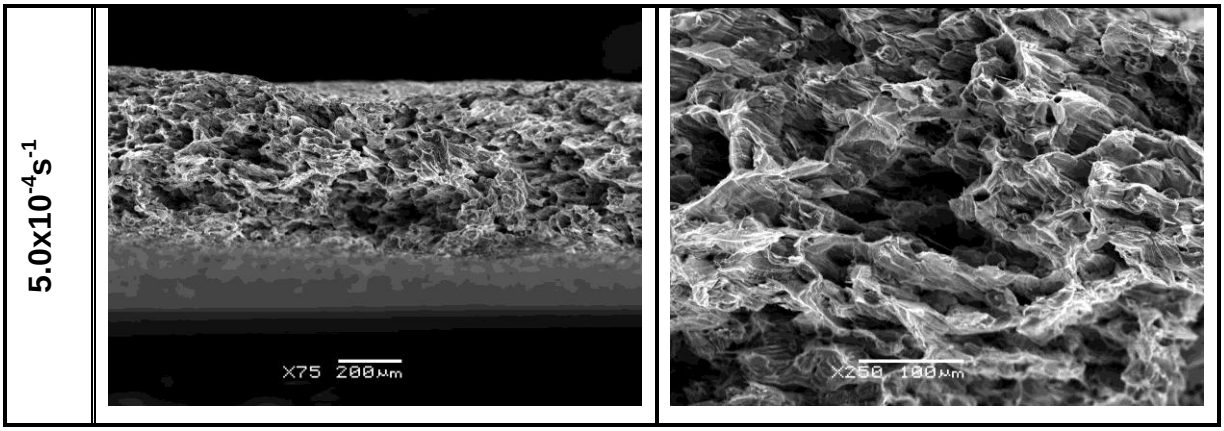

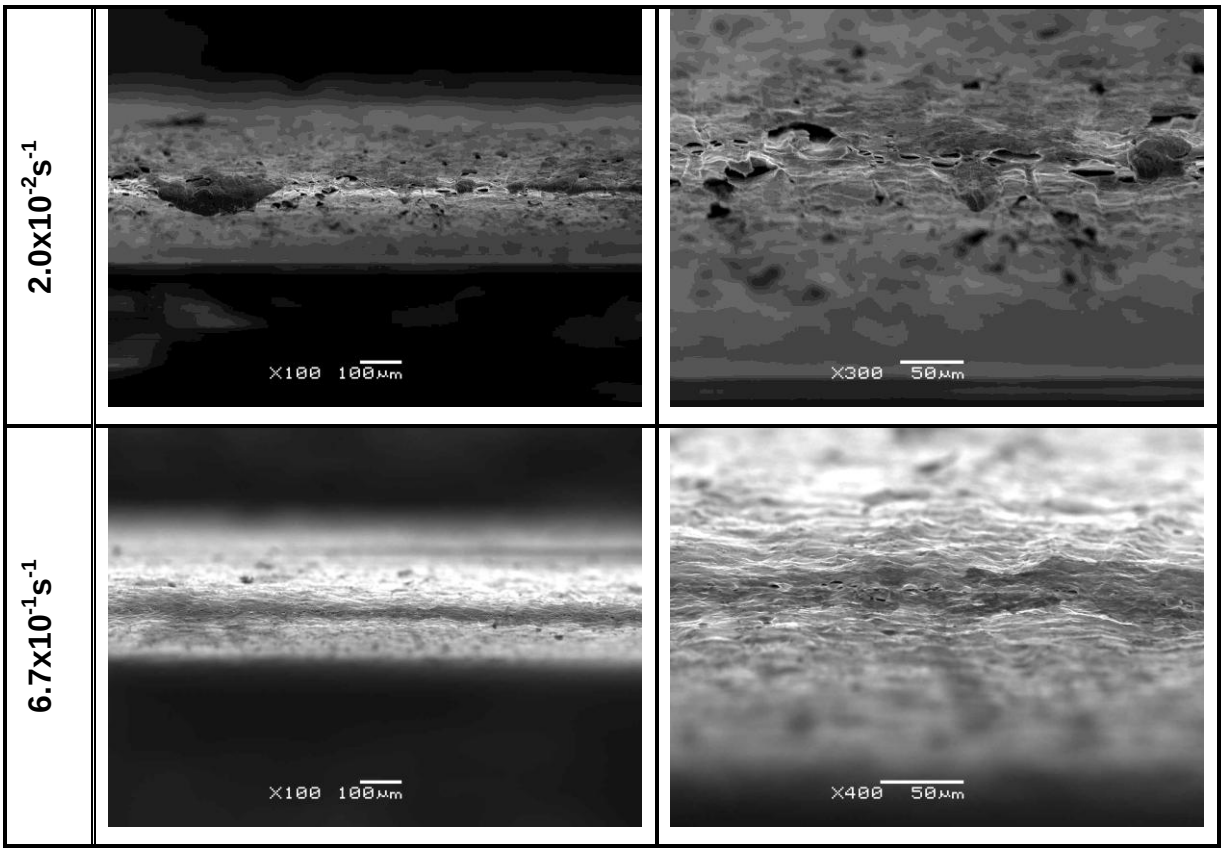

Figure 5.75: FG sheet tensile tested at 550°C fracture surface images (SE mode).

Chapter 6 Discussion

6.1 Introduction

In the following chapter, the results of the study will be discussed, examined and related to existing published knowledge. First, the effect of the microstructure on the deformation and failure behaviour at room temperature is discussed. Next, the deformation behaviour at elevated temperatures is examined, with emphasis placed on relating stress and strain behaviour to the initial microstructure and the microstructure produced during exposure to elevated temperature. Additionally, the strain-rate sensitivity and activation energy are discussed and related to the deformation behaviour. The effect of elevated temperature and deformation on the evolution of the grain structure is then discussed. Next, the effect of temperature and deformation on cavitation and failure is examined. Finally, the elongation to failure of the materials is examined.

6.2 The Effect of Microstructure on the Deformation Behaviour and Failure at Ambient Temperature

The most marked difference between behaviour of the two materials at room temperature is seen in the yield strength, as seen in Figure 6.1.

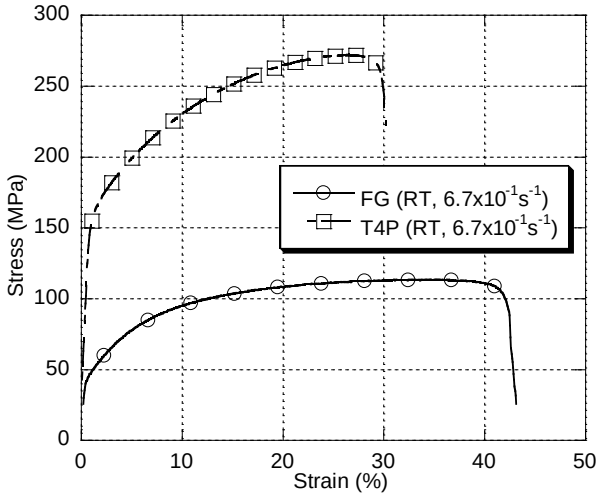

Figure 6.1: Comparison of the stress-strain curves of the FG and T4P materials at room temperature.

The T4P material has a yield strength of approximately 149MPa while the FG material has a yield strength of only ~41MPa. The two major microstructural differences between the two materials are the precipitate structure and the grain size. Examining the precipitate structure, the FG material is in an overaged state (final annealing stage is 20min@380°C), while the T4P material is in the underaged state (low temperature pre-aging plus possible natural aging during storage at room temperature). Overaged precipitates, such as those found in the FG material are non-shearable with large spacing between them. Therefore, they can be easily bypassed by dislocations and hence do not significantly strengthen the material [18]. The T4P material, in the underaged condition, will contain many nano-sized precipitates [115,120] which can effectively block dislocations.

If the difference in the materials' grain sizes is considered, the Hall-Petch relationship (Equation 2.2) should hold. The Hall-Petch constant, k_y, has been extensively studied and recorded in literature for aluminium and aluminium alloys. For pure aluminium, k_y=0.068 [24] and for a 6000 series aluminium in the T4 state (therefore similar to our T4P material condition), k_y was found to be statistically zero [136]. This suggests that grain size has little effect on the strength of these AA6xxx alloy sheets, at least in the range of grain sizes we are concerned with, and therefore, the discrepancy in strength between the T4P and FG materials at ambient temperature can be attributed solely to the initial precipitate structure.

From Figure 6.1, it can be seen that there is a difference in the work hardening rate (WHR) between the two materials, as indicated by the slope of the stress-strain curve beyond the yield point. Work hardening can be seen as a competition between dislocation storage and thermally dependent dynamic recovery [137]. Obstacles such as non-shearable precipitates can lead to increased storage of dislocations, and therefore more work hardening. The stress-strain plots show that the T4P material has a significantly higher work hardening rate than the FG material. The WHR of the FG material is particularly low between 20% and 40% elongation. It has been shown previously in AA6111 by Poole *et al.* [138] that the material in the supersaturated solid

solution condition exhibits a very high work hardening rate, likely caused by the decreased rate of recovery created by the presence of solute atoms [139]. As the material is aged, the WHR decreases until the precipitates reach the point where they are no longer shearable, after which, the initial (i.e. $\sigma = \sigma_y$) WHR sharply increases, while the WHR at higher elongations decreases dramatically [138]. In the case of the T4P material, the material is in the underaged condition, with significant amounts of solute still in solution, which creates its high WHR. In the case of the FG material, the material is significantly overaged, with precipitates that are non-shearable and that could therefore lead to increased storage of dislocations. The amount of work hardening that the precipitates can contribute is, however, dependent on the density of the precipitates [138], and for a heavily overaged material such as the FG material, the density is very low, leading the material to behave more closely to pure aluminium. As material failure at room temperature is often considered in terms of a critical stress, such as Tresca's critical shear stress criterion [125], it is to be expected that materials with higher WHR will reach this stress at an earlier strain, and therefore fail earlier. The T4P and FG materials followed this behaviour as the T4P material with the higher WHR rate failed at lower strains than the FG material. Similarly, a lower yield stress can allow longer elongations before the critical stress is reached, allowing materials with lower yield stresses to achieve larger elongations to failure; the T4P and FG materials follow this trend. Increased fracture strain with decreasing yield strength has been similarly reported for AA6111 by Lloyd [125].

The fracture surfaces of the FG and T4P material show differences, as well. In the T4P material (Figure 5.10) evidence of ductile shear failure is observed in the elongated dimples. This matches well with the ductile shear failure caused by the void sheeting mechanism of failure, commonly seen in precipitation hardened aluminium alloys [125]. Additionally, the fracture surface is angled at 45°, which matches well with a sample that had failed upon reaching a critical shear stress, resulting from the propagation of a crack along the highest stress path (i.e. brittle). In the FG material (Figure 5.12), the fracture surface exhibits a cup/cone morphology. This suggests that failure was due to the formation of voids in the interior of the sample, which eventually

led to the failure of the sample, rather than a brittle shear type failure [140]. In both cases, large particles close to the fracture surface were seen to crack, or lose cohesion to the matrix material. The voids created by these particle failures did not appear to grow substantially in the observed samples; however, they would act as excellent crack initiation points, and may have played a large role in the initiation of failure in both materials. The micrographs show that the FG sample thinned more substantially at the fracture tip than the T4P material. The dimples in the FG sample appear deeper suggesting that voids at the fracture surface were able to grow to a larger size before failure. This is likely due to the much lower stresses seen in the FG material during deformation, and allowed the larger elongation to failure of the FG material. In both materials, necking was localized to an area very close to the fracture tip, although more pronounced in the T4P material. This is indicative of a low strain-rate sensitivity, as strain-rate sensitivity is a primary factor in retarding neck formation [11]. This low strain-rate sensitivity was seen in the very slight increases in flow stress seen in each material as the strain-rate was increased. It has been shown in literature that similar alloys do indeed exhibit a very low strain-rate sensitivity at room temperature [125,137].

6.3 The Effect of Initial Microstructure on the Deformation Behaviour at Elevated Temperatures

In this section, the deformation behaviour between 350°C and 550°C of the FG and T4P materials is discussed.

6.3.1 Stress-Strain Relationships

Comparing the peak stresses of the T4P and FG materials, it is clear that at lower temperatures (<450°C) the materials behave very differently, while at higher temperatures (>450°C) they behave similarly, as seen in Figure 6.2.

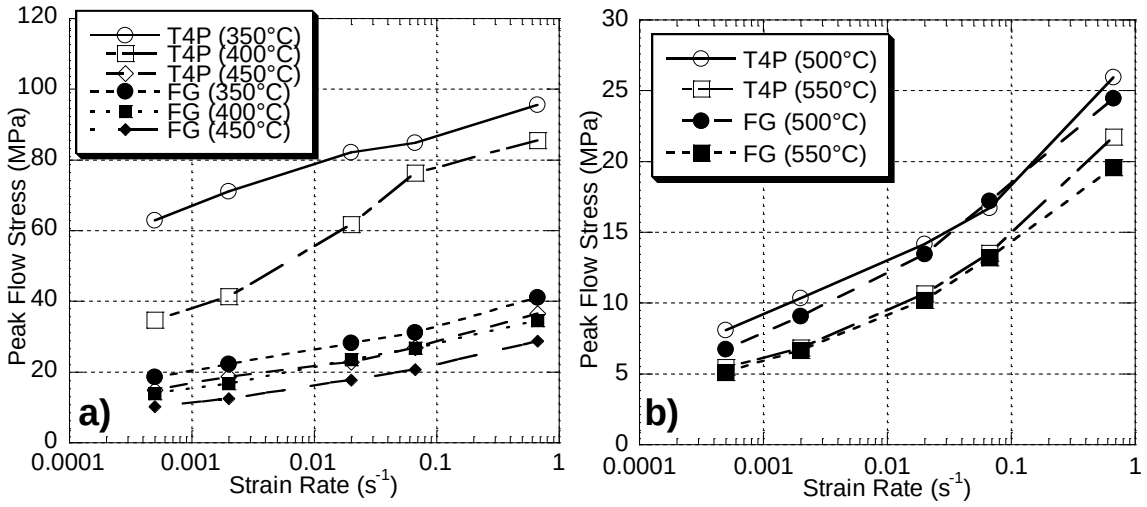

Figure 6.2: Comparison of the peak flow stress of the FG and T4P materials at a) low temperatures and b) high temperatures.

Examining the stress-strain curves of the T4P and FG materials at 350°C and 400°C, the T4P material exhibits much higher stresses during deformation than the FG material. As seen in Figure 6.2, the elevated stress of the T4P material is more prominently seen at high strain-rates. The difference in the stresses (σ_{T4P}-σ_{FG}) at each temperature and strain-rate is listed in Table 6.1.

Table 6.1: Peak stress difference between the two materials in each condition (values in MPa)

Strain-Rate (s^{-1})	σ_{T4P}-σ_{FG} (MPa)				
	350°C	400°C	450°C	500°C	550°C
$5.0x10^{-4}$	44.2	20.8	4.7	1.4	0.3
$2.0x10^{-3}$	48.8	24.6	6.3	1.3	0.2
$2.0x10^{-2}$	53.8	38.1	5.1	0.7	0.5
$6.7x10^{-2}$	53.7	49.5	6.2	0.5	0.3
$6.7x10^{-1}$	54.5	51.0	7.7	1.5	2.1

This temperature and strain-rate relationship suggests that the presence of precipitates is responsible for the elevated stresses. Small, closely spaced precipitates act as obstacles for dislocation glide, similar to their effect at room temperature, however, at elevated temperatures, the primary method of bypassing obstacles in aluminium alloys is dislocation climb [26], rather than Orowan looping or particle shearing. The elevated

stresses seen at the low temperatures and high strain-rates of the T4P material can be indicative of the increased stresses that are required to produce the climb required to bypass an array of particles. Grain size may play an underlying role in the stress difference, however it is impossible to distinguish it from the effect of the precipitates in this study. A fine grain size increases the area fraction of grain boundaries and, as diffusion rates are higher along grain boundaries [18], the total average diffusion rate will also be increased. As dislocation climb is dependent on diffusion, this could make climb easier in the FG material, leading to the lower overall stress required to deform the material. Static ageing of the T4P material at 350°C and 400°C (Figure 5.14) revealed that a fine distribution of small, elongated precipitates were present within the grains. At higher temperatures, the fine precipitates disappear, leaving only large precipitates. These fine precipitates explain the significantly higher stresses seen in the T4P material at the low temperatures. At high strain-rates, the stress difference increases, especially at 400°C. This can be explained by the kinetics of precipitation. Each sample is pre-heated for 2 minutes prior to a test. This produces a preliminary precipitate structure. At 350°C, the precipitates will be smaller and more closely spaced than the precipitates at 400°C (higher driving force for nucleation, lower rate of diffusion). During the test, the precipitate structure will continue to evolve, however the precipitates in the 400°C sample will coarsen more rapidly than the 350°C sample due to the increased rate of diffusion. At the lowest strain-rate, the test can take more than 20 minutes to complete, allowing the precipitates to coarsen significantly, while the highest strain-rate test takes only a few seconds to complete, leaving the precipitate structure very close to the pre-heat structure. The stress difference at the lower strain-rates is much lower at 400°C because of the increased rate of coarsening at this temperature. At 450°C, 500°C and 550°C, this strain-rate dependence is not seen. There are two possible reasons for this. First, the 2 minute pre-heat at these elevated temperatures could be enough time to cause the precipitates to become so heavily overaged that they are not providing any strengthening potential, or, second, the precipitates that provide strengthening (Q phase and β precipitates) simply do not form at these temperatures. Images of the precipitate structure suggest that the precipitates formed at 450°C are too heavily overaged to provide strengthening. At 500°C, some precipitates may form, but only a few, and they

are very coarse; at 550°C, the material becomes solutionized and does not contain precipitates.

The FG material does not show any large jumps in the stress at any temperature. Also, the rate-increase of stress with strain-rate (i.e. slope of the stress vs. strain-rate plot) is very consistent across all temperatures. This suggests that the time and temperature have very little effect on the precipitate structure, or the precipitate structure formed has very little effect on the stress in the material. Examination of the precipitate structure at different temperatures (Figure 5.17) shows that the microstructure does indeed change (i.e. precipitate coarsening and dissolution at higher temperatures). Therefore, we can conclude that the pre-existing structure does not contain any precipitation potential, nor does exposure to increasing temperatures further weaken the material. This matches well with the initial observations of the microstructure: an even distribution of equal sized (i.e. narrow size-distribution) large, overaged precipitates. Equal sized precipitates have a low driving force for coarsening due to the small concentration gradient of solute seen within the matrix [22].

In both materials, the trend was found that the strain to peak stress decreased with increasing temperature, and increased with increasing strain rate. This was especially evident at the lower temperatures. Also, on average, the strain to peak stress was lower in the T4P material than it was in the FG material. In an ideal tensile test, where the necking corrected true stress and strain could be measured, the peak stress would represent the point where hardening and recovery/recrystallization mechanisms are balanced; hardening increases the flow stress, and recovery reduces the flow stress [141]. However, as the difficulties with the measurement of the true stress preclude this simplification, necking must also be considered; necking reduces the cross-sectional area, which will lead to a drop in the measured stress. Ignoring the reduction in cross-sectional area, the later onset of the peak stress suggests either more hardening or less recovery is occurring. As hardening is primarily related to the amount of strain undergone (hardening rate, $H = \left(\partial \sigma_f / \partial \varepsilon\right)_t$ where σ_f is the flow stress [142]), less recovery must explain the extended strains to peak stress at lower temperatures. Recovery is a time

dependent process (recovery rate, $R = \left(\partial \sigma_f / \partial t\right)_\varepsilon$ [142]) which would explain why the peak stress occurred at higher strains, at higher strain-rates. Additionally, recovery is closely linked with diffusion (vacancy diffusion climb of dislocations into lower energy positions [143]), which becomes more rapid at higher temperatures. If necking were considered the only mechanism of stress reduction, separate from the recovery processes, the onset of necking would occur at or just before the peak stress (i.e. UTS). Correlating the effect of necking on the peak stress with the observed strain to peak stress results, this would mean that necking occurs earlier at high temperatures and low strain-rates. The enhanced hardening effect of the strain-rate sensitivity at higher strain rates (enters the rate equations as an exponent) could explain the fact that the strain to peak stress increases with strain-rate by delaying the onset of necking. However, as temperature increased, so too did the strain-rate sensitivity and elongation to failure, both of which would give evidence towards later onset of necking instead of earlier; this does not match with the observed results. Therefore, recovery rather than necking is most likely the dominant effect at higher temperatures. The onset of necking may have some effect on dictating the strain to peak stress; however, without accurate measurement of this factor, it cannot be separated from the effect of recovery. The earlier onset of peak stress in the T4P material when compared to the FG material could be caused by two factors. First, necking likely occurred later in the FG material as indicated by the much larger elongations to failure. Second, due to the fine precipitate structure in the T4P material, dislocations would quickly become tangled, leading the rapid hardening early, where as the FG material would be able to undergo more strain before peak hardening would occur.

At the highest temperature and lowest strain-rate, both materials exhibited a strain that, beyond which, the stress did not significantly decrease until failure of the sample (see Figure 5.21 and Figure 5.30). As these are engineering stress-strain curves, it is difficult to pinpoint the exact cause of this change in the rate-change of stress during the test, but a similar trend can be seen in the stress-strain curves in the tests done by Kim *et al.* [72] (see Figure 2.31). Kim *et al.* determined that deformation in those samples was the result of grain boundary sliding (m=0.5). A decrease in the negative slope of the

stress-strain curve with increasing strain could be caused by an increase in the hardening of the material or a decrease in the rate of recovery of dislocations in the structure. A decrease in the rate of recovery is expected as the subgrain structure reaches a steady state [141]. The other factor that could affect the rate-decrease of stress is the amount of necking; more uniform deformation would decrease the rate-decrease of stress in an engineering stress-strain curve. Less necking caused by an increase in the strain-rate sensitivity resulting from a change in the deformation mechanism (i.e. going from dislocation climb-controlled deformation to grain boundary sliding) would explain the similarities between the data in this study and those by Kim *et al.* [72]. This suggests that grain boundary sliding possibly occurs in both materials at 550°C and the lowest strain rate.

6.3.2 Strain-Rate Sensitivity and Activation Energy

6.3.2.1 High Temperatures (500°C-550°C)

The strain-rate sensitivity and activation energy for deformation were determined from the tensile test data and tabulated in

Table 5.5 (T4P) and Table 5.8 (FG). The deformation behaviour and therefore values of *m* and *Q* of both materials at 500°C and 550°C can be seen to be very similar in both materials. At these temperatures, the strain-rate sensitivity is just below 0.2 (or *N* is slightly greater than 5). This matches well with the strain-rate sensitivity associated with dislocation climb [26]. Also, the activation energy for deformation found for 500°C-550°C is approximately 134kJ/mol, which is close to the activation energy for self diffusion in aluminium (142kJ/mol) [18]. The activation energy is the energy required to by pass an obstacle by the deformation mechanism. This suggests that at the highest temperatures, both materials are deforming by the same mechanism, dislocation climb controlled by the self diffusion of aluminium. While the observed activation energy is also similar to that of the diffusion of Mg in aluminium, 136kJ/mol [134], it is unlikely that this is the rate controlling mechanism as this would suggest a solute drag (SD) mechanism of deformation; the solute content of the alloy is lower than that of alloys that traditionally see SD and the observed strain-rate sensitivity is much lower than would be expected in SD (m=0.3). As discussed in Chapter 2, deformation by dislocation climb is insensitive to grain size (p=0), leading to similar stresses despite the different grain size. It should be emphasized here that the strain-rate sensitivity and activation energies found here are *average* values over the entire range of strain-rates, which is a limitation of this method of determining the strain-rate sensitivity. If, for example, the activation energy at the highest strain-rate was lower than that seen at lower strain-rates due to power law breakdown, it would result in an average activation energy that was lower than expected for most strain-rates. Any speculation on the depression or inflation of the average activation energy would be impossible without more extensive testing on a much more narrow range of strain-rates, or the utilization of a different technique for measuring activation energy. Despite this, comparing these values to those found for similar materials shows good correlation. In the fine-grained 6000 series aluminium developed by Kaibyshev *et al.*[14], they found that in the range of 500°C-550°C, the strain-rate sensitivity is 0.2 at most strain-rates, only peaking to higher values (~0.4) in a short range of strain-rates (~$1x10^{-5}$-$1x10^{-3}s^{-1}$) [14]. A similar trend was found by Troeger and Starke [10] when they tested their fine-grained material, although they only tested under a much smaller range of strain-rates. They showed that the strain-rate sensitivity peaked to 0.4-

0.5 at a strain-rate of $2x10^{-4}s^{-1}$, with lower strain-rate sensitivities seen at lower and higher strain-rates [10]. In both of these studies, these increases in the strain-rate sensitivity were related to the onset of grain boundary sliding within the material [10,14]. In the load relaxation tests conducted by Park *et al.* [15] on a fine-grained 6000 series aluminium alloy, they also found that grain boundary sliding occurs between strain-rates of approximately $1x10^{-5}$ and $1x10^{-3}s^{-1}$at temperatures above 500°C [15]. The strain-rate sensitivity data from the tests in this project do not show evidence of grain boundary sliding in either material. There are several reasons that can explain this difference. First, only the lowest strain-rate that that was examined in this study occurs at the very end of the range of grain boundary sliding friendly strain-rates seen in other studies. It is therefore possible that for our materials, we did not examine the range of strain-rates where grain boundary sliding occurs. Second, the method employed to determine the strain-rate sensitivity averages the value over the entire range of strain-rates, overshadowing any possibility of observing higher values of *m* at the low end of the strain-rates. The other studies examined measured strain-rate sensitivity using strain-rate change tests [10,14] or load relaxation tests [15], which allow measurement of strain-rate sensitivity at an individual strain-rate. This does not mean that grain boundary sliding did not occur, and indeed there is evidence that, at the highest temperatures and lowest strain-rate, grain boundary sliding does occur (such as the stress-strain plot profile change, and the altered failure mechanism), however, without a more precise method of strain-rate sensitivity measurement, or a method of directly observing the sliding of grains, such as the use of microscratches on the surface of specially prepared tensile specimens prior to testing in order to observe grain rotation, it is impossible to definitively identify grain boundary sliding as a deformation mechanism.

6.3.2.2 Low Temperatures (350°C-450°C)

6.3.2.2.1 T4P Material

At 450°C, the strain-rate sensitivity starts to decrease in the T4P material. At 350°C the strain-rate sensitivity becomes very low, only 0.061. The strain-rate sensitivity of the T4P material at 400°C is actually higher than that at 450°C, which does not match the observed trend of decreasing *m* with decreasing temperature seen at all temperatures

in the FG material, and most temperatures in the T4P material. This anomaly can be explained by the effect of the precipitates on the stress. In section 6.3.1, it was shown that at 400°C, the precipitation strengthening is influenced heavily by the time at temperature, or strain-rate, while the precipitates at 450°C quickly became too overaged to provide any strengthening effect. This causes the material to have higher than expected stresses at high strain-rates at 400°C, and when combined with the method of strain-rate sensitivity measurement, leads to a higher value of *m* than would be expected.

The activation energy, *Q*, becomes very large at the low temperatures, as high as 512.6kJ/mol for the 400°C-450°C range. This large jump in the activation energy can be seen in the strain-rate vs. stress/E plot in Figure 6.3.

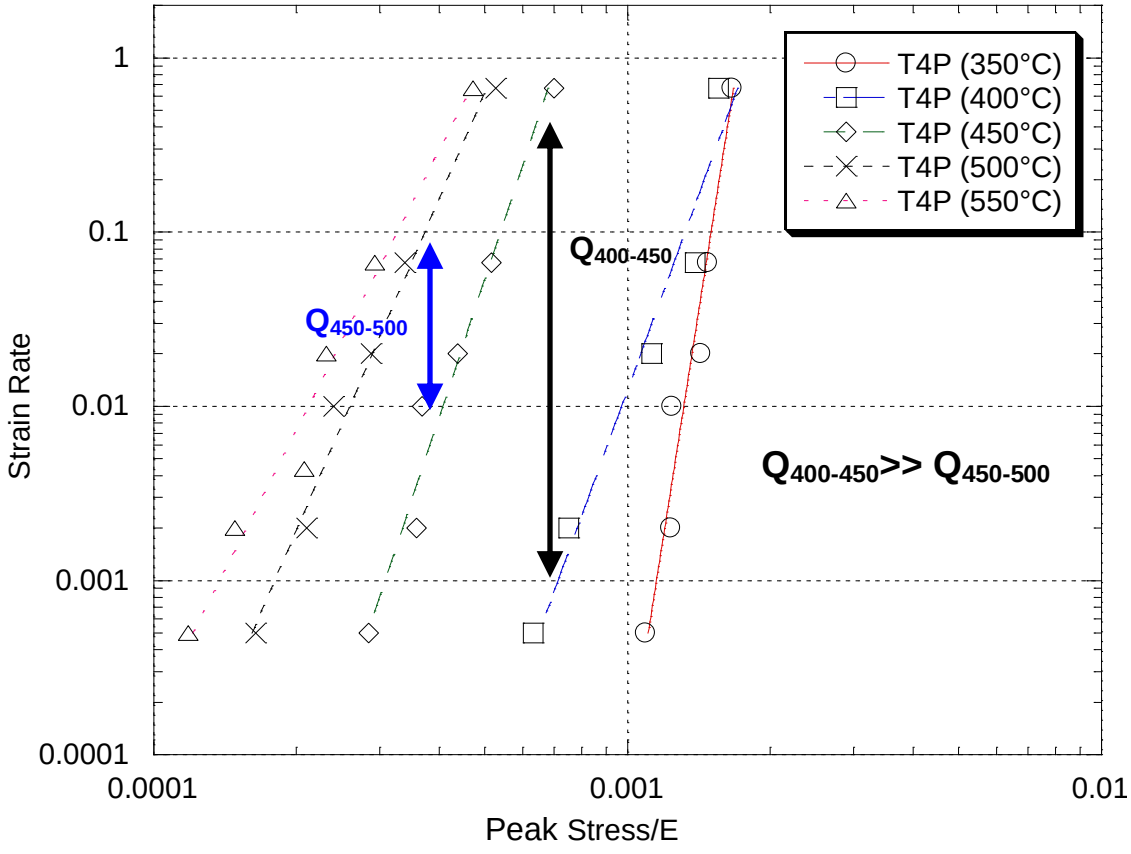

Figure 6.3: Activation energy change between low temperature and high temperature deformation of the T4P material

This high value of *Q*, which is calculated as the difference in strain-rate between two temperatures at a constant stress (see Equation 4.5), is caused by the anomalously

high stresses seen at the low temperatures. This effect is further seen in the normalized strain-rate vs. stress/E plot, shown in Figure 6.4.

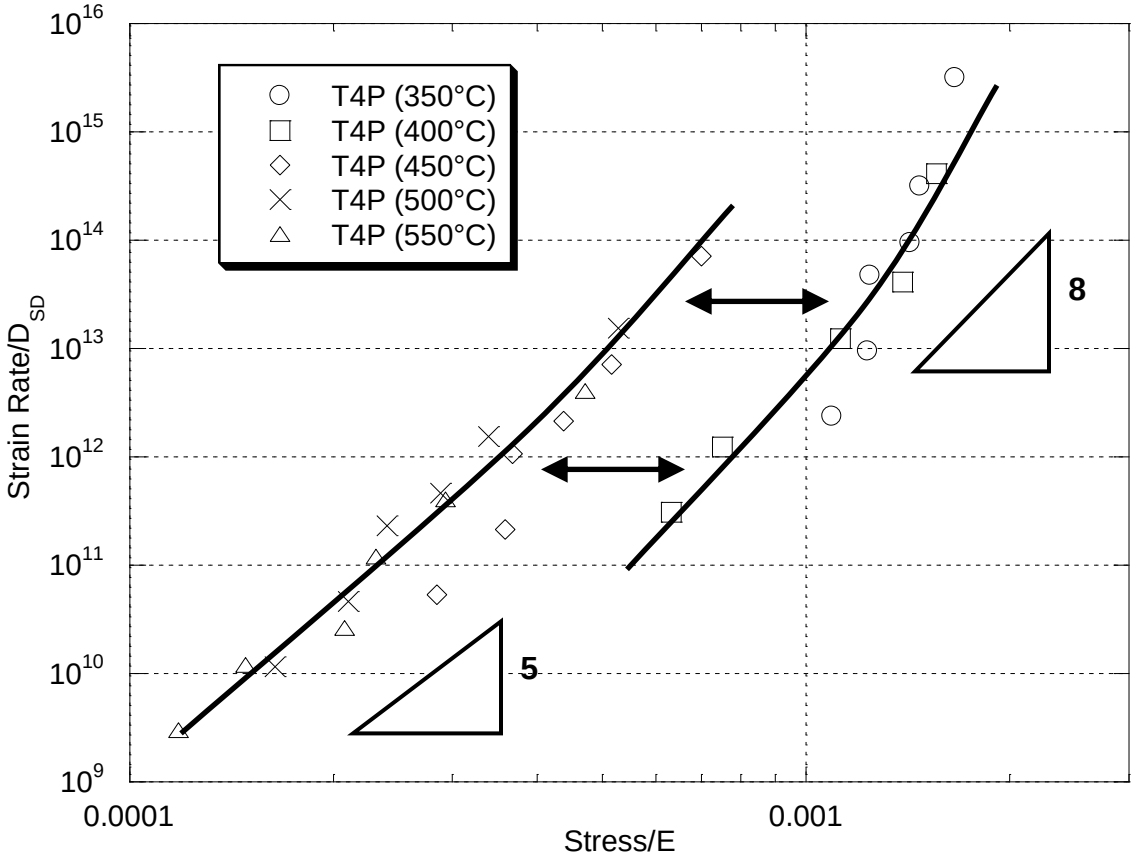

Figure 6.4: Discontinuity in normalized strain-rate vs. stress plot of the T4P material.

As can be seen, the data from the low temperature tests causes a discontinuous curve. This discontinuity matches well with data for particle hardened alloys; the material deforms at stresses higher than seen in the single phase alloy [48,51,53,133] (see Figure 2.9). At 450°C and 500°C the precipitates have dissolved or coarsened so much that they do not provide strengthening, and at 550°C, the material is in a solutionized state with no precipitates present. This discontinuity is associated with the appearance of a threshold stress during deformation [48,51,53,133]. The threshold stress is essentially an internal stress that is in opposition to the applied stress (i.e. $\sigma_{eff} = \sigma_a - \sigma_i$, where σ_{eff} is the effective stress, σ_a is the applied stress, and σ_i is the internal threshold stress). As the material requires the same effective stress to deform, an internal stress causes the required applied stress to be increased. The very large value of Q is also reported to be

associated with the existence of a particle hardened material [48,51,53,133]. From an atomistic point of view, the hardening particles, in our case, hardening precipitates, provide obstacles for dislocations. In order for deformation to continue, the dislocation must bypass the precipitate. In a single phase material, dislocations bypass small obstacles by dislocation climb, accommodated by self diffusion. Precipitates however, generate a stress field around themselves due to lattice mismatch in coherent and semi-coherent interfaces, and stresses caused by elastic mismatches [53]. Additionally, or, in the case where particles do not create a stress field (i.e. fully incoherent particles), primarily, an internal stress is generated by the extra dislocation line length created as the dislocation bows around the particle [53]. This stress is an extra obstacle the dislocation must overcome. As such, additional stress must be applied (the threshold stress) to bypass the obstacle. This also causes the activation energy for deformation to be inflated as the activation energy is the energy required to by pass an obstacle by the deformation mechanism plus the energy required to overcome the additional internal stress [48,51,53,133].

6.3.2.2.2 FG Material

In the FG material, the strain-rate sensitivity decreases with decreasing temperature, reaching a minimum value of 0.11 at 350°C. In contrast to the T4P material, when the data for the FG material is plotted on normalized strain-rate vs. stress/E plot (Figure 6.5), a single, continuous curve is generated.

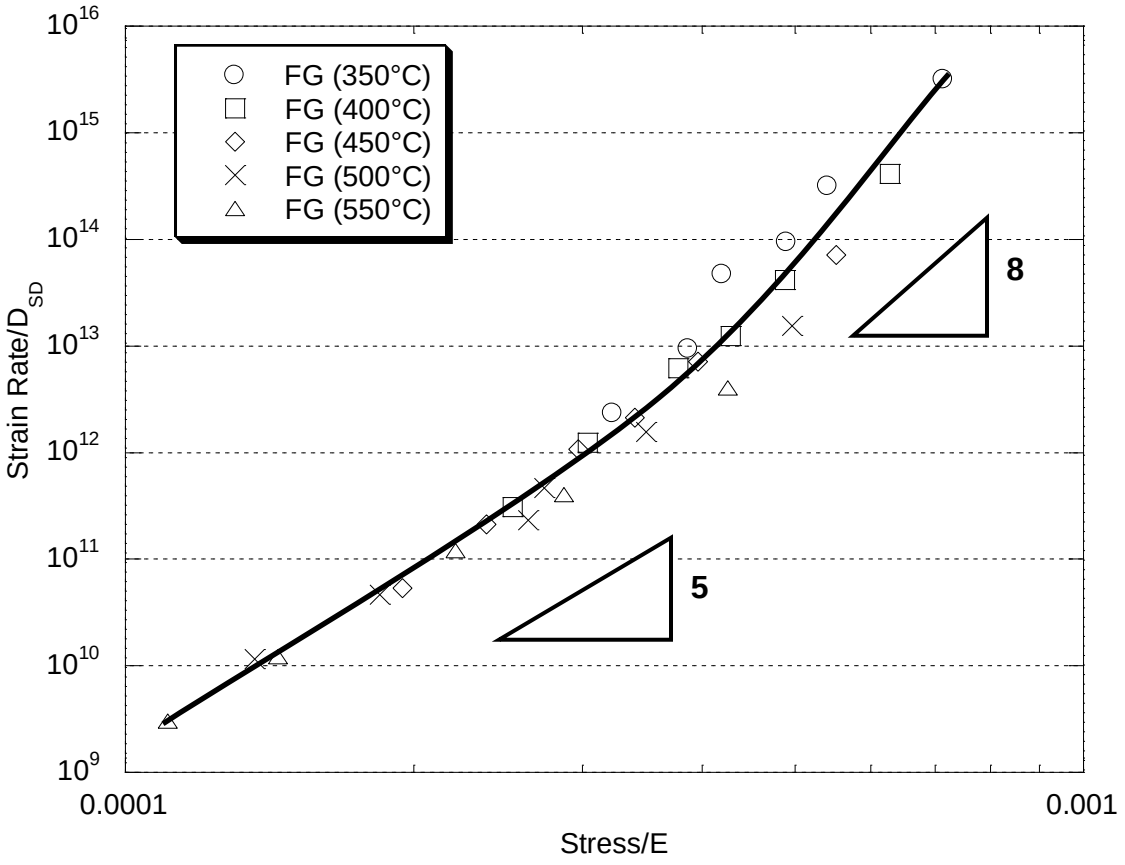

Figure 6.5: Normalized strain-rate vs. stress/E plot for FG showing a continuous curve.

This curve shows clearly how the stress exponent (N=1/m), or the slope of the curve, increases with increasing stress, or decreasing temperature. As can be seen, the slope changes from ~5 to a value of ~8 at approximately SR/D=10^{13}. This matches very well with the onset of power-law breakdown in pure aluminium [48]. Examining the activation energy for deformation of the data in this regime (350°C -400°C), it can be seen that Q is only 93.5kJ/mol. This value is much lower than the activation energy for self diffusion in aluminium, 142kJ/mol. It is however closer to the value reported for diffusion of vacancies through dislocation cores (core diffusion), 82kJ/mol, and diffusion of vacancies along high energy boundaries (boundary diffusion), 84kJ/mol [18]. The lowered value of Q also agrees with the onset of power-law breakdown [26,48]. Power-law breakdown is defined as an increase in the creep-rate of a material beyond what is seen in Stage II creep. In other words, the material is deforming more rapidly under an applied load than would be predicted at lower stresses. One theory suggests that an

increased level of diffusion caused by an excess of vacancies in the material [19] or by diffusion along substructure boundaries is the reason for the increased creep-rates[26]. In the FG material in the 350°C to 400°C, the increased creep-rates could be enhanced due to the fine grain structure (more boundary diffusion) or increased diffusion rates along the surfaces of large precipitates uniformly distributed in the microstructure at these temperatures. The exact reason for the decrease of m and Q during power-law breakdown is still widely debated (see 2.3.2), and this study does not provide any additional insight into the problem.

6.3.3 Constitutive Analysis through Load Relaxation Behaviour

In the temperature range of 350°C-450°C, the internal variable theory approach matched very well with the load relaxation test data, assuming the GMD mechanism, for both materials. The dislocation permeability, p^*, was found to be 0.15, which is identical to results found for AA6013 [15]. Also, the trend of decreasing stress parameter and increasing strain-rate parameter with increasing temperature matches results found in literature [15]. As the stress parameter represents internal stresses generated by long range dislocation interaction and internal friction forces, it is expected that this value decrease with increasing temperature. Likewise, as the strain-rate parameter represents a thermally activated process, an increase in temperature will raise this value. At higher temperatures, the fit to the GMD equation becomes much poorer. In literature, GBS becomes evident at temperatures above 500°C [15], however a clear fit to the present data using the GBS equation could not be found. It is possible that the load cell used in the experiments was not sensitive enough to detect the very fine fluctuations in the stress as the stresses were well below the load cell's rated capacity (the stress was only 1-2MPa at these temperatures) or deformation outside the gauge area affected the results. GBS would be represented on the stress vs. strain-rate plots as a slightly lower than expected flow stress over a short range of strain-rates (see Figure 2.11). Additionally, the lower strain-rates could not be clearly resolved as fine disturbances generated by the hydraulic system caused small fluctuations in the stress signal meaning strain-rates below $10^{-4}s^{-1}$ could not be resolved. This means that the "window" for the occurrence of grain boundary sliding may not have been visible in our experiments.

6.4 The Effect of Initial Microstructure and Deformation Conditions on Grain Structure Evolution

When tested in the 350°C to 400°C range, the T4P material's grain structure underwent little change. The grain size did not change significantly, which was expected after the static ageing tests, and the grain shape only showed a slight elongation in the tensile direction. The FG material's grains, after testing in the same temperature interval, showed little growth, but did show extensive elongation in the tensile direction. The grain size stability in this temperature range was estimated by the static ageing tests conducted when dynamic recrystallization does not occur. The grain size stability in each of these materials at these temperatures can be explained by similar mechanisms. For grain growth to occur, grain boundary migration must occur. The driving force for this migration is the reduction of boundary area, and as such, there is a differential energy created between grains with large boundary areas and those with small boundary areas. Therefore, migration of boundaries generally causes grain sizes to increase. When the grain size in a material is relatively consistent, the driving force for migration becomes quite small. In both the T4P and FG material, the original grain structure appeared to consist of grains with a relatively narrow grain size distribution. Additionally, any small imperfections such as particles, at the boundary front can impede the migration of the boundary (Zener pinning [43]). The T4P material had undergone a solutionizing treatment at high temperatures prior to testing, and it is possible that any boundary migration that would have occurred (at the conditions of this study), did occur, leaving a thermally stable grain structure. The FG material's grain structure contained much smaller grains than the T4P material, and therefore would be subject to higher driving forces for grain growth because of the larger grain boundary area of the fine grains. The uniform distribution of precipitates produced by the heat treatment procedure used to produce this material likely aided in retaining the fine grain structure through the pinning effect of these particles on the boundaries; images of precipitates on the grain boundaries could not be obtained, however this possibility should be further explored in the future. The elongation of the grains in the failed material increased as the total elongation to failure of the sample increased.

The microstructures of the T4P and FG samples tested at 450°C both showed significantly elongated grains. This matches well with the elongation to failures seen in both materials. The average grain size of the T4P material does not increase, which matches well with the static ageing tests suggesting deformation does not strongly affect the grain size at this temperature. The grain size of the FG material does begin to increase at these testing conditions. The static ageing tests revealed that there was a small amount grain growth at this temperature. Interestingly, the grain boundaries of the FG material appear serrated, not smooth, as shown schematically in Figure 6.6.

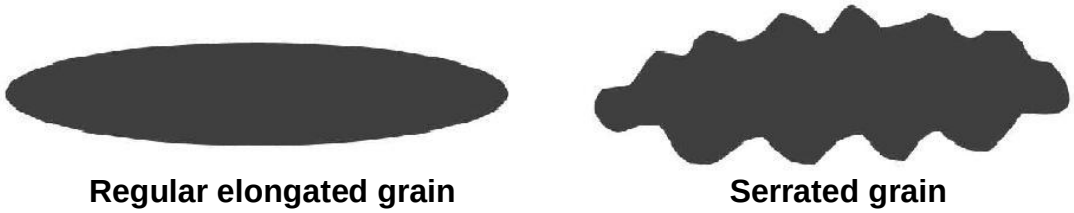

Figure 6.6: Schematic of elongated grains with regular and serrated boundaries

There are two possible reasons for this grain morphology. First, as the grain boundaries migrate during grain growth, sections of the boundary could become pinned on precipitates within the material, causing the boundary to bow around these particles. The spacing between the serrations matches satisfactorily with the spacing between the particles in the FG material at this temperature (~2μm). Second, the serrations could be due to surface tension effects generated by subgrains within the grains [43]. This phenomenon is seen during deformation of high stacking fault materials to very high strains [43]. There are several reasons why the serrations were not seen at lower temperatures. First, the elongations to failure at lower temperatures were not as high as at 450°C, leading to less total strain undergone by the sample. Second, lower temperatures do not facilitate the migration of dislocations into subgrain structures as readily as higher temperatures due to the lower diffusion rates. Finally, the migration of grain boundaries is slower at lower temperatures due to a lower level of thermal activation.

At 500°C, the grain structure of both materials became similar. Both materials appear to exhibit a bimodal grain size distribution from the observed microstructure

images. Large, elongated grains can be seen in both materials, as well as smaller, equiaxed grains, which are most defined around the edges of the large grains; faint outlines of equiaxed grains can be seen in the interior of the large grains (e.g. Figure 5.50). This was seen more extensively in the T4P material than the FG material. This suggests the existence of a well defined recovery structure within the material (i.e. the beginning of dynamic recrystallization). Drawing from the observed strain-rate sensitivity and activation energy and relating it to similar results found in literature, this structure could be the cell structure created during dislocation climb controlled creep [26]. The outer edges of the grain would be exposed to higher stresses, and undergo higher levels of strain than the interior of the grain [26], particularly in the presence of any grain boundary precipitates [83]. During deformation, the grain boundary precipitates would create high levels of stress around themselves due to the elastic mismatch between the precipitates and the matrix, which would create a large number of dislocations localized in these areas. This higher dislocation density would create an environment that would promote the subgrains in these areas to obtain higher levels of misorientation [43]. This would account for the larger population of "clear" boundaries at the exterior edges of the grains, particularly in the T4P material where grain boundary precipitation was pronounced. At 550°C, most evidence of the original, large grain structure has disappeared, leaving a primarily equiaxed grain structure in both materials. The presence of a similar cell structure, albeit less defined (i.e. lower misorientation angle) in the center of the grains suggests that the transition from an elongated grain structure to a recrystallized structure is a continuous recovery/recrystallization process, rather than a discontinuous process involving nucleation and growth of undeformed grains. It is therefore likely that the refinement in the grain structure during deformation at these high temperatures is due to the evolution of low angle cell boundaries into high angle boundaries. Both the elevated temperature (increased dislocation mobility) and the strain (increased dislocation density) likely play a role in this evolution. The high temperatures would increase the rate at which dislocations move into the cellular structure through increased diffusion rates. The high strain levels seen at the elevated temperatures would increase the dislocation densities in the cell boundaries, increasing the misorientation angle of the boundaries. All of this evidence points towards a

continuous recrystallization process, however, a definitive conclusion can not be made without further characterization of the microstructure at various stages of deformation, using methods such as electron back scatter diffraction (EBSD).

Comparing the recrystallized grain sizes at 500°C and 550°C, it can be seen that the grain size decreases with increasing strain-rate. The higher strain-rates lead to less time that the sample is at temperature. It is likely that the same process of dynamic recrystallization occurred at the lower strain-rates, however, longer exposure to high temperatures during testing caused some grain growth. Additionally, it has been shown that the size of subgrains that form during deformation is a function of the stress; higher stress leads to smaller subgrain sizes [144]. Higher strain-rates generate higher stresses, which could also be an influencing factor on the recrystallized grain size. The fact that both materials exhibited similar gain sizes under the same deformation conditions suggests that the process that created the recrystallized grains could be the same in both cases. In the case of the T4P material, this meant subdivision of large grains by subgrain boundaries to produce a finer grain structure. The FG material underwent some grain growth, and the fact that the grains stabilized to the same size as the T4P material suggests that the recrystallized grains are not growth-limited in the same manner as the original grain structure (that underwent little grain growth at similar temperatures, see Figure 5.13).

The evidence of abnormal grain growth at the fracture tips of the tested samples was most baffling. No reports of similar phenomena could be found in literature, however several explanations are presented by the author which could explain this phenomenon. First, as abnormal grain growth was only observed at the highest temperatures (>450°C), and highest strain-rates, we can assume this process requires both high temperatures and high stresses. This is emphasized by the fact that the abnormal grain growth occurred only at the fracture tip, where the stress and strain would be the highest. The subgrain structure in this region may evolve to higher energy boundaries (larger misorientation) earlier than other areas of the sample due to the higher strains seen as a result of higher stresses. These higher misorientation boundaries have a higher

mobility than lower angle boundaries, and therefore could rapidly consume the surrounding grains and subgrains [145]. The high levels of stress and strain could also induce localized heating, which would lead to even higher diffusion rates, also enhanced by the boundary diffusion along the highly developed cellular structure. All of these factors could lead to increased grain boundary mobility in these regions. Additionally, once the abnormal grain growth had initiated, it would continue rapidly; the larger the size discrepancy, the larger the boundary energy disparity, leading to increased growth rates of the large grain [145].

6.5 The Effect of Initial Microstructure and High Temperature Deformation on Damage and Failure

At most deformation conditions, except the lowest stress conditions (i.e. high temperature and low strain-rate), there was very minimal cavitation (<1%) seen in the tensile tested samples. The small cavities that do form appear to initiate from large particles within the samples. These large particles were earlier identified as iron-containing dispersoids. At elevated temperatures, the voids appear to initiate from decohesion of the particle from the matrix, while at room temperature, void initiation appears to be a combination of decohesion, and particle fracture. Particle fracture is seen at room temperature only because of the significantly higher stresses seen at that temperature compared to the elevated temperature tests. Large iron-containing dispersoids can be clearly seen in high resolution images of the fracture surfaces as observed in the work of Sooky Winkler [146] at the base of voids, suggesting either initiation of voids from these particles or termination of void growth at the particles. Figure 6.7 shows an SEM image of the fracture surface, with arrows highlighting large particles at the base of the dimples.

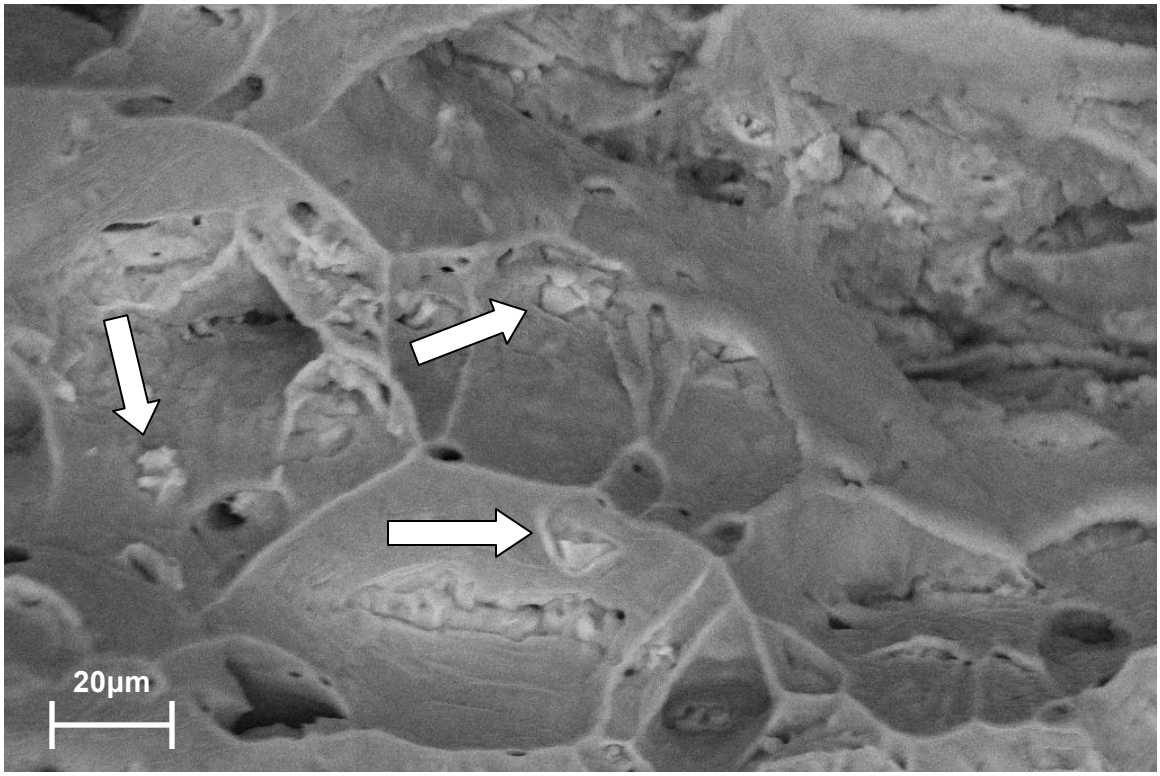

Figure 6.7: Fracture surface showing large iron containing particles at the base of dimples (T4P, 350°C, $5.0x10^{-4}s^{-1}$) (SE mode) [146].

As the cavities grow, they form elongated cavities, or "stringers" which are generally aligned with the tensile direction. These stringers are common in aluminium alloys that have been deformed at elevated temperatures [147]. Close examination of these stringers showed that they are not simply aligned with the tensile direction, but appear to follow a specific path in the tensile direction. From the as-polished through-thickness images of the fracture areas, it appeared that the stringer path involved short jumps from particle to particle in the general tensile direction. By etching the samples and observing them under high resolution SEM, Sooky Winkler was able to reveal that not only do they jump from particle to particle, the paths generally coincide with grain boundaries, as seen in Figure 6.8 [146].

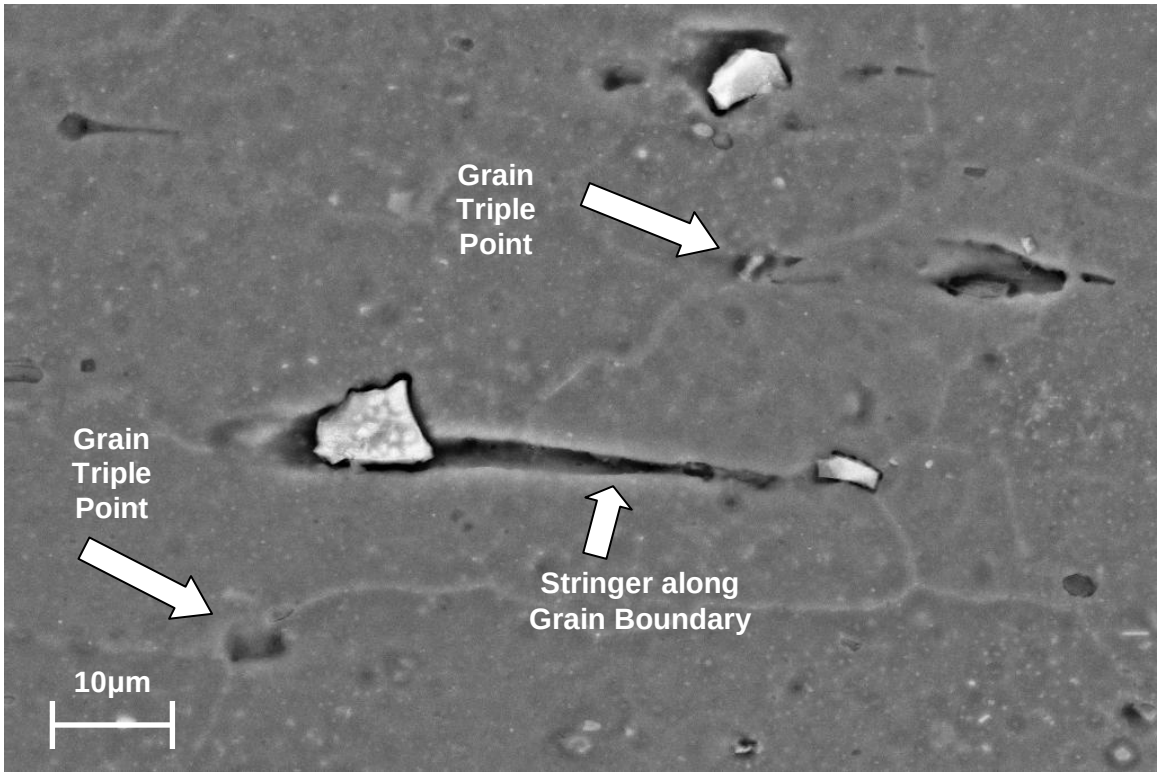

Figure 6.8: Stringer formation along grain boundaries (Backscatter mode) [146].

The above observations allow insight into the processes of void formation and growth in these materials. First, the voids initiate from the largest particles in the material because they represent the largest local differential strain within the material. For example, if the matrix undergoes a strain of 20%, the particle, due to high elastic moduli and yield strengths, may only undergo a strain of 0.1%. This will place large stresses at the interface of the particle with the matrix [143], particularly at the ends aligned with the tensile direction. This eventually leads to decohesion of the particle from the matrix. "Ligaments", or the precursors to stringers, then form between voids [148]. These ligaments then grow into stringers. The principles described in literature match well with those observed in this study [147]. From the observations in our samples (e.g. as seen in Figure 6.8), it is unclear if the ligaments form as a link between two existing voids (i.e. the initial void nucleated on a large particle and a very small void on a nearby particle), or whether the ligament forms between the initial void and the adjacent particle, and initiates a void to form upon that particle. Another factor that must be taken into account is the microscopic fracture and void formation on small precipitates not

visible with the applied observation techniques. Small precipitates, particularly the ones formed in the T4P material at low temperatures, could produce very small voids either through fracture under applied stress as dislocations pass through them [138], or through similar strain mismatch processes discussed for larger precipitates. Elongated precipitates, such as those observed in the T4P material after static aging at high temperatures, are much more susceptible to fracture than the round precipitates found in the FG material. The microvoids formed at precipitates could aid in the growth rate of larger voids, aid in the formation of ligaments between voids or grow into larger voids themselves. Understanding the details of these processes is the subject of a parallel study [146].

The additional effect of grain boundaries must also be accounted for as they evidently play a large role in ligament formation and cavity growth. Grain boundaries themselves represent interruptions in the crystal structure of the grains and are therefore of lower strength than the grain matrixes themselves [149]. Additionally, diffusion of vacancies can happen very rapidly along grain boundaries which can aid the early growth of these cavity stringers. Finally, the formation of grain boundary precipitates, as seen in the T4P material at certain conditions, creates a higher concentration of large precipitates along the grain boundaries than in the grain matrix. The formation of these large precipitates also results in the creation of a region around the grain boundaries depleted of solute, and therefore devoid of any strengthening precipitates (precipitate free zones). Additionally, the grain boundary precipitates are significantly larger than the other precipitates, and therefore much more prone to nucleate voids due to strain mismatch. These weakened zones around the grain boundaries and the high concentration of large precipitates on grain boundaries in the conditions where grain boundary precipitation occurred could also cause the void stringers to grow along grain boundaries. The very low concentration of voids in the T4P and FG material after deformation at most conditions prevents any meaningful comparison to understand how much of an effect grain boundary precipitation has on the process.

At the conditions where high levels of cavitation were found (high temperature, low strain-rate), the applied stress was low. At first, this appears at odds with the above described mechanism of cavity nucleation and growth, however, these conditions are also ideal for the diffusion of vacancies. At high temperature, the vacancy concentration in the material is high [22], and the high temperature allows rapid diffusion of these vacancies. Additionally, the low strain-rates allow lots of time for vacancies to diffuse large distances. Vacancy diffusion is most rapid along grain boundaries, and as a result, the voids form between grains and grow. This is evident in the observation of the fracture surfaces of these samples as failure was caused by coalescence of these voids without necking. High resolution images of these fracture surfaces taken by Sooky Winkler are shown in Figure 6.10 and Figure 6.10. Arrows highlight areas were the voids have penetrated along grain boundaries, leaving a fracture surface similar to that which would be seen during intergranular failure. Interestingly, this mechanism of failure is similar to that observed in the failure of a material undergoing grain boundary sliding [14].

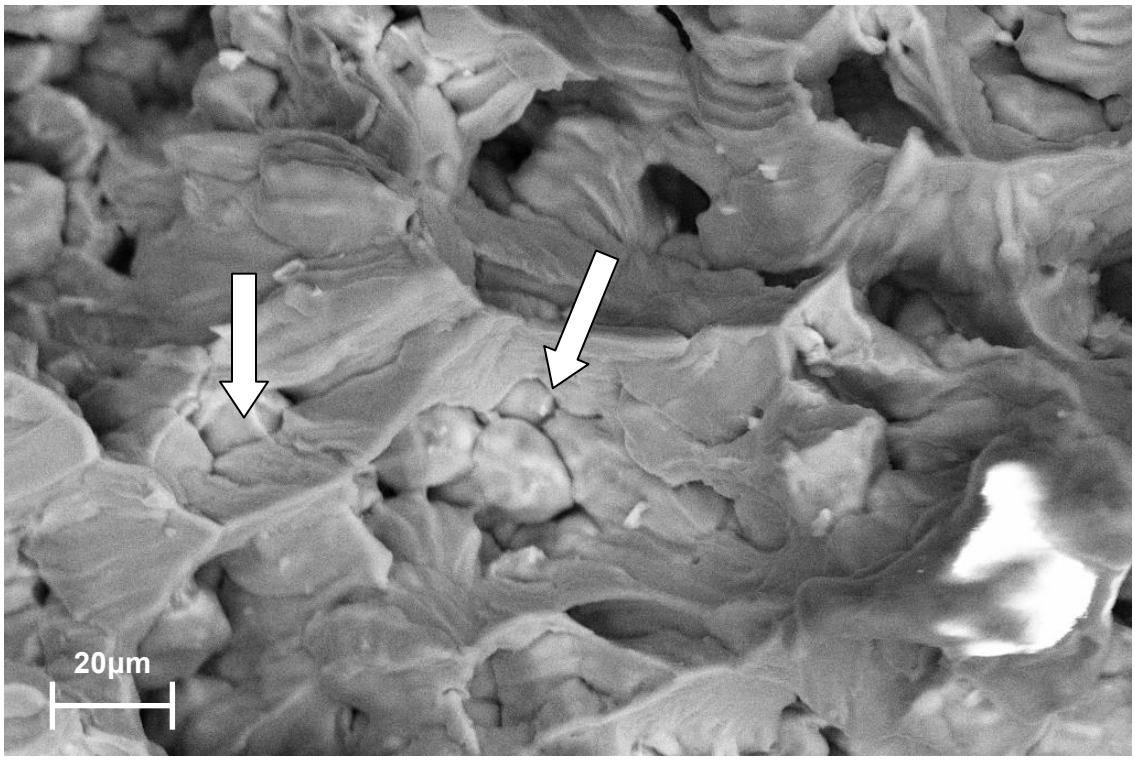

Figure 6.9: Fracture surface illustrating fracture path along grain boundaries in the FG material (500°C, $5.0 \times 10^{-4} s^{-1}$) [146].

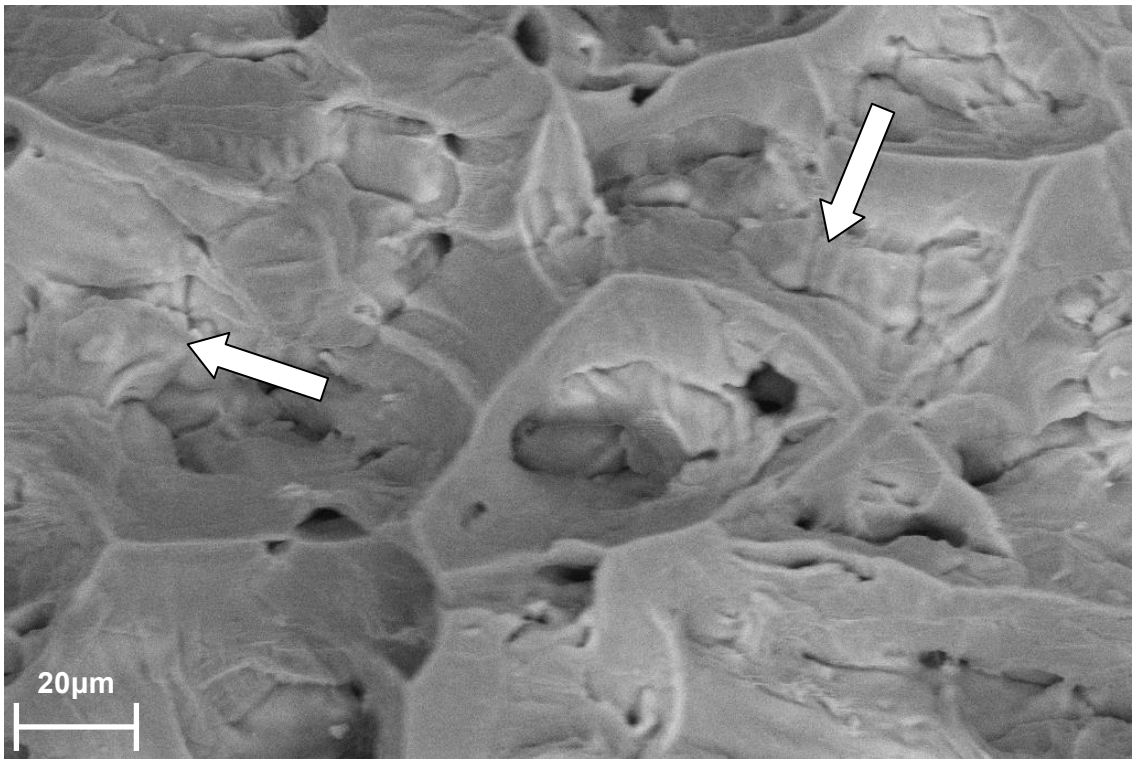

Figure 6.10: Fracture surface illustrating fracture path along grain boundaries in the T4P material (500°C, $5.0x10^{-4}s^{-1}$) [146].

Growth by vacancy diffusion explains why the voids at these conditions are less aligned with the tensile direction than the stringers found in other conditions; growth is more controlled by grain boundaries than the applied stress. It has been suggested in literature that as the size of the cavity increases, the growth mechanism changes from diffusion controlled growth to plastic controlled growth [147]. This can be observed in the samples as some voids exist as a central void surrounded by many thin "arms" which extend along surrounding grain boundaries (see Figure 5.68). The large void is likely plastically controlled, while the arms along the grain boundaries are much more affected by the diffusion of vacancies.

By examining the fractures surfaces of samples, it is possible to get an estimation of the level of cavitation present at the point of fracture. From examination of these images (Figure 5.70 to Figure 5.75) it can be seen that both the FG and T4P samples failed primarily by necking (except for the previously discussed high temperature and

low strain rates), as shown by the thinning of the sample to a point at fracture, but some clear differences between the fracture surfaces of the FG and T4P material can be seen. At 350°C, the T4P material clearly shows higher levels of cavitation than the FG material at all strain-rates. One possible explanation for this difference is the very great difference in the stresses seen between the T4P material and the FG material. The greater stresses in the T4P material would promote the formation of voids at large particles, and indeed, there are extensive levels of large precipitates, particularly on grain boundaries, formed during deformation of the T4P material at these temperatures. Examining the fracture surfaces at 450°C, the situation is reversed; the FG material exhibits more voids at the fracture surface than the T4P material. In this case, the stress in the FG material is still lower than the T4P material, however the differences is not as large as at 350°C. This could be explained by the similar mechanism behind the large levels of cavitation seen at higher temperatures; high levels of vacancy diffusion, particularly along grain boundaries. The lower grain size of the FG material would explain the elevated levels of cavitation because of the increased diffusion rates. This mechanism would also explain why the level of cavitation in the FG material at 450°C decreased with increasing strain-rate.

The observed trend of increased elongation to failure and decreased area fraction of cavities in both materials could be related. Clearly, at the conditions where very large area fractions of cavities are observed (>500°C and $5.0x10^{-4}s^{-1}$), the inter-linkage of these cavities caused the premature failure of material, without even the onset of necking. However, even as the mode of failure became necking, with little influence of the cavities, as was the case in both materials tested at 500°C and 550°C and the strain-rate is increased from $5.0x10^{-4}s^{-1}$ to $2.0x10^{-3}s^{-1}$, the elongation to failure increased. It has been suggested that the decreased level of cavitation at higher strain-rates is due to the effect of the strain-rate sensitivity [11]. Localized plastic strains (like around a cavity) will see higher strain-rates than the bulk material. The strain-rate sensitivity will cause stresses around these zones to increase locally, retarding the growth rate of the cavities, as the primary growth mechanism of large cavities is plastic deformation. The higher the strain-rates, the more strengthening occurs. The same can be said for necking. Necking

increases local strain-rates, and strain-rate sensitivity can cause deformation to occur in regions undergoing lower strain-rates (i.e. out of the necked region), therefore making the deformation more uniform and extending elongation. As the strain-rate sensitivity enters the equations as an exponent, this effect increases with increasing strain-rate. This effect, combined with the decreased time for diffusion could explain the decreased levels of cavitation seen in both materials as strain-rate increased.

6.6 Elongation to Failure Summary

Using the conclusions gathered from the examination of the stress behaviour, the strain-rate sensitivity, microstructural evolution, and the cavitation and failure behaviour, the elongation to failure of the FG and T4P materials can be properly summarized. A comparison of the elongations to failure of the two materials at lower and higher temperatures can be found in Figure 5.37 and Figure 5.38, respectively.

At lower temperatures (i.e. 350°C to 450°C), the FG material achieved significantly larger elongations to failure than the T4P material under all deformation conditions. The deformation of both materials, however, followed similar trends. First, at 350°C and 400°C, the elongation to failure of both materials did not change significantly with strain-rate. At 450°C, both materials saw a slight increase in elongation to failure with increasing strain-rate. Also, both materials saw increasing elongation to failure with every increment of temperature. The constant elongation to failure at 350°C and 400°C could be explained by the low strain-rate sensitivity seen in both materials at these temperatures. Strain-rate sensitivity plays a primary role in reducing necking at elevated temperatures. The strain-rate sensitivity enters the deformation equations as an exponent to the strain-rate and, therefore, should be better at retarding necking at higher strain-rates. However, when the strain-rate sensitivities are very low, the material necking behaviour will remain relatively constant across different strain-rates. At 450°C, the strain-rate sensitivity increased in value, which correlates well with the increased elongations to failure seen in both materials at this temperature. The differences in the elongations to failure of both materials were likely a combination of

many factors, relating primarily to the stability of the FG microstructure and the variability of the T4P microstructure. Through static ageing tests, the FG precipitate and grain structure was found to change very little with exposure to temperature, while the T4P material underwent extensive precipitation. The result of this precipitation was a structure that impeded the glide and climb of dislocations, which led to flow stresses much greater than those seen in the FG material. During deformation of the T4P material, necking would occur readily and continue until failure of the sample due to the low strain-rate sensitivity. At the same time, the necked region would be exposed to elevated stresses; these elevated stresses acted upon the large precipitates (especially grain boundary precipitates) and dispersoids, causing cavities to form. This local increase in void density weakened the material, causing a rapid progression of necking, and finally failure. The FG material, which consisted of an overaged microstructure, did not undergo the same levels of stress that the T4P material did, and therefore, did not see the same amount of localized void formation which dramatically expedited necking, allowing the material to undergo higher strains to failure. Additionally, the elongated shape of the precipitates in the T4P material make them more prone to create stress concentrations (at their tips), or fracture than the rounded precipitates found in the FG material. In both materials, increasing the temperature resulted in decreased stresses which helped to minimize cavity formation, aiding in the increased elongations to failure seen with increasing temperatures.

At 500°C and 550°C, both materials achieved similar elongations to failure. This matched well with other similarities that the materials had at these temperatures: similar flow stresses, similar levels of cavitation, similar activation energies and similar strain-rate sensitivities. These similarities were facilitated by a general homogenization of the microstructures. Both materials showed increasing elongation to failure with increasing strain-rate and, with the exception of the lowest strain-rate, exhibited low levels of average cavitation as well as low levels of cavitation at the fracture tip. This suggests that failure was primarily linked with necking at these conditions. This matches well with the higher strain-rate sensitivities found at these temperatures. At the lowest strain-rate, the cavitation levels increased dramatically, and there was little evidence of necking

at the fracture tip. There was a fair amount of variability in the elongation to failure between the two materials at this temperature, however, this is likely due to the highly unstable nature of the heavily cavitated microstructure. If many more tests were conducted, the average results would likely become quite similar. In conclusion, the increased ductility seen in the FG and T4P materials at 500°C and 550°C was a result primarily of increased strain-rate sensitivity which helped to reduce necking. The low stresses caused by high dislocation mobility, dynamic recovery/recrystallization and the largely precipitate free microstructure helped prevent the formation of voids which would cause early failure of the material.

Chapter 7 Conclusions and Recommendations

7.1 Conclusions

The aim of this project was to characterize the microstructural evolution and mechanical properties at elevated temperatures, as well as room temperature, of a recently developed fine-grained AA6xxx aluminium alloy and compare it to a commercially-produced equivalent alloy in the pre-aged condition (T4P). Understanding of the connection between the microstructure and the deformation behaviour was found through comparison of these two materials. This goal was accomplished through conducting optical and scanning electron microscopy, room temperature and high temperature tensile tests (between 350°C and 550°C), stress relaxation tests, and fracture analysis. The important conclusions from this study are as follows:

- Exposure of the T4P material to high temperatures without deformation (below 500°C) resulted in significant evolution of precipitates, including extensive grain boundary precipitation. Grain size did not change during high temperature exposures as an equilibrium grain size had likely been established during prior solutionizing treatments.
- The precipitate structure of the FG material did not change as significantly with exposure to high temperatures, although there was some coarsening of the existing precipitates at the higher temperatures. The grain size of the FG material did not increase significantly until the temperature was raised above 450°C likely due to the pinning effect of precipitates and the low driving force for grain growth caused by a low scatter of grain sizes.
- At room temperature, the FG material achieved larger elongations to failure than the T4P material, but also deformed at a much lower yield stress than the T4P material. In both materials, failure was caused by necking followed by void sheeting leading to the ductile shear failure mechanism; shear was more pronounced in the T4P material. The lower deformation stress of the FG material, aided by less work hardening, led to increased ductility by delaying void formation.

- The FG material exhibited significantly larger elongations to failure than the T4P material during deformation in the temperature range of 350°C to 450°C. Both materials exhibited similar elongations to failure at 500°C and 550°C.
- The poor elongation of the T4P material at the lower temperatures was determined to be the result of significant precipitation at these temperatures and coarsening of elongated-shaped precipitates, resulting in high deformation stresses, causing localized void formation during necking. The effect was most pronounced at high strain-rates, as the precipitates had less time to overage at those conditions.
- At 500°C and 550°C, the strain-rate sensitivity and activation energy for deformation of both materials suggested deformation by dislocation climb accommodated by self diffusion of aluminium.
- For the FG material at lower temperatures, the strain-rate sensitivity and activation energy decrease. This was due to the transition from climb controlled creep to power law breakdown. The diffusion compensated strain-rate at the onset of this change matched well with that reported for power law breakdown in pure aluminium.
- For the T4P material at lower temperatures, the strain-rate sensitivity decreased more rapidly than the FG material, but the activation energy significantly increased. It was determined that this was caused by a threshold stress induced by the precipitates on the dislocations, similar to other reports of particle hardened materials.
- Load relaxation tests found excellent agreement with the constitutive equation for grain matrix deformation at the lower temperatures (350°C-450°C). The parameters also matched well with those reported for other aluminium alloys. At the highest temperatures, the data did not fit either the equation for grain matrix deformation, nor grain boundary sliding, well.
- Examination of the grain structure after deformation revealed that at lower temperatures (<450°C), the grains primarily changed shape by elongating in the tensile direction. The amount of grain-elongation was primarily related the amount of strain the sample underwent.

- At 500°C and 550°C, equiaxed, small grains were formed within the large elongated grains. These grains were the result of the evolution of the dislocation cell structure formed during deformation from low angle boundaries to high angle boundaries.
- Cavitation was found to be very high in both materials at the lowest strain-rate and highest temperatures, but quickly decreased to very low levels with increasing strain-rates.
- Cavitation at high temperatures and low strain-rates was due to diffusion of vacancies, primarily along grain boundaries, to high energy locations to form small voids, followed by plastic growth of those voids to larger sizes.
- At higher stress conditions, cavitation was due to decohesion of large particles from the matrix followed by stringer formation to other nearby particles aligned with the tensile direction, and primarily along grain boundaries due to increased populations of large particles and the increased diffusion mechanics along these boundaries.
- The deformation behaviour of the T4P and FG materials were found to be highly dependent on the initial microstructure, particularly the precipitation state. When fine, elongated-shaped precipitates were formed during deformation (i.e. T4P at 350°C and 400°C), the ductility was much lower than the material that had rounded and finely distributed overaged precipitates. Strengthening precipitates also increased the deformation stress which promoted the formation of cavities.
- Strain-rate sensitivity played a primary role in determining the ductility of both materials. When strain-rate sensitivity was high, the ductility was also high. This behaviour was related primarily to the retardation of necking due to the hardening effect of strain-rate sensitivity, allowing higher elongations to failure.
- Several observations, such as cavitation morphology, stress-strain profile and necking behaviour pointed to the possibility of grain boundary sliding in both materials at 550°C and a strain-rate of $5.0 \times 10^{-4} s^{-1}$.
- The effect of a finer grain-size on deformation at elevated temperatures was primarily related to enhanced diffusion through grain boundaries, and also may

have aided in allowing grain-boundary sliding during deformation at the highest temperatures and lowest strain-rates.

- The precipitation characteristics of the materials were suggested to be the primary cause of differences in the behaviour of the two materials; when precipitates were present, they behaved differently, and when precipitates dissolved at high temperatures, the materials with similar reduced grain-sizes behaved similarly.

7.2 Recommendations

The following are recommendations for future work involving high temperature deformation of the FG material and comparison with the T4P material.

- Expand the range of strain-rates tested to lower values to investigate the possibility of grain boundary sliding further. Also, higher strain-rate values can be tested to determine if the ductility remains constant or decreases with very high strain-rates.
- Conduct strain-rate change tests to determine strain-rate sensitivity at individual strain-rates and allow more accurate identification of changes in the deformation mechanism.
- Repeat the load relaxation tests on a system with a higher rate of data acquisition and a more sensitive load cell, preferably a servo-mechanical system to eliminate small fluctuations caused by the hydraulic system. Additionally, an enhanced specimen holder should be created to hold the sample more securely and eliminate any possible effects from outside of the reduced area of the specimen.
- Evaluate possible solutionizing and ageing treatments to strengthen the FG material after deformation.

References

[1] W.S. Miller, L. Zhuang, J. Bottema, A.J. Wittebrood, P.D. Smet, A. Haszler, and A. Vieregge, "Recent development in aluminium alloys for the automotive industry," *Materials Science and Engineering A*, vol. 280, Mar. 2000, pp. 37-49.

[2] S. Esmaeili and Lloyd D.J., "Modeling of precipitation hardening in pre-aged AlMgSi(Cu) alloys," *Acta Materialia*, vol. 53, 2005, pp. 5257-5271.

[3] J. Sarkar, T.R.G. Kutty, D.S. Wilkinson, J.D. Embury, and D.J. Lloyd, "Tensile properties and bendability of T4 treated AA6111 aluminum alloys," *Materials Science and Engineering A*, vol. 369, Mar. 2004, pp. 258-266.

[4] D. Li and A. Ghosh, "Tensile deformation behavior of aluminum alloys at warm forming temperatures," *Materials Science and Engineering A*, vol. 352, Jul. 2003, pp. 279-286.

[5] K.T. Park, E.J. Lavernia, and F.A. Mohamed, "High-temperature deformation of 6061 Al," *Acta Metall.* , vol. 42, 1994, pp. 667-667.

[6] P. Cavaliere, "Hot and warm forming of 2618 aluminium alloy," *Journal of Light Metals*, vol. 2, Nov. 2002, pp. 247-252.

[7] E. Taleff and P. Nevland, "The high-temperature deformation and tensile ductility of Al alloys," *JOM Journal of the Minerals, Metals and Materials Society*, vol. 51, Jan. 1999, pp. 34-36.

[8] E. Taleff, G.A. Henshall, Lesuer D.R., and T.G. Nieh, "Warm forming of aluminum-magnesium alloys," Atlanta, GA: 1994.

[9] K.I. Aastorp, "Plastic Deformation at Moderate Temperatures of 6XXX-series Aluminium Alloys," Doctorate, The Norwegian University of Science and Technology, 2002.

[10] L.P. Troeger and E.A. StarkeJr, "Particle-stimulated nucleation of recrystallization for grain-size control and superplasticity in an Al–Mg–Si–Cu alloy," *Materials Science and Engineering A*, vol. 293, Nov. 2000, pp. 19-29.

[11] D. Lassance, D. Fabregue, F. Delannay, and T. Pardoen, "Micromechanics of room and high temperature fracture in 6xxx Al alloys," *Progress in Materials Science*, vol. 52, Jan. 2007, pp. 62-129.

[12] D. Li and A.K. Ghosh, "Biaxial warm forming behavior of aluminum sheet alloys," *Journal of Materials Processing Technology*, vol. 145, Feb. 2004, pp. 281-293.

[13] L.P. Troeger and E.A. Starke, "Microstructural and mechanical characterization of a superplastic 6xxx aluminum alloy," *Materials Science and Engineering A*, vol. 277, Jan. 2000, pp. 102-113.

[14] Kaibyshev R., Musin F., Gromov D., Nieh T.G., and Lesuer D.R., "Grain refinement and superplastic behaviour of a modified 6061 aluminium alloy," *Materials Science and Technology*, vol. 19, Apr. 2003, pp. 483-490.

[15] S.S. Park, H. Garmestani, G. Bae, N.J. Kim, P.E. Krajewski, S. Kim, and E.W. Lee, "Constitutive analysis on the superplastic deformation of warm-rolled 6013 Al alloy," *Materials Science and Engineering*, Nov. 2006, pp. 687-692.

[16] W.R. Tyson, "Theoretical strength of perfect crystals," *Philosophical Magazine*, vol. 14, 1966, p. 925.

[17] D. Roundy, C.R. Krenn, M.L. Cohen, and J.W. Morris, "Ideal Shear Strengths of fcc Aluminum and Copper," *Physical Review Letters*, vol. 82, Mar. 1999, p. 2713.
[18] H.J. Frost and M.F. Ashby, *Deformation-Mechanism Maps: The Plasticity and Creep of Metals and Ceramics*, Pergamon Pr, 1982.
[19] O.D. Sherby and P.M. Burke, "Mechanical behavior of crystalline solids at elevated temperature," *Progress in Materials Science*, vol. 13, 1968, pp. 323-390.
[20] D. Askeland, *The Science and Engineering of Materials*, Boston, MA: PWS, 1994.
[21] J. Holloman, *AMIE*, 1945, p. 268.
[22] D.A. Porter and K.E. Easterling, *Phase transformation in metals and alloys*, Van Nostrand Reinhold New York, 1981.
[23] F.R.N. Nabarro, *Dislocations in Solids*, North Holland, 1979.
[24] T.H. Courtney, *Mechanical Behavior of Materials*, McGraw-Hill Science/Engineering/Math, 1999.
[25] H. Conrad and J. Narayan, "On the grain size softening in nanocrystalline materials," *Scripta Materialia*, vol. 42, May. 2000, pp. 1025-1030.
[26] M.E. Kassner and M.T. Perez-Prado, "Five-power-law creep in single phase metals and alloys," *Progress in Materials Science*, vol. 45, Jan. 2000, pp. 1-102.
[27] J. Hedworth and M.J. Stowell, "The measurement of strain-rate sensitivity in superplastic alloys," *Journal of Materials Science*, vol. 6, 1971, pp. 1061-1069.
[28] J. Tallon and A. Wolfenden, "Temperature Dependence of the Elastic Constants of Aluminium," *Journal of Physics and Chemistry of Solids*, vol. 40, pp. 831-847.
[29] D. Gerlich and E. Fisher, "The High-Temperature Elastic Moduli of Aluminum," *Journal of Physics and Chemistry of Solids*, vol. 30, 1969, pp. 1197-1205.
[30] T. Ke, "Experimental evidence of the viscous behavior of grain boundaries in metals," *Physical Review*, vol. 71, 1947, pp. 533-546.
[31] F.A. Mohamed and T.G. Langdon, "Deformation Mechanism Maps Based on Grain Size," *Metall. Trans. Vol. 5*, vol. 2339, 1974.
[32] N. Wang, Z. Wang, K. Aust, and U. Erb, "Effect of grain size on mechanical properties of nanocrystalline materials," *Acta Metall.* , vol. 43, pp. 519-528.
[33] M.E. Kassner and X. Li, "The Effect of Grain Size on the Elevated Temperature Yield Strength of Polycrystalline Aluminum.," *Scripta Metallurgica*, vol. 25, 1991, pp. 2833-2838.
[34] P. Yavari and T.G. Langdon, "An Examination of the Breakdown in Creep by Viscous Glide in Solid Solution Alloys," *Acta Metallurgica*, vol. 30, 1982, pp. 2182-2196.
[35] W.R. Cannon and O.D. Sherby, "High-Temperature Creep Behavior of Class 1 and Class 2 Solid-Solution Alloys," *Metallurgical Transactions*, vol. 1, 1970, pp. 1030-1032.
[36] F.A. Mohamed and T.G. Langdon, "Transition From Dislocation Climb to Viscous Glide in Creep of Solid Solution Alloys," *Acta Met. Vol. 22*, 1974, pp. 779-788.
[37] G. Schoeck and J. Dorn, *Mechanical Behavior of Materials at Elevated Temperature*, McGraw-Hill, New York, NY, 1961.
[38] J. Weertman, "Creep of Indium, Lead and Some of Their Alloys with Various Metals," *Trans. the Metall. Soc. AIME*, vol. 218, 1960, pp. 207-218.

[39] A.H. Cottrell and M.A. Jaswon, "Distribution of Solute Atoms Round a Slow Dislocation," *Proceedings of the Royal Society of London. Series A, Mathematical and Physical Sciences (1934-1990)*, vol. 199, 1949, pp. 104-114.
[40] J.C. Fisher, "On the Strength of Solid Solution Alloys," *Acta Met*, vol. 2, 1954, p. 9.
[41] T. Naka, Y. Nakayama, T. Uemori, R. Hino, and F. Yoshida, "Effects of temperature on yield locus for 5083 aluminum alloy sheet," *Journal of Materials Processing Technology*, vol. 140, Sep. 2003, pp. 494-499.
[42] M.E. Kassner, "Taylor hardening in five-power-law creep of metals and Class M alloys," *Acta Materialia*, vol. 52, Jan. 2004, pp. 1-9.
[43] Doherty R.D., Hughes D.A., Humphreys F.J., Jonas J.J., Jensen D.J., Kassner M.E.[1], King W.E., McNelley T.R., McQueen H.J., and Rollett A.D., "Current issues in recrystallization: a review," *Materials Science and Engineering: A*, vol. 238, Nov. 1997, pp. 219-274.
[44] A. Argon and S. Takeuchi, "Internal Stresses in Power-Law Creep," *Acta Metall.* , vol. 29, 1984, pp. 1877-1884.
[45] J. Gibeling and W. Nix, "Numerical Study of Long Range Internal Stresses Associated with Subgrain Boundaries," *Acta Metall.* , vol. 28, 1980, pp. 1743-1748.
[46] M. Morris and J. Martin, "Evolution of internal stresses and substructure during creep at intermediate temperatures," *Acta Metallurgica*, vol. 32, 1984, pp. 549-561.
[47] B. Derby and M.F. Ashby, "A Microstructural Model for Primary Creep," *Acta Metall.* , vol. 35, 1987, pp. 1345-1352.
[48] D.R. Lesuer, C.K. Syn, and O.D. Sherby, "An Evaluation of Power Law Breakdown in Metals, Alloys, Dispersion Hardened Materials and Compounds," 1999.
[49] B.Y. Zong and B. Derby, "Creep behaviour of a SiC particulate reinforced Al-2618 metal matrix composite," *Acta Materialia*, vol. 45, Jan. 1997, pp. 41-49.
[50] B. Walser and O. Sherby, "The Structure dependence of power law creep," *Scripta Metallurgica*, vol. 16, Feb. 1982, pp. 213-219.
[51] O.D. Sherby and E.M. Taleff, "Influence of grain size, solute atoms and second-phase particles on creep behavior of polycrystalline solids," *Materials Science and Engineering A*, vol. 322, Jan. 2002, pp. 89-99.
[52] W. Blum, "Creep of crystalline materials: experimental basis, mechanisms and models," *Materials Science and Engineering A*, Dec. 2001, pp. 8-15.
[53] R. Lagneborg, "Bypassing of dislocations past particles by a climb mechanism," *Scripta Metallurgica*, vol. 7, Jun. 1973, pp. 605-613.
[54] F.R.N. Nabarro, "Report of a Conference on the Strength of Solids," *The Physical Society, London*, vol. 75, 1948.
[55] C. Herring, "Diffusional Creep Viscosity of a Polycrystalline Solid," *J. Appl. Phys*, vol. 21, 1950, pp. 437-45.
[56] R.L. Coble, "A Model for Boundary Diffusion Controlled Creep in Polycrystalline Materials," *Journal of Applied Physics*, vol. 34, Jun. 1963, pp. 1679-1682.
[57] J. Harper and J. Dorn, "Viscous Creep of Aluminum Near Its Melting Point," *Acta Metall.* , vol. 5, 1957, p. 654.

[58] T.G. Langdon and P. Yavari, "An Investigation of Harper--Dorn Creep. Pt. 2. The Flow Process," *Acta Metall.* , vol. 30, 1982, p. 881.
[59] M.Y. Wu and O.D. Sherby, "Unification of Harper--Dorn and Power Law Creep Through Consideration of Internal Stress," *Acta Metall.* , vol. 32, 1984, p. 1561.
[60] A.J. Ardell, "Harper-Dorn Creep--Predictions of the Dislocation Network Theory of High Temperature Deformation," *Acta Materialia*, vol. 45, Jul. 1997, pp. 2971-2981.
[61] W. Blum and W. Maier, "Harper-Dorn Creep - a Myth?," *physica status solidi (a)*, vol. 171, 1999, pp. 467-474.
[62] F. Mohamed, "Creep and superplasticity in Al alloys," *Third Symposium on Hot Deformation of Aluminum Alloys III*, 2003.
[63] R.E. Reed-Hill, *Physical Metallurgy Principles*, Van Nostrand, 1973.
[64] T.K. Ha, Sung H.J., Kim K.S., and Chang Y.W., "An internal variable approach to the grain size effect on the superplastic deformation behavior of a 7475 Al alloy," *Materials Science and Engineering: A*, vol. 271, Nov. 1999, pp. 160-166.
[65] Ma Z.Y., Mishra R.S.[1], and Mahoney M.W., "Superplastic deformation behaviour of friction stir processed 7075Al alloy," *Acta Materialia*, vol. 50, Oct. 2002, pp. 4419-4430.
[66] O.D. Sherby and J. Wadsworth, "Superplasticity—Recent advances and future directions," *Progress in Materials Science*, vol. 33, pp. 169-221.
[67] T.K. Ha and Y.W. Chang, "An internal variable theory of structural superplasticity," *Acta Materialia*, vol. 46, May. 1998, pp. 2741-2749.
[68] H. Iwasaki, M. Takeuchi, T. Mori, M. Mabuchi, and K. Higashi, "A comparative study of cavitation characteristics in Si [sub 3] N [sub 4p]/Al-Mg-Si composite and 7475 aluminum alloy," *Scripta Metallurgica et Materialia*, vol. 31, 1994.
[69] M. Kawasaki and T. Langdon, "Principles of superplasticity in ultrafine-grained materials," *Journal of Materials Science*, vol. 42, Mar. 2007, pp. 1782-1796.
[70] K. Kitazano, R. Hirasuka, E. Sato, K. Kuribayashi, and T. Motegi, "Internal stress superplasticity in anisotropic polycrystalline materials," *Acta Materialia*, vol. 49, 2001, pp. 473-486.
[71] D. Lee and E. Hart, "Stress relaxation and mechanical behavior of metals," *Metallurgical and Materials Transactions B*, vol. 2, 1971, pp. 1245-1248.
[72] W.J. Kim, J.K. Kim, T.Y. Park, S.I. Hong, D.I. Kim, Y.S. Kim, and J.D. Lee, "Enhancement of Strength and Superplasticity in a 6061 Al Alloy Processed by Equal-Channel-Angular-Pressing," *Metallurgical and Materials Transactions A (USA). Vol. 33A*, 2002, pp. 3155-3164.
[73] S.J. Lillywhite, P.B. Prangnell, and F.J. Humphreys, "Interactions between precipitation and recrystallization in an Al-Mg-Si alloy," *Materials Science and Technology*, vol. 16, 2000, pp. 1112-1120.
[74] D. Wilkinson and C. Ceceres, "On the mechanism of strain-enhanced grain growth during superplastic deformation," *Acta Metallurgica*, vol. 32, Sep. 1984, pp. 1335-1345.
[75] Weatherly G.C., Perovic A., Mukhopadhyay N.K., Lloyd D.J., and Perovic D.D., "The Precipitation of the Q Phase in an AA6111 Alloy," *Metallurgical and Materials Transactions A*, vol. 32, Feb. 2001, pp. 213-218.

[76] G. Le Roy, J.D. Embury, G. Edward, and M.F. Ashby, "A Model of Ductile Fracture Based on the Nucleation and Growth of Voids," *Acta Metall. Vol. 29,* 1981, pp. 1509-1522.
[77] D.J. Benson, "An analysis of void distribution effects on the dynamic growth and coalescence of voids in ductile metals," *Journal of the Mechanics and Physics of Solids,* vol. 41, Aug. 1993, pp. 1285-1308.
[78] Z. Cvijovic, I. Cvijovic, and M. Vratnica, "Fracture micromechanisms in overaged 7000 alloy forgings," *Journal of Alloys and Compounds,* vol. 441, Aug. 2007, pp. 66-75.
[79] M. Kawasaki, C. Xu, and T.G. Langdon, "An investigation of cavity growth in a superplastic aluminum alloy processed by ECAP," *Acta Materialia,* vol. 53, Dec. 2005, pp. 5353-5364.
[80] M.E. Kassner and T.A. Hayes, "Creep cavitation in metals," *International Journal of Plasticity,* vol. 19, Oct. 2003, pp. 1715-1748.
[81] B. Dyson, "Continuous cavity nucleation and creep fracture," *Scripta Metallurgica,* vol. 17, Jan. 1983, pp. 31-37.
[82] M. Yoo and H. Trinkaus, "Interaction of slip with grain boundary and its role in cavity nucleation," *Acta Metall.* , vol. 34, 1986, pp. 2381-2390.
[83] A.K. Vasudevan and R.D. Doherty, "Grain Boundary Ductile Fracture in Precipitation Hardened Aluminum Alloys," *Acta Metall. Vol. 35,* 1987, pp. 1193-1219.
[84] T. Pardoen, D. Dumont, A. Deschamps, and Y. Brechet, "Grain boundary versus transgranular ductile failure," *Journal of the Mechanics and Physics of Solids,* vol. 51, Apr. 2003, pp. 637-665.
[85] H. Jiang and R. Faulkner, "Modelling of grain boundary segregation, precipitation and precipitate-free zones of high strength aluminium alloys—I. The model," *Acta Materialia,* vol. 44, May. 1996, pp. 1857-1864.
[86] L. Xia, "Ductile crack growth---II. Void nucleation and geometry effects on macroscopic fracture behavior," *Journal of Mechanics Physics of Solids,* vol. 43, Dec. 1995, pp. 1953-1981.
[87] M. de Hass and J.T.M. De Hosson, "Grain boundary segregation and precipitation in aluminium alloys," *Scripta Materialia (USA). Vol. 44,* 2001, pp. 281-286.
[88] C. Gandin and A. Jacot, "Modeling of precipitate-free zone formed upon homogenization in a multi-component alloy," *Acta Materialia,* vol. 55, Apr. 2007, pp. 2539-2553.
[89] J. Hirsch, "Automotive Trends in Aluminium - The European Perspective," *Materials Forum,* vol. 28, 2004, pp. 15-23.
[90] E.A. Starke and J.T. Staley, "Application of modern aluminum alloys to aircraft," *Progress in Aerospace Sciences,* vol. 32, 1996, pp. 131-172.
[91] J. Davis, *Aluminum and Aluminum Alloys,* ASM International, 1993.
[92] A.K. Gupta, P.H. Marois, and D.J. Lloyd, "Study of the precipitation kinetics in a 6000 series automotive sheet material," *Materials Science Forum,* vol. 217/222, 1996, pp. 801-808.
[93] L.P. Troeger and E.A. Starke, "New process produces superplastic aerospace/automotive aluminum alloy," *Advanced engineering materials,* vol. 2, 2000, pp. 802-806.

[94] N.E. Paton and C.H. Hamilton, "Method of imparting a fine grain structure to aluminum alloys having precipitating constituents," U.S. Patent 40921881.
[95] J. Waldman, H. Sulinski, and H. Markus, "New processing techniques for aluminum alloys," U.S. Patent 38476811974.
[96] E. Kovacs-Csetenyi, T. Torma, T. Turmezey, and N. Chinh, "Superplasticity of AIMgSi alloys," *Journal of Materials Science*, vol. 27, 1992, pp. 6141-6145.
[97] Y. Chung, L.P. Troeger, and E.A. Starke Jr, "Grain refining and superplastic forming of aluminum alloy 6013," 1994.
[98] H.J. Roven, H. Nesboe, J.C. Werenskiold, and T. Seibert, "Mechanical properties of aluminium alloys processed by SPD: Comparison of different alloy systems and possible product areas," *Materials Science and Engineering*, Nov. 2005, pp. 426-429.
[99] Z. Horita, T. Fujinami, M. Nemoto, and T.G. Langdon, "Improvement of mechanical properties for Al alloys using equal-channel angular pressing," *Journal of Materials Processing Technology*, vol. 117, Nov. 2001, pp. 288-292.
[100] C. Xu, M. Furukawa, Z. Horita, and T.G. Langdon, "The evolution of homogeneity and grain refinement during equal-channel angular pressing: A model for grain refinement in ECAP," *Materials Science and Engineering A*, vol. 398, May. 2005, pp. 66-76.
[101] R.K. Islamgaliev, N.F. Yunusova, I.N. Sabirov, A.V. Sergueeva, and R.Z. Valiev, "Deformation behavior of nanostructured aluminum alloy processed by severe plastic deformation," *Materials Science and Engineering A*, Dec. 2001, pp. 877-881.
[102] H. Jin and D.J. Lloyd, "The tensile response of a fine-grained AA5754 alloy produced by asymmetric rolling and annealing," *Metallurgical and Materials Transactions A*, vol. 35, Mar. 2004, pp. 997-1006.
[103] S. Kang, B. Min, H. Kim, D. Wilkinson, and J. Kang, "Effect of asymmetric rolling on the texture and mechanical properties of AA6111-aluminum sheet," *Metallurgical and Materials Transactions A*, vol. 36, Nov. 2005, pp. 3141-3149.
[104] S.H. Lee, Y. Saito, T. Sakai, and H. Utsunomiya, "Microstructures and mechanical properties of 6061 aluminum alloy processed by accumulative roll-bonding," *Materials Science and Engineering A*, vol. 325, Feb. 2002, pp. 228-235.
[105] Terhune S.D., Swisher D.L., Oh-Ishi K., Horita Z., Langdon T.G., and McNelley T.R., "An Investigation of Microstructure and Grain-Boundary Evolution during ECA Pressing of Pure Aluminum," *Metallurgical and Materials Transactions A*, vol. 33, Jul. 2002, pp. 2173-2184.
[106] Y. Iwahashi, Z. Horita, M. Nemoto, and T.G. Langdon, "The process of grain refinement in equal-channel angular pressing," *Acta Materialia*, vol. 46, May. 1998, pp. 3317-3331.
[107] D. Morris, I. Gutierrez-Urrutia, and M. Muñoz-Morris, "Analysis of strengthening mechanisms in a severely-plastically-deformed Al–Mg–Si alloy with submicron grain size," *Journal of Materials Science*, vol. 42, Mar. 2007, pp. 1439-1443.
[108] I. Dutta and S.M. Allen, "A calorimetric study of precipitation in commercial aluminium alloy 6061," *Journal of Materials Science Letters*, vol. 10, Jan. 1991, pp. 323-326.

[109] S. Esmaeili and D.J. Lloyd, "Characterization of the evolution of the volume fraction of precipitates in aged AlMgSiCu alloys using DSC technique," *Materials Characterization*, vol. 55, Nov. 2005, pp. 307-319.
[110] W. Miao and D. Laughlin, "Effects of Cu content and preaging on precipitation characteristics in aluminum alloy 6022," *Metallurgical and Materials Transactions A*, vol. 31, Feb. 2000, pp. 361-371.
[111] L. Zhen, W. Fei, S. Kang, and H. Kim, "Precipitation behaviour of Al-Mg-Si alloys with high silicon content," *Journal of Materials Science*, vol. 32, Apr. 1997, pp. 1895-1902.
[112] A.K. Gupta, D.J. Lloyd, and S.A. Court, "Precipitation hardening in Al–Mg–Si alloys with and without excess Si," *Materials Science and Engineering A*, vol. 316, Nov. 2001, pp. 11-17.
[113] Perovic A., Perovic D.D., Weatherly G.C., and Lloyd D.J., "Precipitation in aluminum alloys AA6111 and AA6016," *Scripta Materialia*, vol. 41, Aug. 1999, pp. 703-708.
[114] K. Matsuda, Y. Sakaguchi, Y. Miyata, Y. Uetani, T. Sato, A. Kamio, and S. Ikeno, "Precipitation sequence of various kinds of metastable phases in Al-1.0mass% Mg2Si-0.4mass% Si alloy," *Journal of Materials Science*, vol. 35, Jan. 2000, pp. 179-189.
[115] X. Wang, W.J. Poole, S. Esmaeili, D.J. Lloyd, and J.D. Embury, "Precipitation Strengthening of the Aluminum Alloy AA6111," *Metallurgical and Materials Transactions A*, vol. 34, 2003, pp. 2913-2924.
[116] C.D. Marioara, S.J. Andersen, T.N. Stene, H. Hasting, J. Walmsley, A.T.J. Van Helvoort, and R. Holmestad, "The effect of Cu on precipitation in Al-Mg-Si alloys," *Philosophical Magazine. Vol. 87*, 2007, pp. 3385-3413.
[117] J. Man, L. Jing, and S.G. Jie, "The effects of Cu addition on the microstructure and thermal stability of an Al-Mg-Si alloy," *Journal of Alloys and Compounds. Vol. 437*, 2007, pp. 146-150.
[118] G.A. Edwards, K. Stiller, G.L. Dunlop, and M.J. Couper, "The precipitation sequence in Al–Mg–Si alloys," *Acta Materialia*, vol. 46, Jul. 1998, pp. 3893-3904.
[119] D.J. Chakrabarti and D.E. Laughlin, "Phase relations and precipitation in Al–Mg–Si alloys with Cu additions*1," *Progress in Materials Science*, vol. 49, pp. 389-410.
[120] X. Wang, S. Esmaeili, and D. Lloyd, "The sequence of precipitation in the Al-Mg-Si-Cu alloy AA6111," *Metallurgical and Materials Transactions A*, vol. 37, 2006, pp. 2691-2699.
[121] K. Matsuda, T. Kawabata, Y. Uetani, T. Sato, and S. Ikeno, "Hexagonal tabular β-phase in Al–Mg–Si–Cu alloy," *Scripta Materialia*, vol. 47, Oct. 2002, pp. 467-471.
[122] S. Esmaeili, X. Wang, D. Lloyd, and W. Poole, "On the precipitation-hardening behavior of the Al−Mg−Si−Cu alloy AA6111," *Metallurgical and Materials Transactions A*, vol. 34, Mar. 2003, pp. 751-763.
[123] C. Ravi and C. Wolverton, "Comparison of thermodynamic databases for 3xx and 6xxx aluminum alloys," *Metallurgical and Materials Transactions A*, vol. 36, 2005, pp. 2013-2023.

[124] D. Steele, D. Evans, P. Nolan, and D. Lloyd, "Quantification of grain boundary precipitation and the influence of quench rate in 6XXX aluminum alloys," *Materials Characterization*, vol. 58, Jan. 2007, pp. 40-45.
[125] D.J. Lloyd, "The scaling of the tensile ductile fracture strain with yield strength in Al alloys," *Scripta Materialia*, vol. 48, Feb. 2003, pp. 341-344.
[126] W.J. Poole, D. Lloyd, and J.D. Embury, "The effect of natural ageing on the evolution of yield strength during artificial ageing for Al-Mg-Si-Cu alloys," *Materials Science and Engineering A*, vol. 234-236, 1997, pp. 306-309.
[127] D. Teirlinck, F. Zok, J.D. Embury, and M.F. Ashby, "Fracture Mechanism Maps in Stress Space," *Acta Metall. Vol. 36*, 1988, pp. 1213-1228.
[128] R. Kaibyshev, F. Musin, D. Gromov, T.G. Nieh, and D.R. Lesuer, "Effect of liquid phase on superplastic behavior of a modified 6061 aluminum alloy.," *Scripta Materialia. Vol. 47*, vol. 569, 2002.
[129] S. Esmaeili, D. Lloyd, and H. Jin, "New Thermomechanical Processing Method to Achieve Extended High Temperature Ductility in Precipitation Hardenable Alloys," U.S. Patent Pending.
[130] ASTM Standard E8/E8M, *Standard Test Methods for Tension Testing of Metallic Materials*, West Conshohocken, PA: ASTM International, 2008.
[131] Z. Zhang, Hauge M., Odegard J., and Thaulow C., "Determining material true stress-strain curve from tensile specimens with rectangular cross-section," *International Journal of Solids and Structures*, vol. 36, Aug. 1999, pp. 3497-3516.
[132] I. Scheider, W. Brocks, and A. Cornec, "Procedure for the Determination of True Stress-Strain Curves From Tensile Tests With Rectangular Cross-Section Specimens," *Journal of Engineering Materials and Technology*, vol. 126, Jan. 2004, pp. 70-76.
[133] L. Briottet, J.J. Jonas, and F. Montheillet, "A mechanical interpretation of the activation energy of high temperature deformation in two phase materials," *Acta Materialia*, vol. 44, Apr. 1996, pp. 1665-1672.
[134] M. Kulas, W. Green, E. Taleff, P. Krajewski, and T. McNelley, "Deformation mechanisms in superplastic AA5083 materials," *Metallurgical and Materials Transactions A*, vol. 36, May. 2005, pp. 1249-1261.
[135] J. Davis, *Metals Handbook Desk Edition 2nd Edition*, CRC, 1998.
[136] G.B. Burger, A.K. Gupta, P.W. Jeffrey, and D.J. Lloyd, "Microstructural control of aluminum sheet used in automotive applications*1," *Materials Characterization*, vol. 35, Jul. 1995, pp. 23-39.
[137] S. Esmaeili, L. Cheng, A. Deschamps, D.J. Lloyd, and W.J. Poole, "The deformation behaviour of AA6111 as a function of temperature and precipitation state," *Materials Science and Engineering A*, vol. 319-321, 2001, pp. 461-465.
[138] W.J. Poole, X. Wang, D.J. Lloyd, and J.D. Embury, "The shearable–non-shearable transition in Al–Mg–Si–Cu precipitation hardening alloys: implications on the distribution of slip, work hardening and fracture," *Philosophical Magazine*, vol. 85, 2005, p. 3113.
[139] A. Rollett, U. Kocks, and R. Doherty , *Formability and Metallurgical Structure*, Warredale, USA: TMS, 1987.
[140] W. Callister, *Materials Science and Engineering (An Introduction)*, New York: John Wiley & Sons Inc., 1994.

[141] O. Ajaja, "High-Temperature Deformation and Internal Stress," *Scripta Metallurgica*, 1981, pp. 975-979.
[142] S.O. Ojediran and O. Ajaja, "The Bailey-Orowan equation," *Journal of Materials Science*, vol. 23, 1988, pp. 4037-4040.
[143] *Metalworking: Bulk Forming*, ASM International Handbook Committee, 2002.
[144] A. Orlava and F. Dobe, "On the stress–subgrain size relationships derived from the composite model of dislocation structure ," *Materials Science and Engineering A*, vol. 381, 2004, pp. 171-174.
[145] F.J. Humphreys, "A unified theory of recovery, recrystallization and grain growth, based on the stability and growth of cellular microstructures—I. The basic model," *Acta Materialia*, vol. 45, Oct. 1997, pp. 4231-4240.
[146] S. Winkler, R. Carrick, and S. Esmaeili, "Unpublished Work."
[147] M.J. Worswick, Z.T. Chen, A.K. Pilkey, D. Lloyd, and S. Court, "Damage characterization and damage percolation modelling in aluminum alloy sheet," *Acta Materialia*, vol. 49, Aug. 2001, pp. 2791-2803.
[148] C. Thomson, M.J. Worswick, A.K. Pilkey, Lloyd D.J., and G.B. Burger, "Modeling void nucleation and growth within periodic clusters of particles," *Journal of the Mechanics and Physics of Solids*, vol. 47, 1998, pp. 1-26.
[149] G. Lu, "Theoretical tensile strength of an Al grain boundary," *Physical Review B*, vol. 69, 2004, p. 134106.

Appendix

Tensile Test Data

T4P Tensile Test Data (Note that C or MT8131 refers to the T4P material)

Sample	T (°C)	Strain Rate (s^{-1})	Engineering Strain (%)	Max Flow Stress (MPa)	Stress@3.3%	Stress@6.6%
MT8131-350-LXHS	350	5.00E-04	33.58	60.8	59.78	56.46
C-350-LXHS-1	**350**	**5.00E-04**	30.81	**64.81**	**62.49**	**56.45**
MT8131-350-HXHS	350	2.00E-03	29.96	69.24	68.78	67.87
C-350-HXHS-1	**350**	**2.00E-03**	33.62	**72.79**	**72.35**	**69.14**
C-350-UHXHS-1	350	2.00E-02	33.18	71.48	70.77	70.03
C-350-0.03-1	**350**	**3.00E-02**	29.16	**80.96**	**80.47**	**80.26**
C-350-0.03-2	**350**	**3.00E-02**	35.41	**83.1**	**82.52**	**82.11**
C-350-0.1-1	350	6.70E-02	35.10	**78.41**	**77.91**	**77.87**
C-350-0.1-3	**350**	**6.70E-02**	32.53	**91.22**	**90.46**	**90.56**
C-350-1-1	350	6.70E-01	25.31	**93.03**	**91.11**	**92.77**
C-350-1-2	350	6.70E-01	26.35	**92.42**	**89.81**	**91.48**
C-350-1-3	**350**	**6.70E-01**	29.13	**101.24**	**98.56**	**100.47**
MT8131-400-LXHS	400	5.00E-04	49.85	**33.37**	**32.68**	**30.38**
C-400-LXHS-1	**400**	**5.00E-04**	56.06	**36.04**	**34.19**	**30.33**
MT8131-400-HXHS	400	2.00E-03	55.73	**38.06**	**37.84**	**36.5**
C-400-HXHS-1	400	2.00E-03	47.68	**44.6**	**43.83**	**40.9**
C-400-UHXHS-1	400	2.00E-02	48.62	38.94	38.84	38.04
C-400-0.03-1	**400**	**3.00E-02**	38.45	**58.78**	**58.42**	**58.23**
C-400-0.03-2	**400**	**3.00E-02**	46.00	**64.58**	**64.15**	**64**
C-400-0.1-1	400	6.70E-02	55.84	**45.57**	**44.84**	**45.26**
C-400-0.1-3	**400**	**6.70E-02**	37.43	**76.34**	**75.12**	**75.83**
C-400-1-1	400	6.70E-01	45.75	**61.6**	59.51	**60.64**
C-400-1-3	**400**	**6.70E-01**	40.12	**85.51**	**83.03**	**85.15**
MT8131-450-LXHS-1	450	5.00E-04	96.59	**14.92**	**14.29**	**13.6**
MT8131-450-	450	5.00E-04	88.42	**14.71**	**14.27**	**13.53**

LXHS-2						
MT8131-450-HXHS	450	2.00E-03	97.34	**17.29**	**17.03**	**16.37**
C-450-HXHS-1	**450**	**2.00E-03**	102.31	**20.13**	**19.72**	**18.37**
C-450-UHXHS-1	450	2.00E-02	87.70	19.19	18.97	18.37
C-450-0.03-5	**450**	**3.00E-02**	78.58	**22.84**	**22.69**	**22.43**
C-450-0.1-1	450	6.70E-02	86.69	23.61	23.59	23.52
C-450-0.1-3	**450**	**6.70E-02**	113.75	**30.13**	**29.58**	**29.92**
C-450-1-1	450	6.70E-01	134.71	34.3	32.66	33.61
C-450-1-3	**450**	**6.70E-01**	115.12	**38.72**	**37.2**	**38.51**
MT8131-500-LXHS	500	5.00E-04	111.56	7.92	7.69	7.71
C-500-LXHS-4	**500**	**5.00E-04**	109.44	**8.22**	**7.43**	**7.25**
MT8131-500-HXHS-1	500	2.00E-03	135.90	10.23	9.48	9.28
MT8131-500-HXHS-2	500	2.00E-03	146.98	**10.44**	**9.91**	**9.76**
C-500-UHXHS-1	500	2.00E-02	179.97	11.8	11.35	11.44
MT8192-500-Com-1	500	3.00E-02	178.09	**13.65**	**13.49**	**12.46**
MT8192-500-Com-2	500	3.00E-02	164.47	14.19	14.01	13.11
MT8192-500-Com-3	500	3.00E-02	183.88	**14.41**	**14.27**	**13.12**
MT8192-500-Com-4	500	3.00E-02	173.13	13.84	13.79	12.84
MT8192-500-Com-5	500	3.00E-02	202.78	**14.26**	**13.89**	**12.92**
MT8192-500-Com-6	500	3.00E-02	198.07	14.26	14.18	13.08
MT8192-500-Com-7	500	3.00E-02	169.64	**14.19**	**13.84**	**12.76**
MT8192-500-Com-8	500	3.00E-02	181.70	14.39	14.18	13.16
C-500-0.1-1	500	6.70E-02	186.68	16.48	16.39	16.32
C-500-0.1-3	**500**	**6.70E-02**	194.75	**16.89**	**16.58**	**16.53**
C-500-1-1	500	6.70E-01	211.57	26.12	25.36	25.88
C-500-1-3	**500**	**6.70E-01**	194.42	**25.72**	**24.81**	**24.89**
MT8131-550-LXHS	550	5.00E-04	110.15	6.13	5.84	5.56
C-550-LXHS-4	**550**	**5.00E-04**	164.24	**4.75**	**4.52**	**4.39**
MT8131-550-HXHS	550	2.00E-03	87.54	7.68	7.17	7.01
C-550-HXHS-2	**550**	**2.00E-03**	172.04	**6.21**	**5.85**	**5.74**
C-550-HXHS-4	**550**	**2.00E-03**	135.33	**6.61**	**6.43**	**6.16**

C-550-0.1-3 (5mm min)	**550**	**6.56E-03**	169.60	**9.57**	**9.5**	**9.06**
MT8192-550-Com-1	550	3.00E-02	192.21	**10.35**	**10.29**	**9.49**
MT8192-550-Com-2	550	3.00E-02	195.51	**10.47**	**10.36**	**9.5**
MT8192-550-Com-3	550	3.00E-02	188.06	**10.2**	**10.17**	**9.44**
MT8192-550-Com-4	550	3.00E-02	218.31	**10.38**	**9.8**	**9.89**
MT8192-550-Com-5	550	3.00E-02	181.39	**10.9**	**10.74**	**9.86**
MT8192-550-Com-6	550	3.00E-02	196.50	**11.41**	**11.19**	**10.33**
MT8192-550-Com-7	550	3.00E-02	183.13	**10.49**	**10.43**	**9.63**
MT8192-550-Com-8	550	3.00E-02	182.34	**11.02**	**10.77**	**9.73**
C-550-0.1-1	550	6.70E-02	190.94	12.07	11.95	11.71
C-550-0.1-4	**550**	**6.70E-02**	201.67	**14.94**	**14.64**	**14.48**
C-550-1-1	550	6.70E-01	216.82	21.11	19.87	20.66
C-550-1-3	**550**	**6.70E-01**	223.28	**22.31**	**21.79**	**21.92**

FG Tensile Test Data (Note that MT8145 refers to the FG material)

Sample	T (°C)	Strain Rate (s^{-1})	Engineering Strain (%)	Max Flow Stress (MPa)	Stress@3.3%	Stress@6.6%
MT8145-350-LXHS-1	350	5.00E-04	133.248	18.55	17.8	18.46
MT8145-350-LXHS-2	350	5.00E-04	126.486	18.58	18.080	18.25
MT8145-350-HXHS-1	350	2.00E-03	112.884	22.01	21.580	21.65
MT8145-350-HXHS-3	350	2.00E-03	112.704	22.49	21.780	22.33
FG-350-UHXHS-2	350	1.00E-02	105.177	23.53	22.29	22.08
FG-350-UHXHS-1	350	1.00E-02	79.429	25.11	23.03	24.38
F-350-UHXHS-2	350	1.00E-02	129.469	23.740	23.040	23.380
F-350-UHXHS-1	350	1.00E-02	97.329	24.22	23.250	23.94
F-350-0.03-1	**350**	**2.00E-02**	120.906	27.83	26.470	27.12
F-350-0.03-2	**350**	**2.00E-02**	120.177	28.55	27.350	27.81
F-350-0.1-1	350	6.70E-02	105.118	30.47	28.000	29.46
F-350-0.1-2	350	6.70E-02	102.697	31.35	28.84	30.39
F-350-0.1-3	**350**	**6.70E-02**	126.732	31.51	29.550	30.56
F-350-1-1	350	6.70E-01	119.581	40.58	33.73	37.43
F-350-1-3	**350**	**6.70E-01**	129.291	41.6	36.18	39.06

MT8145-400-LXHS-1	400	5.00E-04	128.592	13.92	13.62	13.77
MT8145-400-LXHSa	400	5.00E-04	128.431	13.96	13.720	13.68
MT8145-400-HXHS-1	400	2.00E-03	130.833	16.66	16.3	16.29
MT8145-400-HXHS-2	400	2.00E-03	141.621	16.74	16.620	16.33
F-400-UHXHS-2	400	1.00E-02	129.278	20.65	19.87	20.29
F-400-UHXHS-1	400	1.00E-02	108.269	20.87	20.3	19.75
F-400-0.03-1	**400**	**2.00E-02**	127.395	23.47	22.56	23.12
F-400-0.03-2	**400**	**2.00E-02**	111.188	23.63	22.48	23.22
F-400-0.1-1	400	6.70E-02	143.294	25.67	24.64	25.34
F-400-0.1-3	**400**	**6.70E-02**	109.836	27.35	25.88	26.69
F-400-0.1-4	**400**	**6.70E-02**	108.990	27.46	25.57	26.73
F-400-1-1	400	6.70E-01	134.762	34.09	30.094	32.66
F-400-1-4	**400**	**6.70E-01**	139.364	**34.95**	**31.81**	**33.54**
MT8145-450-LXHS-1	450	5.00E-04	138.305	10.05	9.66	9.79
MT8145-450-LXHS-2	450	5.00E-04	146.973	10.23	9.900	9.69
MT8145-450-HXHS-1	450	2.00E-03	151.414	12.72	12.41	12.35
MT8145-450-HXHS-2	450	2.00E-03	143.781	12.1	11.940	11.88
F-450-UHXHS-2	450	1.00E-02	189.869	14.78	14.13	14.07
F-450-UHXHS-1	450	1.00E-02	161.142	16.18	15.29	15.12
F-450-0.03-4	**450**	**2.00E-02**	125.394	**17.75**	**17.43**	**17.59**
F-450-0.03-5	**450**	**2.00E-02**	165.092	**17.71**	**17.23**	**17.54**
F-450-0.1-1	450	6.70E-02	167.789	20.59	20.05	20.29
F-450-0.1-4	**450**	**6.70E-02**	163.386	**20.67**	**19.7**	**20.41**
F-450-1-1	450	6.70E-01	172.165	28.05	26.51	27.97
F-450-1-4	**450**	**6.70E-01**	174.383	**29.54**	**26.44**	**28.29**
MT8145-500-LXHS-1	500	5.00E-04	151.219	6.84	6.21	6.5
MT8145-500-LXHS-2	500	5.00E-04	163.778	**6.58**	6.240	**6.3**
MT8145-500-HXHS-1	500	2.00E-03	173.294	9.31	9.11	8.92
MT8145-500-HXHS-2	500	2.00E-03	173.326	8.82	8.190	8.56
F-500-UHXHS-2	500	1.00E-02	174.213	12.41	12.04	12
F-500-UHXHS-1	500	1.00E-02	186.155	13.5	13.040	12.86
MT8192-500-FG	500	2.00E-02	248.141	12.72	12.700	12.12
F-500-0.03-4	**500**	**2.00E-02**	169.495	**13.74**	**13.850**	**13.35**
F-500-0.03-5	**500**	**2.00E-02**	155.026	**13.89**	**13.710**	**13.73**
F-500-0.1-1	500	6.70E-02	200.525	17.64	17.22	17.06
F-500-0.1-4	**500**	**6.70E-02**	178.379	**16.75**	**15.47**	**16.38**
F-500-1-1	500	6.70E-01	179.593	24.41	23.75	24.05
F-500-1-2	**500**	**6.70E-01**	196.260	**24.79**	**23.87**	**24.18**
F-500-1-4	**500**	**6.70E-01**	200.105	**24.1**	**22.72**	**22.93**
MT8145-550-LXHS-1	550	5.00E-04	150.843	**5.27**	**4.8**	**4.84**

MT8145-550-LXHS-4	550	5.00E-04	165.429	**4.9**	**4.86**	**4.61**
MT8145-550-LXHS-5	550	5.00E-04	178.812	**5.14**	4.950	**4.85**
MT8145-550-HXHS	550	2.00E-03	139.304	**6.34**	**6.2**	**6.32**
MT8145-550-HXHS-1	550	2.00E-03	169.226	7.01	6.52	6.41
MT8145-550-HXHS-2	550	2.00E-03	140.433	6.58	6.410	6.39
MT8192-550-FG-1	550	2.00E-02	191.673	10.23	10.1	9.25
MT8192-550-FG-2	550	2.00E-02	244.262	10.13	10.060	9.39
F-550-0.1-1	550	6.70E-02	221.343	14.2	13.48	13.17
F-550-0.1-4	**550**	**6.70E-02**	196.437	**12.22**	**11.88**	**11.88**
F-550-1-1	550	6.70E-01	229.543	20.76	19.61	19.44
F-550-1-4	**550**	**6.70E-01**	204.278	**19.37**	**18.16**	**18.42**
F-550-1-5	**550**	**6.70E-01**	196.437	**18.62**	**17.89**	**18.08**